UNIVERSIDAD COMPLUTENSE DE MADRID
FACULTAD DE CIENCIAS FÍSICAS

TESIS DOCTORAL

Measurement of the delayed neutron emission probability of ^{86}As and ^{91}Br

Medida de la probabilidad de emisión de neutrones retardados de ^{86}As y ^{91}Br

MEMORIA PARA OPTAR AL GRADO DE DOCTOR

PRESENTADA POR

Aczel Regino García Ríos

Directores

Daniel Cano Ott
Trinitario Martínez Pérez

Madrid

UNIVERSIDAD COMPLUTENSE DE MADRID
FACULTAD DE CIENCIAS FÍSICAS

TESIS DOCTORAL

Measurement of the delayed neutron emission probability of 86As and 91Br
Medida de la probabilidad de emisión de neutrones retardados de 86As y 91Br

MEMORIA PARA OPTAR AL GRADO DE DOCTOR

PRESENTADA POR

Aczel Regino García Ríos

DIRECTOR

Dr. Daniel Cano Ott
Dr. Trinitario Martínez Pérez

Universidad Complutense de Madrid
Facultad de Ciencias Físicas

Measurement of the delayed neutron emission probability of ^{86}As and ^{91}Br

Medida de la probabilidad de emisión de neutrones retardados de ^{86}As y ^{91}Br

A dissertation presented by

Aczel Regino García Ríos

in partial fulfilment of the requirements for the degree of
Doctor of Philosophy in the subject of Nuclear Physics

Advisors:

Dr. Daniel Cano Ott
Dr. Trinitario Martínez Pérez

GOBIERNO DE ESPAÑA
MINISTERIO DE CIENCIA E INNOVACIÓN
Ciemat
Centro de Investigaciones Energéticas, Medioambientales y Tecnológicas

To my parents,
with love and endless gratitude.

Table of Contents

List of Figures

List of Tables

List of Acronyms

ADC	Analogue to Digital Converter	40
BELEN	BEta deLayEd Neutron detector	13
BE	Bayesian Estimation	92
CERN	European Organization for Nuclear Research	11
CIEMAT	Research Center for Energy, Environment and Technology	12
CRP	Coordinated Research Project	131
DACQ	Data ACQuisition system	13
EFIT	European Facility for Industrial Transmutation	12
EMLF	Extended Maximum Likelihood Fit	115
ENDF	Evaluated Nuclear Data File	15
ENSDF	Evaluated Nuclear Structure Data File	2
ESFR	European Sodium-cooled Fast Reactor	12
EU	European Union	15
FA	Fuel Assembly	18
FIR	Finite Impulse Response	40
FPGA	Field-Programmable Gate Array	40
GEANT	GEometry ANd Tracking	42
G4NDL	GEANT4 Neutron Data Library	46
GOD	Genealogically Ordered Decay	87
GRS	Generation Random Sampled	24
HMWPE	High-Molecular-Weight PolyEthylene	37
HPDI	Highest Posterior Density Interval	92
HPGe	High-Purity Germanium	33
IAEA	International Atomic Energy Agency	5
IFIC	Institute of Corpuscular Physics	12
IGISOL	Ion Guide Isotope Separator On-Line	13
ILL	Laue-Langevin Institute	11
ISOL	Isotope Separator On-Line	31
ISOLDE	Isotope Separator On-Line DEvice	11
JYFL	Department of Physics of the University of Jyväskylä	13
JYFLTRAP	JYFL Penning TRAP	31
JEFF	Joint Evaluated Fission and Fusion file	15
JENDL	Japanese Evaluated Nuclear Data Library	15
LMD	List-Mode Data	72
MA	Minor Actinide	8

Chapter 1

Introduction

1.1 The β-delayed neutron emission process

β-delayed neutron emission is a common decay mode of isotopes far from the stability valley in the neutron-rich side. The term "delayed" refers in this context to the emission of neutrons following the beta decay and is used as distinction from prompt neutron emission in fission reactions.

Roberts et al. [1] discovered the process in 1939 while investigating the effects of bombarding uranium and thorium with neutrons. They placed a boron-lined ionization chamber close to a deuterium-lithium neutron source and intercalated a bottle with 100 g of uranium nitrate between the lithium target and the chamber. Both the target and the chamber were surrounded with paraffin for a higher neutron detection efficiency. When the beam was stopped, neutron signals continued to be observed for as long as 90 s. The neutron emission showed a similar half-life than observed before by Meitner et al. [2] for the beta emission, indicating the possibility of prompt neutron emission following a beta decay process. Roberts et al. confirmed later with L. R. Hafstad that this was indeed the nature of the process and not photodisintegration as they had also considered [3].

Figure 1.1 shows a schematic representation of the β-delayed neutron emission process. When the Q value of the β^- decay of a neutron rich nucleus ${}^{A}_{Z}X$ (hereafter precursor) exceeds the one-neutron separation energy of the ${}^{A}_{Z+1}X$ nucleus (hereafter emitter, not to be confused with delayed neutron emitter, which refers to the precursor), unbound states of the latter can be populated and neutron emission becomes energetically allowed. In general, the emission of $n > 1$ neutrons is energetically allowed when Q_β exceeds the n-neutron separation energy.

A high Q value is characteristic of β-delayed neutron emitters. The density of bound and unbound states of the emitter over the Q window is in consequence generally high, and the beta decay process is better described in statistical terms using the β-strength function $S_\beta(E)$ [4]. The total delayed neutron emission probability (the probability of emitting one

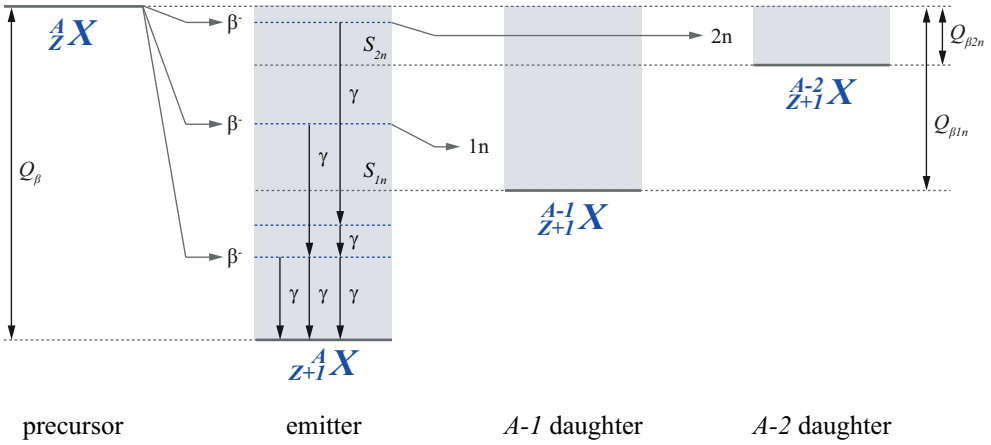

Figure 1.1: β-delayed neutron emission process. One- and two-neutron emission are represented to illustrate the general case of multiple neutron emission.

or more delayed neutrons) can be expressed in these terms as:

$$P_n = \frac{\int_{S_n}^{Q_\beta} S_\beta(E) f(Z+1, Q_\beta - E) \frac{\Gamma_n(E)}{\Gamma_{\rm tot}(E)} dE}{\int_{0}^{Q_\beta} S_\beta(E) f(Z+1, Q_\beta - E) dE} \tag{1.1}$$

where S_n is the neutron separation energy of the emitter, $f(Z+1, Q_\beta - E)$ the Fermi function, and $\Gamma_n(E)$ and $\Gamma_{\rm tot}(E)$ denote the neutron and total decay widths respectively. The presence of $\Gamma_n(E)/\Gamma_{\rm tot}(E)$ in the numerator reflects the fact that neutron emission from unbound states of the emitter competes with electromagnetic deexcitation to the ground state. Such competition has been observed with High-Resolution Gamma Spectrometry (HRGS) and Total Absorption Gamma Spectrometry (TAGS) (see for instance [5] and citations therein).

The recent large-scale theoretical evaluation by Marketin et al. [6] on 5409 neutron-rich nuclei[1] predicts that 90 % of them are β-delayed neutron emitters (figure 1.2). Of those, 87 % are one-neutron emitters, and the fractions of multiple-neutron emitters are: 79 % (two), 68 % (three), 53 % (four), and 66 % (five). To date, β-delayed neutron emission probabilities have been measured for about 210 nuclides according to the Evaluated Nuclear Structure Data File (ENSDF) [7,8] (figure 1.3), most of them in the fission ($70 \leq A \leq 150$) and light non-fission ($A < 70$) regions. The same library contains two-neutron emission probabilities for 19 nuclides, and three- and four-neutron emission probabilities just for ^{17}B. There may be more multiple-neutron emitters among those identified as one-neutron

[1] Calculations by Marketin et al. [6] must be interpreted within the limitations of the theoretical model used.

emitters, because multiple-neutron emission channels are difficult to distinguish experimentally. In fact, about 190 nuclides with β-delayed neutron emission probabilities in ENSDF are also two-neutron emitters according to Marketin et al. [6]. All this illustrates the complexity behind β-delayed neutron emission studies.

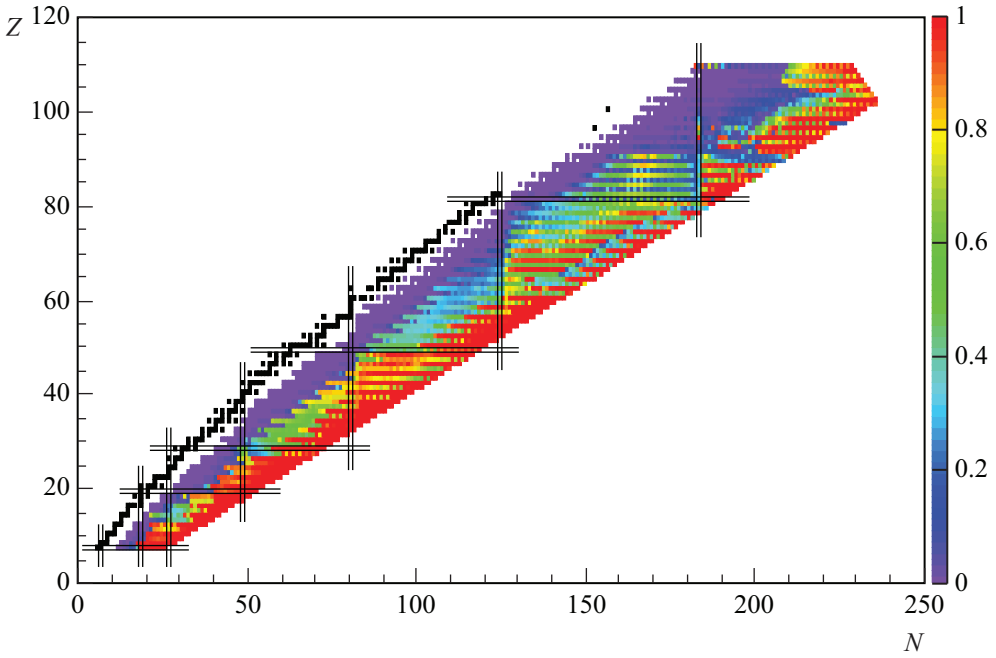

Figure 1.2: Total β-delayed neutron emission probabilities from the theoretical evaluation of Marketin et al. [6] represented over the chart of nuclides. Stable isotopes are also represented in black for reference.

Back to the nature of the process, note the gap in figure 1.2 between the stability valley and the delayed neutron emitters. It corresponds to nuclides for which the delayed neutron emission is not energetically allowed. Moving away from the stability valley at constant Z to the right, Q_β increases and the n-neutron separation energies of the $Z+1$ isobar decrease. Thus, as the energy window $Q_\beta - S_n$ for the beta decay to unbound states of the emitter extends, the more likely the emission of delayed neutrons and the higher the average number emitted neutrons becomes. The latter can be verified in figure 1.4.

Figure 1.2 also shows two interesting quantum effects. On the one hand, a shell effect: the process is favored for nuclides with only a few neutrons in excess with respect to a neutron closed shell. The other is a pairing effect manifested as an even-odd staggering of the neutron emission probability in both the number of protons and neutrons. Such staggering mirrors the staggering of the Q value and the neutron separation energies.

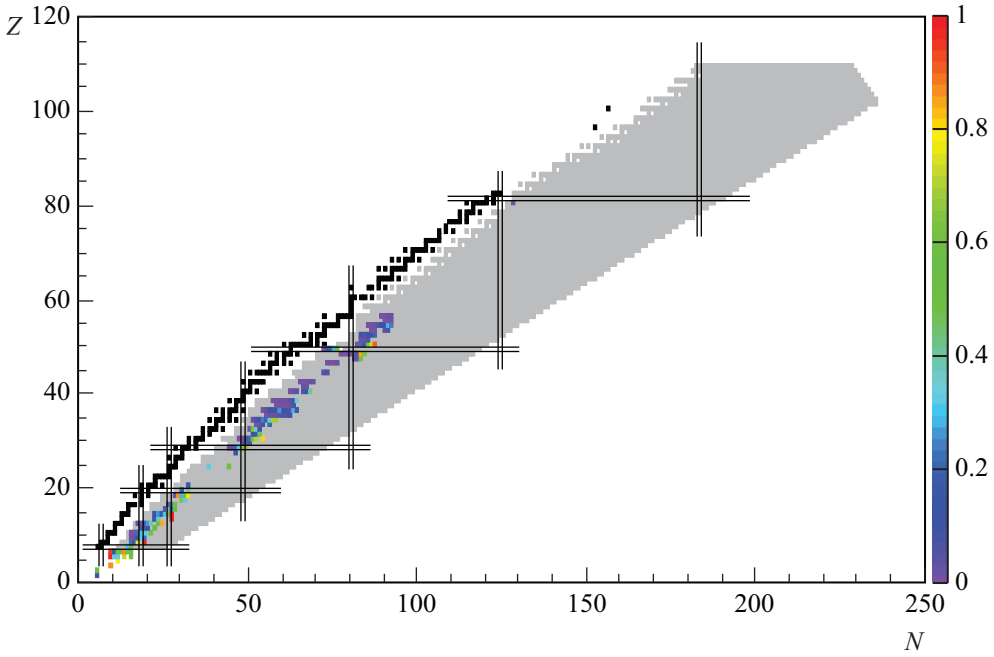

Figure 1.3: Total β-delayed neutron emission probabilities in ENSDF [7,8] represented over the chart of nuclides. Stable isotopes and the delayed neutron emitters studied by Marketin et al. [6] are represented in black and gray respectively for reference.

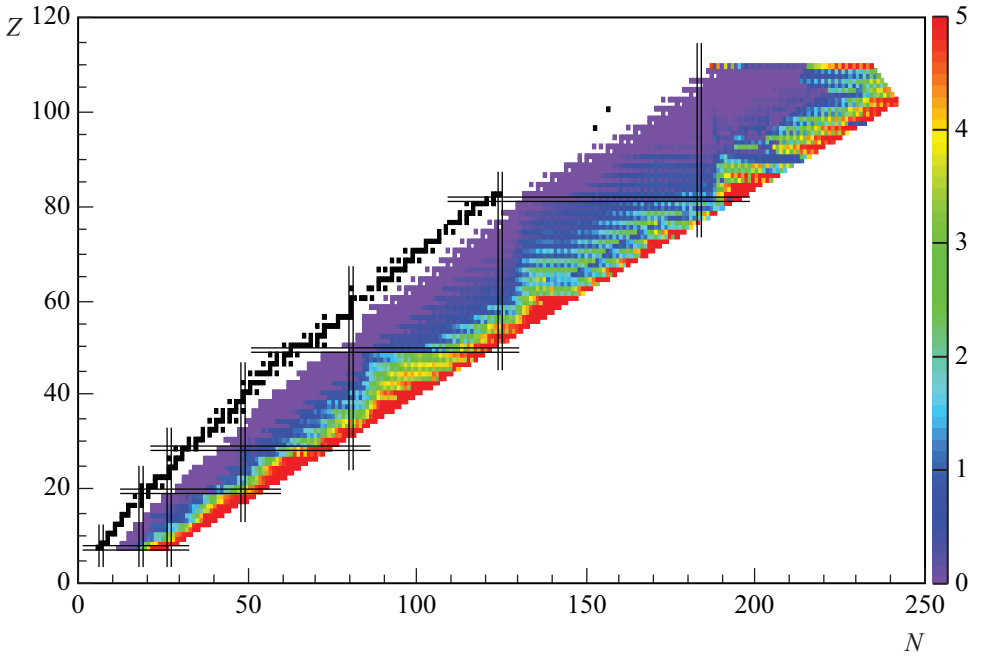

Figure 1.4: Average number of neutrons emitted per β^- decay from the theoretical evaluation of Marketin et al. [6] represented over the chart of nuclides. Stable isotopes are represented in black for reference.

1.2 β-delayed neutron emission data for science and technology

The β-delayed neutron emission process is of interest across different fields in nuclear science and technology [9], it is the latter though which has driven most of the interest after the discovery of the process. Progress in both fields demands more and higher-quality delayed neutron emission data than available nowadays as highlighted by the Nuclear Energy Agency (NEA) [10] and the International Atomic Energy Agency (IAEA) [11]. This section reviews the most relevant roles of the process in those fields and the specific data needs. For a comprehensive review see [9].

Nuclear technology

65% of the β-delayed neutron emitters with delayed neutron emission probabilities in ENSDF are in the fission region. This is no coincidence given the importance of delayed neutrons in nuclear technology. Fission is also the most common nuclear reaction used in the production of delayed neutron emitters in nuclear research.

Delayed neutrons are typically less than 1 % of the overall neutron emission in nuclear fission induced by thermal neutrons. 30 % of them are emitted within the first second after the fission event. The rest of the emission extends up to a few minutes, and it is this and not their contribution to the power generation what makes delayed neutrons so important for the design and operation of nuclear reactors [12].

Nuclear reactors can be susceptible to unexpected reactivity increases that may lead to a prompt-criticality accident with severe consequences. Without delayed neutrons, even a slight increase in the reactivity above criticality would cause the neutron flux in the core —and therefore the reactor power— to increase at a rate too high for the control systems to be effective. The reactor may in consequence result irreparably damaged or its containment may end up breached, releasing radioactivity into the environment in the worst-case scenario. Delayed neutrons slow the reactor response to reactivity changes, enough to make it controllable [12].

Consider, for the sake of illustration, ^{235}U in a Pressurized Water Reactor (PWR) [13, example given in section 4.2.2]. The average prompt neutron generation time at criticality is τ_p =25 ns and the average life-time of the delayed neutron precursors is τ_d =11.31 s. With a total fraction of delayed to prompt neutrons $\beta = \langle\nu_d\rangle/\langle\nu_p\rangle$=0.00679 for thermal neutron-induced fission, the weighted average of the prompt and delayed neutron generation times (i.e., the mean generation time) is $\tau = \tau_p(1-\beta)+\beta(\tau_p+\tau_d) = \tau_p+\beta\tau_d = 77$ ms. Such a large increment in the mean generation time extends the reactor period (the time required for the neutron density $n(t)$ in the reactor to change by a factor e) from 0.25 s to 12.8 min for a slight increase of 0.01 % in the neutron multiplication factor k from criticality according to the point kinetics approximation:

$$n(t) = n(0)e^{\left(\frac{k-1}{\tau}\right)t} \tag{1.2}$$

Prompt and delayed neutrons are emitted with different energy distributions. For instance,

2 MeV is the average energy of prompt neutrons from the thermal neutron-induced fission of ^{235}U, whereas for delayed neutrons it is 400 keV. Hence, delayed neutrons are more effective than prompt neutrons in inducing fission. The effectiveness is also a function of the position inside the reactor where the fission event occurs. For these reasons, it is an effective fraction of delayed to prompt neutrons β_{eff} and not β what actually determines the margin of control in a nuclear reactor.

β_{eff} relates to β and the fractions β_i for individual delayed neutron emitters or delayed neutron emitter groups in the multigroup representation as $\beta_{\text{eff}} = \gamma\beta = \sum_i \gamma_i\beta_i$, where γ and γ_i represent the average and individual effectiveness factors respectively. The delayed neutron data required for reactor calculations depends thus on the calculation approach, i.e., whether delayed neutron emitters considered individually (summation calculations) or grouped conveniently for simplicity (multigroup calculations). Both approaches rely on fission yields, decay constants, and average —delayed and prompt— neutron yields, and only summation calculations requires in addition delayed neutron emission probabilities. Large uncertainties in these data may result in excess of conservatism in the reactor design and operation. It is clear then that high-quality data on delayed neutron emission are required for the development of reactor technology [10].

The need for delayed neutron data also stems from decay heat calculations [14]. Decay heat is produced by gamma, beta, and alpha particles emitted in the decay of fission products. It accounts for 8 to 12 % of the energy generation during reactor operation and becomes the dominant source when the reactor is shut down. The β-delayed neutron emission process needs to be well quantified to avoid the misdetermination of the average gamma and beta energies, essential for the accuracy and predictive power of decay heat summation calculations.

Nuclear astrophysics

The isotopic abundance distribution in the Universe hides the history of matter, as it results from multiple complex nucleosynthesis processes (e.g., H and He burning; and α-, e-, s-, r-, p-, and γ-processes) that have occurred in different scenarios upon the Universe creation. It has long been a challenge in astrophysics to unveil such history, and for that, a deep knowledge of those processes is required.

The synthesis of about 50 % of the elements heavier than iron in our solar system and presumably all elements heavier than bismuth is driven by the so called *rapid* process (hereafter r-process) [15], which occurs in scenarios of relatively high neutron density ($>10^{20}$ g cm^{-3}) and temperature ($>10^9$ K). The process consists in the progressive build-up of heavier isotopes in a succession of rapid neutron captures interspersed with beta decays. It is thus a complex interplay between weak, strong and electromagnetic interactions that occurs on the neutron-rich side of the stability valley.

Along the r-process path, the $(n,\gamma) \rightleftarrows (\gamma,n)$ equilibrium can be reached at points where neutron capture occurs at a higher rate than beta decay. Those points on the chart of nuclides are known as *waiting points*. The flow of the process slows down around them, as the build-up can only proceed by beta decay. As a result, the isotopic abundance around the waiting points is higher. This can be observed in the isotopic abundance distribution in

our solar system shown in figure 1.5. The prominent peaks at A =80, 130 and 195 indicate that nuclei with a magic number of neutrons (50, 82 and 126) constitute the dominant waiting points as expected from their enhanced stability.

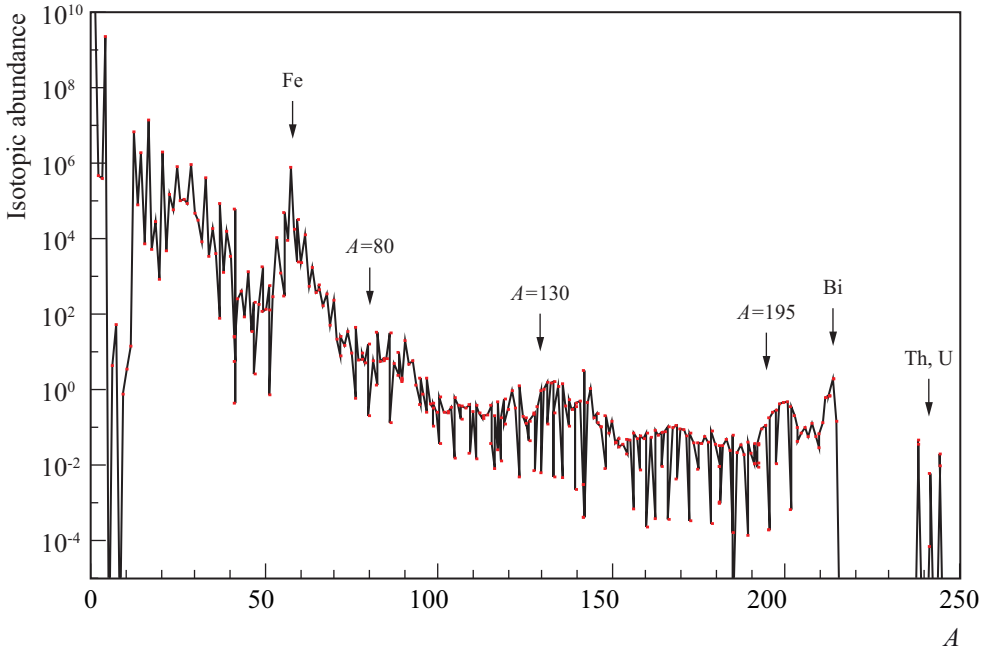

Figure 1.5: Isotopic abundance distribution in our solar system relative to the abundance of Si ($\equiv 10^6$) [16, table 6].

It is in the waiting points where the β-delayed neutron emission is more relevant to the dynamics of the r-process, it can occur though at any other stage if energetically allowed. The β^- decay followed by neutron emission takes the r-process path to a lower mass chain. As a result, the isotopic abundance distribution is shifted to lower masses and modulated. Thus, it becomes clear that the radioactive decay properties of β-delayed neutron emitters are essential data to r-process calculations.

Nuclear structure

r-process calculations involve nuclear and radioactive properties of a large number of nuclides, most of which cannot be produced or investigated with the technology of nowadays. To make them possible, there is no alternative but to resort to nuclear structure models. The accuracy of r-process calculations depends thus to a large extent on the predictive capacity of the theoretical models used. Accurate measurements of the gross decay properties improve r-process calculations not only as direct input, but also helping refine the nuclear structure models.

The delayed neutron emission probabilities in particular can provide valuable structural information, specially on the most neutron-rich nuclei. Equation 1.1 showed the relationship

between the total β-delayed neutron emission probability and nuclear structure quantities. P_n alone has a limited physical significance, but combined with the half-life, which is the inverse of the term in the denominator, it can unveil information about the feeding to unbound states of the emitter.

1.3 Why measuring the delayed neutron emission probability of ^{86}As and ^{91}Br?

^{86}As and ^{91}Br are close to the $N = 50$ isotones on the r-process path. The proximity to dominant waiting points right at the beginning of the r-process path makes them particularly important to r-process calculations. In addition to the macroscopic effects on the isotopic abundance distribution, r-process calculations can be expected to be highly sensitive to the gross decay properties of nuclei in this region.

Advanced nuclear energy systems are being designed nowadays with a focus on closed fuel cycles and transmutation of Minor Actinides (MAs) partitioned from nuclear waste. In consequence, they differ significantly from conventional nuclear reactors in fuel and MAs inventories. Summation calculations could improve their designs by accounting for the delayed neutron emission of MAs that lack multigroup representation based on integral measurements and for which models based on systematics are not accurate enough. ^{86}As and ^{91}Br happen to be important contributors to the delayed neutron emission of major and minor actinides. Accurate measurements of their delayed neutron emission probabilities can improve the accuracy of summation calculations.

1.3.1 Experimental methods

Multiple experimental methods to measure β-delayed neutron emission probabilities have been developed since the discovery of the process. The simplest in concept to measure the one-neutron emission probability stems straight from the definition of the magnitude itself, i.e., the ratio of the number of beta decays followed by neutron emission to the total number of decays. For one-neutron emitters, the number of emitted neutrons determines the former. Thus, by separate counting of neutrons and beta particles, the delayed one-neutron emission probability can be estimated as:

$$P_n = \frac{\varepsilon_\beta}{\varepsilon_n}\frac{N_n}{N_\beta} \tag{1.3}$$

where, for beta particles and neutrons emitted by the precursor, ε denotes the detection efficiency and N the number of detected events. This is the so called $n - \beta$ method[2]. Note that it requires a prior efficiency characterization of the detection system, which is a major inconvenient because the detection efficiencies depend on the spectrum of the emitted radiation and therefore are isotope-dependent. Attempts to use calibration sources

[2]For consistency with Abriola et al. [11] and the compilation of Rudstam et al. [17], the same terminology therein is used throughout this manuscript.

or Monte Carlo simulations to estimate the efficiencies may result in large systematic uncertainties. On the other hand, the method relies on the identification of the decay events of the precursor —among events from the decay of other nuclei in the radioactive decay chain and contaminants, electronic noise, and room background— and that may be challenging. Other methods that rely on beta and neutron counting face the same inconvenients and challenges.

A similar method known as n/β is based on counting beta particles and beta-neutron coincidences. It enhances the sensitivity to the detection of delayed neutrons. Early applications of this method highlighted its independence of the beta detection efficiency as an advantage [18,19], which is true if the energy dependence of the beta detection efficiency is neglected. More recently, however, Agramunt et al. [20] pointed out that such an assumption may lead to significant systematic uncertainties. Indeed, the probability of detecting a beta-neutron coincidence is the conditional probability of detecting a delayed neutron, provided that the beta particle from the decay of the precursor was detected and that the decay was followed by neutron emission. That yields:

$$N_{\beta-n} = \frac{N_\beta}{\varepsilon_\beta} P_n \varepsilon_{\beta n} \varepsilon_n \tag{1.4}$$

where $\varepsilon_{\beta n}$ is the efficiency of detecting a beta particle from the decay of the precursor followed by neutron emission. Solving the previous equation for P_n gives:

$$P_n = \frac{\varepsilon_\beta}{\varepsilon_{\beta n}\varepsilon_n} \frac{N_{\beta-n}}{N_\beta} \tag{1.5}$$

Note that, if the energy dependence of the beta detection efficiency is neglected, $\varepsilon_{\beta n} = \varepsilon_\beta$ and P_n does not depend at all on the beta detection efficiency. But this is not the general case. It will be shown in chapter 4 how the beta detection efficiency can vary with the end-point of the beta distribution. Monte Carlo simulations could be used to estimate the beta detection efficiencies provided that the beta intensity distribution is known over the entire energy window, but they would not be exempt of large systematic uncertainties.

The P_n ${}^{A}_{Z}X$ method, which is the one used in this work, does not require an absolute efficiency characterization of the detection system unlike the previous two. The idea behind is to normalize the detection system to the well known P_n value of a reference β-delayed neutron emitter ${}^{A}_{Z}X$. Whereas this is a significant advantage, the method is not exempt of systematic uncertainties originating from the energy dependence of the detection efficiencies. By normalizing to a reference nuclide, it ignores the effects of the beta and neutron emission spectra on the efficiencies. Such effects can be considered though a posteriori by Monte Carlo simulations to avoid the corresponding systematic uncertainty.

Another method is based on ion counting and any suitable method to identify decays followed by neutron emission. With this, P_n can be estimated as the ratio of the number delayed neutron emissions to the number of precursor ions. Despite its conceptual simplicity, the *ion* method —as it is called— has the same disadvantages of the n/β and $n-\beta$ methods, namely the need for an efficiency characterization of the detection system.

An alternative to ion counting with dedicated instruments is the use of fission yields when fission is the production method. This is the so called *fiss* method. According to Abriola et al. [11] this method may be the least reliable of all, because in addition to the disadvantages of the ion method, it relies on the quality of the fission yields data.

Finally, the β-delayed neutron emission probabilities can also be estimated (entirely by or in combination with) gamma counting. The $n-\gamma$ method combines gamma and neutron counting, while the alternative method $\gamma-\gamma$ relies only on gamma counting. In either case, the absolute gamma intensities are needed. Those are an important source of systematic uncertainty in both methods, unlike the gamma detection efficiency, which can be determined with high accuracy.

1.3.2 Previous measurements

^{86}As

Few measurements of the delayed one-neutron emission probability of ^{86}As have been performed to date. Here is a review:

Kratz et al. [21] in 1973 measured the delayed one-neutron emission probability of ^{86}As and two other arsenic isotopes at the Institut für Anorganische und Kernchemie der Universität Mainz, Germany, via the thermal neutron-induced fission of ^{235}U and subsequent isolation by volatilization of arsenic hydride. They reported that "a new isotope, 0.9 ± 0.2 s ^{86}As, was detected by delayed neutron counting and by following the decay of its most prominent γ-ray. (...) Using the measured delayed-neutron yields and measured or estimated fission yields, the following neutron emission probabilities were obtained: (...) $P_n(^{86}\text{As}) = 3.8^{+1.7}_{-1.0}$ %."

Crançon et al. [22] in 1978 measured the β-delayed neutron emission probability of short-lived isotopes in several mass chains including A =86. The experiment and the method of analysis will be summarized in section 1.3.2 (see Asghar et al. [23] therein). For ^{86}As, the estimated value was 10.5 ± 2.2 %.

Rudstam et al. [17] in 1993 measured the β-delayed neutron emission probability of multiple fission products in the mass range between A =79 and A =150 at the OSIRIS isotope separator at the Studsvik Science Research Laboratory, Nyköping, Sweden. The experiment consisted of ions implanted on an aluminized Mylar tape at the center of a 4π neutron detector that measured the neutron counting rate. The detector consisted of 40 long BF_3 counters embedded in three concentric cylindrical layers of graphite with polyethylene in between. A 1 mm thick plastic scintillator (NE102A) was also placed in front of the implantation point to measure the beta counting rate simultaneously. Both detectors had previously been calibrated in efficiency. For ^{86}As, the measured value was 33.0 ± 3.6 %. Rudstam et al. also reported the revised values 15 ± 11 % and 12 ± 8 % of the Kratz et al. [21] and Crançon et al. [22] results respectively obtained with higher-quality fission yields from [24].

^{91}Br

A few more measurements of the delayed neutron emission probability of ^{91}Br than for ^{86}As have been performed in the past, most of them based on the same experimental method used in this work. Here is a review:

Kratz & Herrmann [25] applied in 1974 rapid radiochemical separation techniques to investigate the delayed neutron emission of bromine and iodine isotopes. The investigated isotopes were produced by the thermal neutron irradiation of a 90 % enriched uranium target at the TRIGA reactor of the Institut für Kernchemie, Universität Mainz, Germany. The delayed neutron emission probabilities were estimated from the measured neutron abundances and known cumulative fission yields. For ^{91}Br, the estimated value was 8.3 ± 2.5 %. This value deviates more than 50 % from other values measured to date. The uncertainty in the fission yields and the presence of contaminants make the experimental method used unreliable.

Asghar et al. [23] used in 1975 the recoil focusing parabola-type mass separator for unslowed fission products LOHENGRIN installed at the high flux reactor of the Laue-Langevin Institute (ILL), Grenoble, France, to separate ions of β-delayed neutron emitters in several mass chains between A =90 and A =138. Those ions were implanted onto a tape that transported them through the detection setup, where the beta and neutron counting rates were measured simultaneously. The implantation was not concentrated on a single point of the tape, but over 72 cm due to the energy spread of the separated ions. Upon implantation, the tape was moved at different speeds, and the dependence of the counting rate with the speed was used to derive the delayed neutron emission probabilities. For ^{91}Br, the measured value was 9.86 ± 1.97 %. As in the latter work, this new value is affected by uncertainties in the fission yields of ^{235}U, which was used as a target to produce the isotopes investigated. The fission yields were used to fix the ratio between the number of implanted ions of different isotopes per unit length of the tape.

Aleklett et al. [26] measured in 1980 the β-delayed neutron emission probability of bromine and iodine isotopes at OSIRIS [27]. Ions were implanted on an aluminized Mylar tape at the center of a 4π neutron detector and in front of a 5 mm thick plastic scintillator for beta detection. The neutron detector consisted of 29 ^{3}He counters embedded in paraffin and arranged in two concentric crowns around the implantation point. Both detectors had previously been calibrated in efficiency. The delayed neutron emission probabilities were derived by measuring the beta and neutron counting rates simultaneously. For ^{91}Br, the measured value was 19.2 ± 1.3 %.

Ewan et al. [28] investigated in 1984 the delayed neutron emission of $^{89-92}$Br with the Isotope Separator On-Line DEvice (ISOLDE) at the European Organization for Nuclear Research (CERN), Switzerland. Ions were implanted on an aluminized tape, and the beta and neutron counting rates were measured simultaneously with a plastic scintillator and a neutron detector of ^{3}He counters embedded in paraffin respectively. In contrast with Aleklett et al. [26], Ewan et al. did not perform an absolute calibration of the detection system. Instead, they applied the P_n $^{A}_{Z}X$ method using the assumed well known P_n value of ^{89}Br. For ^{91}Br, the measured value was 30.1 ± 2.1 %.

Kratz et al. [29] in 1988 published a short note on a systematic investigation of the decay properties of several bromine isotopes performed at ISOLDE and at the mass separator OSTIS at ILL, Grenoble, France. The P_n values were obtained by measuring the beta and neutron counting rates simultaneously. For ^{91}Br, the measured value was $25.5 \pm 3.5\,\%$.

Rudstam et al. [17] obtained $P_n = 22 \pm 10\,\%$ for ^{91}Br, which has the worst relative uncertainty of all the previous measurements. The measurement was described in the previous section. They also reported the revised value $16 \pm 5\,\%$ of the Kratz & Herrmann [25] measurement obtained with higher-quality fission yields from [24].

1.4 Scope, angle and outline of this work

An overview of the β-delayed neutron emission process and its relevance for nuclear science and technology was encompassed in sections 1.1 and 1.2 respectively. The subject is vast and complex, hence the need to delimit the scope of this work.

This is a manuscript on an experimental scientific research aimed at measuring the β-delayed neutron emission probability of ^{86}As and ^{91}Br with high accuracy. The research was conducted within a collaboration between the Research Center for Energy, Environment and Technology (CIEMAT), the Spanish Institute of Corpuscular Physics (IFIC), the Polytechnic University of Catalonia (UPC) and the University of Jyväskylä. All four institutions have diverse but also common interests in the subject.

The Nuclear Innovation Unit at CIEMAT contributes to the development of advanced nuclear energy systems [30]. The field is characterized by low target uncertainty requirements on the relevant nuclear data to meet ambitious goals such as closed fuel cycles and transmutation of MAs partitioned from nuclear waste with an emphasis on operational safety. Hence the focus of this manuscript on nuclear data —and on β-delayed neutron emission probabilities in particular— from the beginning, which is one of the main research activities at the Nuclear Innovation Unit. The next chapter presents the motivation of this work by illustrating the specific roles of ^{86}As and ^{91}Br in delayed neutron calculations on two European advanced reactor concepts: the European Sodium-cooled Fast Reactor (ESFR) and the European Facility for Industrial Transmutation (EFIT).

Section 1.3.1 reviewed the existing experimental methods for measuring β-delayed one-neutron emission probabilities. The discussion therein on the advantages and disadvantages of the different methods showed why the $P_n\,{}^{A}_{Z}X$ method based on beta and neutron counting was chosen in this work. Whereas the extension of this method to multiple neutron emission is possible, all β-delayed neutron emitters on which the experiment was conducted are considered in this work one-neutron emitters, avoiding thus the complexity of distinguishing between delayed neutron emission events with different multiplicities (see for instance [31] and [32, section 4]). ^{86}As is, among them, the only multiple(two)-neutron emitter candidate according to theoretical calculations by Kawano et al. [33], but the predicted two-neutron emission probability is so low ($6.2991 \times 10^{-4}\,\%$) that the manifestation of the two-neutron emission process would negligible. An experimental confirmation requires high production rates, high detection efficiency and a significant reduction of sys-

tematic uncertainties. This work is a major step in those three directions.

Chapter 3 describes the experimental facility, the detection system, and how the experiment was planned and executed. It lays out from the beginning the unique quality of the Ion Guide Isotope Separator On-Line (IGISOL) facility at the Accelerator Laboratory of the Department of Physics of the University of Jyväskylä (JYFL), Finland, for performing high-precision decay experiments on β-delayed neutron emitters. Then, it goes on to describing the BEta deLayEd Neutron detector (BELEN) and its coupling with the implantation setup and other elements of the detection system for a near 4π geometrical efficiency. The digital Data ACQuisition system (DACQ) designed *ad hoc* for BELEN at IFIC is also presented in the chapter. Finally, the chapter describes how the experiment was performed in measurement cycles divided in three well defined intervals of different dynamics.

The fourth chapter addresses the efficiency characterization of the detection system by Monte Carlo simulations. The chapter is divided in two main sections, one for neutron detection with BELEN and another one for beta detection with a silicon detector. It dives deep into the underlying physics at the beginning of each section, focusing on how it is modeled in the simulation codes used. The results presented therein were essential to account for the isotope-dependent effects on the detection efficiencies in the application of the $P_n\,{}^{A}_{Z}X$ method presented later in chapter 6.

Chapter 5 describes how the data was prepared for the analysis, i.e., how it was unpacked and sorted, explored, cleaned and reconstructed. The cleaning entailed the energy calibration of the detection system to separate most unwanted events.

The methodology of analysis, its application, and the results obtained are finally presented in chapter 6. For modeling the time distribution of neutron and beta particle events, from which the delayed neutron emission probability is estimated, detailed models are drawn at the beginning. These are then conveniently reduced and reparameterized to render identifiable the parameters of interest. The analysis proceeds then in two stages: the efficiency characterization of the detection system with measurements on reference nuclei, and the estimation of the β-delayed one-neutron emission probability of ^{86}As and ^{91}Br. At the end of the chapter, the results are discussed and compared with previous measurements and evaluations.

Chapter 2

Motivation from nuclear technology

Contemporary and future nuclear energy programs aim to reach a high level of sustainability, safety, competitiveness and robustness [34]. The viability of those programs to meet such ambitious goals depends on the accurate description of the underlying physics in computational simulations [35], given the lack of practical experience with advanced nuclear energy systems in contrast with the existing ones.

Computational simulations are generally cheaper and faster than experiments and can also provide more information about the underlying processes. They are inherently dependent on models and experimental data. A rich experience has been gathered to date with simulation codes in support of nuclear energy systems. Those codes continue to be improved in modeling accuracy and performance. The precision, accuracy and completeness of the nuclear data are, however, insufficient to perform reliable computational simulations of future systems.

Delayed neutrons in nuclear energy systems originate from the radioactive decay of neutron rich fission products. The fission yields are therefore the starting point of delayed neutron calculations. Other data are required depending on the calculation approach.

Summation calculations, the most fundamental approach, consider the independent contributions of delayed neutron emitters. It relies on radioactive decay data, which for many short-lived nuclei are unreliable or unknown. For this reason, summation calculations are to date not suitable to describe the delayed neutron emission at short times after the fission event. The extent to which radioactive decay data —specially on delayed neutron emitters— are complete and accurate determines the accuracy of delayed neutron summation calculations.

Multigroup calculations are a more practical approach proposed by Keepin & Weinberg [36] that consists in grouping the delayed neutron emitters based on their half-lives. Each group is characterized by an exponential function with an effective decay constant and abundance, such that combined they describe the overall time distribution of delayed neutron emission. This approach, despite its simplicity, has a major disadvantage. The

effective decay constants and abundances are obtained from the non-linear Least Squares Fit (LSF) of the aggregate function to data that can be experimental (from the irradiation of a sample of the fissioning material with a neutron source) or resulting from summation calculations for the less common fissioning isotopes. In consequence, the values obtained differ between fissioning isotopes and depend on the incident neutron energy.

The present chapter illustrates the role of ^{86}As and ^{91}Br in the development of advanced nuclear energy systems with delayed neutron summation calculations on two European advanced reactor concepts.

2.1 Completeness of evaluated nuclear data libraries

Theoretical models and experimental data are combined together to produce evaluated nuclear data libraries that provide a complete description of nuclear reactions to satisfy particular national interests and requirements of specific applications. General-purpose libraries are developed by countries with strong nuclear programs, e.g., the Evaluated Nuclear Data File (ENDF) by the United States of America (USA), the Joint Evaluated Fission and Fusion file (JEFF) by the European Union (EU) and the Japanese Evaluated Nuclear Data Library (JENDL) by Japan. Unlike special-purpose libraries, they are not limited to specific applications nor users, and that is why they are more complete and consistent.

ENDF/B, JEFF and JENDL have been extensively validated against integral measurements and continuously improved and updated since they were first released. Hence their extended use by the nuclear scientific community and industry. Here is a brief overview on each one:

ENDF/B: Produced by the Cross Section Evaluation Working Group (CSEWG), an organization nourished from the cooperative efforts of different institutions and industrial sectors in the USA and Canada [37]. It is the most complete of the three libraries in terms of physical quantities and processes. The latest stable release ENDF/B-VIII.0 [38,39] was distributed on February 2, 2018.

JEFF: Results from a collaboration between the NEA Data Bank member countries to produce a common set of evaluated nuclear data for fission and fusion applications [40]. The latest release JEFF-3.3 [41] was distributed on November 2017.

JENDL: Maintained by the Nuclear Data Center (NDC) of the Japan Atomic Energy Agency (JAEA) in cooperation with the Japanese Nuclear Data Committee (JNDC), has been available for over four decades in support of the Research and Development (R&D) on advanced nuclear energy systems. The latest release JENDL-4.0 [42,43], less complete though than ENDF/B-VIII.0 and JEFF-3.3, is among the most extensive sources of independent evaluations after ENDF/B [44].

Table 2.1 summarizes the completeness of the data relevant for delayed neutron calculations in the latest releases of these libraries. Bear in mind that evaluated nuclear data libraries often share evaluations or base their evaluations on the evaluations of the others. Library ENDF/B-VII.1 is also included in the table, because ^{91}Br was not considered a delayed

neutron emitter in ENDF/B-VIII.0. Delayed neutron calculations with ENDF/B presented in this chapter used ENDF/B-VII.1 accordingly.

Data type	ENDF/B		JEFF-3.3	JENDL-4.0
	VII.1	VIII.0		
Fission yields	31	31	19	31[a)]
Radioactive decay	3562	3562	3626	2993[b)]
Delayed neutron emission probabilities	390	388	224	348[b)]
Delayed neutron energy spectra	314	312	80	0[b)]
Multigroup representation	82	82	65	81[a)]

Table 2.1: Completeness of the data relevant for delayed neutron calculations in ENDF/B-VII.1 [45], ENDF/B-VIII.0 [38,39], JEFF-3.3 [41], and JENDL-4.0 [42,43]. The number of nuclides with each type of data are indicated.

[a] JENDL FP Fission Yields Data File 2011 (JENDL/FPY-2011) [46].
[b] JENDL Decay Data File 2015 (JENDL/DDF-2015) [47,48].

2.1.1 Fission yields

Fission yields in ENDF/B-VII.1 are based on the evaluation of England & Rider [49], except for ^{239}Pu, whose yields were improved for all but thermal neutron energies [45, section IV.A]. JEFF-3.3, on the other hand, contains fission yields from the TALYS Evaluated Nuclear Data Library (TENDL) [50]. In JENDL-4.0, the fission yields are based on theoretical calculations that considered only fission products for which radioactive decay data are given to guarantee the consistency between both data sets [42,51].

2.1.2 Radioactive decay

Table 2.1 shows that JEFF-3.3 is the most complete library attending to the number of nuclides with radioactive decay data, not far from ENDF/B-VII.1 though. The least complete is JENDL-4.0, with data for about 60 % less nuclides. However, JEFF-3.3 is the most incomplete attending the number of β-delayed one-neutron emitters with decay data. As for delayed multiple-neutron emitters, only ENDF/B-VII.1 and JEFF-3.3 have decay data for a handful of them.

The main source of radioactive decay data in ENDF/B-VII.1 [45] and JENDL-4.0 [52] is the Evaluated Nuclear Structure Data File (ENSDF) [7,8], which is maintained by an international cooperation coordinated by the IAEA. It contains evaluated nuclear structure and decay data for over 2900 nuclides. Decay data in JEFF-3.3, on the other hand, is based on the NUBASE 2003 evaluation of nuclear and decay properties distributed by the Atomic Mass Data Center (AMDC) [53]. Most of the radioactive decay data in NUBASE 2003 —given for about 600 nuclides— are included in ENSDF [54].

ENDF/B-VII.1 contains radioactive decay data for 3562 nuclides. The β-delayed neutron emission spectra are based to the largest extent on the scarce experimental data available. Theoretical calculations by Kawano et al. [33] were used in the preparation of the library to complete or entirely provide those spectra for all nuclei produced in the thermal neutron-induced fission of ^{235}U and ^{239}Pu. The same calculations provided delayed neutron emission probabilities missing in ENSDF, while missing half-lives were taken from the compilation of Pfeiffer et al. [55].

JEFF-3.3 was released with its own special-purpose library for radioactive decay data covering 3626 nuclides. Unlike ENDF/B, JEFF does not aim at completion, but at representing measured decay data accurately without global adjustments or theoretical calculations [56]. JEFF-3.3 is however complete in the sense that the radioactive decay chain of any of nuclide with decay data can be entirely propagated. To meet in accuracy and completeness the requirements of nowadays applications, in the preparation of JEFF-3.3 the data from NUBASE 2003 was replaced or completed with more comprehensive and higher-quality data from other sources.

Radioactive decay data in JENDL-4.0 are distributed in the special-purpose library JENDL /DDF-2015. The latter incorporates data for 1953 nuclides from ENDF/B-VII.1, in addition to its own evaluation for 1284 nuclides more [47,48]. The delayed neutron emission probabilities incorporated from ENSDF were completed with the theoretical calculations by Pfeiffer et al. [55] with the empirical Kratz-Herrmann formula [57]. It should be noted that the use of JENDL for delayed neutron calculations is limited, because it contains no delayed neutron emission spectra.

2.1.3 Multigroup representation

5 or 6 groups have traditionally been used for the multigroup representation of delayed neutron emission. Gudkov et al. [58] showed that over 80 % of delayed neutrons for the most common fissioning isotopes are emitted by a handful of fission products. Thus, a representation with one group per dominant precursor should allow for a unique set of energy-independent decay constants for all fissioning isotopes without significant implications on the outcome of delayed neutron calculations. Indeed, the 8-groups representation proposed by Spriggs et al. [59] confirmed such hypothesis and for that it has been recommended by the NEA for future use in delayed neutron calculations [10]. JEFF adopted the 8-groups representation since JEFF-3.3 for 30 fissioning isotopes. ENDF/B-VII.1 and JENDL-4.0, as well as JEFF-3.3 for other 19 fissioning isotopes, still use the 6-group representation. The 8-groups representation simplifies the simulation of the dynamics of advanced nuclear energy systems involving multiple fissioning isotopes.

Early versions of ENDF/B based the multigroup representation on selected experimental results [60]. In the preparation of ENDF/B-VI and later releases, summation calculations were used instead [45]. This new approach was kept in ENDF/B-VII.1, noting that the predictive power of summation calculations was in general weak. The same approach was embraced for JENDL-4.0 [42]. However, the latest multigroup representation evaluation recommended by the IAEA for the major actinides is based on experimental data from integral experiments [61,62].

2.2 Two advanced reactor concepts in Europe

There is a worldwide recognition of the maturity of fast reactor technology given the operational experience gathered for over 50 years and its unique potential as sustainable energy source in terms of utilization of the nuclear fuel and minimization of the nuclear waste. Hence the ongoing ambitious projects of countries with strong nuclear energy programs to deploy fast reactors in the short-term [63]. Among the fast reactors, the sodium-cooled has the most viable technological basis. The EU has adopted this technology with the European Sodium-cooled Fast Reactor (ESFR) [64,65] in a renewed vision of future nuclear energy systems after several realizations of Sodium-cooled Fast Reactors (SFRs).

Fast reactors are also among the main strategies in the development of advanced nuclear fuel cycles for their potential to operate with closed cycles and to transmute MAs partitioned from nuclear waste [66]. The Partitioning and Transmutation (P&T) of MAs reduces the volume, heat load and toxicity of High-Level Nuclear Waste (HLNW), relaxing the constraints and reducing the safety concerns of geological disposal [67]. The EU has been supporting in the last years the development of advanced fuel cycles based on fast critical and/or subcritical reactors and P&T [68]. Accelerator-Driven Systems (ADSs) are also of particular interest to this purpose, as they can burn nuclear fuels with a higher content of MAs than critical fast reactors. In line with this interest, the EURopean ATOMic energy community (EURATOM) has executed in the last years an ambitious R&D agenda toward an industrial-scale transmutation facility in Europe: the European Facility for Industrial Transmutation (EFIT). The conceptual design of EFIT was developed for the demonstration of efficient transmutation and the associated technology.

A detailed presentation of the technological aspects of ESFR and EFIT are out of the scope of this work and can be found in the references aforecited. Next in this section, the core of both systems are described, for it is the relevant technological input to the burn-up calculations presented and discussed later.

ESFR

Figure 2.1 shows a radial cross section of the so called CONF2 core of ESFR [69]. It consists of two concentric regions of driver fuel with 225 Fuel Assemblies (FAs) in the inner and 228 in the outer, surrounded by three concentric rings of reflector assemblies. In the bottom, it has a fertile blanket of depleted uranium with a gas plenum underneath. A sodium plenum and an absorbent and a reflector layer close the core from the top. Each FA has 271 pins loaded with Mixed OXide (MOX) fuel containing a small amount of ^{241}Am from the decay of ^{241}Pu. FAs in the inner and outer regions of the active core have a plutonium content of 14.76 wt% and 17.15 wt% respectively.

Transmutation of MAs is one of the main design goals of ESFR, but MA loading has a negative impact on multiple aspects of the reactor, e.g., on safety parameters and reactivity coefficients (see for instance [70,71]). Different MA loadings have been proposed after carefully addressing these effects. Among them, the following two have been considered in the burn-up calculations presented in the next section:

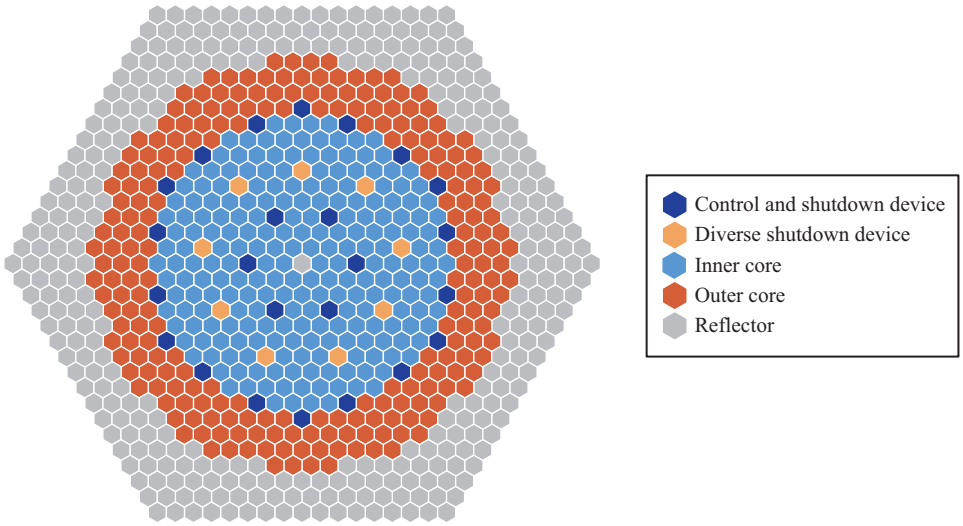

Figure 2.1: Core of the European Sodium-cooled Fast Reactor (ESFR).

HOM4: Homogeneous distribution of a mixture of MAs (4 wt%) with other fuel components throughout the core fuel.

HET2: Mixture of MAs (20 wt%) and depleted uranium in a radial blanket replacing the first ring of reflector assemblies that surrounds the outer region of driver fuel.

EFIT

The EFIT reference design features a LINear ACcelerator (LINAC) delivering a 20 mA beam of 800 MeV protons onto a windowless spallation target at the center of the core. The target is surrounded by 6 hexagonal concentric rings of FAs and other 4 of reflector assemblies as shown in figure 2.2. The 180 FAs in the active core guarantee the subcriticality without relying on control rods. Each one contains 168 rods loaded with uranium-free fuel in a MgO matrix.

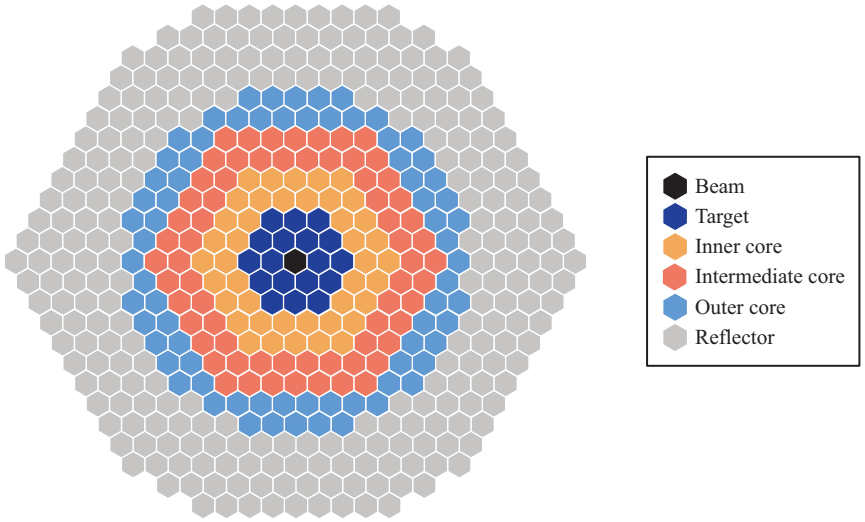

Figure 2.2: Core of the European Facility for Industrial Transmutation (EFIT) [72]. The different regions of the core (inner, intermediate and outer) differ in fuel content and pin diameter to produce a flat radial power distribution.

2.3 Burn-up calculations

Burn-up calculations performed by F. Álvarez-Velarde at CIEMAT were used in this work to obtain the contributions to the total fission rate of the individual elements of the isotopic inventories in ESFR and EFIT as they evolve in time. The contributions were averaged over the periods of Equivalent Full Power Days (EFPDs) the irradiation cycle was divided in, which are defined by the moments when real core reloading would be envisaged. However, a *single batch* approach for the entire irradiation cycle starting from a fresh core was adopted in the calculations. Álvarez-Velarde used the Monte Carlo N-Particle eXtended (MCNPX) simulation code with JEFF-3.1.1 as the source of evaluated nuclear data, coupled to the depletion code ORIGEN [73] through the EVOLCODE 2.0 interface [74]. See [70] for a detailed description of the burn-up calculations.

Figure 2.3 shows the fuel and MAs vectors used in the burn-up calculations for ESFR and EFIT. Note that the fuel vector is the same in both systems. The evolution of the isotopic contribution to the fission rate in ESFR for the two MAs loading patterns aforementioned is shown in figure 2.4. In both cases, ^{238}U and $^{239-241}$Pu are major contributors (>3 %). ^{238}Pu is a major contributor as well in the case of HOM4. Note that, only the ^{238,239}Pu contributions increase with time, gathering relevance in the overall delay neutron emission. For EFIT, the evolution of the isotopic contribution to the fission rate is shown in figure 2.5. Note that more isotopes than in ESFR contribute in more than 3 %, and about 30 % of the fission rate comes from MAs. This is in line with the design goal of a high MAs burning [75]. The two major contributors in this case are ^{239}Pu and ^{241m}Am.

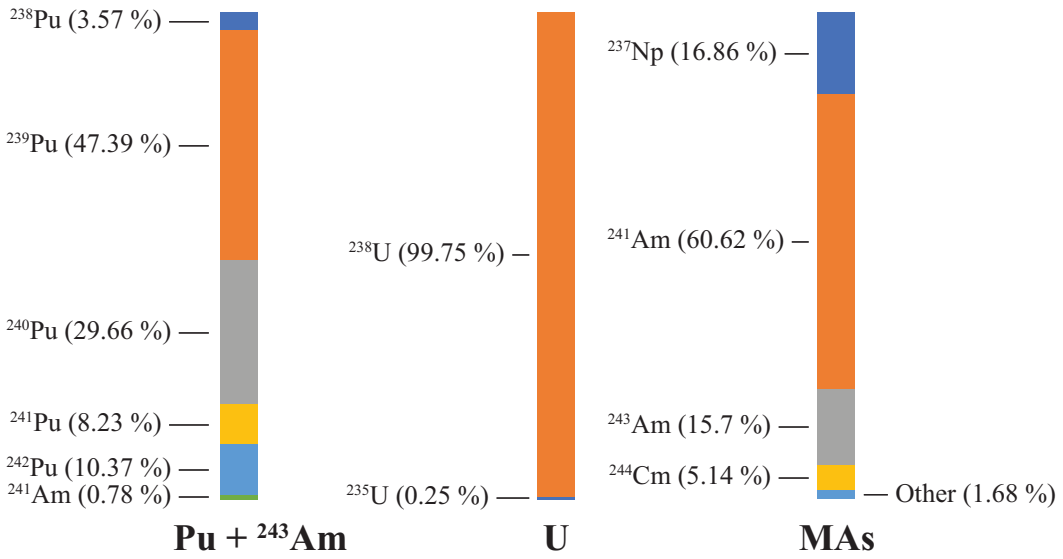

(a) ESFR

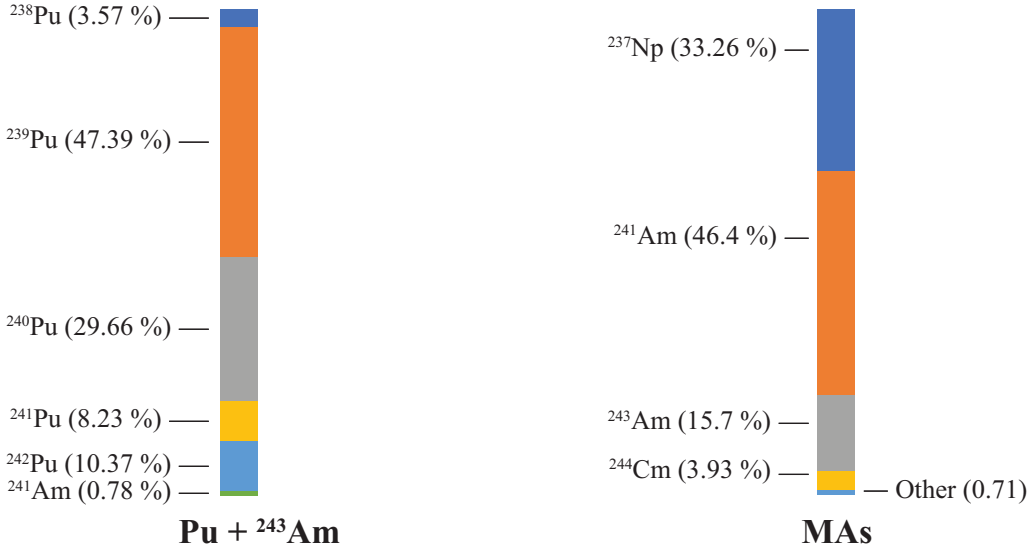

(b) EFIT

Figure 2.3: Fuel and MAs isotopic vectors in ESFR [70] and EFIT. The weight percent with respect to the vector is indicated in parenthesis. Category "other" in the MAs vector includes, for ESFR: ^{242m}Am (0.24 wt%), ^{242}Cm (0.02 wt%), ^{243}Cm (0.07 wt%), ^{245}Cm (1.26 wt%), and ^{246}Cm (0.09 wt%); and for EFIT: ^{242m}Am (0.09 wt%), ^{242}Cm (0.0002 wt%), ^{243}Cm (0.07 wt%), and ^{245}Cm (0.54 wt%).

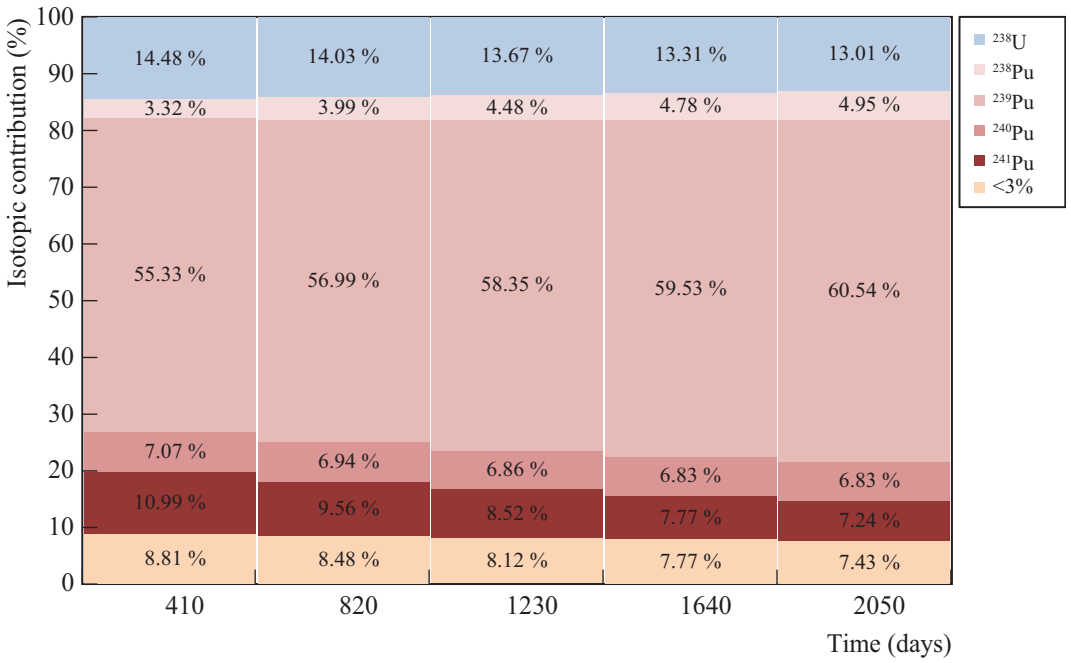

(a) HOM4

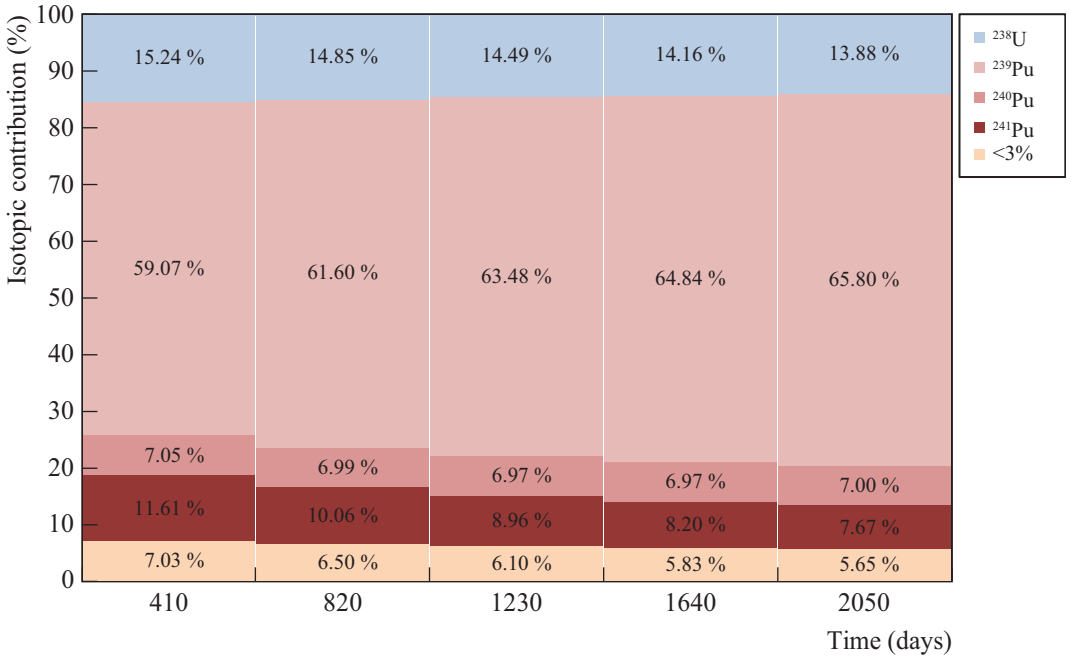

(b) HET2

Figure 2.4: Evolution of the isotopic contributions to the fission rate in ESFR for different MAs loading patterns.

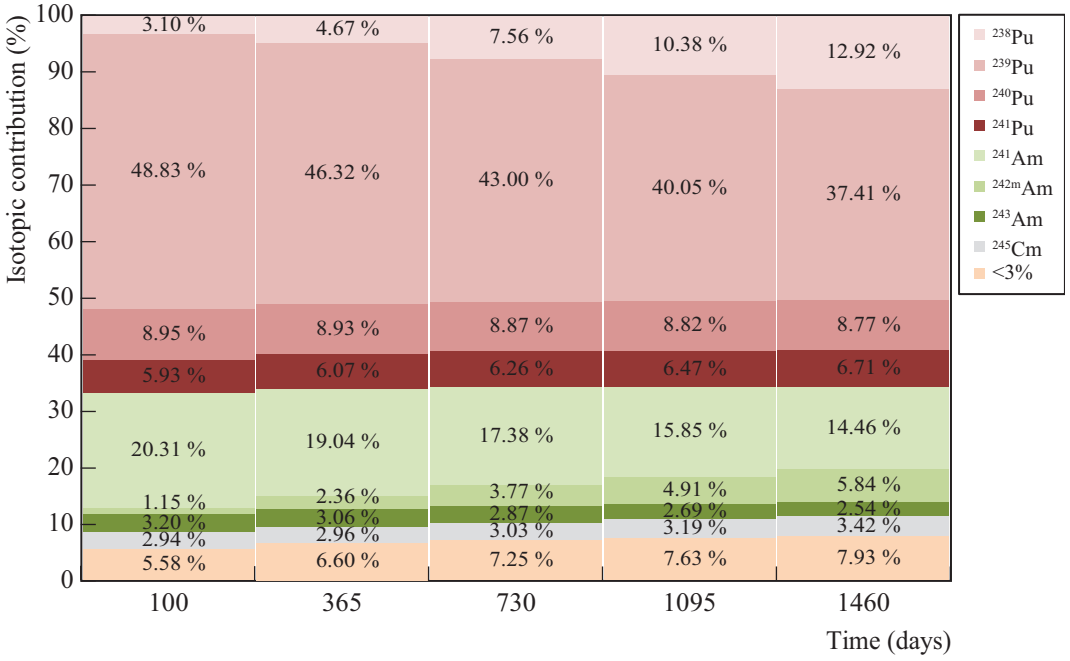

Figure 2.5: Evolution of the isotopic contributions to the fission rate in EFIT.

2.4 Delayed neutron calculations

Summation and multigroup calculations were performed with ENDF/B-VII.1, JEFF-3.3 and JENDL-4.0 on 20 fissioning isotopes over a broad energy range spanning from thermal to fast neutron energies. The goals behind were: 1) to illustrate first the uncertainty in delayed neutron calculations from using different calculation approaches and standard evaluated nuclear data libraries; and 2) to identify with summation calculations the delayed neutron emitters of utmost importance for the design of advanced nuclear energy systems, highlighting the role of ^{86}As and ^{91}Br. Most of the results presented and discussed in this section are, for brevity, only for the fissioning isotopes which are the major contributors to the fission rate in ESFR and EFIT.

Isotopic inventory calculations were the starting point for summation calculations. They were performed with a Monte Carlo simulation code developed by E. Mendoza at CIEMAT. The code samples primary fission products from an independent fission yield distribution, propagates their radioactive decay chain, and tallies the number of each fission product produced and delayed neutrons emitted within consecutive time intervals after the fission event. From its output, the average number of delayed neutrons emitted per fission event (hereafter delayed neutron yield) was calculated as:

$$\nu_d = \sum_{i,k} \left(c_{ik} \sum_j n_{ij} b_{ij} \right) \tag{2.1}$$

where, for the ith fission product, c_{ik} is the calculated cumulative yield in the kth time interval, n_{ij} the number of delayed neutrons emitted in the decay to the jth decay channel, and b_{ij} the branching ratio of the jth channel.

Table 2.2 presents the delayed neutron yield per hundred fission events calculated from the simulation of 10^8 fission events. Note the significant differences between libraries and between the values given in the libraries and the results from summation calculations. This indicates that the independent fission yields and radioactive decay data are not yet accurate and complete enough for summation calculations to be reliable for the development of nuclear energy systems.

Further insight into these discrepancies is revealed by the evolution of the delayed neutron emission rate. It was straight forward to derive from the isotopic inventory calculations. From the multigroup representation of the delayed neutron emission, on the other hand, it was derived as:

$$r(t) = \sum_i \nu_i \lambda_i e^{-\lambda_i t} \tag{2.2}$$

where ν_i and λ_i are the delayed neutron yield and decay constant of the ith group. Note in figure 2.6 that most of the discrepancy is concentrated within the first second after the fission event, where short-lived primary fission products —^{86}As and ^{91}Br among them— contribute most. Accurate measurements of the delayed neutron emission probabilities of those nuclei will therefore contribute to improve the accuracy of delayed neutron summation calculations.

Uncertainties in table 2.2, figure 2.6 and every other result from summation calculations presented hereafter are epistemic, i.e., from the limited knowledge on the nuclear data. However, 10^8 fission events were enough to guarantee a statistical relative uncertainty lower than 1 % for the chosen time binning. How epistemic and statistical uncertainties were separated using the fast Generation Random Sampled (GRS) method developed by Zwermann et al. [76] is described in appendix A.

The isotopic contributions to the delayed neutron emission rate were also calculated to identify the fission products that contribute most. Figures 2.7 and 2.8 show respectively the contributions of ^{86}As and ^{91}Br for all the fissioning isotopes for which independent fission yields are given in the three libraries and ENDF/B-VIII.0. They range from 0 % to 5 %, with the only exception of ^{86}As in the thermal neutron-induced fission on ^{235}U according to ENDF/B-VIII.0, where the contribution reaches 10.9 %. The delayed neutron emission probability of ^{86}As in ENDF/B-VIII.0 is an experimental value, more than twice the theoretical value of 12.485 37 % adopted in the preparation of ENDF/B-VII.1. Hence the higher contribution. This confirms how sensitive delayed neutron calculations can be to the delayed neutron emission probability of short-lived nuclei. Both ^{86}As and ^{91}Br contribute most to the delayed neutron emission of the thorium and uranium isotopes, and plutonium isotopes at high neutron energies. Some of these are among the most relevant contributors to the fission rate in ESFR and EFIT. The accurate measurement of the delayed neutron emission probability of ^{86}As and ^{91}Br will therefore improve the accuracy of delayed neutron summation calculations on advanced energy systems.

Isotope	2.53×10^{-8} MeV			0.5 MeV			2 MeV			14 MeV		
	ν_d^{sum}	ν_d^{lib}	Δ(%)	ν_d^{sum}	ν_d^{lib}	Δ(%)	ν_d^{sum}	ν_d^{lib}	Δ(%)	ν_d^{sum}	ν_d^{lib}	Δ(%)
ENDF/B-VII.1												
^{238}U		4.40		4.23 ± 0.12	4.40	-4		4.40		2.74 ± 0.14	2.60	-5
^{239}Pu	0.718 ± 0.012	0.65	11	0.63 ± 0.02	0.65	-3	0.58 ± 0.03	0.65	-5	0.41 ± 0.04	0.43	5
^{240}Pu	0.92 ± 0.04	0.90	3	0.88 ± 0.04	0.90	-2		0.90		0.67 ± 0.04	0.62	8
^{241}Pu	1.34 ± 0.03	1.62	-17	1.77 ± 0.07	1.62	-9		1.62			0.84	
^{243}Am		0.80			0.80			0.80			0.48	
^{245}Cm	0.71 ± 0.03	0.65	10		0.65			0.65			0.52	
JEFF-3.3												
^{238}U		4.78			4.78			4.78		2.23 ± 0.08	2.66	-16
^{239}Pu	0.60 ± 0.02	0.65	-7		0.65			0.67			0.30	
^{240}Pu		0.90			0.90			0.90			0.62	
^{241}Pu	1.23 ± 0.03	1.60	-23		1.60			1.60			0.91	
^{243}Am	0.84 ± 0.03	0.85	-1		0.85			0.85			0.48	
^{245}Cm	0.53 ± 0.02	0.64	-18		0.64			0.64			0.44	
JENDL-4.0												
^{238}U		4.63		4.25 ± 0.14	4.63	-8		4.63		2.9 ± 0.1	2.85	1
^{239}Pu	0.79 ± 0.02	0.62	26	0.70 ± 0.03	0.63	11		0.65		0.60 ± 0.04	0.43	41
^{240}Pu	1.00 ± 0.05	0.91	10	0.96 ± 0.04	0.91	5		0.91		0.74 ± 0.04	0.74	1
^{241}Pu	1.39 ± 0.04	1.60	-13	1.44 ± 0.05	1.60	-10		1.60			0.99	
^{243}Am		0.85		0.92 ± 0.04	0.85	8		0.85			0.77	
^{245}Cm	0.77 ± 0.04	0.65	19		0.65			0.65			0.52	

Table 2.2: Delayed neutron yields (per hundred fission events) from summation calculations (sum) and standard evaluated nuclear data libraries (lib). $\Delta = (\nu_d^{\mathrm{sum}} - \nu_d^{\mathrm{lib}})/\nu_d^{\mathrm{lib}}$ represents the deviation of the calculations from the libraries.

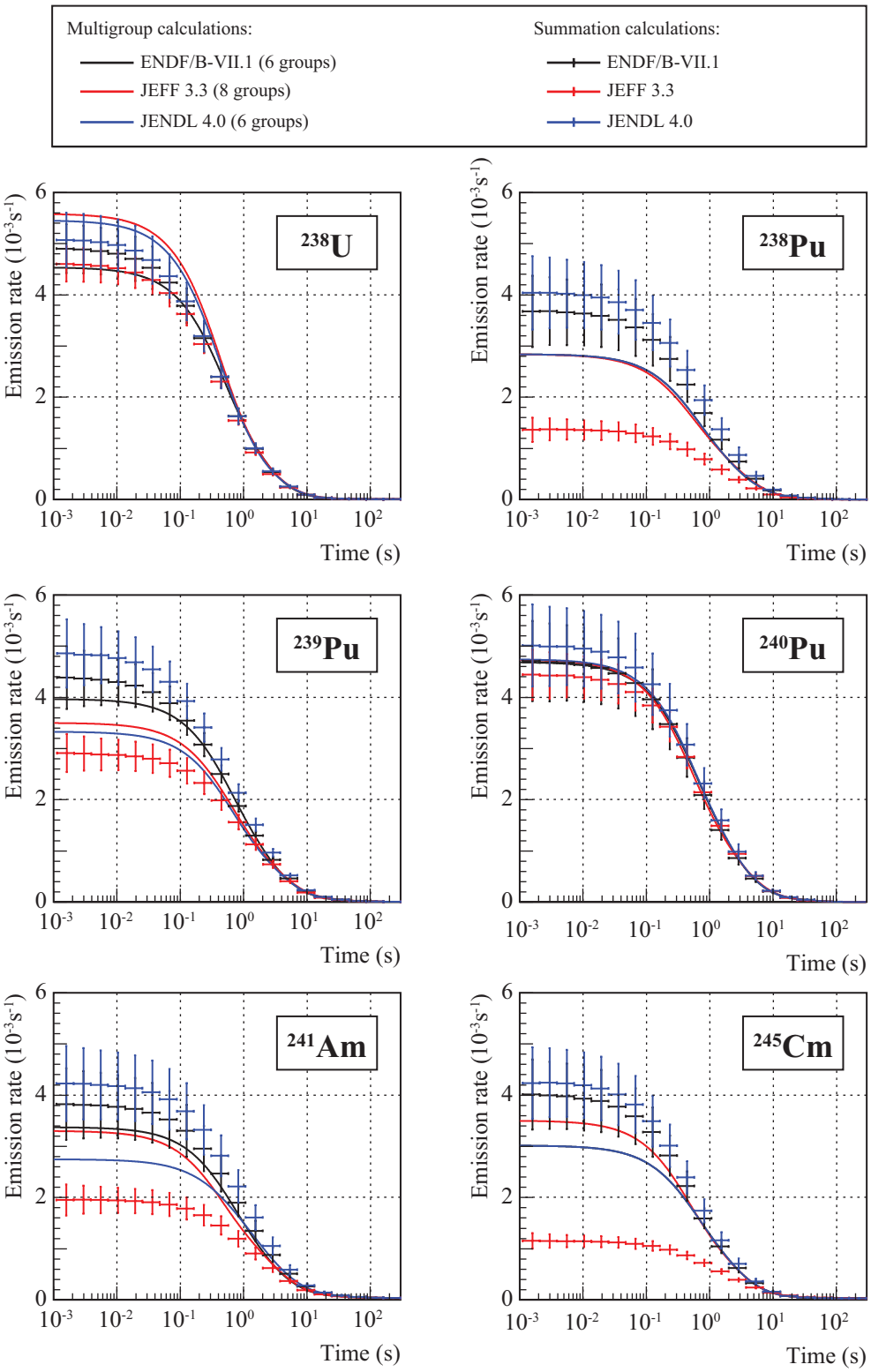

Figure 2.6: Evolution of the delayed neutron emission rate after a fission event induced by thermal neutrons, resulting from multigroup and summation calculations with ENDF/B-VII.1, JEFF-3.3, and JENDL-4.0. The distributions are normalized to the total number of delayed neutrons emitted.

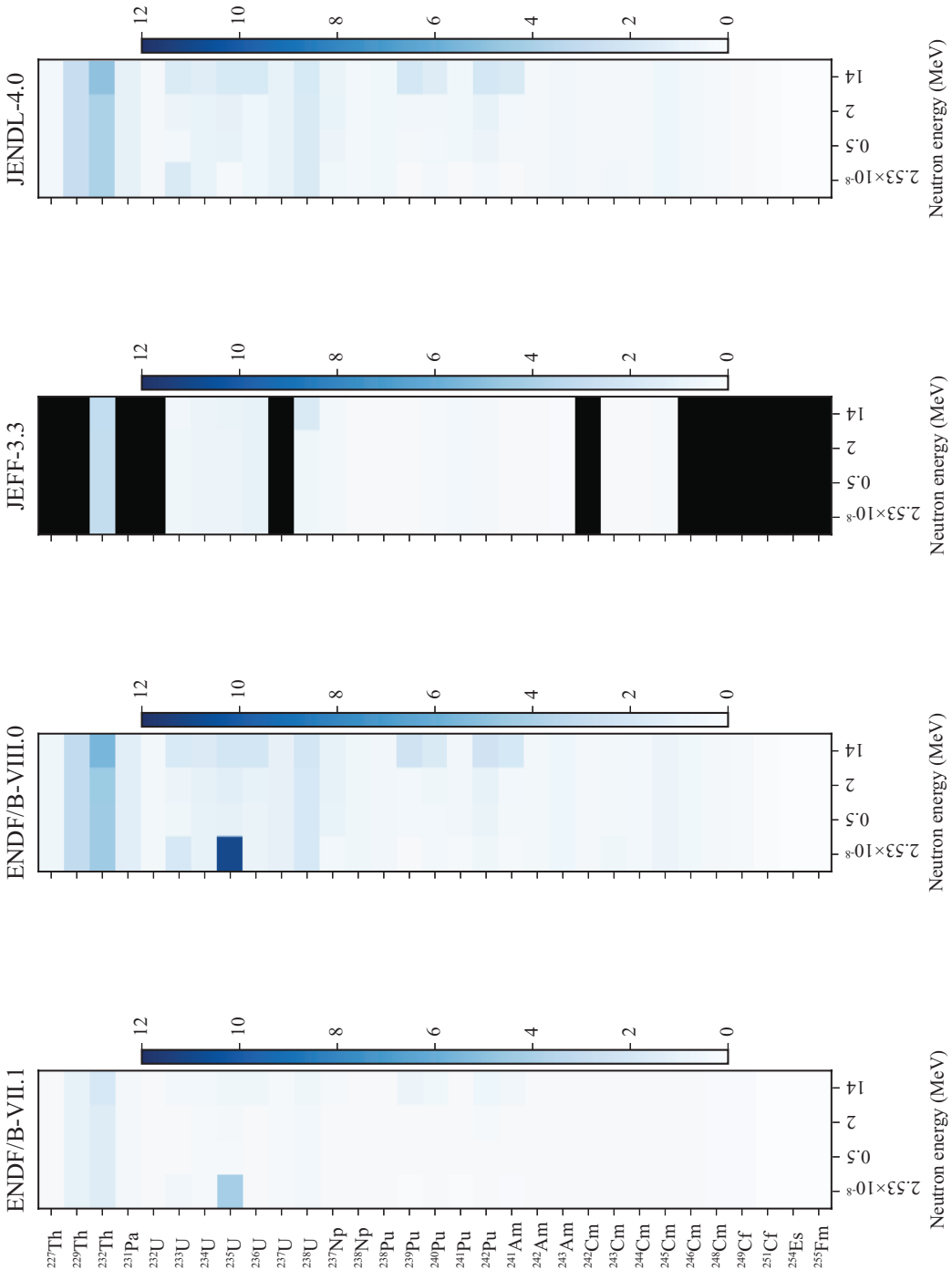

Figure 2.7: ^{86}As contribution to the delayed neutron emission of fissioning isotopes with fission yields in ENDF/B-VII.1, ENDF/B-VIII.0, JEFF-3.3, and JENDL-4.0. The maximum contribution is 10.9 % for thermal neutron-induced fission on ^{235}U according to ENDF/B-VIII.0.

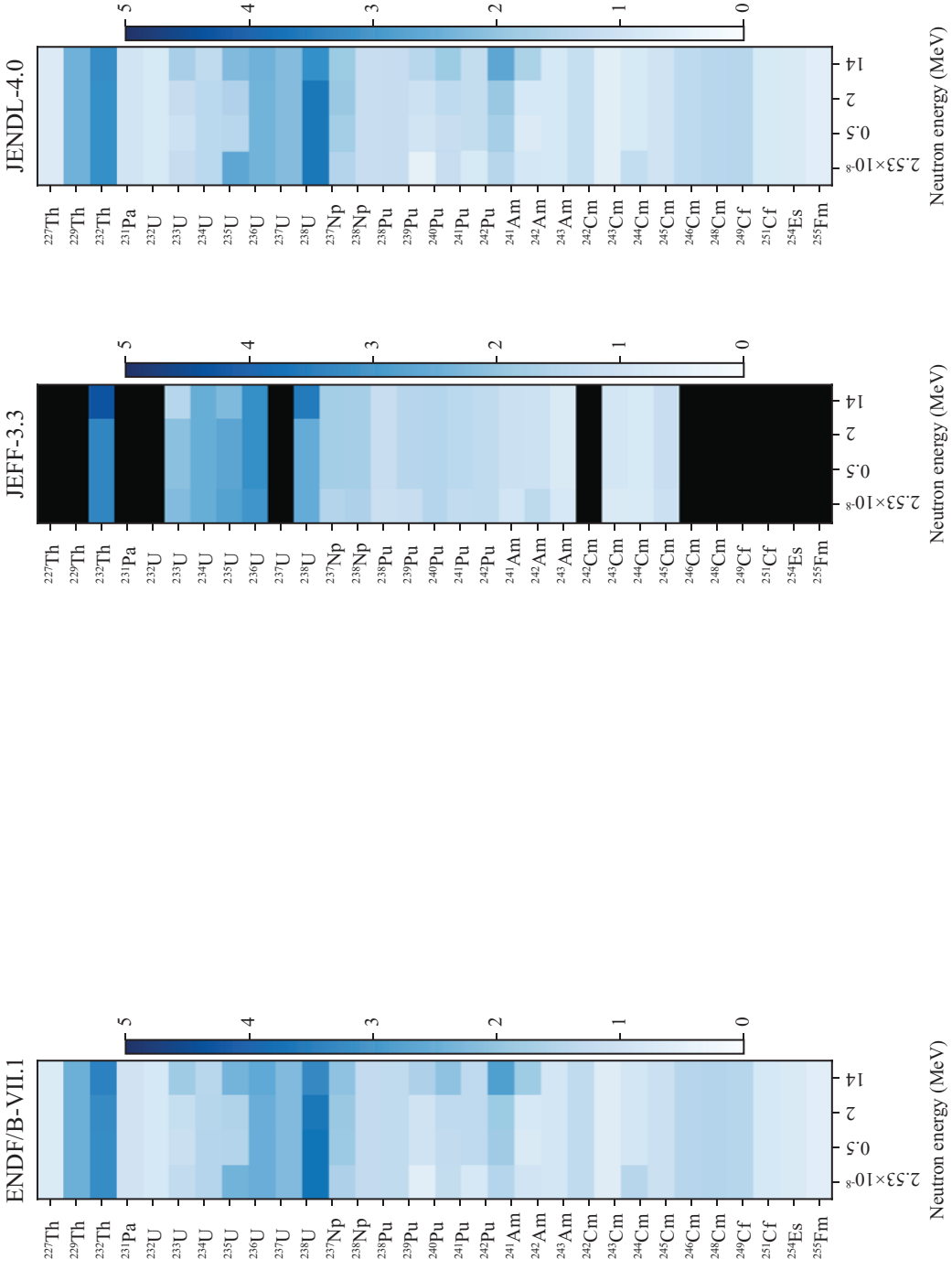

Figure 2.8: ^{91}Br contribution to the delayed neutron emission of fissioning isotopes with fission yields in ENDF/B-VII.1, JEFF-3.3, and JENDL-4.0. The maximum contribution is 4.3 % for 14 MeV neutron-induced fission on ^{232}Th according to JEFF-3.3. ENDF/B-VIII.0 contains no delayed neutron emission data on ^{91}Br whatsoever.

Chapter 3

Experiment at JYFL

The Accelerator Laboratory of the Department of Physics of the University of Jyväskylä (JYFL), Finland [77] (hereafter the Accelerator Laboratory) has been for years part of a Center of Excellence of the Academy of Finland for basic and applied research in nuclear physics. Its facility IGISOL can produce high-purity and intense beams of very short-lived nuclei (with half-lives down to the milliseconds). It is this great quality why the laboratory was chosen for performing high-precision measurements of the delayed neutron emission probability of ^{86}As and ^{91}Br in summer 2010 (hereafter the experiment).

3.1 Production and separation of radioactive nuclei at IGISOL

The Accelerator Laboratory is nowadays significantly different than it was in June 2010 when the experiment was performed. A few weeks after the experiment, IGISOL started to be dismantled and moved to an extension hall built for a new MCC-30/15 cyclotron. It was until then as resulted from the last major upgrade that took place between 2003 and 2005 (figure 3.1) [78]. That is the technical realization of the Accelerator Laboratory and IGISOL in particular (hereafter IGISOL3, as it is known by) described in this chapter.

At the laboratory, two external Electron Cyclotron Resonance Ion Sources (ECRISs) (6.4 GHz and 14 GHz) and a multicusp ion source can produce a wide variety of light and heavy ions to be accelerated up to 130 q^2/A MeV by a K130 cyclotron [77]. The resulting beam is guided by a magnetic quadrupole lens and an XY-steering magnet onto the target chamber at IGISOL3. The chamber is a 60 cm × 100 cm × 33 cm aluminum box, big enough to house an ion guide and a double radiofrequency SextuPole Ion Guide (SPIG) to guide the ion extraction. 1.5 meters behind, a water-cooled beam dump stops the primary beam.

Three ion guides are available at IGISOL3, each one based on a different type of nuclear reaction: light-ion fusion-evaporation, heavy-ion fusion-evaporation and light-ion induced fission. The latter was the one used in the experiment. Ions are first dragged out of the guide by a buffer gas flow, most of which is removed by a differential pumping system before the ions are extracted from the target chamber. Then, the SPIG guides them into an

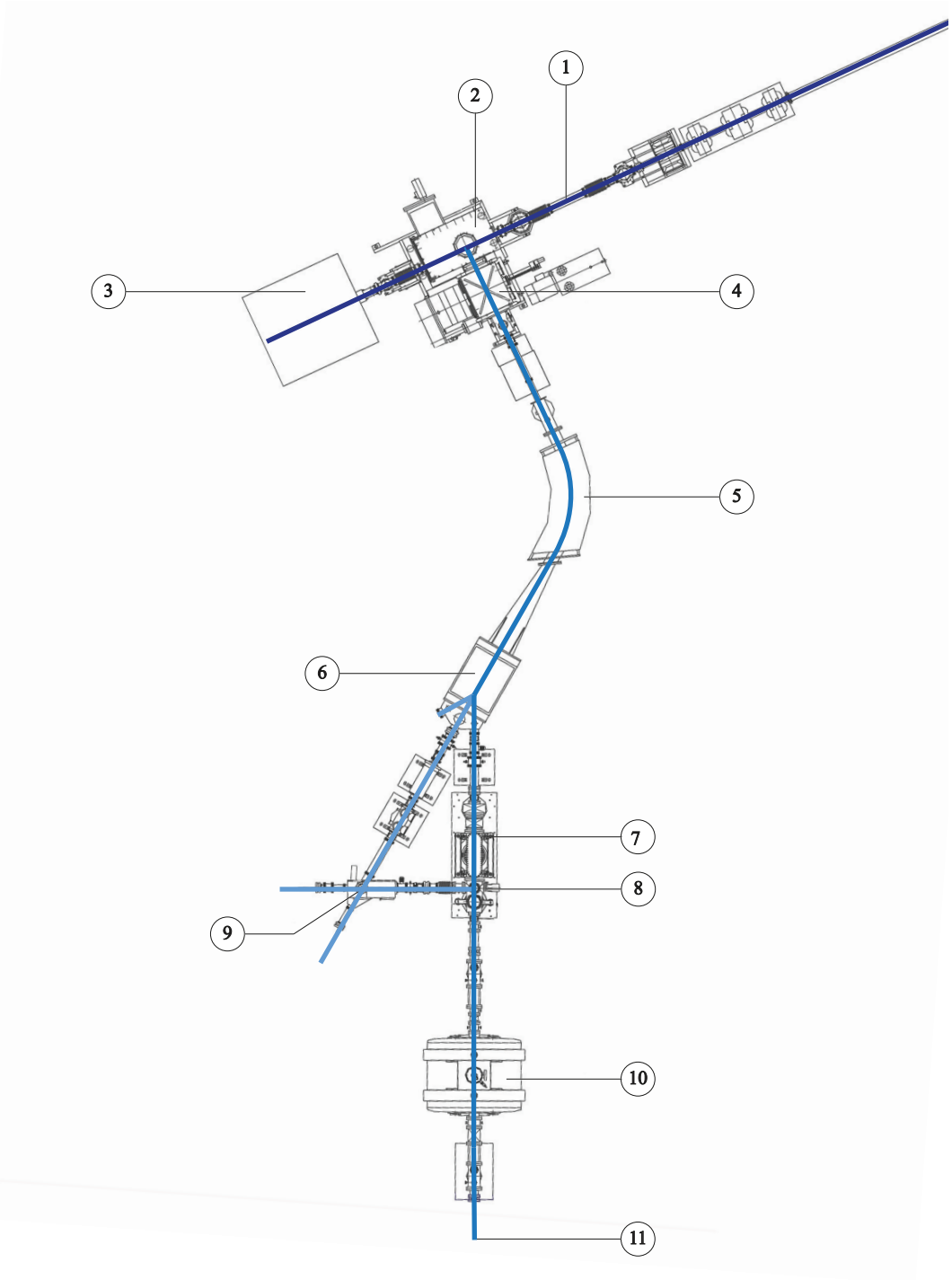

Figure 3.1: Layout of the IGISOL3 facility [78]. — 1) K130 cyclotron beamline; 2) target chamber; 3) primary beam dump; 4) extraction and acceleration chambers; 5) dipole magnet; 6) switchyard; 7) RadioFrequency Quadrupole (RFQ) cooler; 8) miniquadrupole beam deflector; 9) electrostatic deflector and beamline upstairs to collinear laser experiments; 10) JYFL Penning TRAP (JYFLTRAP); 11) beamline for experimental setups.

adjacent chamber (the extraction chamber), where a conical electrode drives them into the acceleration stage of a mass separator and the rest of the buffer gas is pumped out. After a first isotopic separation, the beam can be delivered directly to the central beamline, or steered 30° at the focal plane of the separator dipole magnet for precision in-trap measurements [79] or further purification [80] in the JYFL Penning TRAP (JYFLTRAP).

3.1.1 Fission ion guide

In the classical Isotope Separator On-Line (ISOL) technique, isotopes produced in a thick target are driven out by thermal diffusion at high temperature, then ionized, extracted and accelerated into a mass separator. The resistance to diffusion depends on the chemical properties of the element, and this is an inconvenient for the production of radioactive beams of very short-lived nuclei, because of the dramatic efficiency loss due to the long delay time[1].

The production of radioactive ion beams at IGISOL3 combines features from the ISOL technique with the ion guide technique developed at JYFL in the 1980s [81,82]. Ions are produced in a thin target, from where they recoil out into a rare gas flow where they are first thermalized, then swept out and injected into a high vacuum section for acceleration and isotopic separation. This is the so called Ion Guide Isotope Separator On-Line (IGISOL) technique, after which the facility is named. The thin target and rare gas flow provide the technique with chemical independence, as it does not rely on diffusion. On the other hand, the delay time is shorter compared with the ISOL technique. Radioactive beams of very short-lived nuclei can thus be produced at IGISOL3 with higher intensities.

A thin target is at the same time a limitation of the IGISOL technique. It cannot be thicker than the maximum range of the recoil ions of interest for those ions to escape without colliding. The technique is also limited in efficiency by constrains on the gas pressure [83]. Recoil ions emerging from the target with a range longer than the distance to the guide walls are lost. Whereas increasing the gas pressure reduces the range, it enhances at the same time the process of molecule formation with the gas impurities and recombination with electrons from the intense ionization of the gas by the primary beam. The optimum pressure (usually 100 mbar to 300 mbar) is a trade-off between these factors and a limited pumping capacity.

To minimize the efficiency loss, most experiments at IGISOL3 use high-purity helium (99.996 %) as buffer gas [78]. The choice of helium as a noble gas and its high purity reduces the molecule formation. Helium has also the highest first ionization potential of all chemical elements (24.59 eV) [84]. In consequence, helium gas preserves the charge state of recoil ions more than any other gas, maximizing the number of ions available for extraction.

Figure 3.2 shows a layout of the fission ion guide at IGISOL3. The guide is used to produce a wide range of neutron-rich ion beams via neutron- or proton-induced fission on actinide targets. To increase its effective thickness, the target is tilt 7° with respect to the beam.

[1]The "delay time" is the average time ions take to arrive to the detection setup from the moment they are produced.

The target and the primary beam are separated from the stopping chamber by a $1\,\mathrm{mg\,cm^{-2}}$ nickel foil that acts as a barrier to contain the electron plasma created by the primary beam away from the guide exit, where most of the ions that will conform the secondary beam are thermalized [81].

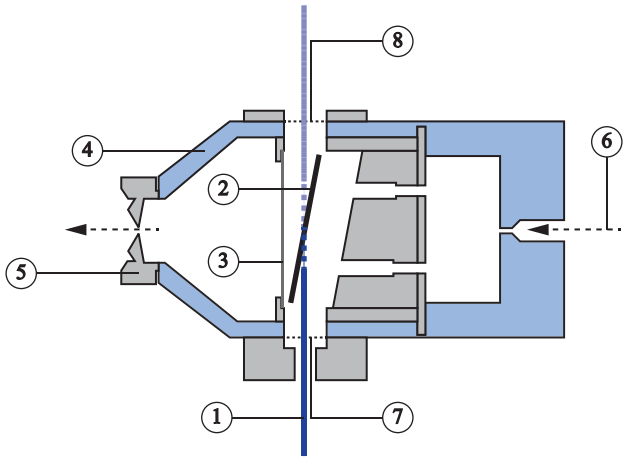

Figure 3.2: Fission ion guide at IGISOL3 [85]. — 1) Primary beam from the K130 cyclotron; 2) fission target; 3) plasma screen; 4) ion guide housing; 5) exit nozzle; 6) helium flow; 7 and 8) entrance and exit Havar windows respectively.

A fission target has multiple advantages. On the one hand, compared with the products of light-ion fusion reactions, the emission of the fission fragments is isotropic to the first order. In consequence, less ions enter the region of higher concentration of plasma electrons around the path of the primary beam, lowering the efficiency loss due to ion neutralization. On the other hand, fission fragments are produced at high kinetic energy —enough to penetrate the nickel foil— and charge state. The target can then be thicker than in the fusion guides for achieving higher yields.

3.1.2 Isobaric separation with the JYFLTRAP

The resolving power of the mass separator at IGISOL3 is not enough for isobaric separation due to the energy spread of the ions coming from the extraction chamber. Isobaric separation is achieved with a trap setup consisting of a cooler-buncher [86] followed by a double Penning trap system known as the JYFLTRAP [87].

The cooler-buncher, located next downstream of the mass separator, is essential for ion manipulation with the JYFLTRAP. It provides a bunched beam with a high optical quality (i.e., low emittance and energy spread) that ensures an effective ion injection. Ions in the cooler-buncher are confined radially by a RFQ field. As they enter, they loose kinetic energy in collisions with a buffer gas. A weak axial electric field guides them toward the end of the device, where an end-plate electrode creates a potential barrier for ion accumulation during

a few hundred milliseconds that is lowered 100 µs to release the ion bunch. The result is a bunch duration between 10 µs to 20 µs, and an energy spread less than 1 eV.

Upon release from the cooler-buncher, the ions are guided by a lens system into the purification trap [80]. There, an electrostatic quadrupole field produced by cylindrical electrodes keeps the ions confined in the axial direction oscillating around the trap center. A buffer gas is used again for ion cooling, this time to reduce the amplitude of the axial oscillations so that the motion is restricted to a region of pure electrostatic quadrupole field. The radial trapping, on the other hand, is accomplished with a homogeneous magnetic field produced by a 7 T superconducting magnet.

Both fields combined produce a complex radial motion that is the superposition of two independent circular eigenmotions: *magnetron* and *reduced cyclotron* [88]. After the cooling period, the motion is manipulated by connecting radiofrequency signals to the electrodes. First, the magnetron motion is excited to an orbit that exceeds the extraction hole in radius. Then, the ions of interest are recentered by exciting the cyclotron motion, which, unlike the magnetron motion, is strongly mass dependent. Those ions are finally extracted by opening the extraction potential wall for about 2 µs.

Another trap used for high precision measurements[2] lays symmetrically 10 cm with respect to the center of the magnet in a region of magnetic field with a higher homogeneity. That trap was not used in the experiment. Instead, the ion beam went right through, to be finally accelerated to 40 keV and delivered to the detection system.

3.2 Detection system

Radioactive ion beams were produced in the experiment by a 25 MeV primary proton beam impinging onto a thin thorium target located inside the fission ion guide. After the isobaric separation in the purification trap, the ion beam was implanted 2 m downstream on a thin movable tape 12.7 mm wide held vertically by two rollers separated 20.1 mm from each other. The rollers and their support frame created a slit of the same width of the tape leaving no gaps. Close behind the tape, a hexagonal 0.5 mm thick silicon detector was placed for the detection of beta particles. Such a thin detector minimizes the interaction of gamma-rays at the expense of a lower beta detection efficiency, but the large sensitive area (500 mm^2) and proximity to the implantation point (6 mm) of the detector compensated for this inconvenient. The tape and the detector were enclosed in the beampipe under vacuum by an end-cap with a LEMO connector for the detector high-voltage input and signal output. Figure 3.3 shows the implantation system.

The beampipe was inserted into the central cavity of BELEN, all the way in until the implantation point centered at the widest section. A Eurisys Mesures High-Purity Germanium (HPGe) detector was inserted from the opposite side of BELEN into the same cavity, and placed at 8.5 cm from the implantation point. It was used to monitor the purity of the ion beam by gamma-ray spectrometry. Figures 3.4 and 3.5 show the detection setup.

[2]The purification trap provides a mass resolving power up to 2×10^5. Values higher than 10^6 can be achieved in combination with the precision trap [87].

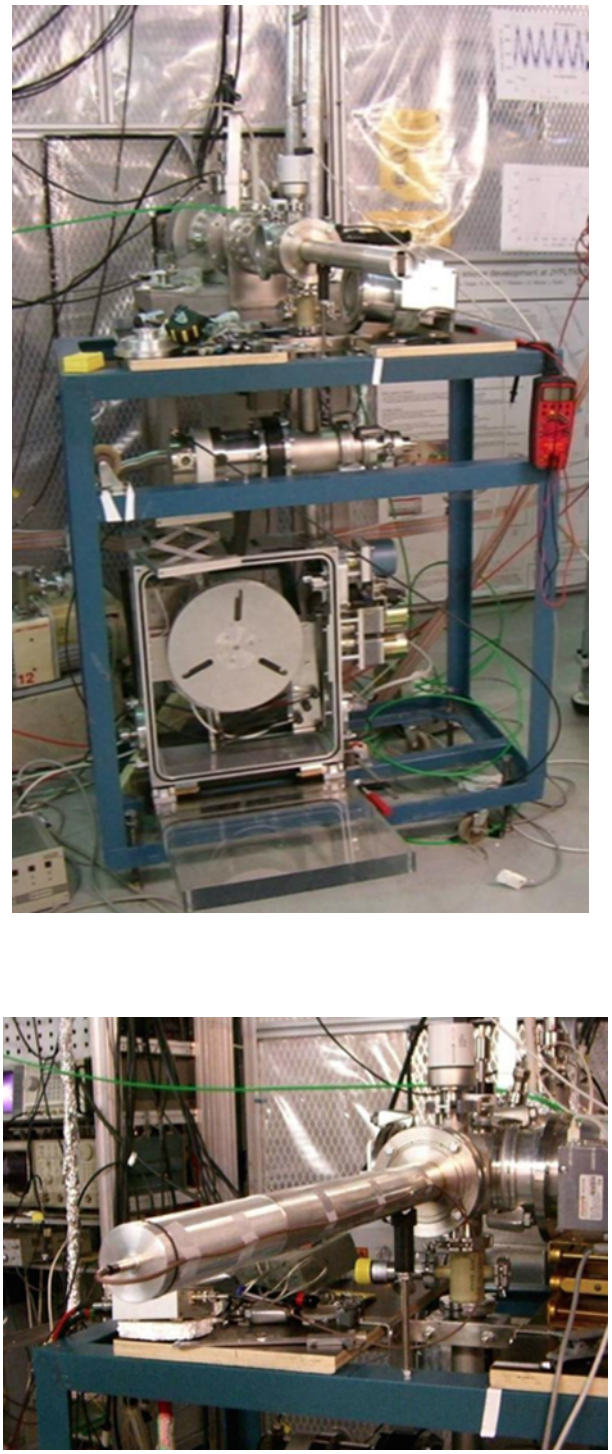

Figure 3.3: Implantation system.

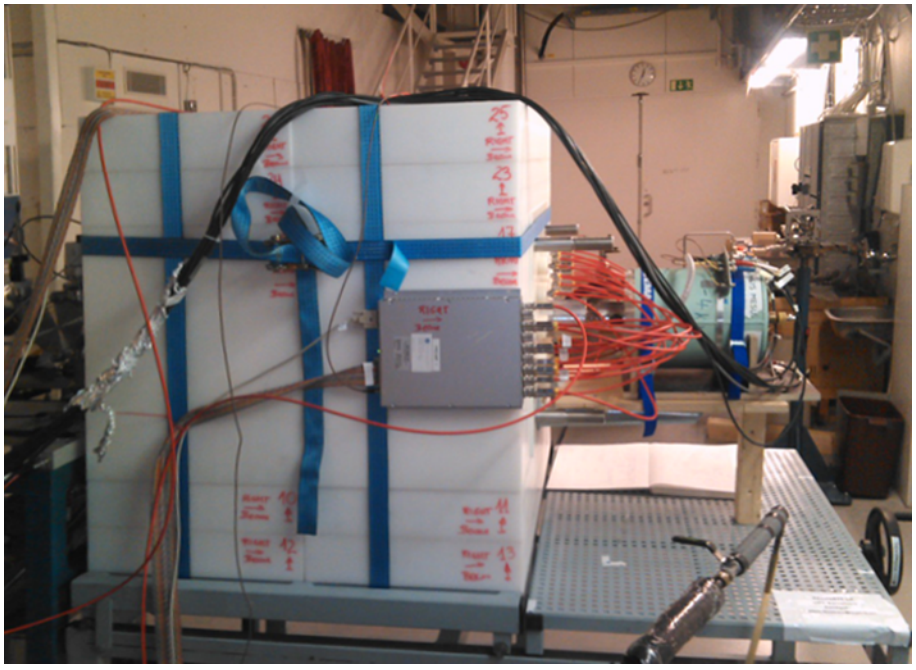

(a) Side view

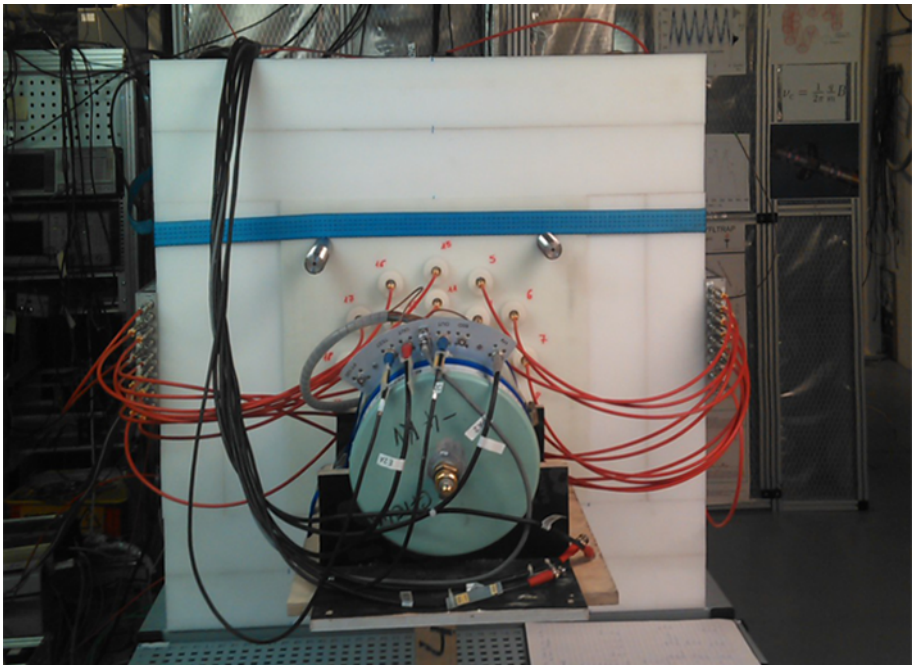

(b) Rear view

Figure 3.4: Detection setup.

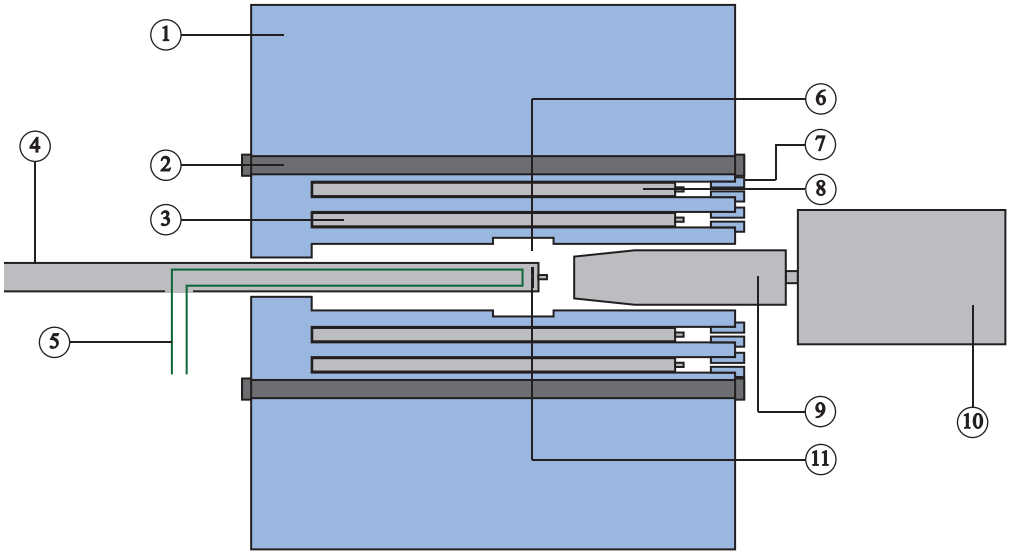

(a) Side view

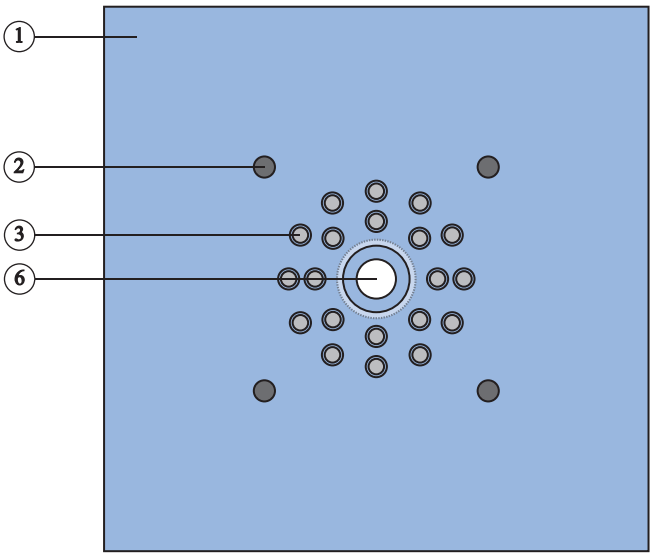

(b) Front and rear views of BELEN20b

Figure 3.5: Layout of the detection setup. — 1) Moderation block; 2) holding bars; 3) ^{3}He neutron counters; 4) beampipe; 5) implantation tape; 6) implantation cavity; 7) neutron counter cavity plug; 8) ^{3}He neutron counters in the outer ring; 9) HPGe detector; 10) HPGe detector cryostat; 11) silicon detector. The front view shows only the elements of BELEN.

3.2.1 BEta deLayEd Neutron detector (BELEN)

BELEN was designed [89] at the Polytechnic University of Catalonia (UPC), Spain, for the DEcay SPECtroscopy experiment at FAIR (DESPEC), Germany [90,91]. Its 20b configuration, the one used in the experiment, consists of 20 cylindrical ^{3}He neutron counters embedded in a $90 \times 90 \times 80$ cm block of High-Molecular-Weight PolyEthylene (HMWPE). The counters are symmetrically distributed around the shortest C_4 axis (the one joining the centroids of the opposite 90×90 cm faces) in two concentric rings: 8 in the inner and 12 in the outer at radial distances of 9.5 cm and 14.5 cm respectively (figure 3.5(b)).

The polyethylene block is conformed by $50 \times 50 \times 10$ cm slabs. Four stainless steel bars hold its core of eight vertical slabs, where most of the neutron moderation occurs and therefore where the neutron counters are embedded. The other slabs conform a 20 cm thick shielding against the room neutron background. The core and the shielding are held together by two load straps.

A cavity of contiguous cylindrical sections with different diameters traverses the core along the symmetry axis to allow from one side for the implantation of ions at the center, and the placement of auxiliary detectors close to the implantation point from the other. From the side where the beampipe is inserted, the cavity is 3.25 cm in radius for 10 cm. It widens to 5.5 cm in radius across the rest of the block, except for the 10 cm long and 6.5 cm in radius section at the center (hereafter the implantation cavity) conceived to leave room for mounting operations at the implantation point. The implantation cavity is shifted 5 cm from the center of the block in the direction of the beam traversing the fifth slab in that direction entirely. The core has 20 more cavities for the neutron counters, which do not traverse the entire core but just seven of the eight slabs, so that when the neutron counters are inserted from one side of the core all the way in, they are almost centered with respect to the implantation point. Polyethylene plugs are used to hold the tubes in position, while shielding them as much as possible from the open side. A hole in the plugs allows for the high-voltage connection and the signal output.

During the experiment, the detection setup was raised 90 cm above the floor with a support structure that could be moved forth and back in the direction of the beampipe, thanks to a sliding tray controlled with a steering wheel. The tray allowed to adjust the position of the implantation point and a quick access to it when required. In combination with adjustable legs, the tray also allowed to align the detector with the beampipe.

The neutron counters are proportional counters model 252248 manufactured by LND INC [92] (figure 3.6). Little information on key technological aspects and construction and operation features of this model is available [93], but a comprehensive overview of this kind of detector may be found in [94]. The counters are filled with a gas mixture of ^{3}He (99 %) and CO_2 (1 %) [92, private communication with the manufacturer] at a total pressure of 20 atm. On one end, they have a Safe High Voltage (SHV) connector for the high-voltage input and the signal output. The total length including the connector is 67.59 cm. The cathode, made of stainless steel, is a 0.51 mm thick cylindrical tube with an external diameter of 2.54 cm. Two guard rings stretch the anode over 60 cm along the symmetry axis, protecting the output signal from the abrupt drop of the electric field —and the gas multiplication in consequence— at the extremes of the counter (hereafter

end-effect). The rings limit the active volume to an effective region where the electric field is not disturbed. These counters must operate in the voltage range between 2150 V to 2400 V.

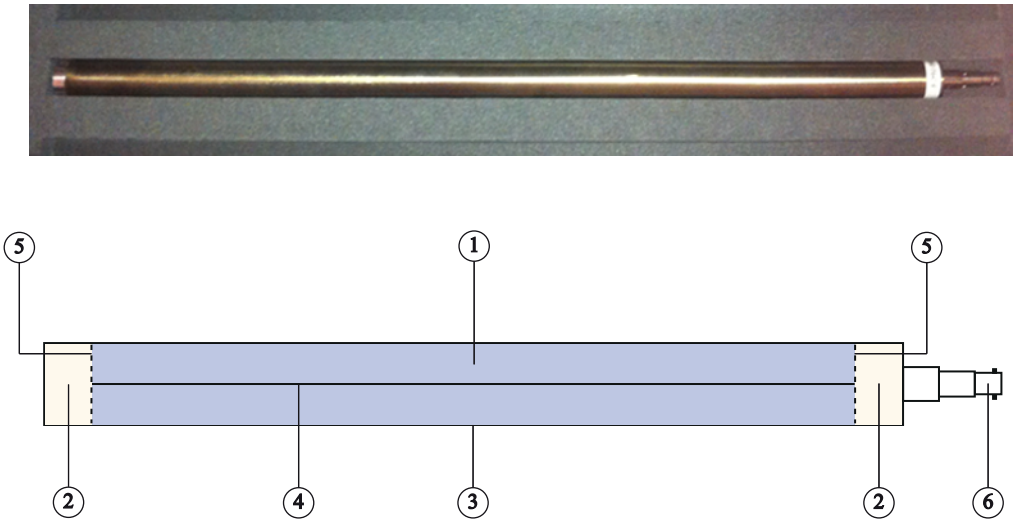

Figure 3.6: ^{3}He LND 252248 neutron counters in BELEN20b. — 1) Active volume; 2) inactive volume; 3) cathode; 4) anode; 5) guard rings; 6) SHV connector.

3.2.2 Data acquisition system

The DACQ used in the experiment was developed at Institute of Corpuscular Physics (IFIC), Spain, specifically for experiments with BELEN [20]. The hardware is however generic enough to be used with other types of detectors. A diagram of the DACQ is shown in figure 3.7. The whole system is based on commercial electronics except for the frequency clock.

The neutron counters were connected to two Mesytec MPR-16-HV charge sensitive preamplifiers screwed one on each side of BELEN (figure 3.4). Only 10 of the 16 channels of each preamplifier were used, with the counters connected to the closest preamplifier. The differential output of each preamplifier was connected to a Mesytec STM-16+ spectroscopy amplifier with the same number of channels, where signals were shaped to a Gaussian form with a 1 µs shaping time for later digitization. The signals from the silicon and HPGe detectors were also integrated and shaped with the same shaping time but in different modules. A TC170 charge sensitive preamplifier from Tennelec and an ORTEC 671 spectroscopy amplifier were used for the silicon detector. As for the HPGe detector, it comes with an integrated preamplifier whose output was fed to an ORTEC 855 spectroscopy amplifier.

A frequency clock was used to trigger pulse generators from the Berkeley Nucleonics Corporation to measure the real, live, and dead times. A BH-1 generator was used for the

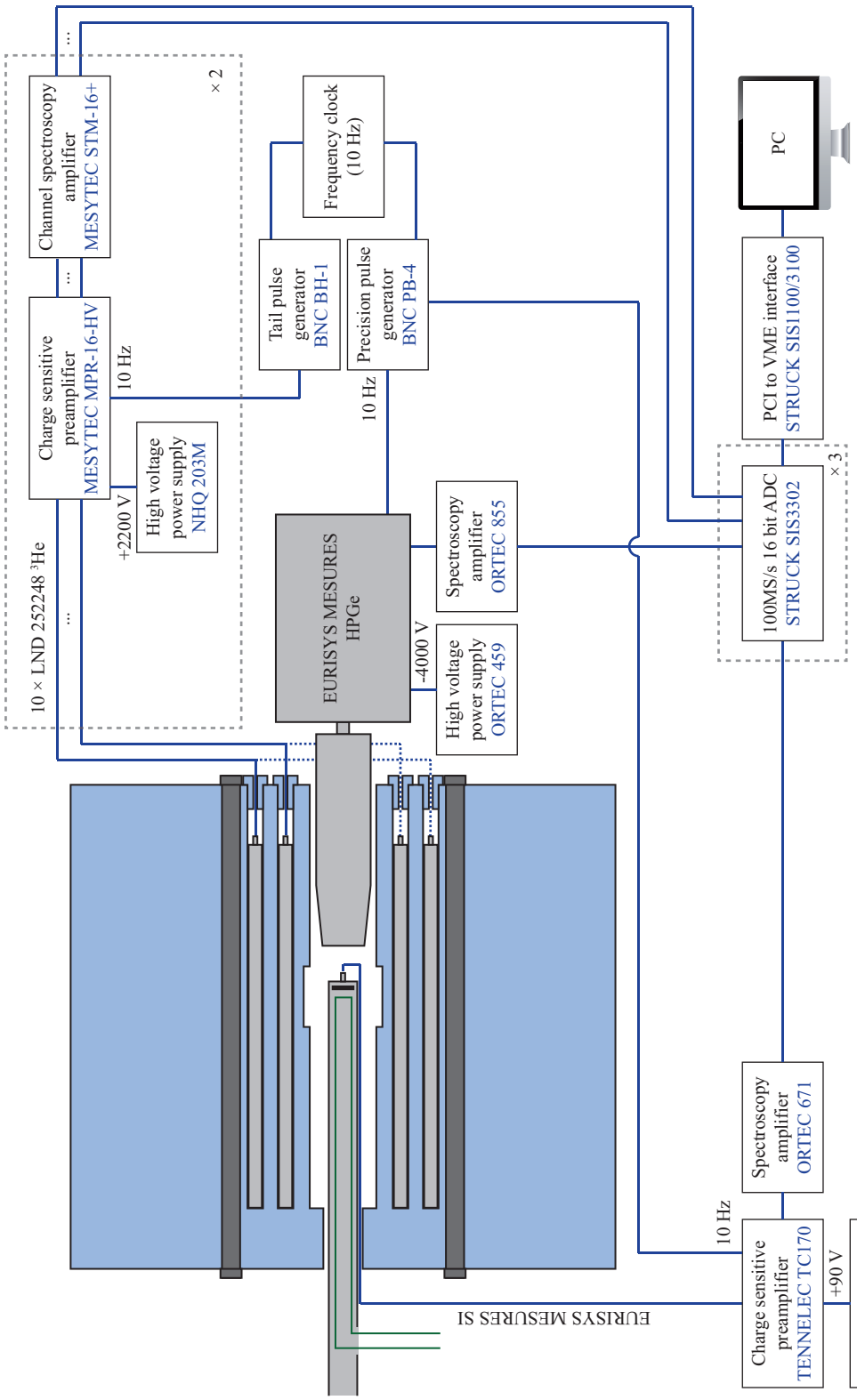

Figure 3.7: Diagram of the Data ACQuisition system (DACQ).

neutron counters, whereas a PB-4 generator was used for the silicon and HPGe detectors. Pulses were generated at a frequency of 10 Hz and sent to the test input of the preamplifiers. The pulse height was adjusted conveniently to contribute to a range in the pulse height distribution of the detectors where they could be discriminated from detection events.

The signals from the spectroscopy amplifiers were delivered to three SIS3302 flash Analogue to Digital Converters (ADCs) from Struck Innovative Systeme, where they were processed at a 100 MHz sampling frequency with a 16 bits resolution. Each digitizer has 8 channels, every two of which share a Field-Programmable Gate Array (FPGA) with the firmware to process the digitized signals. The FPGA applies first a fast trapezoidal Finite Impulse Response (FIR) filter on the digitized signal. Then, if the resulting signal exceeds a given amplitude threshold, a slow trapezoidal FIR filter is applied on the digitized signal for a precise amplitude determination. Simultaneously, the output signal from the fast filter is used to generate a timestamp with a 10 ns resolution. The optimum configuration of both filters required a signal processing time of 10 µs.

A 64 MB on-board memory unit is available in the digitizers for each channel to store the generated data (timestamp, amplitude, pileup flag...). Each unit is divided in two banks working in alternating mode, i.e, while data from the FPGA are being written to one bank, the other bank is ready for readout. Such feature reduces the readout dead time of the DACQ. The banks are swapped in all memory units when the active bank (the one being written) of any unit is almost full or after a predefined time. Then, all inactive banks are read out and the data are transferred for storage and monitoring to the DACQ master host via a PCI to VME SIS110-SIS3100 interface from Struck Innovative Systeme. This interface is also used to configure and control the digitizers from the master host.

The DACQ was used in a triggerless mode, i.e., it registered all signals from each detector exceeding a given amplitude threshold. The idea behind was to remove the inconvenients of conventional triggered DACQs in coincidence measurements. A detection in coincidence of the emitted prompt radiation in a decay event with a triggered DACQ requires an event gate that, for experiments with BELEN, would have to be extended to several hundreds of microseconds to account for the late detection of neutrons due to the moderation process. Such a large gate would cause a long dead time and enhance the probability of random coincidences. The triggerless mode allows to distinguish true from random coincidence events without the significant loss of statistics of the triggered mode. Moreover, this distinction can be done off-line, offering the flexibility to tune the analysis method and parameters. These advantages come at the expense of a larger amount of data generated.

3.3 Planification and execution of the experiment

Measurements were planned on a broader set of β-delayed neutron emitters than ^{91}Br and ^{86}As [95]. A combination of convenience and practical issues that arose during the experiment resulted in measurements on a reduced set that included ^{85}As and ^{85}Ge, in addition to ^{88}Br, ^{94,95}Rb and ^{137}I intended for the efficiency characterization of the detection system [20]. The beam times were reestimated based on a preliminary study of the performance of the detection system by Monte Carlo simulations, the prior knowledge of

the production and implantation yields, and the dynamics of the implantation and decay processes optimized for each isotope [95].

The first measurements were performed on June 8 with ^{94}Rb, ^{88}Br and ^{137}I ion beams (in that order). It was soon observed that the implantation rate estimated from the beta counting rate was significantly lower than the calculated from the gamma and neutron counting rates, indicating the possible implantation outside of the tape on the rollers and/or their support frame. Moreover, the beta counting rate showed variations in time that were not reflected in the gamma and neutron counting rates. All this suggested a drift of the ion beam at the exit of the JYFLTRAP that did not kept the beam focused on the tape. To correct this undesired effect, two collimators 10 mm and 5 mm in diameter were placed inside the beampipe at optimum positions. Combined with a frequent tuning of the trap extraction voltage and implantation tests, the drift of the beam at the implantation point became negligible.

The experiment was performed in measurement cycles with a time structure optimized for each isotope according to its half-life. The background was measured during approximately 1.35 s at the beginning of each cycle. Then, the ion beam was implanted during a period about three times the half-life of the precursor, after which the implantation was stopped and the measurement continued for about another seven half-lives. At the end of each cycle, the tape was moved out for 1.5 s to remove the remaining activity and the timestamp scaler of the DACQ was reset to zero for the new cycle starting 0.5 s later. The cycle was repeated until enough statistics was gathered with the constraint of a limited beam time.

Figure 3.8 shows a timeline of the execution of the experiment. The experiment took nine days in total. The four days prior to June 8 were used to set up the detection system, tune the DACQ, calibrate the HPGe detector with standard gamma sources and perform background measurements. The next four days were devoted to measuring with ion beams, and further background measurements performed in between. Occasionally, test measurements were performed for tuning the Einzel lens and XY-steerers downstream the JYFLTRAP to focus the beam on the implantation tape. On June 11 —the last day—, background measurements were performed and the HPGe detector was recalibrated. A measurement with a ^{252}Cf source was also performed for estimating the efficiency of BELEN.

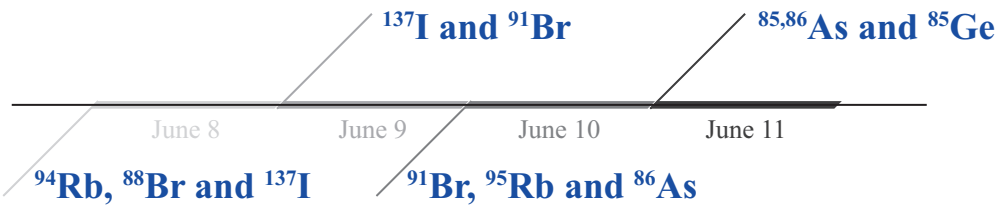

Figure 3.8: Experiment execution timeline. Only measurements with ion beams are indicated.

Chapter 4

Efficiency characterization of the detection system

The $P_n\,{}^{A}_{Z}X$ method of measuring β-delayed neutron emission probabilities presented in section 1.3.1 may result in large systematic uncertainties if not corrected by the energy dependence of the detection efficiencies. Monte Carlo simulations can help reduce those uncertainties by providing detailed information on the detector performance at a much lower effort and cost than an experimental characterization. In view of this, simulations of BELEN20b and the silicon detector (the HPGe detector was only used for monitoring the beam purity) were performed. The details and results of those simulations are presented and discussed in this chapter.

4.1 Neutron detection with BELEN

BELEN, in its 20b configuration, was presented in section 3.2.1. It was designed to achieve a high neutron detection efficiency as constant as possible between a few keV and a few MeV (hereafter the design energy range) [96], which is the energy range of interest for β-delayed neutron emission studies. A constant detection efficiency was desired to remove the systematic uncertainty in neutron counting caused by the dependence of the efficiency on the initial neutron energy. However, despite the effort devoted, a slight non-constant dependence remained up to 400 keV and a steady decrease of about 4 % per MeV was obtained at higher energies. In consequence, the systematic uncertainty in β-delayed neutron emission measurements will be larger the more the neutron emission spectrum extends beyond 400 keV if the energy dependence of the efficiency is ignored. Monte Carlo simulations allow to quantify and reduce that uncertainty provided that the neutron emission spectrum is known.

BELEN20b was designed and optimized with two of the most popular radiation transport codes: MCNPX and GEometry ANd Tracking (GEANT)4 [97]. The former is an extension of the Monte Carlo N-Particle (MCNP) code developed at Los Álamos National Laboratory (LANL) [98], which is a standard and well validated tool for the simulation of neutron interactions below 20 MeV. The extension entails the simulation of the interactions of over

30 other particle types and over 2000 heavy ions in a broad energy range. GEANT4, on the other hand, is a toolkit rather than an end-code. Developed at CERN, Switzerland, with high energy physics applications in mind, it stands out for its flexibility and versatility. Hence its use in low-energy nuclear physics applications as well. Both codes were complementary in the design of BELEN20b, exploiting the best capabilities of each one [99,100]: MCNPX was used to simulate the neutron transport and the energy deposition in the active volume of the neutron counters, and GEANT4 to obtain detailed tracking information.

Characterizing BELEN20b in efficiency by Monte Carlo simulations entails the correct description of the neutron moderation process and the response of the neutron counters. MCNPX —since release 2.5.0— can score pulse height distributions with a similar accuracy than GEANT4, but in the thermal neutron transport both codes have long disagreed [99,101,102]. Before the release of GEANT4.10.00 late in 2013, the discrepancies were significant and could not be ignored in the simulation of BELEN. Hence, the complementary use of MCNPX and GEANT4 in the design of BELEN20b also aimed at estimating the systematic uncertainty associated with the choice of simulation code. GEANT4 has been adopted in this work for its flexibility, but only after the discrepancies with MCNPX in the thermal neutron transport were investigated and reduced to an acceptable level (see appendix B).

MCNPX and GEANT4 continue to be in active development nowadays, improving and incorporating new functionalities, data, and physics models in every new release. The overview on low-energy neutron transport presented in this section refers to MCNPX2.7.0 and GEANT4.10.02.p02, which were the main releases used in this work. Throughout the rest of the manuscript, the release identifiers will be omitted for brevity. The reader should bear in mind that the discussion refers to these specific releases unless otherwise specified.

4.1.1 Simulation of low-energy neutron interactions

Scattering and absorption are the neutron-induced nuclear reactions of relevance at low energies[1] [13]. Scattering plays the most important role in the moderation process in the polyethylene block of BELEN, and absorption in the conversion reaction in the active volume of the neutron counters.

Neutron cross sections depend on the relative energy between the neutron and the target nucleus. As the neutron slows down and its energy approaches the characteristic energies of the thermal motion of the target atoms in the medium[2] (hereafter thermal energies), the spread in the relative energy increases. This enhances the broadening of the cross section dependence on the neutron energy, known in neutron physics as the "Doppler" effect by similarity with the effect of the same name in wave theory. The enhancement is negligible

[1] Within the context of this section, the term "low-energy" refers to energies below 20 MeV, up to which neutron cross section data exist in ENDF/B [103].

[2] 25.3 meV is the energy at the most probable velocity of the target atoms at 293.15 K [13, appendix D.4.3].

in slow-varying ranges of the cross sections, but significant in the resonance range, where cross sections exhibit strong variations.

At thermal energies, scattering from individual atoms may result in a significant energy change for the neutron, both gain and loss depending on the relative motion. But the presence of chemical bonds complicates the scattering process further by restricting the movement of atoms. Neutrons in molecular materials can excite or relax vibrational and rotational modes of the molecules. In solids, lattice vibrational modes can also be excited. The concept of neutron scattering at thermal energies has in consequence a different meaning than at higher energies: it is considered from the bulk material, not from individual atoms. With such a massive target, neutrons do not loose energy in elastic scattering, and inelastic scattering can lead to either loss or gain of energy. The thermal motion of the target atoms affects thus, not only the scattering cross sections, but also the final sate of the scattered neutron.

MCNPX and GEANT4 apply the Free Gas model by default to sample the final state. The model assumes that the target atoms are unbound and distributes the thermal energy according to the Maxwell-Boltzmann distribution among the translational degrees of freedom. This is a bad approximation for the scattering of neutrons at thermal energies (hereafter thermal neutrons) in most media. The effects of the thermal motion on the final state in thermal neutron scattering requires a special treatment.

The most accurate approach in MCNPX and GEANT4 to simulate low-energy neutron interactions is based on evaluated data. Key aspects of this approach are presented next in this section. Further information may be found for GEANT4 in its physics reference manual [104] and for MCNPX in its user's manual [105].

ENDF/B is the default source of evaluated data for low-energy neutron interactions in MCNPX and GEANT4, but other libraries may also be used if processed and converted into their code-specific data formats[3]. Evaluated nuclear data libraries are far from complete. Thus, when data on a given interaction, isotope or energy range are missing, both codes can use theoretical models instead. MCNPX offers a handful of fixed and well validated combinations of theoretical models covering different energy ranges. GEANT4, on the contrary, is more flexible and allows to register any combination of models along with *G4ParticleHP*, the high precision model for simulating low-energy hadronic interactions up to 20 MeV employing evaluated nuclear data. Unlike MCNPX, GEANT4 leaves the validation of some of its models to the user.

Scattering and absorption total cross sections are produced for MCNPX at a given temperature by broadening the cross sections at 0 K, which is free of thermal motion effects. G4ParticleHP in GEANT4, on the contrary, uses cross sections at 0 K and applies the broadening on-the-fly (thermal scattering cross sections are an exception). This approach gives GEANT4 the flexibility to simulate low-energy neutron interactions at any temperature with a single data library, at the expense of a lower computational performance.

[3] JENDL, the Chinese and Russian evaluated neutron data libraries (CENDL and BROND respectively) and other standard evaluated nuclear data libraries are available for GEANT4 at the Nuclear Data Service of the IAEA [102,106–108].

Upon scattering, the outgoing waves from individual atoms can interfere with each other or not, cases that define coherent and incoherent components respectively. Coherent elastic scattering is described by MCNPX and G4ParticleHP in GEANT4 by a parameterization of the double differential cross section $\frac{d^2\sigma}{d\Omega dE'}$ in terms of the Bragg edges and structure factors. Energy-angle distributions are used instead to sample the final state of incoherent elastic scattering and both components of inelastic scattering. These, however, are not given in most evaluated nuclear data libraries, but produced with pre-processing codes from other parameterizations of the double differential cross section. In the case of incoherent elastic scattering, the parameterization is typically in terms of the Debye-Waller integral. For inelastic scattering, both coherent and incoherent, it is in terms of the scattering matrix $S(\alpha, \beta)$ (aka the scattering law), where α and β denote the momentum and energy transfer respectively [109].

ENDF/B-VIII.0, which is the latest stable release of ENDF/B to date, has scattering matrices for 34 materials [38] at various temperatures. Whereas these data are not required for neutron transport by either MCNPX or GEANT4, they should be used when available, as they are essential to get accurate results in applications where neutron thermalization is relevant.

Like cross sections, final state data are produced at a given temperature for MCNPX and interpolated or extrapolated at any temperature by GEANT4 at initialization stage. In this sense, GEANT4 is again more flexible than MCNPX.

4.1.2 Neutron moderation in polyethylene

The highest maximum fractional energy transfer in neutron elastic collisions is produced with hydrogen atoms [110, section 15.III.A.1]. It is 100 % with ^{1}H, which is the most abundant isotope in natural hydrogen (hereafter just hydrogen) with an isotopic fraction of 99.99 % [111]. Hence the frequent use of hydrogenous materials as neutron moderators. Another reason lies in the low radiative capture cross section of ^{1}H as shown in figure 4.1.

Polyethylene is formed by chains of CH_2 molecules. The presence of carbon has a larger or lesser impact on neutron moderation depending on the neutron energy. Figure 4.2 shows the neutron elastic scattering, non-elastic and total cross sections for natural carbon (hereafter just carbon) in ENDF/B-VII.1 [45] between 10^{-5} eV and 20 MeV. As opposed to hydrogen (figure 4.1), carbon exhibits a resonant behavior in the elastic scattering cross section above 2 MeV. Below the resonance region, hydrogen has clearly a larger impact than carbon, because the total cross section of ^{1}H (mostly from elastic scattering) is one order of magnitude larger. Other factors that enhance the impact of hydrogen —not only below the resonance region but at any neutron energy— are the twice higher atomic fraction in polyethylene and the higher maximum fractional energy transfer in neutron elastic collisions (it is about 28 % with carbon atoms). In the resonance region, the elastic scattering cross sections of hydrogen and carbon are similar in average, but the strong variations in the cross section of carbon makes the moderation process more sensitive to the thermal motion of the target atoms. Above, the elastic scattering on carbon dominates and the strong variations disappear, but a different complication arises: inelastic reactions are

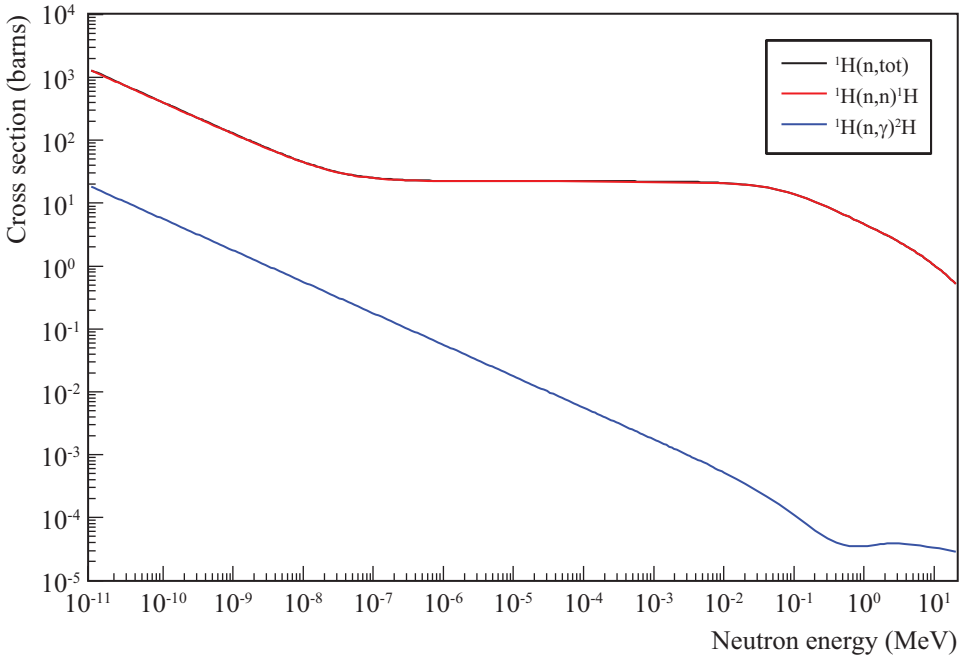

Figure 4.1: Cross sections of neutron-induced reactions on ^{1}H in ENDF/B-VIII.0 [38]. The elastic scattering cross section cannot be distinguished from the total cross section because it dominates over the entire energy interval.

energetically possible[4]. Of all inelastic reactions, only inelastic scattering and the (n,n′3α) reaction keep the neutron balance. Other like (n,α), (n,p), and (n,d) do not.

Scattering matrices for polyethylene in ENDF/B-VII.1 are only given for hydrogen at 296 K and 350 K. They are based on the evaluation performed by Koppel & Houston [112] in 1969 with the unified code for thermal neutron scattering GASKET [113] considering infinite non-interacting chains of CH_2 molecules. GASKET applies the *incoherent approximation*, which neglects coherent scattering. This is a good approximation for polyethylene, because the incoherent cross section of ^{1}H dominates the scattering process as shown in table 4.1.

Figure 4.3 compares the free and bound thermal elastic scattering cross sections of hydrogen in polyethylene given in libraries *endf70a* (table *1001.70c*) and *sab2002* (table *poly.60t*) of MCNPX respectively, and in the GEANT4 Neutron Data Library (G4NDL)-4.5. Note that the bound cross sections of the same type coincide in both codes, whereas the free elastic cross sections differ. The free elastic scattering cross section is already broadened in endf70a at 293.6 K. G4NDL-4.5, on the other hand, has data at 0 K to be broadened on-the-fly. Also note that, at thermal energies, the total bound cross section is higher than the elastic free cross section broadened at 293.6 K. This illustrates the importance of using scattering law data in the simulation of neutron moderation in polyethylene.

[4]The threshold for neutron-induced inelastic reactions on carbon is 4.81 MeV, which corresponds to the inelastic scattering to the first excited state of ^{12}C.

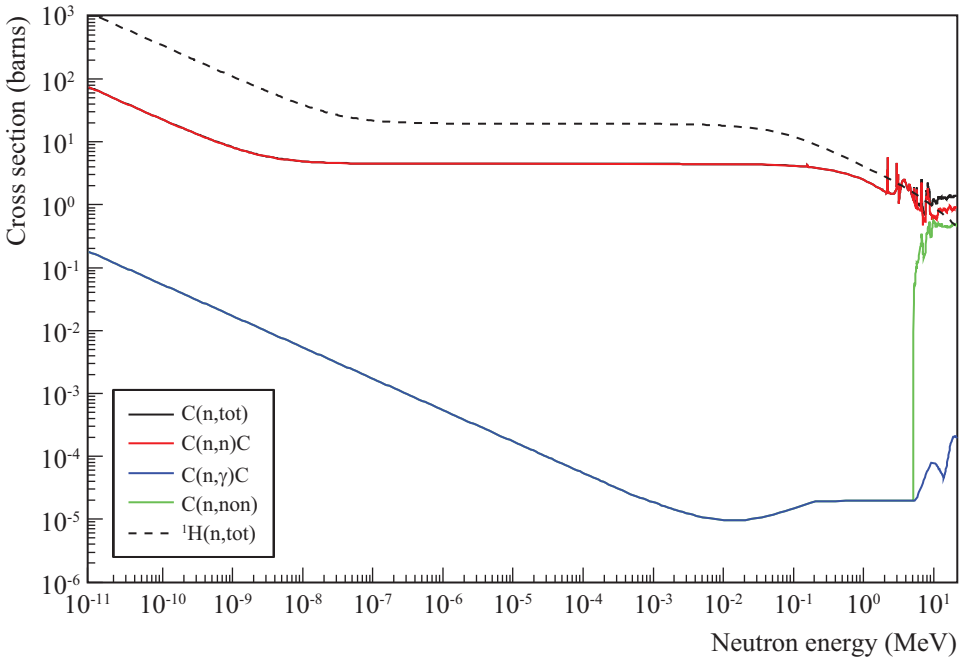

Figure 4.2: Cross sections of neutron-induced reactions on natural carbon in ENDF/B-VIII.0 [38].

Isotope	**Ground state** I^π	**Isotopic fraction** (%)	$\sigma_{\mathbf{coh}}$(b)	$\sigma_{\mathbf{inc}}$(b)
^{1}H	$1/2^+$	99.9885 ± 0.0070	1.7583 ± 0.0010	80.27 ± 0.06
^{2}H	1^+	0.0115 ± 0.0070	5.592 ± 0.007	2.05 ± 0.03
^{12}C	0^+	98.93 ± 0.08	5.559 ± 0.003	0
^{13}C	$1/2^-$	1.07 ± 0.08	4.81 ± 0.14	0.034 ± 0.011

Table 4.1: Coherent (coh) and incoherent (inc) thermal neutron scattering cross sections of hydrogen and carbon isotopes [114]. Isotopic fractions were taken from [115].

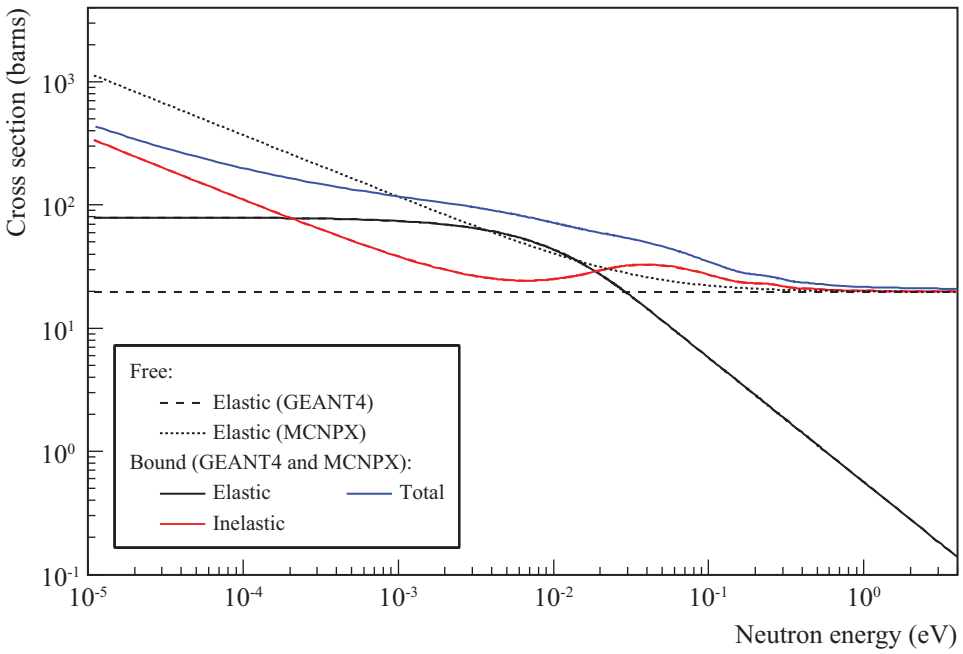

Figure 4.3: Thermal neutron scattering cross sections of free and bound hydrogen in polyethylene given in libraries *endf70a* (table *1001.70c*) and *sab2002* (table *poly.60t*) of MCNPX respectively, and in library G4NDL-4.5 of GEANT.

4.1.3 Response of the neutron counters to thermal neutrons

The neutron detection mechanism in ^{3}He proportional counters is based on the ^{3}He(n,p)^{3}H neutron-induced standard reaction [116]. This reaction has a higher cross section at low energies than other conversion reactions commonly used in slow neutron detection (figure 4.4). Furthermore, it has a high Q value (765 keV) and no energy threshold, which makes suitable for slow neutron detection.

Figure 4.5 shows the cross sections of neutron-induced reactions on ^{3}He between 10^{-5} eV and 20 MeV. At low thermal energies, the ^{3}He(n,p)^{3}H reaction dominates and the other reactions are irrelevant for neutron detection. The $1/v$ dependence of the ^{3}He(n,p)^{3}H reaction is exploited in BELEN with the use of polyethylene as neutron moderator to increase the reaction probability and count fast neutrons with a higher efficiency.

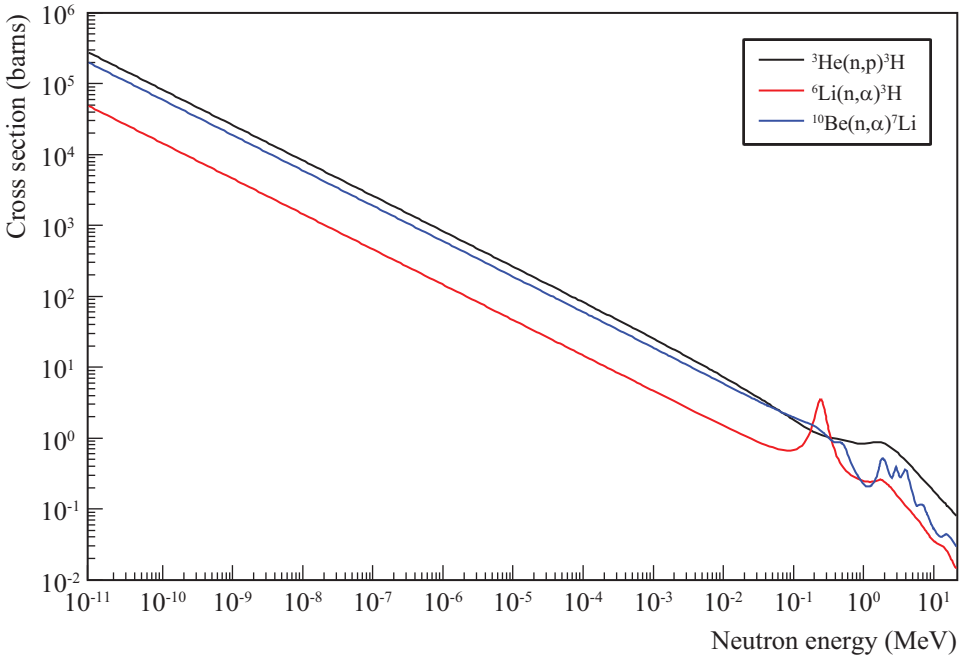

Figure 4.4: Cross sections of neutron-induced standard reactions of interest for slow neutron detection in ENDF/B-VIII.0 [38].

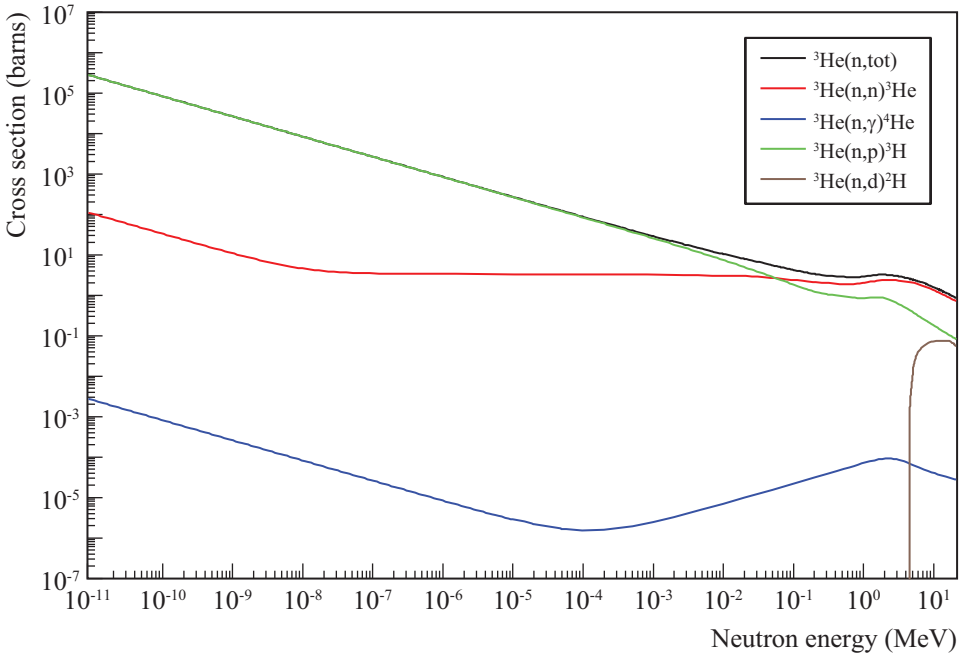

Figure 4.5: Cross sections of neutron-induced reactions on ^{3}He in ENDF/B-VIII.0 [38].

In the center-of-mass system, the proton and the triton are emitted in opposite directions with energies E_p=573 keV and E_t=191 keV respectively. Both ionize the filling gas as they slow down, creating electrons that are collected at the anode by means of an electric field. When the range of the proton or the triton exceeds the distance to the cathode, only part of the reaction energy is deposited in the gas. Such wall effect extends the pulse height distribution to the low pulse height range, where electronic noise and background gamma events contribute. This can be a problem for the identification of neutron events in certain situations[5].

The dimensions and gas pressure of ^{3}He proportional counters are key factors that determine the magnitude of the wall effect and, more importantly, the neutron detection efficiency. The larger the dimensions, the higher the geometric efficiency and the lower the probability of the reaction products colliding with the cathode. On the other hand, the higher the pressure the higher the macroscopic reaction cross section of ^{3}He and with that, the higher the intrinsic efficiency and the shorter the range of the proton and the triton. This is why the counters in BELEN20b operate at 20 atm. At such a high pressure, 2.348 cm of ^{3}He (the diameter of the active volume) are enough to detect thermal neutrons with an efficiency of about 95 % (figure 4.6). ^{3}He proportional counters, however, require a small amount of quench gas to reduce the risk of electrical breakdowns[6], which also reduces the magnitude of the wall effect[7] but has a negative impact on the neutron detection efficiency. The total pressure and the amount of quench gas in ^{3}He proportional counters are therefore optimized for the specific application as a compromise between high detection efficiency and minimum wall effect among other performance and operational requirements [94].

Models have been developed to derive the pulse height distribution of ^{3}He proportional counters taking the wall effect into account, but they have failed to reproduce experimental distributions accurately [117]. Kudo et al. [118] recently measured the position dependence of the relative gas multiplication in counters of different lengths. When removed this effect from the experimental pulse height distributions, they obtained a remarkable agreement with Monte Carlo simulations where it was omitted, showing the relevance of the end effect. Unlike for the wall effect, which only requires to take into account the range of charge particles in the gas, accounting for the end effect requires a prior characterization of the counters. Yet, for the purpose of estimating the neutron detection efficiency of

[5]The cathode of ^{3}He proportional counters is usually made of copper, stainless steel or aluminum. Gamma-rays are therefore more likely to interact with the cathode than with helium gas, and can produce electrons close to the inner wall that drift to the anode generating a low-amplitude pulse. These usually fall below the triton edge, allowing for the discrimination of gamma and neutron events by setting a convenient energy threshold. In the presence of a high gamma flux, however, the discrimination is not effective. Pulses generated by gamma-rays can pile up and contribute to a range of the pulse height distribution that exceeds the triton edge. The wall effect in that case affects the identification of neutron events [117].

[6]Radiation can excite metastable atomic states of ^{3}He that can trigger electrical breakdowns by photoionization or photoelectric effect in the cathode. The quench gas improves the dielectric properties of helium and deexcites those states by collisional quenching.

[7]The range of 573 keV protons and 191 keV tritons in ^{3}He at 20 atm is 2.74 mm and 0.67 mm respectively. A 1 % of CO_2, which is the amount of quench gas in the neutron counters of BELEN, reduces both ranges in about 20 %.

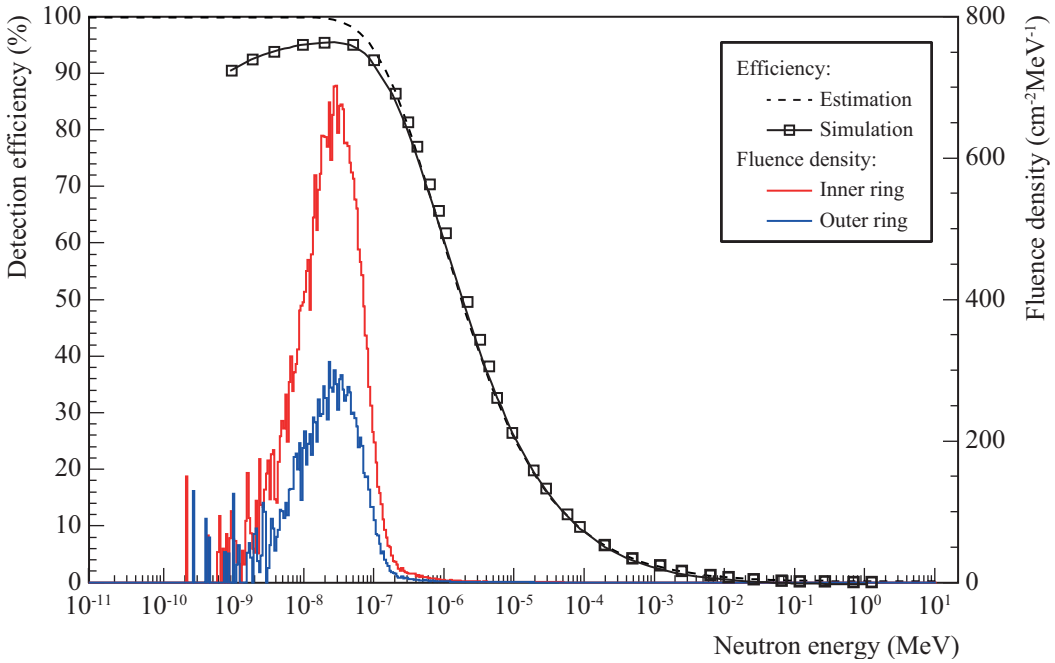

Figure 4.6: Ideonity of LND 252248 counters for neutron counting with BELEN. The detection efficiency is highest (>90 %) at thermal energies, where most of the neutron fluence transmitted into the counters lies. The fluence density is represented per generated neutron.

BELEN20b, the end effect can be ignored, as long as neutron events can be distinguished from events of any other type.

Figure 4.7 shows the simulated and experimental responses of a neutron counter in the inner ring of BELEN20b to a ^{252}Cf source placed at the center of the implantation cavity. The simulated response is presented with (hereafter folded simulated distribution) and without (hereafter unfolded simulated distribution) accounting for the finite resolution effects that affect the detector response (e.g.: statistical fluctuations in the number of electron-ion pairs produced per unit of deposited energy, ion recombination, electronegative impurities in the gas, anode imperfections, pile-up with low-amplitude gamma and electronic noise signals, etc.) [94]. These effects were accounted for in the later case by folding the unfolded distribution with a Gaussian Probability Density Function (PDF) defined by the resolution function $\frac{\Delta E}{E} \backsim \frac{1}{\sqrt{E}}$ [110, section 6.III.C.1.c] that best reproduced the experimental distribution at the full energy peak.

The structure of the response function is better illustrated with the unfolded simulated distribution. Note the full energy peak at 765 keV. At lower energies, the step structure reflects the wall effect. When the proton is emitted toward the cathode, it may reach the internal wall without interacting with the gas. The triton emitted in the opposite direction into the bulk gas deposits all its energy, producing a characteristic edge (triton edge) at 191 keV. The opposite case —when the triton strikes the cathode without interacting with the gas and the proton emitted in the opposite direction deposits all its energy— produces

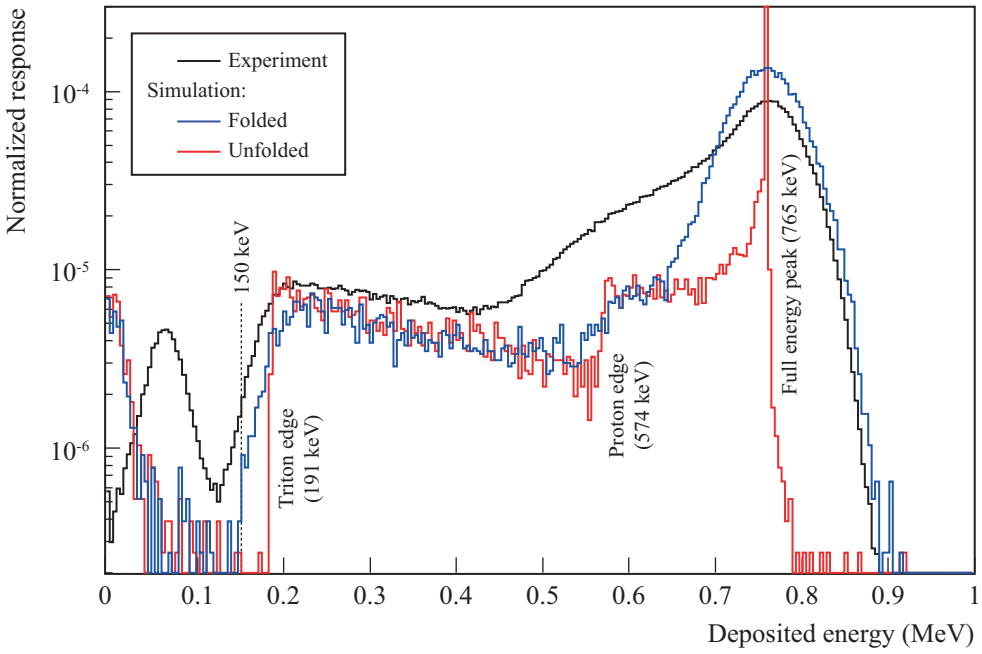

Figure 4.7: Response of a ^{3}He neutron counter in the inner ring of BELEN20b to a standard ^{252}Cf source placed at the center of the implantation cavity. All response functions are normalized to the integral above 150 keV.

the second characteristic edge (proton edge) at 574 keV. The continuum above each edge represents cases when the particle emitted toward the cathode deposits only a fraction of its energy.

Note that considering the finite resolution effects is not enough for an accurate description of the experimental response. The same simulation code has been successful with similar counters at CIEMAT. In consequence, in addition to the end effect, the experimental response must have been severely affected by other processes that were not accounted for in the simulation. The ballistic deficit may have a significant distortive impact on the response function as well. Due to the Bragg effect (the specific ionization of ions is not uniform along the track but concentrated at the end), primary ion tracks perpendicular to the anode can produce double-pulse signals that may extend beyond the preamplifier shaping time, leading to an incomplete signal integration that distorts the response function toward lower pulse heights [94]. Nevertheless, the simulated response in figure 4.7 shows that the contribution of gamma-rays produced in the interaction of neutrons with BELEN20b is negligible. Moreover, the experimental response shows that neutron events can be effectively separated from gamma and electric noise events by setting a threshold at 120 keV, a bit lower than the triton edge to consider all distortive effects on the response function. This confirms that an accurate description of the response function is not necessary for neutron counting with BELEN20b.

Figure 4.6 showed the neutron fluence transmitted into the same counter. Overlapped it also showed the energy dependence of the detection efficiency from: 1) a rough calculation

as $\varepsilon(E) = 1 - e^{-\Sigma(E)D}$, where Σ is the macroscopic cross section for the ^{3}He(n,p)^{3}H reaction and D the internal diameter of the cathode; and 2) GEANT4 simulations of a monoenergetic neutron beam impinging on the cathode along the radial direction at half length. Both efficiency curves agree above a few eV and differ at lower energies because of backscattering. The difference around the thermal peak, where most of the fluence density lies, is lower than 10 %. It is also within this range where the detection efficiency is highest (>90 %), which illustrates the ideonity of LND 252248 counters for BELEN.

4.1.4 Calculation of the detection efficiency

Monte Carlo simulations were performed with MCNPX and GEANT4 to calculate the detection efficiency of BELEN20b. A special emphasis was placed on the detailed modeling of the geometry and the correct specification of material properties to reduce the systematic uncertainty as much as possible. The geometry was modeled as shown in figure 3.5. Material properties, on the other hand, were takem from databases maintained and published by the National Institute of Standards and Technology (NIST), USA [111], namely atomic compositions, densities (except for polyethylene), and mean excitation energies were taken from the Stopping-Power and Range Tables for Electrons, Protons, and Helium Ions (STAR) [119], and isotopic compositions from the Atomic Weights and Isotopic Compositions database [111]. This applies to every other simulation performed in this work.

BELEN20b was constructed of 500 kg mol^{-1} natural HMWPE from two different batches purchased to Plásticos Lutesor, S.A. [120]. One batch was used for the core and the other for the shielding. This was evident by the difference in color, which raised the doubt on whether the two batches were of the same polyethylene type. To investigate this from a macroscopic standpoint, the density of a sample from each batch was measured at CIEMAT resulting in the same value of 0.95 ± 0.01 g cm^{-3} for both. The manufacturer reports 0.955 g cm^{-3}, which is consistent with the measurements and with the density range from 0.935 g cm^{-3} to 0.96 g cm^{-3} typical of HMWPE according to the Prospector Materials Database [121]. Nonetheless, the difference in color indicates the existence of structural and/or chemical differences that could not be accounted for in the simulations and whose effects, if any, are unknown.

Besides polyethylene for its role in the moderation process, another critical material in the performance of BELEN20b is the gas in the neutron counters. The total pressure of the gas mixture in the LND 252248 counters is 20 atm [93], 1 % of which corresponds to CO_2 added as quenching gas according to a private communication with the manufacturer. At such a high pressure, the gas may not behave as an ideal gas. Petersen [122] studied the properties of helium from 1 bar to 100 bar (1 atm = 1.013 25 bar) and from room temperatures to 1800 K. According to him, the real gas law for a noble gas such as helium deviates little from the ideal gas law at the pressure and temperature the counters operated during the experiment (25 °C approximately). That deviation can be expressed in terms of the compressibility factor:

$$Z = \frac{PV}{nRT} \tag{4.1}$$

which for ^{3}He at 20 bar (19.74 atm) and 300 K (26.86 °C) gives $Z = 1.00947$ [122]. Accordingly, the density of ^{3}He adopted in the simulations was the value resulting from the ideal gas law reduced in 1 %. With such a small amount of CO_2, the deviation for this gas was neglected.

Thermal neutron scattering data for polyethylene in ENDF/B-VII.1 are available only for the scattering on hydrogen. Therefore, the Free Gas model was used to describe the scattering on carbon in polyethylene and on the rest of materials. For hydrogen in polyethylene, table poly.60t in library sab2002 was the source of thermal neutron scattering data in the simulations with MCNPX. It was generated from ENDF/B-VII.1 at 293.15 K (20 °C), which happens to be the temperature that material compositions retrieved from the NIST are given at. With GEANT4, on the other hand, the default G4NDL-4.5 library was used. The library contains thermal scattering data generated also from ENDF/B-VII.1, but at 296 K and 350 K. In spite of the temperature difference, 293.15 K was adopted in the simulations with both MCNPX and GEANT4 to guarantee the equivalence of the results. As explained in the previous section, GEANT4 performs a temperature interpolation/extrapolation at initialization stage. The extrapolation in this case guarantees that thermal neutrons are transported by both codes using data generated at the same temperature.

A few standard physics lists are distributed with GEANT4 for different applications featuring different combinations of physics models. *Shielding* [123] was used in these and every other simulation with GEANT4 presented in this work. It features the *Standard Electromagnetic* and G4ParticleHP models, but no special treatment for thermal neutrons whatsoever. In consequence, the G4NeutronHPThermalScattering model was registered and associated with the thermal neutron scattering data in G4NDL-4.5.

The simulations consisted of monoenergetic neutrons generated isotropically from the center of the implantation cavity. Neutrons and all secondary particles were tracked until they were captured, escaped the detector, or decayed. To calculate the neutron detection efficiency, the pulse height distributions of the neutron counters without finite resolution effects were generated from the energy deposited in the active volume and integrated above the triton edge. This was straight forward to achieve with GEANT4 for the access it allows to individual interaction events. With MCNPX three different approaches were followed:

1. tally F4 with the FM multiplier to calculate the reaction rate instead of the flux averaged over the active volume;
2. the special tally treatment FT CAP for tallies F8, which scores the number of captures in specified combinations of nuclides at the end of each neutron track; and
3. the special tally treatment FT PHL, which allows pulse height tallies F8 to be based on energy deposition tallies F6 with any particle designator [124,125].

The latter is a new feature of MCNPX available since release 2.5.0 [125]. It is important to mention that the Neutron Capture Ion Algorithm (NCIA) had to be activated in MCNPX to generate the products of the ^{3}He(n,p)^{3}H reaction [105]. This is an optional feature that was configured to preserve the angular correlation between the proton and the triton,

which is required to account properly for the wall effect. This correlation is guaranteed in GEANT4 by default.

Figure 4.8 shows the dependence of the detection efficiency of BELEN20b on the initial neutron energy calculated for each ring of counters independently and for the two rings together (i.e., the total neutron detection efficiency). The inner ring exhibits a decreasing trend with the increase of the energy. On the contrary, the outer ring shows an increasing trend up to 1.5 MeV, where there is a maximum above which the efficiency drops. The two trends compensate up to about 400 keV to give an almost constant total efficiency of about 47 %. At higher energies, the total efficiency decreases at about 4 % per MeV.

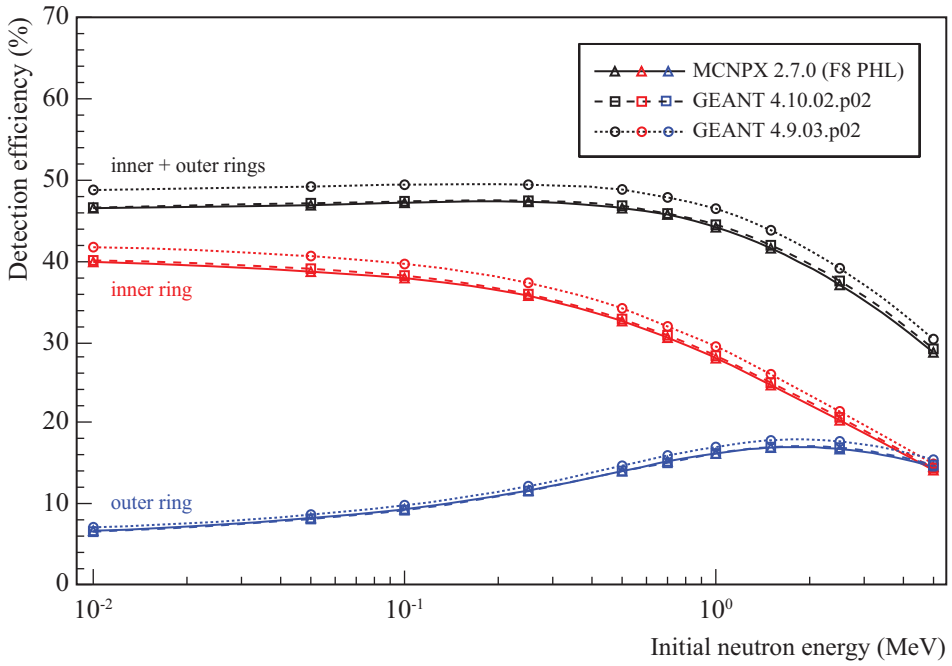

Figure 4.8: Energy dependence of the neutron detection efficiency of BELEN20b calculated by Monte Carlo simulations with MCNPX and GEANT. The GEANT4.9.03.p02 results are shown to illustrate the effect of corrections made to the G4ParticleHP model (appendix B). The relative statistical uncertainty is lower than 1 %.

The GEANT4.10.02.p02 and MCNPX2.7.0 results are consistent with each other within the statistical uncertainty. Yet, despite corrections made to the G4ParticleHP model (see appendix B), GEANT4.10.02.p02 yields a detection efficiency systematically higher. Those corrections, however, reduced the discrepancies between MCNPX2.7.0 and GEANT4 from 7 % to 1 % as shown in figure 4.8.

As discussed at the beginning of this chapter, a non-constant dependence of the neutron detection efficiency of BELEN20b on the initial neutron energy can introduce a significant systematic uncertainty in the measurement of delayed neutron emission probabilities if ignored, larger the more the emission spectrum extends beyond 400 keV. To quantify and reduce that uncertainty in this work, the response of BELEN20b to the delayed neutron

emission of the implanted isotopes was also simulated. Figure 4.9 shows the emission spectra used for primary neutron generation. They are the result of theoretical calculations by Kawano et al. [33] combined with experimental measurements when available, which are scarce and typically incomplete. Note that, to a larger or lesser extent, they all extend beyond 400 keV, in particular the spectra of ^{86}As and ^{91}Br, which are the isotopes of interest.

Table 4.2 shows the estimated efficiencies. Despite the differences in shape and extension of the spectra, they are all very similar. The largest absolute difference in simulations with the same code is just 1.6 %. That may however not always be the case. Figure 4.10 shows the neutron emission spectrum of ^{252}Cf along with the total detection efficiency curve of BELEN20b. Note that, unlike the spectra of the delayed neutron emitters, a large part of the spectrum extends beyond 400 keV. The efficiency estimated for a ^{252}Cf source deviates about 15 % from the average efficiency within the design range.

Isotope	$Q_{\beta n}$ (MeV) [126]	$\langle E_n \rangle$ (MeV)	ε_n (%)		
			MCNPX 2.7.0	**GEANT 4.9.03.p02**	**GEANT 4.10.02.p02**
^{88}Br	1.922 ± 0.003	0.252	46.9 ± 0.3	48.27 ± 0.07	46.75 ± 0.07
^{94}Rb	3.453 ± 0.008	0.442	46.3 ± 0.3	48.89 ± 0.07	46.47 ± 0.07
^{95}Rb	4.880 ± 0.022	0.530	45.8 ± 0.3	48.32 ± 0.07	45.98 ± 0.07
^{137}I	2.001 ± 0.009	0.630	45.8 ± 0.3	48.63 ± 0.07	46.18 ± 0.07
^{86}As	5.380 ± 0.004	0.448	46.1 ± 0.3	48.83 ± 0.07	46.06 ± 0.07
^{91}Br	5.781 ± 0.004	0.707	45.3 ± 0.3	47.90 ± 0.07	45.49 ± 0.07
^{252}Cf		2.2	39.6 ± 0.3	42.39 ± 0.06	40.02 ± 0.06

Table 4.2: Neutron detection efficiency of BELEN20b for the implanted isotopes and a standard ^{252}Cf source.

The excellent agreement between MCNPX and GEANT in the calculation of the neutron detection efficiency of BELEN20b verifies to a satisfactory level the performance of GEANT against MCNPX in the simulation of thermal neutron interactions. Agramunt et al. [20] validated that performance with a well calibrated ^{252}Cf source. The value of 40.9 ± 0.8 % they obtained agrees with the GEANT4.10.02.p02 value obtained in this work. Further experimental validation can be obtained from the ratio of the efficiency of the inner to outer rings ($\varepsilon^n_{\text{inner}}/\varepsilon^n_{\text{outer}}$), which is a relative magnitude. The inner ring shields the outer ring by removing a large part of the thermal neutrons. Therefore, the efficiency ratio is very sensitive to the emission spectrum and the description of the moderation and detection processes, i.e., to the performance of the detector.

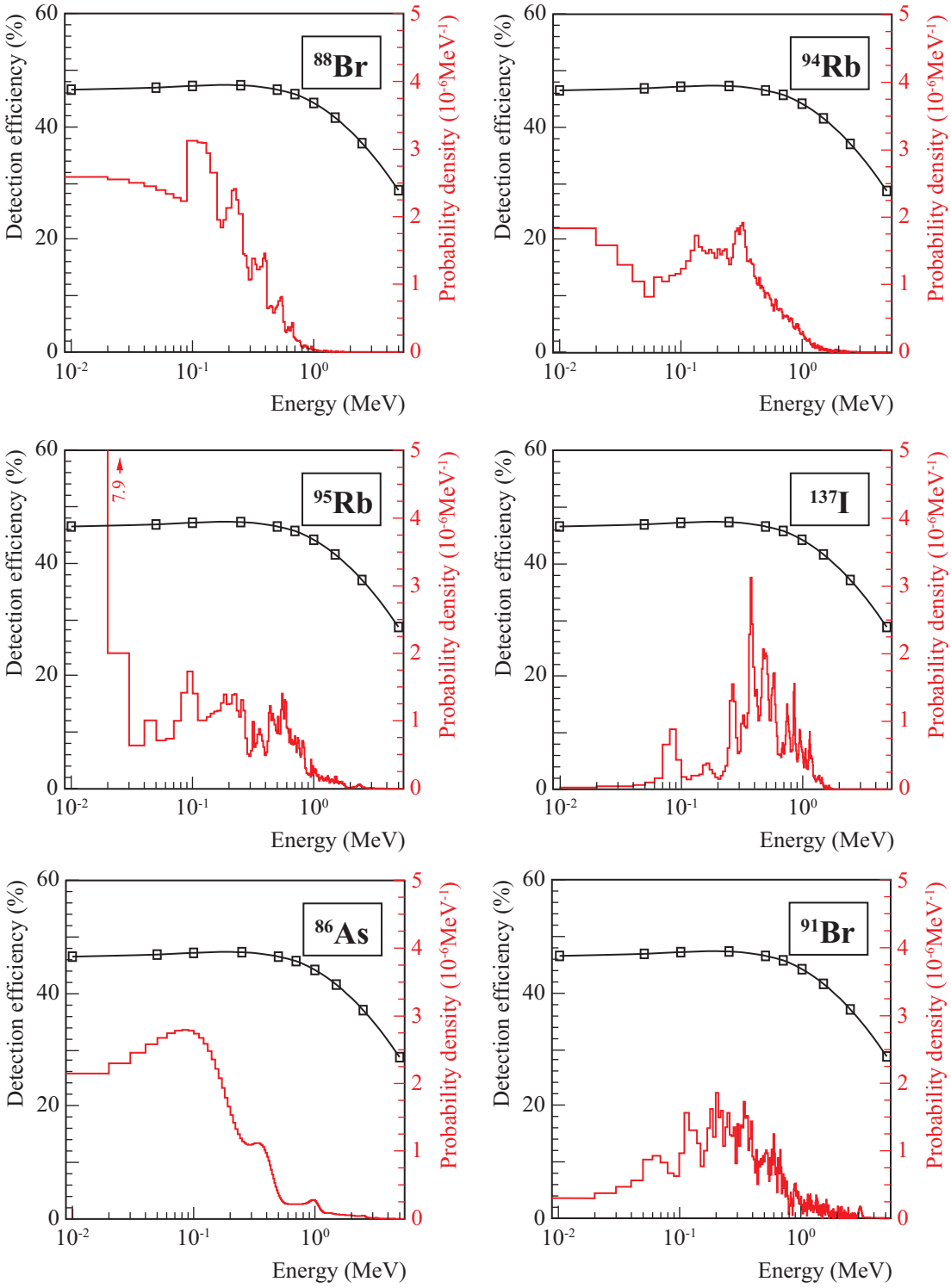

Figure 4.9: Delayed neutron emission spectra of the reference isotopes (^{88}Br, ^{94,95}Rb, and ^{137}I) and the isotopes of interest (^{86}As and ^{91}Br) in ENDF/B-VII.1 [45]. All were ported over to ENDF/B-VII1.0 [38], except the ^{91}Br spectrum, which was excluded. They are the result of theoretical calculations by Kawano et al. [33] combined with experimental measurements when available.

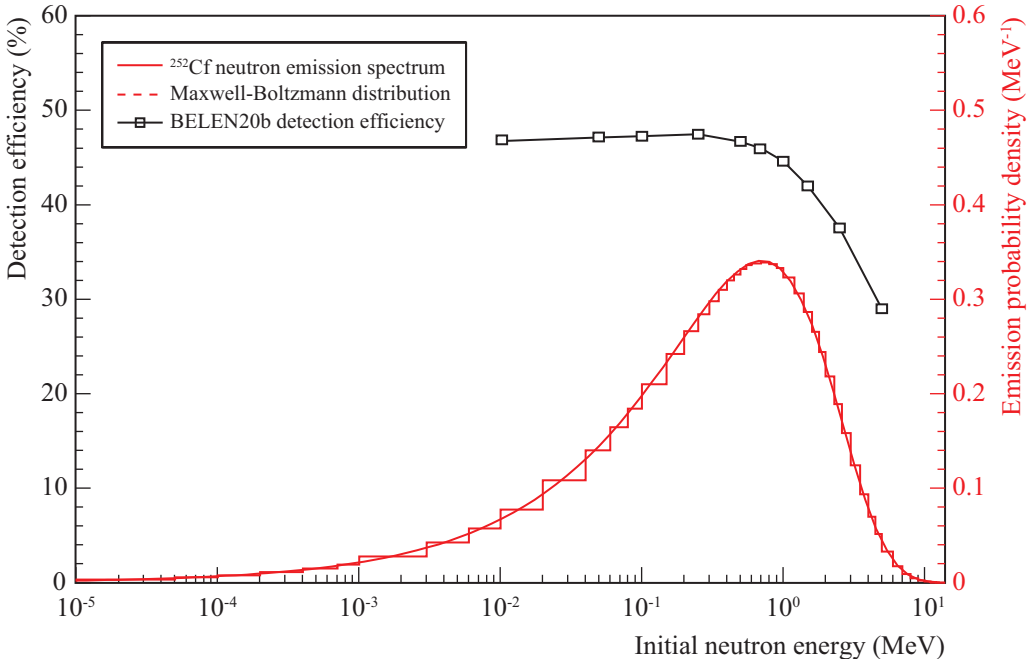

Figure 4.10: Neutron emission spectrum of a standard ^{252}Cf source [127].

Indeed, table 4.3 shows the measured and calculated ratios for the implanted isotopes and the ^{252}Cf source. Uncertainties in the calculated ratios are only statistical, because systematic uncertainties affecting the simulations (neutron emission spectrum, material properties and compositions —of polyethylene and the counter gas in particular—, thermal cross sections and scattering matrix of polyethylene...) are difficult to quantify. Hence, simulations could not be validated against the experimental ratios. Important conclusions may however be drawn. Note that simulations systematically overestimate the ratio. For the ^{252}Cf source, the simulation deviates barely 5 % from the experiment, whereas for the implanted isotopes the deviation reaches 136 % in the case of ^{86}As. On the one hand, the neutron emission spectrum is better known for a ^{252}Cf source than for beta delayed neutron emitters in general. On the other, ^{252}Cf has a harder spectrum. Since the ratio is lower the higher the initial neutron energy, the absolute systematic uncertainty is lower as well. Hence the lower deviation. In any case, the neutron emission spectrum seems to be a relevant source of systematic uncertainty in the simulations, but other sources may also be relevant more at lower than higher energies.

Isotope	MCNPX 2.7.0	GEANT 4.9.03.p02	GEANT 4.10.02.p02	Experiment
^{88}Br	3.265 ± 0.002	3.312 ± 0.011	3.315 ± 0.011	2.755 ± 0.016
^{94}Rb	2.6649 ± 0.0018	2.716 ± 0.009	2.715 ± 0.009	2.351 ± 0.014
^{95}Rb	2.6152 ± 0.0017	2.653 ± 0.009	2.659 ± 0.009	2.08 ± 0.02
^{137}I	2.2217 ± 0.0015	2.256 ± 0.007	2.253 ± 0.007	1.27 ± 0.01
^{86}As	2.900 ± 0.002	2.97 ± 0.01	2.95 ± 0.01	1.25 ± 0.01
^{91}Br	2.3603 ± 0.0016	2.401 ± 0.008	2.384 ± 0.008	1.661 ± 0.016
^{252}Cf	1.5560 ± 0.0010	1.572 ± 0.005	1.575 ± 0.005	1.499 ± 0.001

Table 4.3: Ratio of the neutron detection efficiency of the inner to outer rings of BELEN20b for the implanted isotopes and a standard ^{252}Cf source. Results from simulations reflect only the statistical uncertainty.

4.2 β^- detection with the silicon detector

Beta events registered by a silicon detector can be distinguished from the electronic noise by setting a threshold in the pulse height distribution. The threshold, however, introduces a dependence of the beta detection efficiency on the beta transition energy, especially severe for beta transitions to high excitation energies and different for every isotope. The reason lies in the continuous nature of the beta spectrum, which extends between 0 and an end-point that is isotope-dependent. Such dependence can be an important source of systematic uncertainty in the measurement of delayed neutron emission probabilities. Here as well, Monte Carlo simulations allow to quantify and reduce that uncertainty provided that the beta emission spectrum of the precursor is known.

The response to beta decay of the silicon detector used in the experiment is determined by the interaction of beta particles. The interaction of gamma-rays, neutrons and obviously neutrinos is negligible in such a thin detector. At low energies of a few MeV, electrons interact with matter by ionization, bremsstrahlung and scattering. The accurate description of these processes is therefore essential to the simulation of the detector response and, ultimately, to the calculation of the detection efficiency.

4.2.1 Simulation of low-energy electron interactions

GEANT4 was chosen over MCNPX for the simulation of the response of the silicon detector for its well validated low-energy electromagnetic models. It is distributed with a few physics lists for the simulation of electromagnetic processes that come in different flavors for a variety of applications. Soti et al. [128] tested several of them in simulations of the response of a 1.5 mm Passivated Implanted Planar Silicon (PIPS) detector to a ^{60}Co source and found no significant difference in the choice of flavor other than the computing time. They also found that the response function from simulations with the *Standard* list was

up to 3 % in agreement with an experimental measurement. Based on these results, the default Standard list was used in this work for simulating electromagnetic processes.

The scattering process is a dominant source of systematic uncertainty in the calculation of the detection efficiency, as it is not only an energy loss mechanism, but also responsible for the loss of backscattered electrons. The detailed simulation of electron scattering is only feasible in scenarios where the number of scattering events is low, e.g., in low-density media and thin layers. In most applications, this condition is not fulfilled, and multiple scattering models are used instead. These models describe the average outcome of multiple scattering events (energy loss, spatial displacement and scattering direction), reducing the number of simulation steps. The improved computational performance comes however at the expense of accuracy loss. Special care must be taken then while selecting [129–132] and configuring [128,133] the scattering models.

The Standard list includes both single and multiple electron scattering models. For low-energy electrons (below 100 MeV) only the latter is activated [104]. The model in question is the Urban model [134], which is based on the theory of H.W. Lewis [135]. A detail presentation of the model is out of the scope of this work, but in essence, it uses analytic functions to describe the distribution of moments of the angular and spatial displacements from the theory of H.W. Lewis to sample the final state.

The good agreement between the measured and simulated response functions obtained by Soti et al. [128] validates the electromagnetic models registered in the Standard list. However, that agreement was achieved after a systematic study of the effects of different simulation parameters in the detector response, namely those relevant to the simulation of multiple scattering and the production of secondary electrons. A similar investigation for the silicon detector used in the experiment is presented appendix C.

4.2.2 Simulation of the β^- decay process

Radioactive decay is a stochastic process, i.e., a process that cannot be predicted by knowledge of the prior state of the system. Its simulation is then about generating the decay products according to the physical parameters that govern such stochasticity.

GEANT4 simulates radioactive decay based on data from the Evaluated Nuclear Structure Data File (ENSDF) [7,8], which provides half-lives, branching ratios, emission energies, nuclear level structure, etc. The foundations of the radioactive decay model in GEANT4 are implemented in class *G4RadioactiveDecay* and associated classes [104,136]. G4RadioactiveDecay is responsible for loading and preparing the data for the simulation of the radioactive decay process, either in-flight or at rest. It also handles the creation and initialization of instances of other classes specialized in the simulation of specific decay modes, the application of variance reduction techniques, and the propagation of decay chains.

The β^- decay of unstable nuclei was introduced in chapter 1 as a three-body decay process that involves the emission of an electron and a neutrino, and the production of a residual nucleus that can be left in an excited state. The first two share virtually all the energy available for the decay, and because they are not bound in the final state, their emission

is characterized by continuous energy distributions. *G4BetaMinusDecay* is the class in GEANT4 devoted to the simulation of this process. The simulation begins by sampling the energy of the electron from the theoretical three-body phase space distribution for the specific type of transition [104]. Only allowed; first, second and third unique forbidden; and first non-unique forbidden transitions are considered. The direction of the electron is then sampled isotropically in the reference frame where the parent nucleus is at rest. Finally, the neutrino and the residual nucleus are generated assuring the conservation of energy and momentum. The residual nucleus, when left in an excited state, undergoes nuclear deexcitation via gamma emission or internal conversion.

GEANT4 does not simulate beta decay into the delayed neutron emission channel. The inclusion of this process in the radioactive decay model is an ongoing task.

4.2.3 Calculation of the detection efficiency

Electrons emitted in the beta decay of the implanted isotopes may reach the silicon detector directly traversing the tape or indirectly upon the interaction with other elements of the implantation setup. For reducing as much as possible the systematic uncertainty in the calculation of the beta detection efficiency, the geometry of the implantation and beta detection setups (implantation tape, rollers and their supporting structure, silicon detector and its mounting structure, beampipe, end-cap, etc.) was modeled to the highest level of detail given the information available. The setups as modeled are shown in figure 4.11.

In the simulations, neutrinos and gamma-rays were not produced for the reasons aforementioned. Only electrons were generated and transported until they deposited all their energy or escaped the detection setup. The 10 µm production cut adopted for electrons ensured their emission in the radioactive decay process regardless of the material it occurred in.

Several instrumental effects were considered for performing realistic simulations. Detection events were generated by sorting all interactions with the detector in increasing order of time and integrating the deposited energy within time windows of 1 µs separated 17 µs at least. This is consistent with the preamplifier shaping time in the experiment and the non-paralizable dead time model that applies to the DACQ. Effects affecting the resolution of the detector (charge trapping, electronic noise, etc.) were neglected.

Effect of the beam profile and position at the implantation setup

The beam profile and position are other geometric factors that determine the detection efficiency of the silicon detector. To investigate and account for their effects, a uniform ion beam was generated at the beginning of the beampipe covering the entire inner cross section, then transported along the pipe and implanted onto the different elements of the implantation setup on its way. In-flight decay was deactivated until the ion was implanted for the simulation to proceed.

The implanted isotopes are precursors of a radioactive decay chain, but it is the beta detection efficiency for the individual elements of the chain what is of interest in this work

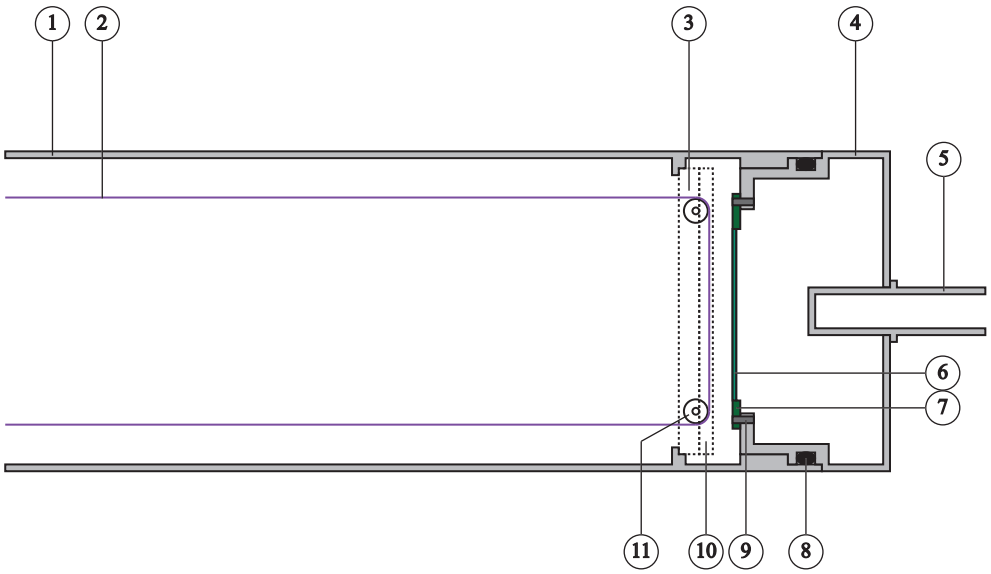

Figure 4.11: Implantation and beta detection setups as modeled for calculating the beta detection efficiency of the silicon detector by Monte Carlo simulations. — 1) Beampipe; 2) implantation tape; 3) rollers support; 4) endcap; 5) LEMO connector for the silicon detector; 6) active volume of the silicon detector; 7) inactive volume of the silicon detector; 8) o-ring; 9) silicon detector holders; 10) tape rollers.

as will be shown in chapter 6. In consequence, the residual nucleus was killed as soon as generated to avoid the propagation of the decay chain.

Figure 4.12 shows dependence of the detection efficiency with the implantation point resulting from the simulation of the decay of ^{95}Rb into the $\beta\gamma$ channel, i.e, to excited states of ^{95}Sr below its neutron separation energy. It was calculated with a 100 keV threshold on the pulse height distribution, which is the value adopted in the analysis. Note that most of the efficiency is concentrated over the area of the implantation tape directly exposed to the beam (hereafter the tape). A beam projected outside this area may cause a significant loss of efficiency.

Profiles of the efficiency spatial distribution along the horizontal and vertical directions crossing at the center of the implantation tape are presented in figure 4.13 for all the implanted isotopes. Note that the efficiency is more or less constant inside the tape along $y = 0$, and only outside the isotope-dependence is appreciable. The efficiency drops rapidly at the edges ($x = \pm 6.35$ mm), where the beam hits the 3 mm thick aluminum support holding the rollers. A similar drop is observed in the $x = 0$ profile, but in this case the dependence is bell shaped due to the interaction with the rollers, which have a cylindrical shape and thus a varying thickness with y in the direction of the beam.

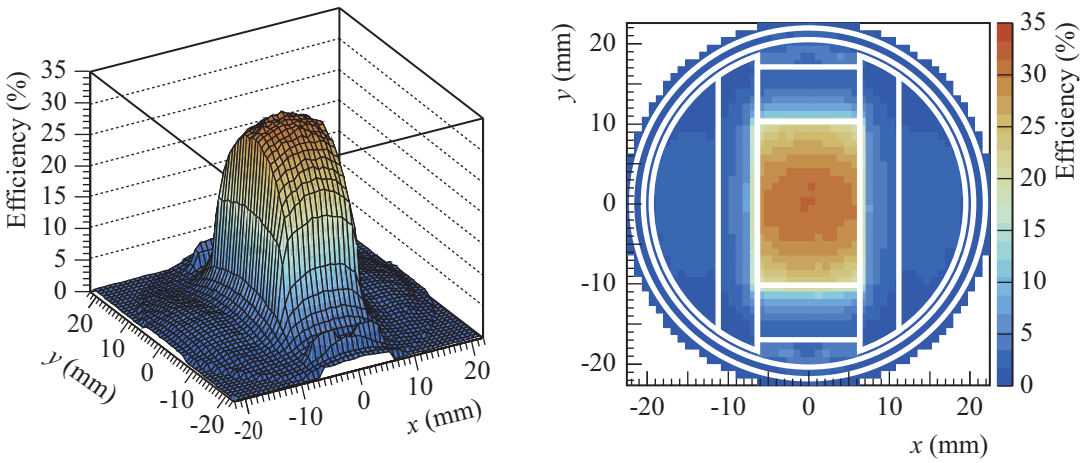

(a) **(b)**

Figure 4.12: Spatial distribution of the beta detection efficiency from the complete simulation of the radioactive decay of ^{95}Rb.

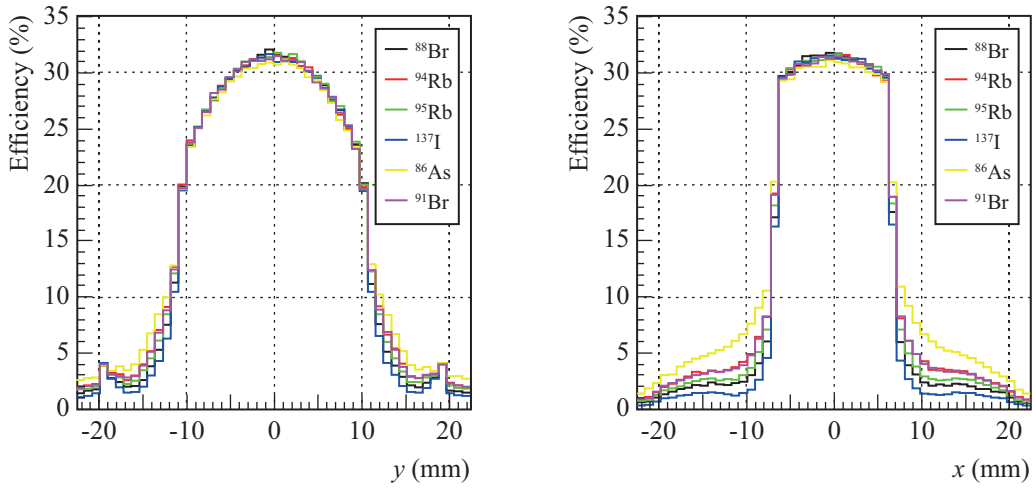

(a) $x = 0$ **(b)** $y = 0$

Figure 4.13: Profiles of the beta efficiency spatial distribution along the horizontal and vertical directions crossing at the center of the implantation tape for the implanted isotopes.

It follows from the interpretation of these figures that the detection efficiency is strongly dependent on the profile and position of the beam at the implantation setup. During the experiment, the implantation was tested with an optical device to center the beam on the tape. The tests showed a circular beam profile about 1 cm in diameter. The beta detection efficiencies presented next were calculated accordingly for a uniform profile of the same shape and size.

Effect of the beta intensity distribution

The effect of the beta intensity distribution on the detection efficiency was investigated by simulating the detector response to an isotropic source of electrons with energies sampled from a Fermi distribution with end-points between 100 keV and 12 MeV. The end-point range covered the Q values of the implanted isotopes and their descendants. Only allowed transitions were considered in the Fermi distribution under the assumption that forbidden transitions have a negligible effect on the efficiency.

Figure 4.14 shows the dependence of the detection efficiency with the end-point (hereafter the efficiency curve). Note the steep increase up to approximately 3 MeV. For higher end-points, the efficiency remains almost constant.

Along with the efficiency curve, figure 4.14 shows the absolute beta intensity distribution I_β calculated from the partial distributions in the $\beta\gamma$ and βn decay channels ($I_{\beta\gamma}$ and $I_{\beta n}$ respectively) as:

$$I_\beta = (1 - P_n)I_{\beta\gamma} + P_n I_{\beta n} \tag{4.2}$$

The former were taken from ENSDF. The βn distributions, on the other hand, were calculated from the neutron emission spectra taken from ENDF/B-VII.1 [45] (figure 4.9), assuming that the neutron emission populates the ground state of the daughter nucleus, i.e., it is not followed by gamma deexcitation. As figure 4.15 shows, that is the most likely outcome of the decay into the βn channel of all the reference isotopes. Thus, the distribution calculated under such consideration is not much different than the real distribution, which is slightly concentrated at higher excited states of the emitter.

For the calculation of $I_{\beta n}\left[E(^{A}_{Z+1}X)\right]$, consider the emitter with an excitation energy $E(^{A}_{Z+1}X)$ above the neutron separation energy $S_n(^{A}_{Z+1}X)$ decaying by neutron emission to an excited state of the daughter with excitation energy $E(^{A-1}_{Z+1}X)$. The energy conservation law in the reference system where the precursor was at rest reads:

$$\left[m(^{A}_{Z+1}X) + T(^{A}_{Z+1}X) + E(^{A}_{Z+1}X)\right] = \left[m(^{A-1}_{Z+1}X) + T(^{A-1}_{Z+1}X) + E(^{A-1}_{Z+1}X)\right] + (m_n + T_n) \tag{4.3}$$

where m denotes mass (in energy units) and T kinetic energy. On the other hand, the

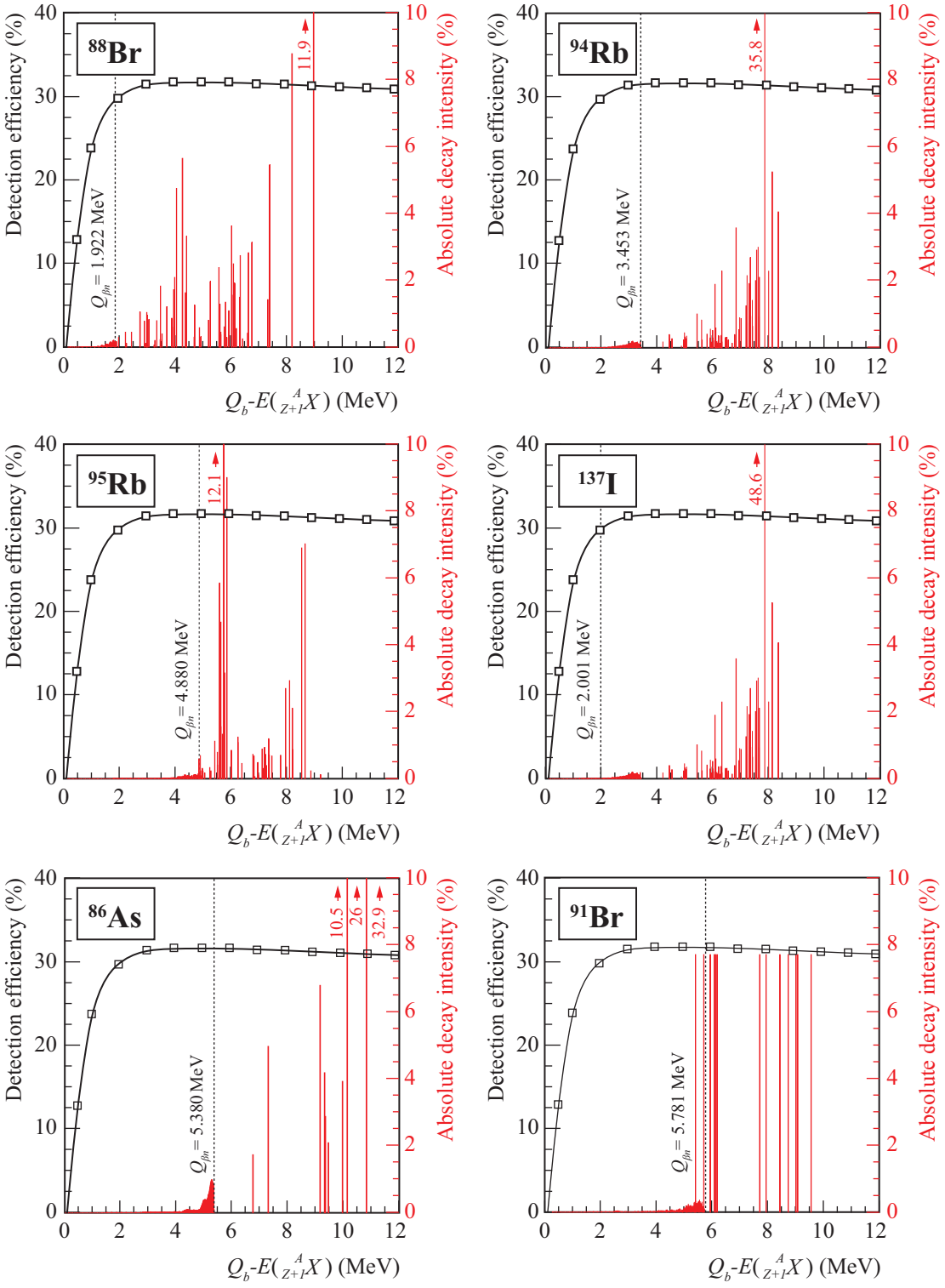

Figure 4.14: Detection efficiency of the silicon detector as a function of the end-point of the Fermi distribution for the implanted isotopes, and the corresponding absolute beta intensity distributions.

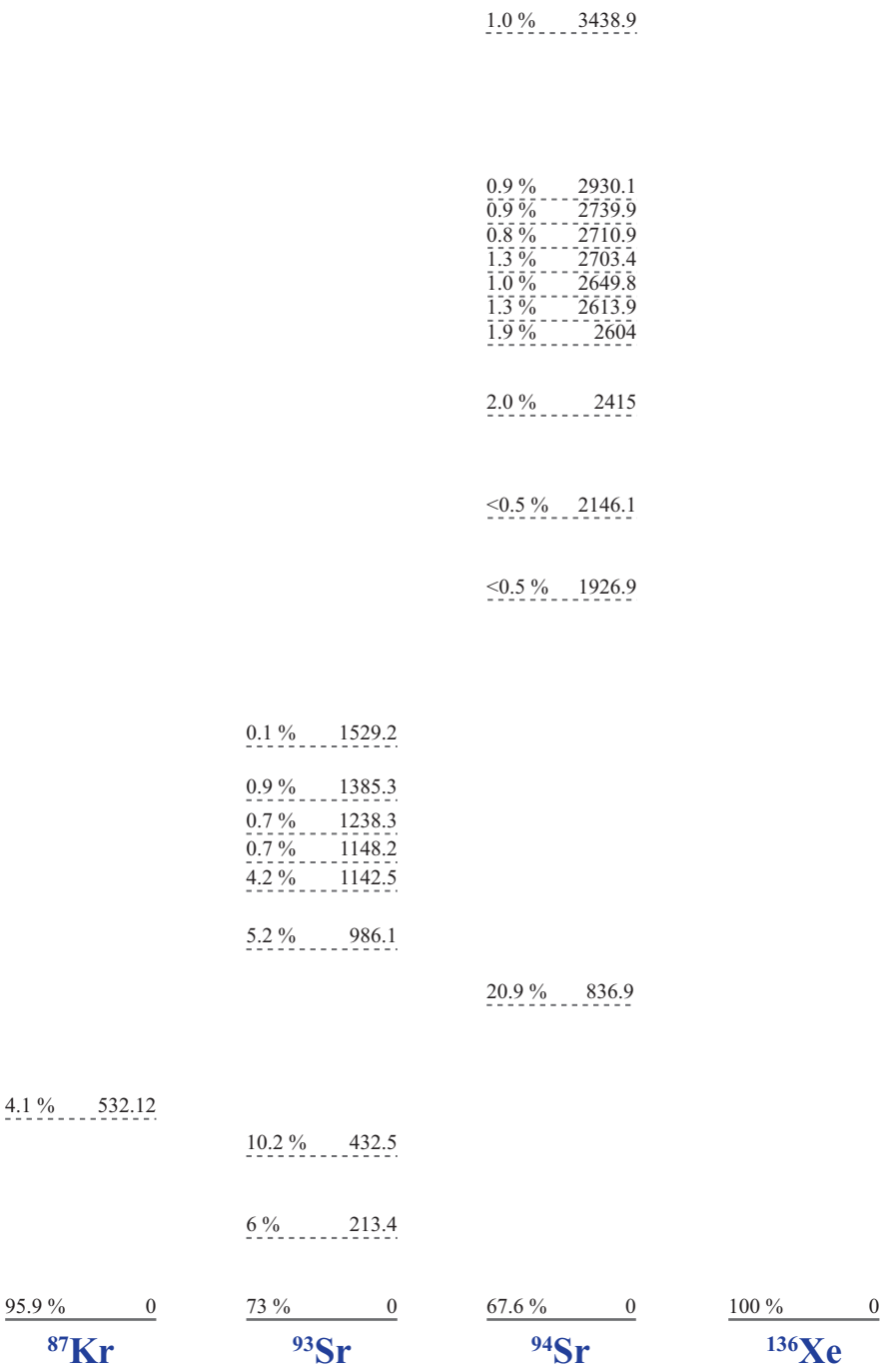

Figure 4.15: Neutron intensity distributions of the reference isotopes in ENSDF. The distributions are represented over the level scheme of the daughter nucleus. Lines were separated when necessary to accommodate the labels above.

neutron separation energy of the emitter is given by [137, equation 3.26]:

$$S_n(^{A}_{Z+1}X) = \left[m(^{A-1}_{Z+1}X) + m_n\right] - m(^{A}_{Z+1}X) \tag{4.4}$$

Combining equations 4.3 and 4.4 and solving $E(^{A}_{Z+1}X)$ leads to:

$$E(^{A}_{Z+1}X) = S_n(^{A}_{Z+1}X) + E(^{A-1}_{Z+1}X) + T(^{A-1}_{Z+1}X) + T_n - T(^{A}_{Z+1}X) \tag{4.5}$$

Since the neutron and the neutrino share virtually all the energy available for the beta decay, the recoil energy of the emitter can be neglected. Then, the linear momentum conservation law in the neutron emission process yields the following equation for the recoil energy of the daughter:

$$T(^{A-1}_{Z+1}X) = T_n \left[\frac{m_n}{m(^{A-1}_{Z+1}X)}\right] \tag{4.6}$$

This equation combined with equation 4.5 leads finally to:

$$E(^{A}_{Z+1}X) \approx S_n(^{A}_{Z+1}X) + E(^{A-1}_{Z+1}X) + T_n \left[1 + \frac{m_n}{m(^{A-1}_{Z+1}X)}\right] \tag{4.7}$$

It is clear from this equation that, for a given neutron energy, the decay of the precursor may proceed through different excited states of the emitter between $E_{\min}(^{A}_{Z+1}X) = S_n(^{A}_{Z+1}X) + T_n \left[1 + \frac{m_n}{m(^{A-1}_{Z+1}X)}\right]$ and $E_{\max}(^{A}_{Z+1}X) = Q_\beta$. Considering $I_n = 100\%$ for $E(^{A-1}_{Z+1}X) = 0$, the equation turns into a bijective function $f : T_n \rightarrow E(^{A}_{Z+1}X)$. Thus, the probability of a decay event populating levels of the emitter between $E(^{A-1}_{Z+1}X)$ and $E(^{A-1}_{Z+1}X) + dE(^{A-1}_{Z+1}X)$ equals the probability of emitting a neutron with energy between T_n and $T_n + dT_n$. In consequence, $I_{\beta n}\left[E(^{A}_{Z+1}X)\right]$ can be obtained from the neutron emission spectrum $\mathcal{P}(T_n)$ as:

$$I_{\beta n}\left[E(^{A}_{Z+1}X)\right] = \frac{dT_n}{dE(^{A}_{Z+1}X)}\mathcal{P}(T_n) = \left[1 + \frac{m_n}{m(^{A-1}_{Z+1}X)}\right]^{-1} \mathcal{P}(T_n) \tag{4.8}$$

ENSDF features neutron intensity distributions of β-delayed neutron emitters, but almost no information on the population of the excited states of the emitter that lead to the neutron emission. Among the implanted isotopes, only ^{135}I has beta intensity distribution into the βn channel in ENSDF. Approximating the absolute beta intensity distribution in the βn channel from the neutron emission spectra from ENDF/B-VII.1 was thus a decision that aimed at using a single, consistent and complete data source.

The beta detection efficiency for a given isotope is the convolution of the efficiency curve with the absolute beta intensity distribution (equation 4.2). This yields:

$$\varepsilon_\beta = (1 - P_n)\varepsilon_{\beta\gamma} + P_n\varepsilon_{\beta n} \tag{4.9}$$

where $\varepsilon_{\beta\gamma}$ and $\varepsilon_{\beta n}$ are the partial efficiencies in the $\beta\gamma$ and βn channels respectively. Now, version 4.3.2 of the radioactive decay data library distributed with GEANT4.10.02.p02 does not include information on the beta decay into the βn channel, not even for ^{135}I. The reason lies in the lack of a model in GEANT4 for describing the β-delayed neutron emission process. Thus, simulations with GEANT4 as released can only be used to calculate $\varepsilon_{\beta\gamma}$ and, ultimately, the first term of equation 4.9, which is an underestimation of ε_β.

GEANT4 was extended in this work to describe the β-delayed neutron emission process based on the approximations that lead to equation 4.8. The extension considered only allowed transitions as in the simulations for calculating the efficiency curve for the same reasons. It conserved linear momentum and energy —except for the neglected recoil energy of the emitter that lead to equation 4.7—, but ignored the parity and angular momentum conservation laws. Because the approximated beta intensity distribution in the neutron emission channel is more concentrated at lower excited states of the emitter than the real distribution, in virtue of the steep drop of the efficiency curve with the end-point below 3 MeV, simulations including this model yield an overestimation of ε_β.

Simulations were performed then with the released and extended versions of GEANT4 to calculate the beta detection efficiency of the implanted isotopes. To avoid the propagation of the decay chain, the emitter and the daughter were killed as soon as generated. The results are shown in table 4.4, with ε_β summarized as:

$$\varepsilon_\beta = \varepsilon^\beta_{\text{min}} + \frac{\left(\varepsilon^\beta_{\text{max}} - \varepsilon^\beta_{\text{min}}\right)}{2} \tag{4.10}$$

$$\sigma_{\varepsilon_\beta} = \frac{\left(\varepsilon^\beta_{\text{max}} + \sigma_{\varepsilon^\beta_{\text{max}}}\right) - \left(\varepsilon^\beta_{\text{min}} - \sigma_{\varepsilon^\beta_{\text{min}}}\right)}{2} \tag{4.11}$$

where $\varepsilon^\beta_{\text{min}}$ and $\varepsilon^\beta_{\text{max}}$ are the underestimation and overestimation of ε_β respectively. The table also shows $\varepsilon_\beta = \varepsilon_{\beta\gamma}$ calculated for some of the descendants of the implanted isotopes involved in the analysis that will be presented in chapter 6.

Note that the absolute beta intensity distributions for ^{86}As and ^{91}Br in figure 4.14 were calculated using the delayed neutron emission probabilities from [11]. But this was just for the sake of illustration, as the latter are the quantities this work aims at estimating and therefore are a priori unknown. For this reason, ε_β was only calculated for the reference isotopes.

Finally, note that the beta intensity distribution for ^{91}Br in the $\beta\gamma$ channel is uniformly distributed over a set of 13 discrete end-point values. This is because ENSDF does not actually contain the distribution, but only the end-points measured by Graefenstedt et al.

Isotope	P_n (%) [11]	$\varepsilon_{\beta\gamma}$ (%)	$\varepsilon^{\beta n}_{\mathbf{max}}$ (%)	$\varepsilon^{\beta}_{\mathbf{min}}$ (%)	$\varepsilon^{\beta}_{\mathbf{max}}$ (%)	ε_{β} (%)
^{88}Br	6.75 ± 0.18	30.67 ± 0.06	28.08 ± 0.05	28.60 ± 0.06	30.50 ± 0.04	29 ± 1
^{88}Kr		17.27 ± 0.04				17.27 ± 0.04
^{87}Kr		29.17 ± 0.05				29.17 ± 0.05
^{94}Rb	10.24 ± 0.21	30.61 ± 0.06	30.57 ± 0.06	27.48 ± 0.06	30.61 ± 0.04	29.0 ± 1.6
^{94}Sr		29.36 ± 0.06				29.36 ± 0.06
^{94}Y		30.57 ± 0.06				30.57 ± 0.06
^{93}Sr		28.20 ± 0.05				28.20 ± 0.05
^{95}Rb	8.87 ± 0.29	30.66 ± 0.06	30.66 ± 0.06	27.94 ± 0.06	30.66 ± 0.04	29.3 ± 1.4
^{95}Sr		30.68 ± 0.06				30.68 ± 0.06
^{137}I	7.33 ± 0.38	30.53 ± 0.06	25.74 ± 0.05	28.29 ± 0.05	30.18 ± 0.05	29 ± 1
^{137}Xe		30.1 ± 0.1				30.1 ± 0.1
^{86}As	?	30.20 ± 0.05	30.05 ± 0.05			
^{86}Se		30.51 ± 0.06				30.51 ± 0.06
^{91}Br	?	30.56 ± 0.06	30.74 ± 0.06			
^{91}Kr		30.82 ± 0.06				30.82 ± 0.06

Table 4.4: Beta detection efficiency of the silicon detector for the implanted isotopes and their descendants involved in the analysis that will be presented in chapter 6. Only $\varepsilon_{\beta\gamma}$ and $\varepsilon_{\beta n}$ are given for ^{86}As and ^{91}Br, because their P_n value is a priori unknown.

[138]. A uniform distribution was adopted to generate the ^{91}Br file in version 4.3.2 of the radioactive decay library of GEANT4. That is a common approximation, and a good one to the effects of calculating $\varepsilon_{\beta\gamma}$ for ^{91}Br, since the end-points fall well above 3 MeV, where the efficiency curve is almost constant. It may be a bad approximation though for other purposes as Pappas & Sverdrup [4] concluded.

4.2.4 Validation against decay measurements

The experimental pulse height distribution of the silicon detector contains the contributions of the decay of the precursor and the rest of the elements of its decay chain. In consequence, to compare simulations with experiment, the entire decay chain must be propagated in the simulations.

The time structure and length of the measurement cycle must also be take into account in the simulations. On the one hand, with the evolution of the decay chain, the contributions of its elements to the detector response vary in time. Multiple implantations of the precursor distributed over the cycles complicates those contributions further as will be shown in chapter 6. On the other hand, decay events past the end of the cycle are lost, i.e., they do not contribute to the detector response. However, reproducing the time structure of the

cycles in the simulations requires the knowledge of the number of ions implanted at each implantation. This inconvenient was circumvented by selecting detection events occurring between the first and second implantations, which result from the first implantation only. Like this, there was no contamination of the response function from events of previous implantations and the number of implanted ions became irrelevant to reproduce the shape of the pulse height distribution.

^{95}Rb was chosen for validating the simulations of the response of the silicon detector against the experiment. Its high production yield and short half-life provided good statistics and facilitated the distinction of the interval between the first and second implantations.

For comparing the simulated and experimental pulse height distributions, the contributions from the electronic noise and room background to the latter were removed. They were assumed to produce events randomly distributed in time. The pulse height distribution of events before the first implantation was subtracted accordingly from the distribution between the first and second implantations after scaling the former to account for the difference in time interval length.

A key difference with respect to the previous simulations was the use of a 0 mm production cut for protons. GEANT4 adopts the same cut for protons and ions, so no production cut for protons ensures that the residual nucleus in the decay process is always produced and the decay chain propagated. The chain was allowed to propagate for 0.192 s, which is the duration of the trap cycle, i.e., the time between successive implantations.

Figure 4.16 shows the response functions calculated from simulations with the beam centered at different positions around the center of the implantation tape. They are normalized to the number of events of the experimental response function above 100 keV. First, note that the simulated responses are in good agreement with each other above the detection threshold. Only below discrepancies arise as the beam moves in the vertical direction away from the center of the tape. This is again an effect of the varying thickness of the rollers with y in the direction of the beam. The fact that such discrepancies are not observed in figure 4.16(b) indicates that the support of the rollers effectively shields the detector from the activity of ions implanted on it. Note second that the experiment agrees best with the simulation with the beam centered on the tape. This is evidence that the beam was well centered on the tape during the ^{95}Rb measurement. Nevertheless, the agreement is not perfect. Light discrepancies are observed between 200 keV to 300 keV. Bear in mind that these simulations do not include the decay into the $\beta\gamma$ channel.

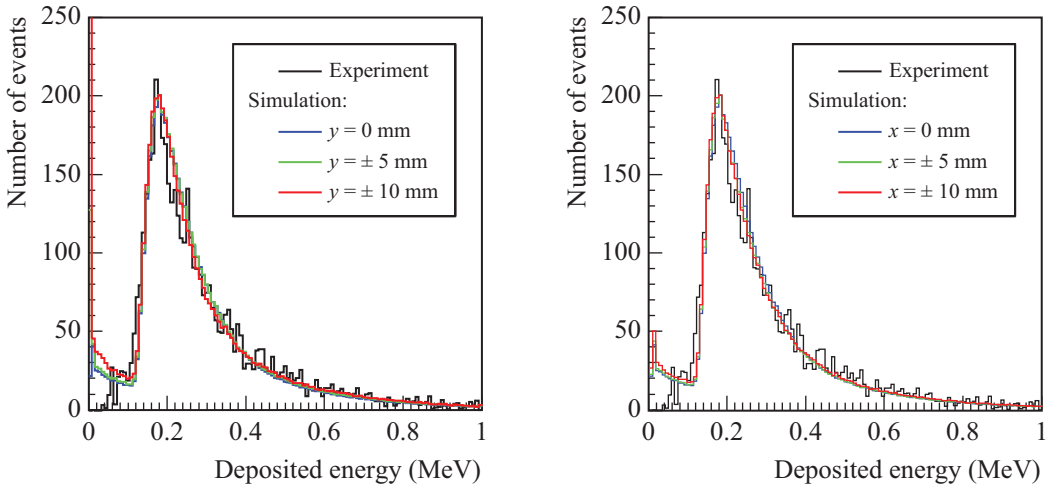

(a) $x = 0$ **(b)** $y = 0$

Figure 4.16: Response of the silicon detector to the radioactive decay of ^{95}Rb. The simulated response is represented for a beam impinging on the tape at different positions (see figure 4.12(b)).

Chapter 5

Data preparation

The time distributions of beta and neutron detected events contain the necessary information for the application of $P_n\,{}^{A}_{Z}X$ method for estimating β-delayed neutron emission probabilities (section 1.3.1). How the physical process is modeled to extract that information is the subject of the next chapter. This one is concerned with the preparation of the data for the analysis, which is as important as the modeling. How consistent and clean time distributions were generated is here described, covering the data munging and the process of exploration and cleansing.

5.1 Raw data unpacking and sort

The software of the DACQ presented in section 3.2.2 writes data streams in List-Mode Data (LMD) files keeping the same format used by the digitizers to store information in memory. A scheme of the format is shown in figure 5.1. It comprises relevant processing and configuration information encoded by the FPGA, and the outputs of the fast and slow filters. Processing and analyzing experimental data directly in this format is inefficient due to the large number of logic and arithmetic operations necessary for unpacking[1] them every time they are read. Hence, the data must be unpacked and organized in more efficient structures that provide selective access.

The order in which events are written in the LMD files makes this format even more inefficient. It was mentioned in section 3.2.2 that the two memory banks of the digitizers are swapped when one of them is almost full or after a certain time. Upon the swap, the data become available for readout and the acquisition continues with the active banks. The computer retrieves the data from the inactive banks one channel at a time, and stores them in a shared memory to make them available for different functions of the DACQ software. This process breaks the overall chronological order of events complicating the selective access to the data based on the timestamp.

Events from the same channel do remain in chronological order nonetheless. They define,

[1]The term "unpacking" refers to the process of transforming the raw data into a more suitable form for processing and analysis.

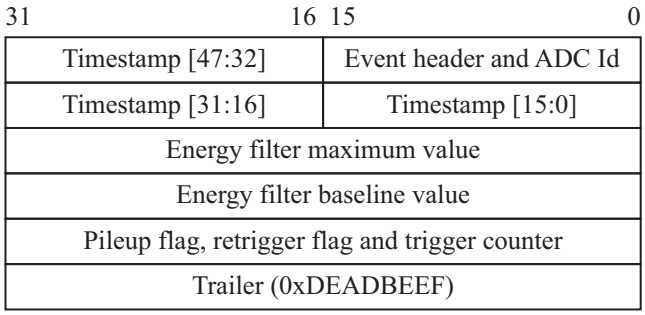

Figure 5.1: Data format of events registered by the Data ACQuisition system. It is the same format used by the digitizers to store information in memory and write data streams to LMD files.

for a single readout, the second level of data packing after the LMD files: the channel buffer. A third level is defined by all channel buffers within the same readout: the readout buffer. Both levels are of variable length, and for this reason, the direct selection of specific channels and readout buffers is not possible without the use of keys. Headers were written for these buffers in the LMD files to facilitate a pipelined access to the data. A more sophisticated format is required for a selective access.

ROOT is a data analysis framework developed at CERN in C++ that offers the possibility to combine vertical and horizontal data partitioning strategies for an efficient handling of large amounts of data [139,140]. Objects of its container class *TTree* (hereafter trees) can store any kind of object regardless of its complexity. Data in a trees are organized in a list of objects of the class *TBranch* (hereafter branch). These branches can store complete objects as a whole or split up into the individual data members. Each one is assigned an independent memory buffer. Like this, when specific data are required, it is not necessary to read the whole tree but only the memory buffers of the associated branches. This allows for a selective data handling and makes ROOT an appropriate tool for efficiently sorting and reducing the experimental data. The organization of the data in branches must be optimized thus for the specific use case.

The horizontal partitioning was kept at a file level, i.e., each LMD file was unpacked and converted into a ROOT file. The new files were considerably smaller than the original, as a consequence of the data reduction and an optimum choice of data types. In addition, the compression algorithms offered by ROOT were activated. This had a negligible effect in the data reading performance.

A vertical partitioning was used instead for the data stored in the ROOT files. A single tree was created in each file, with a single branch containing objects of the new class *TEvent*, which represents a detection event. TEvent objects (hereafter events) hold the timestamp and pulse height of the detection event, and additionally, the channel, buffer and measurement cycle identifiers. The last three values were useful for sorting and verifying the consistency of the data. Each one of these data members were stored separately.

Memory buffers are sequentially written to the LMD files as they are filled, with a specific

header at the beginning that allows to determine the buffer identifier. No indication is however written when timestamps are reset at the beginning of each cycle. The cycle numbers had to be determined then by comparing the timestamps of consecutive events within the same channel and identifying the timestamp resets.

5.2 Exploration and cleansing

5.2.1 Cycle structural problems

One way to verify by visual inspection the consistency of the structure of the measurement cycles is to represent the event timestamp versus the buffer identifier. This helped to identify structural problems that were more evident in measurements with higher counting rates and longer cycles.

Figure 5.2(a) shows the plot for events registered by the silicon detector in the ^{88}Br measurement. A first type of structural problem is observed around the buffers 1100 and 1300 as sets of two incomplete consecutive cycles. The sum of the lengths of the cycles in each set is approximately the length of a complete cycle, suggesting that the second could be the result of an early timestamp reset. Figure 5.2(b) confirms this hypothesis. It shows the time distribution of detected events from the first set of two incomplete cycles above buffer 1100, with events from the second cycle represented with a time offset equal to the timestamp of the last event in the first. The resulting overall distribution is continuous at the time offset and consistent with the distribution of a complete cycle.

A second type of structural problem appeared as gaps in the cycle structure with the typical length of a buffer. Figure 5.3 illustrates the problem with events registered in the ^{94}Rb measurement by a neutron detector in the inner ring of BELEN. Two of these gaps can be observed in the cycle around buffer 110. The time interval of the buffer right before the gaps shows events of the next buffer of the same cycle, which contradicts the chronological order in which events are supposed to be written at channel level.

The two structural problems described before were observed in all channels simultaneously. They can severely affect the structure of the overall time distributions of detected events — which are essential for the analysis— if the affected cycles are not corrected or discarded. The latter was avoided in measurements where the problem affected a large number of cycles, as it had had a significant impact on the measurement accuracy.

The third structural problem identified is illustrated in figure 5.4. The figure represents events registered by a neutron detector in the inner ring of BELEN in the ^{137}I measurement. Note the presence of events between contiguous cycles around 172 s. These events actually belong to the last buffer of the cycle they are next to. In contrast to the other two structural problems, this one was not always observed in all channels simultaneously. Events breaking the cycle structure in this problem were few. Therefore, this problem had a negligible effect on the overall time distributions of detected events.

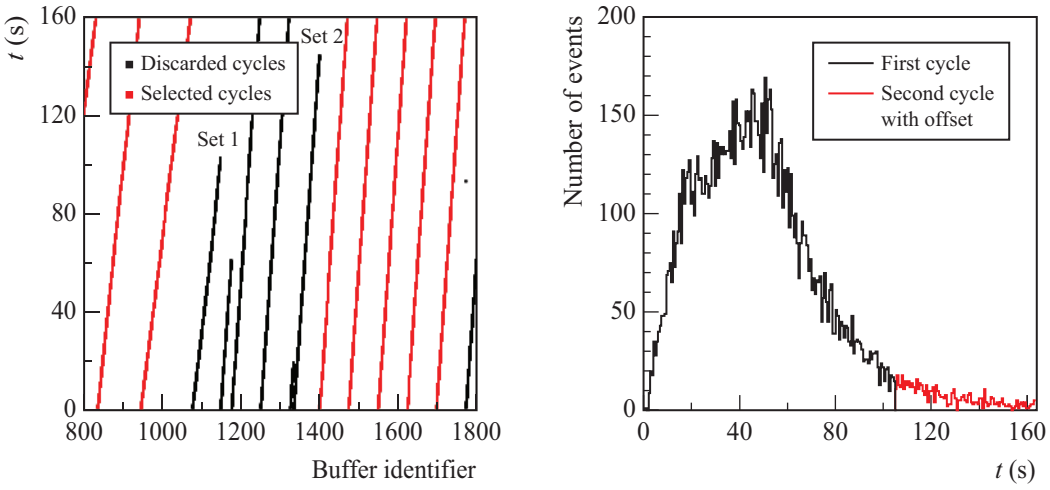

(a) **(b)**

Figure 5.2: Incomplete measurement cycles as the result of early timestamp resets. Events registered by the silicon detector in the ^{88}Br measurement are represented. Figure 5.2(a) represents the data before and after cleansing overlapped to illustrate the efficacy of the pattern recognition algorithm in the identification and exclusion of incomplete cycles around the buffer identifiers 1100 and 1300. Figure 5.2(b) shows the time distribution of beta detected events in the first set of incomplete cycles around the buffer identifier 1100, with events from the second cycle represented with a time offset equal to the timestamp of the last event in the first.

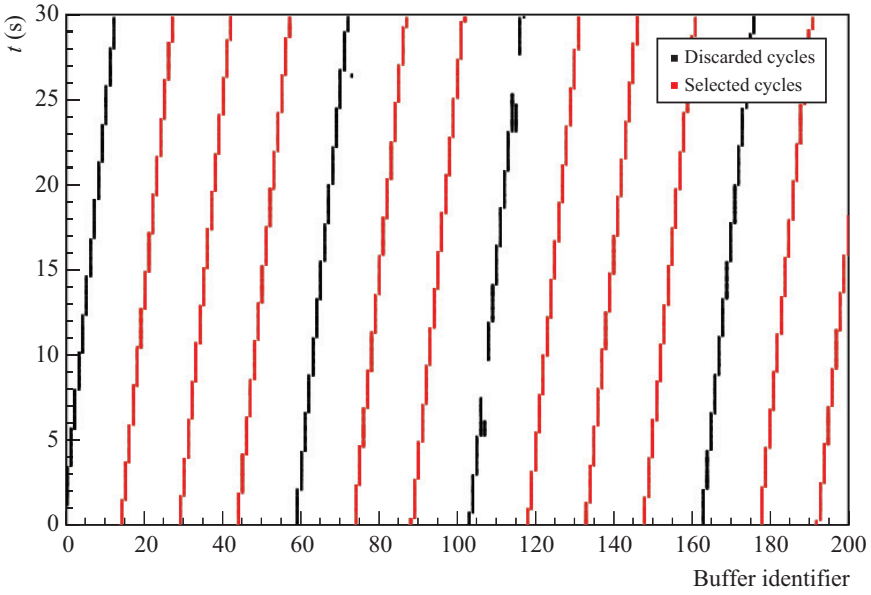

Figure 5.3: Gaps in the measurement cycle. Events registered by a neutron detector in the inner ring of BELEN in the ^{94}Rb measurement are represented. The gaps can be observed around the buffer identifier 110. The data before and after cleansing are overlapped to illustrate the efficacy of the patter recognition algorithm in the identification and exclusion of cycles with structural problems.

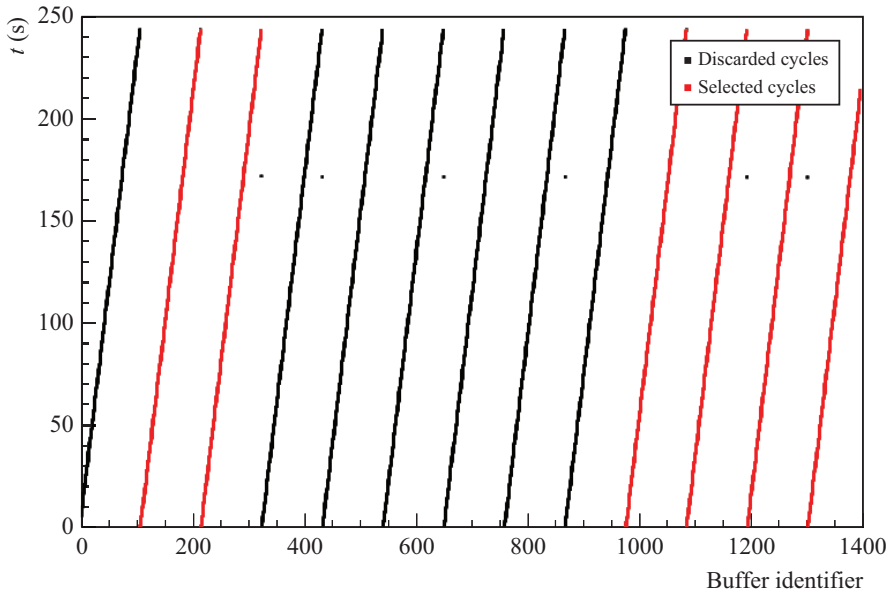

Figure 5.4: Events out of the cycle structure registered by a neutron detector in the inner ring of BELEN in the ^{137}I measurement. The deviation can be observed around t =172 s. The data before and after cleansing are overlapped to illustrate the efficacy of the patter recognition algorithm in the identification and exclusion of cycles with structural problems.

All structural problems so far identified were understood and dealt with, but other forms of data corruption were present that a visual inspection of the timestamp versus the buffer identifier plots did not not reveal. The data was explored accordingly from other angles.

Figure 5.5 shows the time distribution of detected neutron events in the ^{137}I measurement. Note the spike around 160 s. The structural problem of the third type could cause a similar effect, but the spike appears at a different time than the events breaking the cycle structure in figure 5.4. A close look at the time distribution of events in the spike revealed that most them are very close in time and belong to one specific measurement cycle. To investigate the cause of the spike, the time interval distribution of events separated from each other less than 40 µs were represented including and excluding the cycle where the spike occurs (figure 5.6(a)). The difference between both distributions is a peak between 10 µs to 15 µs indicating that the spike is caused by a high-frequency source. Figure 5.6(b) reveals the nature of that source. The energy distribution of all events in the cycle where the spike occurs compared with the same distribution of the subset of those events within a 1 s interval around the spike shows that the events causing the spike are mostly concentrated between 150 keV to 300 keV. This range is above the threshold set to remove the electronic noise, but far from covering the entire range of the response of the neutron counters to thermal neutrons. It becomes clear then that the spike is produced by high-frequency electronic noise events that pile up.

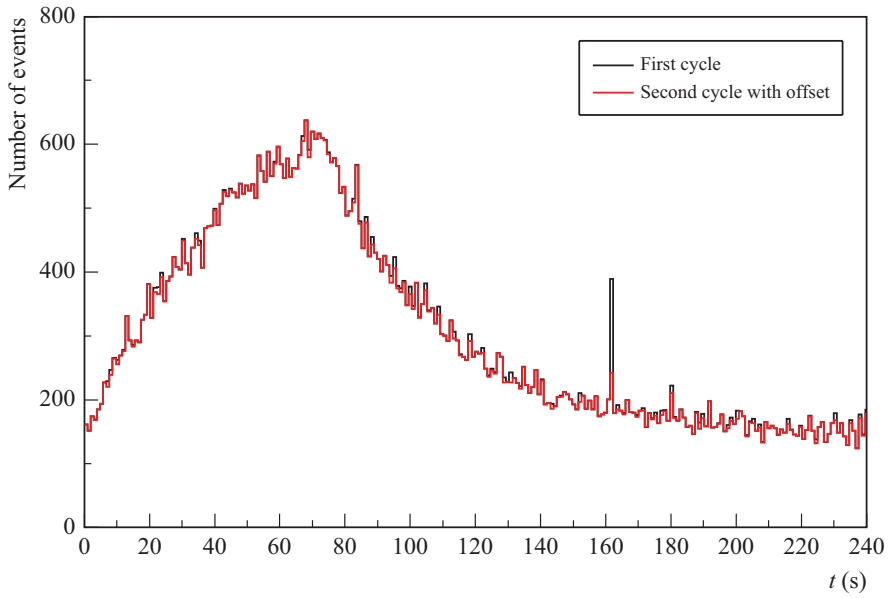

Figure 5.5: Spikes in the time distribution of neutron detected events in the ^{137}I measurement. The data before and after cleansing are overlapped to illustrate the efficacy of the patter recognition algorithm in the identification and exclusion of cycles with structural problems.

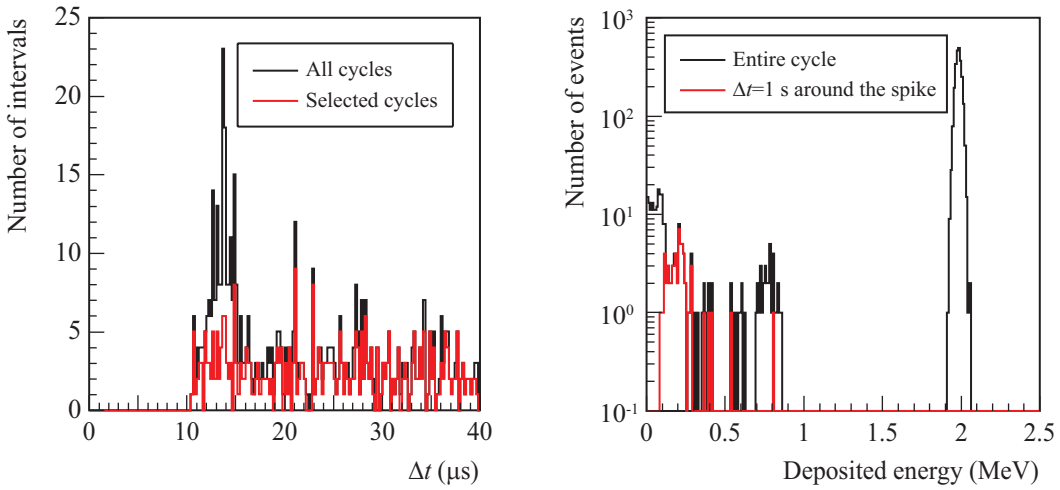

(a) **(b)**

Figure 5.6: High-frequency electronic noise pileup causing spikes the time distribution of neutron detected events. Events registered by a neutron detector in the inner ring of BELEN in the ^{137}I measurement are represented. The selected cycles in figure 5.6(a) exclude the cycle with most events conforming the spike. Figure 5.6(b), on the other hand, shows the detector response conformed with events from that cycle.

The time interval distribution in figure 5.6(a) is shown in figure 5.7 over a wider range. Again, the distributions including and excluding the cycle where the spike in the time distribution occurs are compared. Note the presence of well defined structures separated approximately 50 µs from each other over the entire range. This problem was observed to affect random channels and cycles.

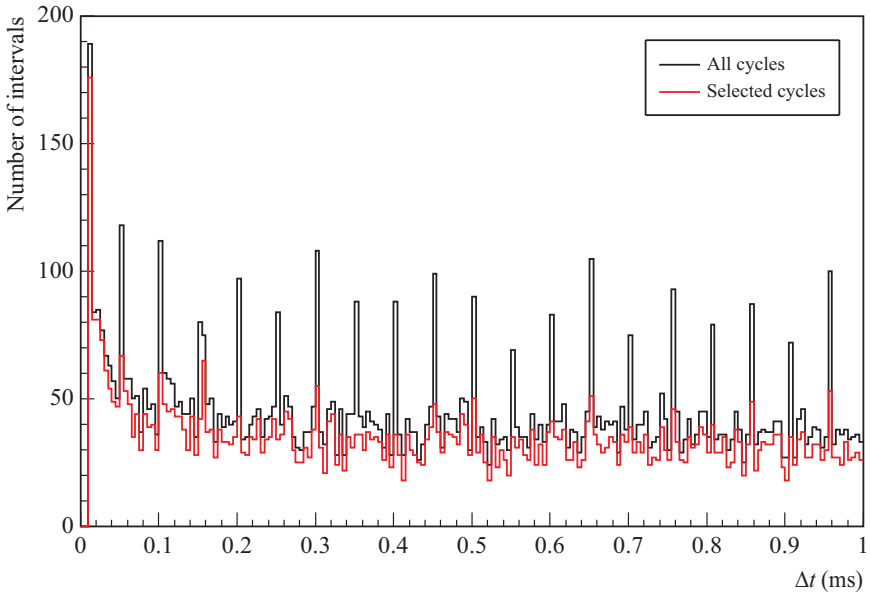

Figure 5.7: Spikes in the time interval distribution of neutron detected events in the ^{137}I measurement. The data before and after cleansing are overlapped to illustrate the efficacy of the patter recognition algorithm in the identification and exclusion of cycles with structural problems.

The cycle structural problems described before affected all measurements to a higher or lesser extent. A pattern recognition algorithm was implemented to identify those problems and reconstruct the data when possible. Cycles with structural problems that could not be corrected were discarded. Table 5.1 summarizes the outcome of the data cleansing. It shows that, despite the effort devoted to data reconstruction, 17 % to 40 % of the data were discarded, being the ^{137}I measurement the most affected.

5.2.2 Energy calibration and separation of unwanted events

The separation of decay events from unwanted events (electronic noise, and gamma and pulser events) was performed by imposing thresholds on the calibrated pulse height distributions. Such separation is not perfect. A fraction of unwanted events always remains and ought to be considered in the analysis. Nevertheless, the separation is essential to minimize the systematic uncertainty in the results.

Figure 5.8(a) shows the calibrated pulse height distribution of a neutron counter in the inner ring of BELEN. A linear calibration $E = cH$, where c is the calibration factor and H the pulse height, was performed on each counter by assigning the Q value of the

Isotope	Measurement time	Number of cycles	Fraction of cycles discarded (%)
^{88}Br	4 h 20 min	93	25
^{94}Rb	3 h 41 min	384	27
^{95}Rb	3 h 24 min	1506	24
^{137}I	16 h	219	39
^{91}Br	10 h 49 min	3330	17
^{86}As	11 h 39 min	2994	17

Table 5.1: Summary of the data before and after cleansing. Discarded cycles are those with structural problems that could not be corrected.

^{3}He(n,p)^{3}H reaction (765 keV) to the centroid of the full energy peak obtained from a Gaussian fit. Note the good separation between neutron events and electronic noise and gamma events in the low-energy range. The separation is perfect between neutron and pulser events, as the latter fall far above the full energy peak. The energy range between 150 keV and 1 MeV and was used to discriminate most unwanted events with a negligible loss of neutron events.

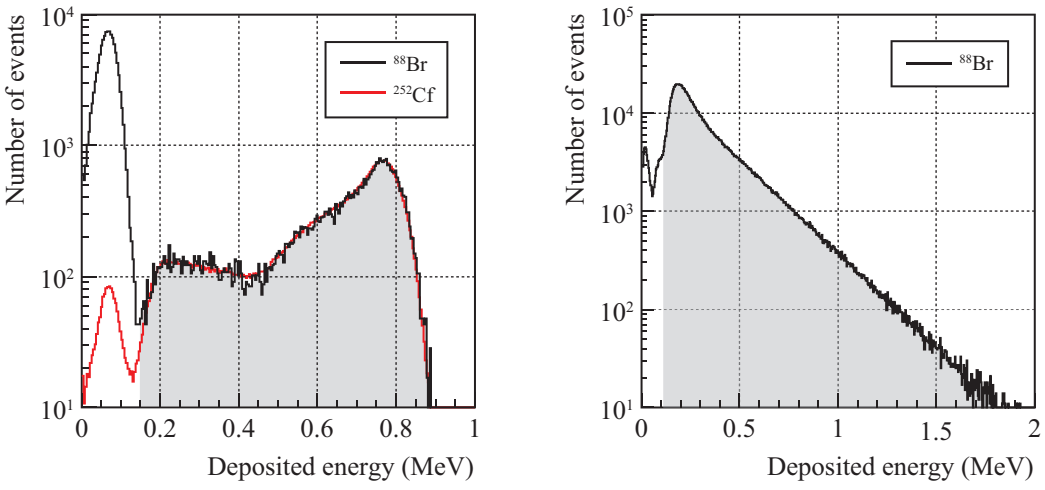

(a) Neutron counter **(b)** Silicon detector

Figure 5.8: Calibrated pulse height distributions from the ^{88}Br measurement. The neutron counter is from the inner ring of BELEN. Its pulse height distribution from a 15 min measurement with a ^{252}Cf source is also represented, normalized to the total number of events between 150 keV and 1 MeV from the ^{88}Br measurement.

A linear calibration was also applied on the pulse height distributions of the silicon detector (figure 5.8(b)). The calibration factor was determined by a Maximum Likelihood (ML) fit of the simulated distribution (section 4.2.4) to the experimental distribution between 100 keV and 6 MeV. The fit range was chosen conveniently to exclude unwanted events. The same range was used for separating those events upon calibration.

Chapter 6

Data analysis and results

The application of the $P_n\,{}^{A}_{Z}X$ method introduced in section 1.3.1 to the estimation of the delayed neutron emission probability of ^{86}As and ^{91}Br is presented in this chapter. The results are also presented and discussed.

The method faces a major difficulty: it depends on the number of beta and neutron detected events from the decay of the precursor, and the disentanglement of these from other detection events requires the prior knowledge of P_n —the very same magnitude to be estimated— and the detection efficiencies for every element of the radioactive decay chain. The methodology proposed here yields a direct estimate of P_n by incorporating equation 1.3 as an external constraint into the simultaneous fit to the time distributions of beta and neutron detected events. Prior knowledge on the efficiencies is still required, but only for the decay of the precursor.

The chapter is structured as follows. First, models for the evolution of the beta and neutron counting rates are derived. The identifiability analysis performed next on those models leads to reparameterizations that improve the model accuracy by reducing the number of parameters and avoiding physical approximations on the detection efficiencies. How statistical inference was performed is then described. Next, the application of the $P_n\,{}^{A}_{Z}X$ is presented, addressing first the efficiency characterization of the detection system required for estimating the delayed neutron emission probabilities of ^{86}As and ^{91}Br. Finally, the results are discussed and compared with previous measurements and evaluations.

Sections 6.1 to 6.3 have a considerable amount of mathematical equations. The reader may refer to the ISO 80000-2:2019 [141] standard for clarifications on the notation used.

6.1 Models for the evolution of the counting rates

The radioactive decay of an isotope leads, in the general case, to a sequential series of decays that conforms a decay chain. A detection system observing the process detects decay events from each element of the chain with an efficiency that depends, among other factors, on the type and energy of the emitted particles. Disentangling the contribution of the decay of the precursor to the time distributions of detected events requires thus

modeling the evolution of the chain and the response of the detection system.

Model uncertainty (i.e, the uncertainty originated from the lack of knowledge of the underlying problem) can be a significant source of uncertainty in modeling. Hence the effort devoted in this work to deriving accurate models. The *general* model presented first in this section reflects such effort, as it is based only on a few well supported assumptions, namely the discrete and instantaneous nature of the implantation process in the experiment, and a stable performance of the detection system. However, in cases where the number of parameters is large, its application may be unpractical. The *equivalent* model presented next arises from the need of dealing with those cases by trading off accuracy and simplicity for an efficient application of the $P_n\,{}^{A}_{Z}X$ method, at the expense of a worse description of the structural features of the data.

6.1.1 General model

Consider a decay chain with n radioactive elements $\{X_1, X_2, \ldots, X_n\}$ and m stable elements $\{X_{n+1}, X_{n+2}, \ldots, X_{n+m}\}$. Let d_{ij}^{p} be the average number of particles of a given type p detected per decay event $X_i \longrightarrow X_j$, where $i \in \mathbb{N}^*_{\leq n}$ and $j \in \mathbb{N}^*_{\leq n+m}$. The evolution of the counting rate of the detection system for that particle type reads:

$$r_p(t) = \sum_{i=1}^{n} \sum_{\substack{j=1 \\ j\neq i}}^{n+m} d_{ij}^{p} b_{ij} \lambda_i N_i(t) \tag{6.1}$$

where b_{ij} is the branching ratio of the decay $X_i \longrightarrow X_j$, λ_i the decay constant of element X_i, and $N_i(t)$ the number of nuclei of that element at time t.

Under a stable performance of the detection system, the terms $N_i(t)$ (hereafter state variables[1]) contain all the time dependence of the counting rate. Posing the basic balance equation for each radioactive element leads to the following linear system of first-order differential equations:

$$\frac{d}{dt}N_i(t) = -\lambda_i N_i(t) + \sum_{\substack{j=1 \\ j\neq i}}^{n} b_{ji}\lambda_j N_j(t) \qquad \forall i \in \mathbb{N}^*_{\leq n} \tag{6.2}$$

where the first and second terms on the right are the destruction and creation rates of element X_i respectively.

Ernest Rutherford (1871–1937) is recognized for being the first to pose these equations. In his work *Radio-activity* published in 1904 [142], he considered a linear chain[2] of only

[1] State variables in the theory of dynamical systems are variables that determine the state of a system at any time.

[2] A linear radioactive decay chain has a single precursor and the rest of the elements are produced by the decay of only one other element.

three radioactive elements and solved the equations by successive substitution. Shortly after, Harry Bateman applied the Laplace transform to obtain the analytic solution for a linear chain with an arbitrary number of radioactive elements [143]. For this, the equations that govern the evolution of a radioactive decay chain are known as the Bateman equations.

The same equations describe many important first-order phenomena in disciplines other than nuclear physics. Hence the great effort made over the years to find a general solution. Some authors have persisted to apply the Laplace transform (see for instance [144]), but still that has not proved to be a convenient method to handle chains with branching, as it becomes unfeasible due to the complex integration and the tedious factorization that follows. Modern techniques of solving systems of ordinary differential equations based on linear algebra offer an easier and perhaps more elegant alternative.

Equations 6.2 can be represented in matrix form as:

$$\frac{d}{dt}\mathbf{N}(t) = \mathbf{A}\mathbf{N}(t) \tag{6.3}$$

where $\mathbf{N}(t)$ is the column vector of the state variables (hereafter state vector), and $\mathbf{A}$ the $n \times n$ constant coefficients matrix:

$$\mathbf{A} = \begin{pmatrix} -\lambda_1 & & & \\ b_{12}\lambda_1 & -\lambda_2 & & \\ \vdots & \vdots & \ddots & \\ b_{1n}\lambda_1 & b_{2n}\lambda_2 & \cdots & -\lambda_n \end{pmatrix} \tag{6.4}$$

The solution for a given initial state vector $\mathbf{N}(t_0)$ is [145, section 7.7]:

$$\mathbf{N}(t) = e^{\mathbf{A}(t-t_0)}\mathbf{N}(t_0) \tag{6.5}$$

This solution, however, does not describe the evolution of the state vector in an entire measurement cycle of the experiment (section 3.3). The counting rates were controlled during the experiment with the implantation of ions delivered by the JYFLTRAP every 191 ms. The extraction voltage of the trap was lowered for just 1 ms each time, which is much lower than the time between successive implantations. Hence, the implantations can be considered instantaneous and, in consequence, they produced jump discontinuities in the evolution of the state vector that equation 6.5 does not describe because the implantation process was not considered in the Bateman equations.

Consider then the sequence of intervals of continuous dynamics within a measurement cycle represented in the following figure, where $t_k : k \in \mathbb{N}^*_{\leq K}$ denotes the time from the beginning of the cycle to the kth implantation, K the total number of implantations, and $T^1_{1/2}$ the half-life of the precursor:

The sequence, which covers the entire cycle, can be divided in three main intervals: a *waiting* interval $[0, t_1]$ (i.e., from the beginning of the cycle to the first implantation), an

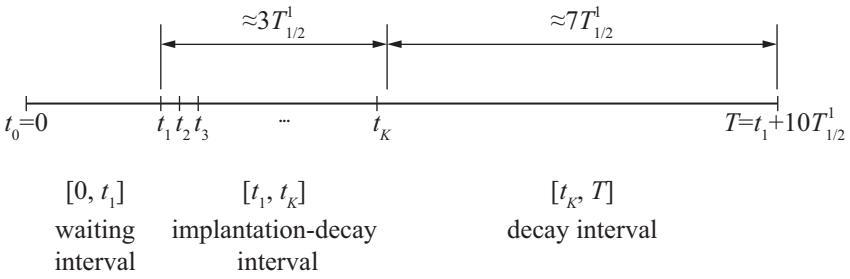

Figure 6.1: Measurement cycle divided in intervals of continuous dynamics.

implantation-decay interval $[t_1, t_K]$ (i.e., from the first to the last implantation), and a *decay* interval $[t_K, T = t_1 + 10T^1_{1/2}]$ (i.e., from the last implantation to the end of the cycle). In the absence of electronic noise, room background and remnant activity from previous implantations, the counting rates would be zero during the waiting interval, since no implantation occurs before t_1. The instantaneous nature of the implantations guarantees that solution 6.5 applies in the rest of the cycle to each subinterval $[t_k, t_{k+1}]$ and $[t_K, T]$ with initial condition $\mathbf{N}^+(t_k) = \mathbf{N}^-(t_k) + \Delta\mathbf{N}(t_k)$, where $\mathbf{N}^\pm(t_k) = \lim_{t\to t_k^\pm} \mathbf{N}(t)$ and $\Delta\mathbf{N}(t_k)$ is the jump in the state vector produced by the kth implantation. The evolution of the state vector during the entire cycle can then be expressed in terms of the solution for each subinterval as:

$$\mathbf{N}(t) = \sum_{k=1}^{K} s(t - t_k) e^{\mathbf{A}(t-t_k)} \Delta\mathbf{N}(t_k) \tag{6.6}$$

where $s(t - t_k)$ is the unit step function shifted by t_k. This equation, together with equation 6.1, define the general model for the evolution of the counting rates during a measurement cycle.

To represent the general model in matrix form, define the $(n + m) \times n$ matrix $\bar{\mathbf{A}}$ as the following extension of matrix $\mathbf{A}$:

$$\bar{\mathbf{A}} = \left(\begin{array}{cccc} & & \mathbf{A} & \\ \hline b_{1,n+1}\lambda_1 & b_{2,n+1}\lambda_2 & \cdots & b_{n,n+1}\lambda_n \\ b_{1,n+2}\lambda_1 & b_{2,n+2}\lambda_2 & \cdots & b_{n,n+2}\lambda_n \\ \vdots & \vdots & \ddots & \\ b_{1,n+m}\lambda_1 & b_{2,n+m}\lambda_2 & \cdots & b_{n,n+m}\lambda_n \end{array} \right) \tag{6.7}$$

Define also the $n \times (n + m)$ matrix $\mathbf{D}_p$ of elements d^p_{ij}. Equation 6.1 can be written in terms of these matrices and the state vector as $r_p(t) = \mathrm{diag}(\mathbf{D}_p\bar{\mathbf{A}})\mathbf{N}(t)$, where $\mathrm{diag}(\mathbf{D}_p\bar{\mathbf{A}})$ is the raw vector with the diagonal elements of the product $\mathbf{D}_p\bar{\mathbf{A}}$. The general model can

then be represented in matrix form as:

$$r_p(t) = \text{diag}(\mathbf{D}_p\bar{\mathbf{A}}) \sum_{k=1}^{K} s(t-t_k) e^{\mathbf{A}(t-t_k)} \Delta\mathbf{N}(t_k) \qquad \forall t \in [0,T] \tag{6.8}$$

where $T = t_1 + 10T^1_{1/2}$ is the cycle length.

Model reduction

The branching ratios of the beta decay channels of the precursor followed by neutron emission (i.e., the delayed neutron emission probabilities) are the ultimate parameters of interest in this work. The rest are nuisance parameters, i.e., of no particular relevance themselves. Reducing the number of nuisance parameters without affecting the model output is an effective way of facilitating the parameter estimation process and reducing its computational cost. A twofold strategy was adopted to achieve this:

1. the reparameterization of the general model; and
2. the use of prior information available on the experiment, underlying physical processes and parameters.

The first step toward the reduction of the general model was to condense the detection parameters in a raw vector $\mathbf{E}_p$, whose elements $\varepsilon_i^p = \sum_{j=1}^{n+m} d_{ij}^p b_{ij}$ are the average number of particles of type p detected per decay of the radioactive element X_i[3]. As a result, the term $\text{diag}(\mathbf{D}_p\bar{\mathbf{A}})$ in equation 6.8 can be written in the simpler form $\mathbf{E}_p\mathbf{\Lambda}$, where $\mathbf{\Lambda}$ is the $n \times n$ diagonal matrix with the decay constants of the radioactive elements in its diagonal. This reparameterization leads to a significant reduction of the number of nuisance parameters, as a d_{ij}^p parameter per decay channel is no longer required, just one ε_i^p parameter per radioactive element instead. The model in the new parameterization reads:

$$r_p(t) = \mathbf{E}_p\mathbf{\Lambda} \sum_{k=1}^{K} s(t-t_k) e^{\mathbf{A}(t-t_k)} \Delta\mathbf{N}(t_k) \qquad \forall t \in [0,T] \tag{6.10}$$

The general model was further reduced assuming that only the precursor was implanted during the experiment. This is a good approximation given the high purity of the beams produced at IGISOL. With no other element of the decay chain implanted, all but the first element $\Delta N_1(t_k)$ of the jumps in the state vectors are null. The jumps in the state vector can then be written in terms of the single parameter $\Delta N_1(t_k)$ as $\Delta\mathbf{N}(t_k) = \Delta N_1(t_k)\boldsymbol{u}_1$,

[3]In general, the average number of particles of a given type detected per decay $X_i \longrightarrow X_j$ is given by:

$$d_{ij} = \sum_{s=1}^{S_{ij}} s \binom{S_{ij}}{s} \varepsilon^s (1-\varepsilon)^{S_{ij}-s} \tag{6.9}$$

where S_{ij} denotes the number of those particles emitted and ε is the average detection efficiency. It follows from this equation that, for decays with one-particle emission, the elements of $\mathbf{E}_p$ are the efficiencies of detecting those particles regardless of the decay channel.

where $\boldsymbol{u}_1 = (1, 0, ..., 0)^T$. Like this, the number of implantation parameters was reduced from nK to K.

Figure 6.2 represents the structure of a particular type of linear radioactive decay chain: the precursor decaying to elements that are, at the same time, precursors of other linear chains independent from each other (hereafter branches). All radioactive elements in each branch have a single decay mode. The general model for a chain like this would not have the branching ratio of those elements as parameters. In other words, only the branching ratios of the precursor would be parameters of the model, one less actually since they all must add up to one.

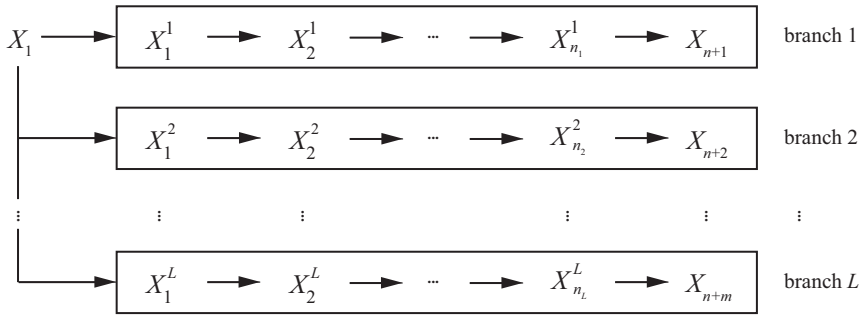

Figure 6.2: Common structure of the radioactive decay chains of the implanted isotopes upon truncation at the first elements with a negligible contribution to the counting rates within the measurement cycle. The structure is that of a linear chain where the precursor decays to elements that are, at the same time, precursors of other linear chains (branches) independent from each other. The superscript on the radioactive elements of the branches denotes the branch index $l \in \mathbb{N}^*_{\leq L}$, and the underscript the index of the element within the branch according to the indexing rules of a GOD chain defined by Yuan & Kernan [146]. n_l is the number of radioactive elements in the lth branch. Stable elements at the end of each branch are given the highest indexes to conform with the definition of matrix $\bar{\mathbf{A}}$.

Not all of the implanted isotopes give rise to a decay chain with the structure represented in figure 6.2, but they can all be truncated at elements that have a negligible contribution to the counting rates within the measurement cycle. The truncated chain in all cases does have the structure in the figure (this statement will be justified later in this chapter for each case). Consequently, for the purpose of model reduction, this particular type of chain was considered.

More information on the decay process is available in nuclear data libraries to further reduce the general model. In ENSDF [7,8], which is the main source of nuclear and radioactive decay data adopted in this work, the half-lives (and consequently the decay constants) of all of the implanted isotopes and their radioactive descendants are available with a relative uncertainty lower than 5 %. Delayed neutron emission probabilities for the reference isotopes are also available, the values from the evaluation of Abriola et al. [11] have been adopted in this work though. This prior information was used in the parameter estimation process. It does not reduce the number of parameters, but constrains the

parameter space. Neglecting the uncertainty on these parameter by fixing them at their mean value leads to the underestimation of the uncertainty of the parameters of interest. How prior information on parameters was included in the parameter estimation process will be explained in section 6.3.1.

Genealogical ordering of decay chains

The elements of a decay chain with the structure represented in figure 6.2 can be arranged in the following way: the precursor X_1 first, followed by the radioactive elements of the branches in the order of decay and increasing order of l (i.e., $\{X_1^1, X_2^1, \ldots, X_{n_1}^1, X_1^2, X_2^2, \ldots, X_{n_2}^2, \ldots, X_1^m, X_2^m, \ldots, X_{n_m}^m\}$), and finally the stable elements at the end of the branches in increasing order of l as well (i.e., $\{X_{n+1}, X_{n+2}, \ldots, X_{n+m}\}$). Such arrangement guarantees that the entire chain and the individual branches meet the definition of a Genealogically Ordered Decay (GOD) by Yuan & Kernan [146, section III][4]. For a linear GOD chain, the definition reads:

1. X_1 is the precursor of the chain.
2. At least one of the following conditions is fulfilled $\forall i \in (1, n)$:
   a) X_i can only be a child of X_j if $i > j$ $\forall j \in [1, n]$.
   b) X_i and X_{i+1} are children of the same parent.

The Bateman equations for a GOD chain have a lower triangular form that allows to obtain an explicit solution with a degree of analytic effort independent from the complexity of the chain [146]. The solution (equation 6.6) for a given set of jumps in the state vector $\Delta\mathbf{N}(t_k)$ reduces to the computation of the exponential matrix $e^{\mathbf{A}(t-t_k)}$ defined by the convergent power series [147]:

$$e^{\mathbf{A}(t-t_k)} = \sum_{n=0}^{\infty} \frac{\mathbf{A}^n (t-t_k)^n}{n!} \tag{6.11}$$

Moler & van Loan [147] compared the effectiveness of multiple methods of computing the previous matrix and concluded that those based on factorizations or decompositions of matrix $\mathbf{A}$ are likely to be the most efficient for problems involving large $\mathbf{A}$ and repeated evaluations of $e^{\mathbf{A}(t-t_k)}$. The later is the case in parameter estimation problems where elements of $\mathbf{A}$ are or depend on free parameters, and that is precisely the case in this work.

Since $\mathbf{A}$ for a GOD chain is a lower triangular matrix, $\mathbf{A}^{-1}$ exists. Then, $e^{\mathbf{A}(t-t_k)}$ can be

[4] Yuan & Kernan [146, section III] defines Genealogically Ordered Exit-only Decay (GOED) chains, where "exit-only" refers to the absence of external sources on the one hand, and to radioactive elements on the other whose descendants are excluded from the chain if truncated. Only the genealogical ordering part of the definition is adopted in this work, as the absence of external sources is not met.

decomposed as:

$$e^{\mathbf{A}(t-t_k)} = \mathbf{V} e^{-\mathbf{\Lambda}(t-t_k)} \mathbf{V}^{-1} \tag{6.12}$$

where $\mathbf{V}$ is the matrix of column eigenvectors of $\mathbf{A}$ [147, see method 14 in page 819]. Simple recurrence relations obtained by Amaku et al. [148] allow the exact analytic computation of $\mathbf{V}$ and its inverse. The computation of $e^{-\mathbf{\Lambda}(t-t_k)}$ is easy as well, since it is just the diagonal matrix of elements $e^{-\lambda_i(t-t_k)}$. Nevertheless, as pointed out by Yuan & Kernan [146], it is still to be proved that any decay chain can be arranged as a GOD chain. In this sense, the assumption of the existence of $\mathbf{A}^{-1}$ might not always hold. It does hold though for all chains with the structure represented in figure 6.2.

6.1.2 Equivalent model

When the half-life of the precursor is much larger than the time between successive implantations, the number of implantations within the implantation-decay interval of the measurement cycle becomes too large for an efficient application of the general model. It is desirable in this case to find a simpler model that approximates the evolution of the counting rates with fewer parameters.

The implantation process seen over the entire implantation-decay interval can be considered continuous when the number of implantations is large. The state vector evolves then according to the non-homogeneous Bateman equations:

$$\frac{d}{dt}\mathbf{N}(t) = \mathbf{A}\mathbf{N}(t) + \mathbf{R}(t) \tag{6.13}$$

where $\mathbf{R}(t)$ is a continuous implantation rate column vector. The solution of the previous equation is [145, section 7.9]:

$$\mathbf{N}(t) = e^{\mathbf{A}(t-t_1)}\mathbf{N}(t_1) + \int_{t_1}^{t} e^{\mathbf{A}(t-t')}\mathbf{R}(t')dt' \tag{6.14}$$

A continuous implantation process in the implantation-decay interval implies the continuity of the state vector at the interval limits. Since no implantation takes place in the waiting interval, the continuity at t_1 makes $\mathbf{N}(t_1) = \mathbf{0}$, which cancels the first term on the right side of equation 6.14. In the decay interval, on the other hand, equations 6.3 and apply, and the state vector evolves then as $\mathbf{N}(t) = e^{\mathbf{A}(t-t_K)}\mathbf{N}(t_K)$ (equation 6.5. The continuity at t_K implies that $\mathbf{N}(t_K)$ in this equation is equation 6.14 evaluated at t_K.

Under the assumption of a stable performance of IGISOL, $\mathbf{R}(t)$ is constant within the implantation-decay interval and the integral term in equation 6.14 can be solved analytically. Moreover, because only the precursor of the chain is implanted, $\mathbf{R}(t) = \mathbf{R}$, like $\Delta\mathbf{N}(t_k)$ in the general model, can be written in terms of a single parameter as $R_1\boldsymbol{u}_1$. With

matrix $\mathbf{A}$ invertible:

$$\mathbf{N}(t) = \int_{t_1}^{t} e^{\mathbf{A}(t-t')}\mathbf{R}(t')dt' = R_1\mathbf{A}^{-1}\left[\mathbf{I} - e^{\mathbf{A}(t-t_1)}\right]\boldsymbol{u}_1 \tag{6.15}$$

where $\mathbf{I}$ is the $n \times n$ identity matrix. The equivalent model for the evolution of the counting rates can be finally written over the entire measurement cycle as:

$$r_p(t) = R_1\mathbf{E}_p\mathbf{\Lambda}\begin{cases} 0 & \forall t \in [0, t_1] \\ \mathbf{A}^{-1}\left[\mathbf{I} - e^{\mathbf{A}(t-t_1)}\right]\boldsymbol{u}_1 & \forall t \in [t_1, t_K] \\ e^{\mathbf{A}(t-t_K)}\mathbf{A}^{-1}\left[\mathbf{I} - e^{\mathbf{A}(t_K-t_1)}\right]\boldsymbol{u}_1 & \forall t \in [t_K, T] \end{cases} \tag{6.16}$$

6.2 Identifiability analysis

The general model describing the evolution of the counting rates was built from the solution of differential equations whose time dependence is contained in the exponential matrix $e^{-\mathbf{\Lambda}(t-t_k)}$, which is the diagonal matrix of elements $e^{-\lambda_i(t-t_k)}$. Performing the matrix multiplication in equation 6.10 using equation 6.12 leads without much effort to a linear combination of the exponential functions $e^{-\lambda_i(t-t_k)}$. Fitting exponential functions to experimental data is a well known sloppy[5] and ill-posed[6] problem. A question arises then, without further considerations, on whether the model parameters are identifiable, i.e., can be estimated with enough certainty.

The identifiability of model parameters can be classified as *structural* and *practical*. The former regards the existence of unique values of the parameters in finite regions of the parameter space (local) or in the entire parameter space (global) independently from the experimental data [150]. Variations in structurally identifiable parameters affect the model output, and therefore, the quality of the fit. The practical identifiability, in contrast, regards the sufficiency and quality of the experimental data to estimate structurally identifiable parameters with enough certainty.

A structural identifiability analysis on either the general or the equivalent model in their most general representations would be an extremely challenging problem given the complex dynamics and the large number of parameters involved. The analysis on the reduced models, on the contrary, is easier, as they have fewer parameters.

Recall that the branching ratio of the beta decay channels of the precursor followed by neutron emission (i.e., the delayed neutron emission probabilities) are the parameters of

[5] *Sloppiness* refers to a much higher sensitivity in certain directions of the parameter space than in others.

[6] *Ill-posed* problems are inverse problems that have none or multiple solutions, or the solution procedure is unstable (i.e., arbitrarily small errors in the measured data may lead to large errors in the solutions) [149].

interest. The rest (the implantation parameters $\Delta N_1(t_k)$ and R_1, the decay parameters λ_i, and the detection parameters ε_i^p) are nuisance parameters.

The structural identifiability of the general and equivalent models is analyzed in appendix D. The analysis concludes that neither the parameters of interest nor the unknown nuisance parameters are structurally identifiable in the current parameterization of the models without resorting to approximations. Based on the results of the analysis, the following final parameterizations were proposed:

General Model

$$r_p(t) = \Delta N_1(t_1)\varepsilon_1^p \boldsymbol{\Xi}_p \boldsymbol{\Lambda} \sum_{k=1}^{K} s(t-t_k) e^{\mathbf{A}(t-t_k)} \eta_k \boldsymbol{u}_1 \qquad \forall t \in [0,T] \tag{6.17}$$

Equivalent Model

$$r_p(t) = R_1 \varepsilon_1^p \boldsymbol{\Xi}_p \boldsymbol{\Lambda} \begin{cases} 0 & \forall t \in [0,t_1] \\ \mathbf{A}^{-1}\left[\mathbf{I} - e^{\mathbf{A}(t-t_1)}\right] \boldsymbol{u}_1 & \forall t \in [t_1,t_K] \\ e^{\mathbf{A}(t-t_K)} \mathbf{A}^{-1}\left[\mathbf{I} - e^{\mathbf{A}(t_K-t_1)}\right] \boldsymbol{u}_1 & \forall t \in [t_K,T] \end{cases} \tag{6.18}$$

where $\boldsymbol{\Xi}_p$ is the row vector of elements $\xi_i^p = {}^{\varepsilon_i^p}/_{\varepsilon_1^p}$ and η_k the ratio ${}^{\Delta N_1(t_k)}/_{\Delta N_1(t_1)}$. Table 6.1 summarizes the mathematical symbols involved.

These parameterizations have multiple advantages over the first ones. On the one hand, the implantation and detection parameters $\Delta N_1(t_1)$ and ε_1^p respectively, like R_1, are scale parameters and, as such, they do not play any role in the parameter estimation method applied in this work as will be explained in section 6.3.4. In consequence, the effective number of model parameters (the shape parameters, which are involved in the parameter estimation process) is reduced by two. On the other hand, unlike in the first parameterizations, knowing P_n (the branching ratio of the beta decay channel of the precursor followed by one-neutron emission) as in the case of the reference isotopes renders the detection parameters ξ_i^p identifiable. The opposite holds as well. Whereas the ξ_i^p parameters are not absolute but relative quantities, this is additional information on the experiment that can be obtained.

Symbol	Definition
Variables:	
t	Time measured from the beginning of the measurement cycle.
$N_i(t)$	State variable of the ith element of the decay chain, i.e., the number of nuclei of that element at a given time t.
r_p	Counting rate for particles of type p.
Decay parameters:	
λ_i	Decay constant of the ith element of the decay chain.
P_n	β-delayed neutron emission probability of the precursor.
$\mathbf{A}$	$n \times n$ constant coefficients matrix of the Bateman equations defined by equation 6.4.
Detection parameters:	
ε_i^p	Average number of particles of type p detected per decay of the ith radioactive element of the decay chain. For decays with one particle emission (of the given type), it is the detection efficiency.
$\boldsymbol{\Xi}_p$	Row vector $(\xi_1^p, \xi_2^p, ..., \xi_n^p)$ of elements $\xi_i^p = {}^{\varepsilon_i^p}/_{\varepsilon_1^p}$.
Implantation parameters:	
t_k	Time elapsed from the beginning of the cycle to the kth implantation.
R_1	Implantation rate of the precursor.
$\Delta N_1(t_1)$	Jump in the state variable of the precursor (i.e., in the number of nuclei of precursor nuclei) produced by the first implantation.
η_k	Ratio ${}^{\Delta N_1(t_k)}/_{\Delta N_1(t_1)}$
Indexes:	
i, j	Elements of the radioactive decay chain.
k	Implantation.
p	Particle type.
Other symbols:	
T	Length of the measurement cycle, i.e., $t_1 + 10T_{1/2}^1$, where $T_{1/2}^1$ is the half-life of the precursor (figure 6.1).
K	Number of implantations within the implantation-decay interval of the measurement cycle (figure 6.1).
$\boldsymbol{u}_1$	Unit column vector $(1, 0, ..., 0)^T$ of n elements.
$\mathbf{I}$	$n \times n$ identity matrix.

Table 6.1: Mathematical symbols in the final parameterizations of the models for the evolution of the counting rates.

6.3 Point and uncertainty estimation

Bayesian Estimation (BE) has been adopted in this work for statistical inference. The preference for BE over other statistical inference frameworks was based on its natural and principled way of incorporating prior information on the parameters and imposing external constraints to improve the model identifiability. It also allows for working with unbinned rather than binned data, which removes the systematic uncertainty introduced by the loss of information that results always from binning.

ROOT has powerful linear algebra classes that facilitate the programmatic implementation of the general and equivalent models. However, it alone is too rigid to address the complexity of BE. RooFit —an optional package of ROOT— offers more advanced, flexible and intuitive functionalities to perform hard-core statistical inference [151]. BE was performed in this work with the RooStats libraries built on RooFit [152].

6.3.1 Bayesian estimation

Conventional Maximum Likelihood Estimation (MLE) seeks to find the set of model parameters $\boldsymbol{\omega}$ that are more likely to produce the observed data $\mathcal{D}$. The ML estimator of $\boldsymbol{\omega}$ is therefore defined as:

$$\hat{\boldsymbol{\omega}}_{ML} = \arg\max_{\boldsymbol{\omega}} \quad \mathcal{L}(\mathcal{D}|\boldsymbol{\omega}) \tag{6.19}$$

where the likelihood function $\mathcal{L}(\mathcal{D}|\boldsymbol{\omega})$ measures the support of hypothesis on model parameters by the experimental data. When prior information on the uncertainty of the parameters exists, the Bayes theorem allows to obtain the posterior joint PDF of the parameters given the data (hereafter posterior PDF) as:

$$\mathcal{P}(\boldsymbol{\omega}|\mathcal{D}) = \frac{\mathcal{L}(\mathcal{D}|\boldsymbol{\omega})\mathcal{P}(\boldsymbol{\omega})}{\mathcal{P}(\mathcal{D})} \tag{6.20}$$

where $\mathcal{P}(\boldsymbol{\omega})$ (hereafter prior PDF) represents the prior belief of the joint PDF of the parameters before the observation of the data, and $\mathcal{P}(\mathcal{D})$, known as "probability of evidence", is:

$$\mathcal{P}(\mathcal{D}) = \int \mathcal{L}(\mathcal{D}|\boldsymbol{\omega})\mathcal{P}(\boldsymbol{\omega})d\boldsymbol{\omega} \tag{6.21}$$

Equation 6.20 is the core of Bayesian Estimation (BE). Note that, unlike in MLE, $\boldsymbol{\omega}$ in BE is a random vector, i.e., model parameters in BE are random variables. In consequence, BE yields no "best estimate" of the parameters, but probabilities that they take different values.

Point and uncertainty estimates reported in this work are respectively marginal Maximum A Posteriori (MAP) and Highest Posterior Density Interval (HPDI) with a 1σ (68.3 %) credible level estimates summarizing the posterior PDF. MAP estimators yield the set of

model parameters $\boldsymbol{\omega}$ that are more likely to produce the observed data $\mathcal{D}$ given the prior information on the parameters, i.e., the mode of the posterior PDF:

$$\hat{\boldsymbol{\omega}}_{MAP} = \arg\max_{\boldsymbol{\omega}} \quad \mathcal{P}(\boldsymbol{\omega}|\mathcal{D}) \tag{6.22}$$

HPDIs, on the other hand, are non equal-tailed credible intervals where the probability density at every point is higher than at any point outside the interval. Hence, HPDIs are the smallest possible credible intervals that can be estimated for a given credible level.

Note from equation 6.21 that $\mathcal{P}(\mathcal{D})$ does not depend on $\boldsymbol{\omega}$ and is always positive. Maximizing $\mathcal{P}(\boldsymbol{\omega}|\mathcal{D})$ is therefore equivalent to maximizing $\mathcal{L}(\mathcal{D}|\boldsymbol{\omega})\mathcal{P}(\boldsymbol{\omega})$. This allows for the computation of MAP estimates to be posed as an optimization problem on the latter, avoiding the calculation of $\mathcal{P}(\mathcal{D})$. The computation of HPDIs, however, does require evaluating $\mathcal{P}(\boldsymbol{\omega}|\mathcal{D})$. Traditional integration methods may be unfeasible to calculate $\mathcal{P}(\mathcal{D})$ when the number of parameters is large or the model is too complex, but with the development of Markov Chain Monte Carlo (MCMC) sampling methods since the early 1950's [153] and the dramatic growth of computational power in the last two decades, multivariate sampling has become more feasible and with it BE increasingly popular. In view of this, the Metropolis-Hastings MCMC method [154,155] with a Gaussian proposal function was used in this work to sample the posterior PDF. HPDIs were estimated from 10^4 $\boldsymbol{\omega}$ samples, generated after 10^2 burn in steps to remove the arbitrariness of the starting point.

The prior PDF adds curvature to the likelihood, improving the practical identifiability of the model. It can be seen as a penalization on the likelihood function that takes Bayesian estimates away from ML estimates toward values that are consistent with the prior information on the parameters. Choosing a prior PDF is therefore a delicate task in BE.

A Gaussian marginal prior PDF was adopted in this work for the decay constants and the delayed neutron emission probability in the efficiency characterization of the detection system with reference isotopes. As for the detection (ε_1^p and ξ_i^p) and implantation ($\Delta N_1(t_1)$, η_k and R_1) parameters, a uniform marginal prior PDF was adopted, indicating no preference for any particular value. The prior PDF was finally constructed as the product of all marginal prior PDFs, ignoring any correlation between parameters.

6.3.2 Extended estimation

Models for the evolution of the counting rates were derived in section 6.1 assuming for simplicity the absence of electronic noise, room background and remnant activity from previous cycles. This, however, is an approximation. Those are sources of detection events that must be accounted for in the parameter estimation process.

Measurement cycles affected by high frequency electronic noise were discarded in the data preparation process. The electronic noise was accordingly assumed to make a uniform contribution to the counting rates over the entire cycle. No evidence supports a different contribution from room background events. As for the remnant activity from previous cycles, if any, it would contribute the counting rates more at the beginning than at the end of the cycle. It was shown in section 4.2.3 how the rollers support in the implantation setup

effectively shields the silicon detector from implantation on it, but the rollers themselves not so much. However, the effective area of the tape (where the beam can imping on) is 12.7 mm × 25.5 mm, meaning that for implantations to occur outside the tape, the beam must deviate from the center of the tape —were it was tuned to be focused on— more than twice the distance in the vertical than in the horizontal direction, making it less likely. On the other hand, little activity from the precursor remains at the end of the decay interval after $7T^1_{1/2}$ since the last implantation. By then, the contributions from its descendants vary little in time, as they are in all cases much longer-lived than the precursor. For all this, a uniform contribution to the counting rates may be assumed as well for the remnant activity from previous cycles. All these contributions (hereafter summarized as background) have been accounted for in this work by adding a constant term r^p_{bg} to the models, i.e., $r_p(t) = r^p_{\text{bg}} + r^p_{\text{dec}}(t)$, where the second term represents the radioactive decay component given by equations 6.17 and 6.18.

The $P_n\,{}^A_Z X$ method requires in the first place separating the total decay yield N^p_{dec} (hereafter decay yield) from the background yield N^p_{bg} for estimating the ratio $\delta = {}^{\varepsilon^\beta_1}/_{\varepsilon^n_1}$ from measurements with reference isotopes. Then, the decay yield of the precursor can be calculated from the former as:

$$N^p_1 = N^p_{\text{dec}} \frac{\int_{t_1}^{T} r^p_1(t)dt}{\int_{t_1}^{T} r^p_{\text{dec}}(t)dt} \tag{6.23}$$

where $r^p_1(t)$ is the contribution of the precursor to the total counting rate. Note that both integrands have ε^p_1 and either $\Delta N_1(t_1)$ or R_1 (depending on the model) as scale parameters. Those are not dependent on time, and can be taken out of the integral and canceled out. With no other dependence on structurally non-identifiable parameters, N^p_1 and therefore δ_{exp} can be determined.

The decay and background yields can be disentangled by fitting the background to a uniform distribution in the waiting interval (where the decay component is null) and using the result to fix the background component over the entire cycle. Whereas this is a simple method, it is not the most accurate, as very few data are used. N^p_{dec} and N^p_{bg} are random variables of independent Poisson counting processes. The corresponding expected values ($\langle N^p_{\text{dec}}\rangle$ and $\langle N^p_{\text{bg}}\rangle$ respectively) are a priori unknown, but the total $\langle N_p\rangle = \langle N^p_{\text{dec}}\rangle + \langle N^p_{\text{bg}}\rangle$ is not and N_p is also Poisson distributed:

$$\mathcal{P}(N_p) = \frac{\langle N_p\rangle^{N_p} e^{-\langle N_p\rangle}}{N_p!} \tag{6.24}$$

The product $\mathcal{L}(\mathcal{D}|\boldsymbol{\omega})\mathcal{P}(N_p)$ known as the *extended likelihood* contains all the information on the decay model parameters and the decay and background yields [156]. It was used in this work instead of just $\mathcal{L}(\mathcal{D}|\boldsymbol{\omega})$ to estimate the yields with higher accuracy.

6.3.3 Switching times

Variations in the implantation rate imply a change of dynamics in the evolution of the counting rates. The moments when dynamical changes occur are known as *switching times* in dynamical systems theory [157].

The switching times for $k > 1$ can be referred to the first one as $t_k = t_1 + (k-1)\Delta t$, where the time between contiguous implantations Δt =191 ms is the period of the JYFLTRAP cycle. Whereas Δt is known with a relative uncertainty of just 0.006 %[7], the uncertainty on t_1 is much higher because of the considerable jitter of the signal produced by the tape system at the end of every tape move, which was used to reset the DACQ clock to start a new measurement cycle. The uncertainty on t_k is therefore dominated by the uncertainty on t_1.

The estimation of switching times can be treated as an optimization problem. So it has in this work by treating t_1 as an unknown parameter, which was used to calculate all t_k at each evaluation of the models. Switching times as unknown parameters introduce a serious difficulty in parameter estimation process: they make the objective function non-differentiable, and this is a problem for applying optimization methods based on differentiation. The statistical estimators can still converge, but one can expect a slow convergence [158].

A close observation of the time distributions of beta detected events (for neutrons the data is more scarce) allowed to limit t_1 for each implanted isotope within the intervals shown in table 6.2. The intervals are more restrictive for isotopes with short half-lives, where jump discontinuities are better observed.

Isotope	$T_{1/2}$ (s)			$t_1^{\min}$(s)	$t_1^{\max}$(s)	Δt_1(s)
^{88}Br	16.34	± 0.08	[17]	1.4	1.6	0.2
^{94}Rb	2.702	± 0.005	[159]	1.397	1.399	0.002
^{95}Rb	0.3777	± 0.0008	[7,8]	1.378	1.379	0.001
^{137}I	24.5	± 0.2	[160]	1.4	1.9	0.5
^{86}As	0.945	± 0.008	[17]	1.390	1.395	0.005
^{91}Br	0.543	± 0.004	[7,8]	1.38	1.39	0.01

Table 6.2: Uncertainty intervals of the first switching time in the time distributions of the beta and neutron detected events determined by visual inspection of the former.

[7] IGISOL3 operated with a 100 MHz clock.

6.3.4 Restriction of the parameter space

Imposing limits on model parameters prevents the minimization algorithms from exploring undesired regions of the parameter space, like regions without a physical meaning. However, limits must be used with caution and avoided as much as possible. MINUIT —the minimization package behind ROOT— applies internal variable transformations to turn constrained optimization problems unconstrained before executing the minimization routines. Unconstrained optimization is simply easier. Those transformations are not linear, and that enhances the non-linearity of the problem, leading to unreliable results when the global optimum is found close to the limits [161, sections 1.2 and 5.3]. In this sense, the recommendation given by James & Winkler [161, section 1.2] were followed in this work, namely, once a satisfactory result was obtained with limits, these were removed and the errors recalculated.

The restricted parameter spaces for the general and equivalent models (Ω_G^p and Ω_E^p respectively) in the final parameterizations are:

$$\Omega_G^p = \{P_n \in [0,1]\,; N_{\text{bg}}^p, N_{\text{dec}}^p, \lambda_i,\, \xi_i^p \text{ and } \eta_k \in [0,+\infty)\,; t_1 \in \left[t_1^{\min}, t_1^{\max}\right]\}$$
$$\Omega_E^p = \{P_n \in [0,1]\,; N_{\text{bg}}^p, N_{\text{dec}}^p, \lambda_i \text{ and } \xi_i^p \in [0,+\infty)\,; t_1 \in \left[t_1^{\min}, t_1^{\max}\right]\}$$

Note that ε_1^p, R_1 and $\Delta N_1(t_1)$ were omitted. They are scale parameters present in both the numerator and denominator of equation 6.20 and therefore cancel out, playing no role in BE. For this reason they were all fixed at 1 (an arbitrary value) in the parameter estimation process.

6.3.5 Choice of initial values

The objective function in optimization problems may have multiple local extremes. In that case, derivative-based optimization algorithms may converge to a local instead of the global optimum. The objective function may also be flat in some regions of the parameter space and cause a slow convergence. For these reasons, a good choice of initial values for the parameters is crucial to reach the global optimum.

Grid and random methods are among the most commonly used to find good initial values. The latter has been used in this work. It is more effective in high-dimensional parameter spaces than the former, because it is not exhaustive.

100 points of the restricted parameter space were sampled from the prior PDF for each implanted isotope. Reasonable closed intervals were used for parameters with non-informative priors (e.g., the uncertainty intervals for t_1 shown in table 6.2). A fit was then performed starting from each point, and the one that lead to the highest value of the posterior distribution for the MAP estimates with a well defined error matrix was chosen.

6.3.6 Improving the model identifiability

Incorporating as much prior information as possible into the parameter estimation process not only facilitates the estimation and reduces its computational cost, but also improves the parameter identifiability, both structural and practical. In addition to the information available on the decay parameters, the structure of the decay chains and the execution of experiment that lead to the reduction of the general and equivalent models, combining independent data sets and imposing physical constraints can also improve the model identifiability or even render non-identifiable parameters identifiable.

Both models share the implantation and decay parameters, but depend on different sets of detection parameters. An independent fit of each model to the corresponding time distribution of detected events may yield different values of the parameters in common. A simultaneous fit, on the other hand, is a better way of exploiting the experimental data, as it yields a single set of values of those parameters describing the physical process best. For this reason, a simultaneous fit to the time distributions of beta and neutron detected events was a strategy adopted for parameter estimation in this work.

6.4 Experimental efficiency characterization of the detection system with reference isotopes

It was pointed out in section 6.2 that the prior knowledge of P_n renders identifiable the detection parameters and vice versa in the new model parameterizations (equations 6.17 and 6.18). But how can P_n be estimated for ^{86}As and ^{91}Br without prior knowledge of the detection parameters? It is here where the $P_n\,{}^{A}_{Z}X$ method for measuring β-delayed neutron emission probabilities introduced in section 1.3.1 comes to play. The measurements performed on the reference isotopes ^{88}Br, ^{94,95}Rb and ^{137}I can be used to characterize the detection system in efficiency with a magnitude that can be used later to constrain the estimation of the delayed neutron emission probability of the isotopes of interest. The characterization, however, cannot consist of estimating the detection efficiencies, because they are structurally non-identifiable on the one hand, and isotope-dependent on the other.

Agramunt et al. [20] used the experimental value of the ratio $\delta = {}^{\varepsilon_1^\beta}/_{\varepsilon_1^n}$ in equation 1.3 as characterizing magnitude of BELEN20b, corrected by Monte Carlo simulations to remove the isotope-dependent effects. The correction consisted first in multiplying the value of δ of each reference isotope by its corresponding fraction ${}^{\kappa_1^\beta}/_{\kappa_1^n}$, where κ_1^β and κ_1^n are the ratios ${}^{\varepsilon_1^\beta}/_{\langle\varepsilon_1^\beta\rangle}$ and ${}^{\varepsilon_1^n}/_{\langle\varepsilon_1^n\rangle}$ respectively obtained by Monte Carlo simulations, and the brackets indicate the average over the reference isotopes. δ was then obtained as the weighted average of the corrected values of the reference isotopes.

The same characterizing magnitude was used in this work, but an alternative approach was followed to account for the isotope-dependent effects on the detection efficiencies. The latter will be discussed in section 6.5. This section presents the results of the first step toward estimating the delayed neutron emission probabilities of ^{86}As and ^{91}Br, namely the efficiency characterization of the detection system with measurements on ^{88}Br, ^{94,95}Rb and ^{137}I. That entails the simultaneous fit of the general or the equivalent model —whichever

applies best in each case— to the time distributions of beta and neutron detected events to estimate:

$$\boxed{\delta = \frac{\varepsilon_1^\beta}{\varepsilon_1^n} = P_n \left(\frac{N_1^\beta}{N_1^n} \right)} \tag{6.25}$$

where N_1^β and N_1^n relate to the model parameters through equation 6.23.

Table 6.3 summarizes the relevant radioactive decay data on the reference isotopes. Further data on those isotopes and their descendant's may be found in appendix E.

Isotope	$T_{1/2}$ (s)			P_n (%) [11]	**Model**
^{88}Br	16.34	$\pm$ 0.08	[17]	6.75 ± 0.18	Equivalent
^{94}Rb	2.702	$\pm$ 0.005	[159]	10.24 ± 0.21	Equivalent
^{95}Rb	0.3777	$\pm$ 0.0008	[7,8]	8.87 ± 0.29	General
^{137}I	24.5	$\pm$ 0.2	[160]	7.33 ± 0.38	Equivalent

Table 6.3: Radioactive decay data on the reference β-delayed neutron emitters used in the experimental efficiency characterization of the detection system. The model for the evolution of the counting rates used in the parameter estimation process in each case is also indicated.

6.4.1 ^{88}Br

The radioactive decay chain of ^{88}Br is represented in figure 6.3 over the chart of nuclides and more in detail in figure E.1 along with relevant nuclear and decay data of its elements. ^{88}Br decays with a half-life of 16.34 ± 0.08 s [17] to ^{88}Kr or ^{87}Kr by β^- decay, followed by one-neutron emission in the latter case. The chain proceeds thus in two linear branches of consecutive β^- decays from the ground state of its elements: the $\beta\gamma$ branch $^{88}\text{Kr} \xrightarrow{\beta^-} {}^{88}\text{Rb} \xrightarrow{\beta^-} {}^{88}\text{Sr}$, and the βn branch $^{87}\text{Kr} \xrightarrow{\beta^-} {}^{87}\text{Rb} \xrightarrow{\beta^-} {}^{87}\text{Sr}$ with a branching ratio of 6.75 ± 0.18 % [11]. Despite the simplicity of the chain, it was not modeled it in its whole extent. The half-lives of ^{87}Kr and ^{88}Kr are two orders of magnitude longer than the precursor's (76.3 ± 0.5 min and 2.825 ± 0.019 h respectively [7,8]). Therefore, their contributions and their descendant's to the beta counting rate are negligible within a measurement cycle. The chain was truncated accordingly at the krypton isotopes for the purpose of model reduction.

256 implantations of ^{88}Br ions per measurement cycle fit within a 48.96 s implantation-decay interval. A simultaneous fit of the general model to the time distributions of beta and neutron detected events would require the estimation of $256-1$ implantation parameters η_k

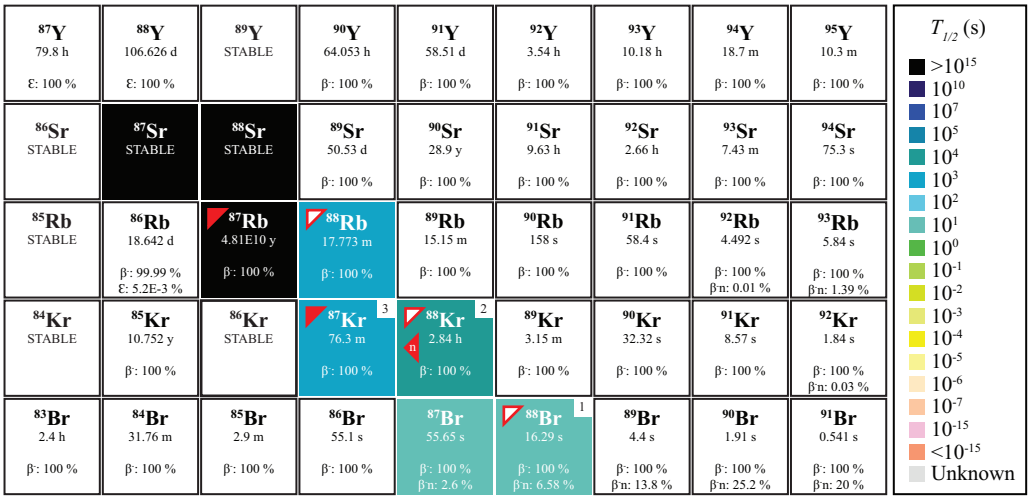

Figure 6.3: Radioactive decay chain of ^{88}Br represented over the chart of nuclides. The $\beta\gamma$ and βn branches are indicated with white and red arrows respectively. The elements considered in the models for the evolution of the counting rates are indexed (upper right corners) according to the indexing rules of a GOD chain (section 6.1.1).

in addition to other parameters of different nature. This is clearly unfeasible and suggests the application of the equivalent model instead.

With the chain truncated at the krypton isotopes, the equivalent model takes the simple analytic forms $r_\beta(t) = r_{\text{bg}}^\beta + \varepsilon_1^\beta \lambda_1 N_1(t)$ and $r_n(t) = r_{\text{bg}}^n + P_n \varepsilon_1^n \lambda_1 N_1(t)$ for the beta and neutron counting rates respectively, with:

$$N_1(t) = \frac{R_1}{\lambda_1} \begin{cases} 0 & \forall t \in [0, t_1] \\ 1 - e^{-\lambda_1 (t - t_1)} & \forall t \in [t_1, t_K] \\ e^{-\lambda_1 (t - t_K)} \left[1 - e^{-\lambda_1 (t_K - t_1)}\right] & \forall t \in [t_K, T] \end{cases} \tag{6.26}$$

The model for the neutron counting rate has the same form for all the implanted isotopes to which the equivalent model applies. Therefore, it will be omitted for those isotopes in the following sections.

Figure 6.4 shows the simultaneous fit of the equivalent model to the time distributions of beta and neutron detected events. The parameter estimates and derived quantities are shown in table 6.4 including the quantity of interest $\delta = \varepsilon_1^\beta / \varepsilon_1^n$. The resulting estimate of δ is 0.512 ± 0.015. Only the switching time t_1, the decay (N_{dec}^β and N_{dec}^n) and background (N_{bg}^β and N_{bg}^n) yields, and the decay constant λ_1 were considered uncertain parameters, with the latter constrained by a Gaussian prior PDF as described at the end of section 6.3.2 to propagate its uncertainty to the rest of the parameters. Not P_n —even though prior information on it is available—, because it is only present in the model for the neutron counting rate as a scale parameter and, like R_1 and ε_1^n, it does not affect the estimation

of other parameters.

Decay parameters:

$T^1_{1/2} \overset{c}{=} 16.34 \pm 0.08\,\mathrm{s}$

Implantation parameters:

$t_1 = 1.308^{+0.021}_{-0.016}\ \mathrm{s}$

Yield parameters:

$N^\beta_{\mathrm{dec}} = 1119400^{+1200}_{-1400}$ $N^\beta_{\mathrm{bg}} = 14100^{+700}_{-600}$ $N^n_{\mathrm{dec}} = 147\,500 \pm 500$ $N^n_{\mathrm{bg}} = 10\,200 \pm 300$

Derived quantities:

$N^\beta_{\mathrm{dec}}(^{88}\mathrm{Br}) = N^\beta_{\mathrm{dec}}$ $N^n_{\mathrm{dec}}(^{88}\mathrm{Br}) = N^n_{\mathrm{dec}}$ $\delta = \varepsilon^\beta_1/\varepsilon^n_1 = 0.512 \pm 0.015$

Table 6.4: Parameter estimates and derived quantities resulting from the analysis of the ^{88}Br measurement. $\overset{c}{=}$ denotes constrained parameter (see section 6.3.2). The half-lives $T^i_{1/2}$ enter the model transformed into λ_i.

The quality of the fit is excellent over the implantation-decay and decay intervals. Only in the waiting interval of the distribution of beta detected events the fit seems to slightly overestimate the background yield. Fitting a uniform distribution in the waiting interval gives a beta background yield of $11\,900 \pm 1200$ over the entire cycle. This is about 16 % less yield than obtained from the fit of the equivalent model over the entire measurement cycle (14100^{+700}_{-600}). Note that both estimates are at variance, which indicates the presence of a bias in the beta background yield in table 6.4 that may stem from any of the model hypothesis and approximations (non-stable performance of IGISOL within the implantation-decay interval, non-constant background, truncation of the decay chain, etc.) or a failure of the optimization algorithm to find the global maximum of the posterior PDF. A bias in the background yield propagates to the decay yield and ultimately to δ, in such a way that the total yield follows a Poisson distribution with mean value at the total observed yield [162, see discussion in section 4]. The bias of δ was estimated to be just 0.2 %, which is negligible.

A glance at the Pearson (hereafter omitted) correlation matrix shown in figure 6.5 reveals some structural features of the model. First, note that the decay and background yields of each distribution are strongly anticorrelated. This is expected, since the total yield is preserved. The yields (the beta yields the most), on the other hand, exhibit correlation with λ_1 that ranges from -0.4 to 0.7. Such correlation reflects how important the accurate knowledge of the decay constants can be for the determination of quantities like δ derived from the yields. Last, note that t_1 exhibits correlation with all the other parameters. t_1 and λ_1 are the only shape parameters in the models, and both models have them as parameters in common. The correlation between t_1 and the yields suggests that the overestimation of the beta background yield and the obtained value of t_1 falling below 1.4 s (the lower limit of t_1 from table 6.2) may stem from the same cause. Beware that the dependence between parameters may be stronger than suggested by the correlation matrix, as the Pearson correlation coefficient captures linear dependence.

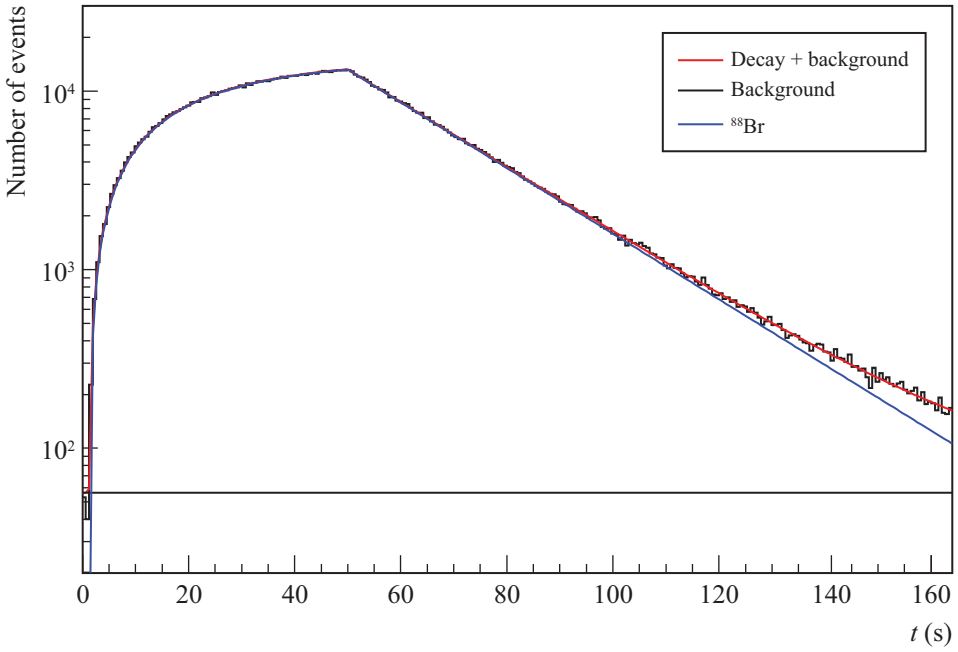

(a) Silicon detector

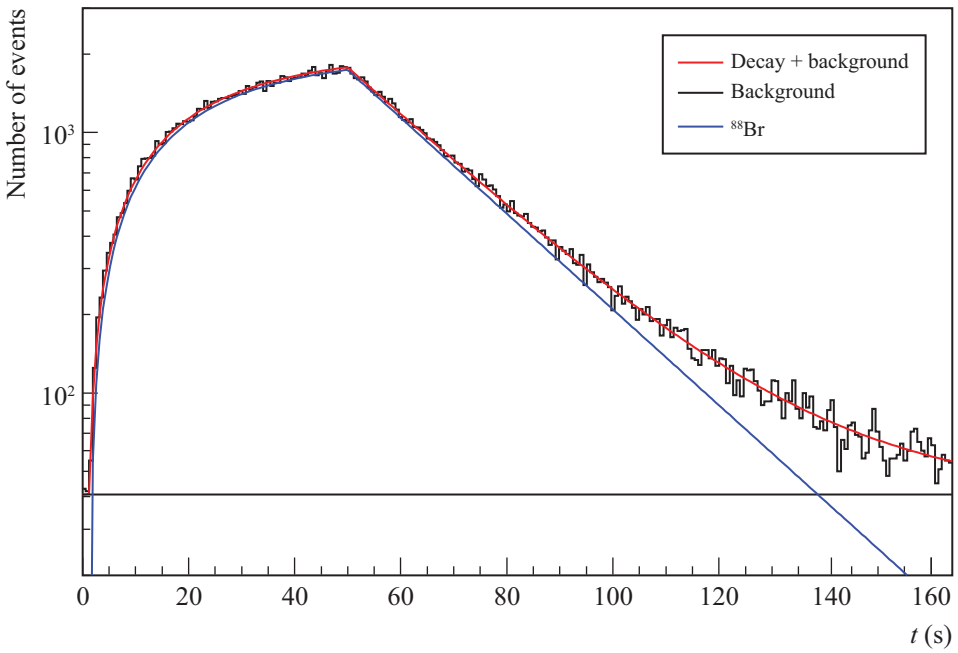

(b) BELEN20b

Figure 6.4: Simultaneous fit to the time distributions of beta and neutron detected events from the radioactive decay of ^{88}Br.

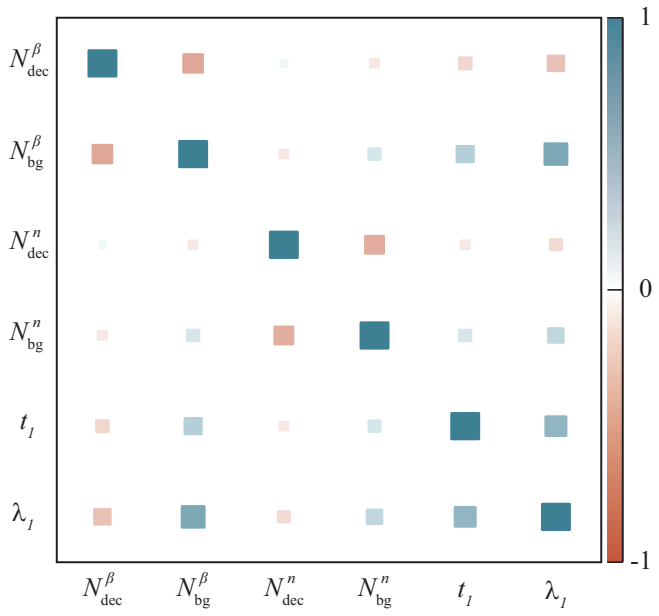

Figure 6.5: Correlation matrix of the parameters of the equivalent model of the evolution of the beta and neutron counting rates in the measurement of ^{88}Br.

6.4.2 ^{94}Rb

^{94}Rb undergoes beta decay with a half-life of 2.702 ± 0.005 s [159] to ^{94}Sr or ^{93}Sr with delayed one-neutron emission in the latter case. The decay proceeds in two linear branches (figures 6.6 and E.2): the $\beta\gamma$ branch $^{94}\mathrm{Sr} \xrightarrow{\beta^-} {}^{94}\mathrm{Y} \xrightarrow{\beta^-} {}^{94}\mathrm{Zr} \xrightarrow{2\beta^-} {}^{94}\mathrm{Mo}$, and the βn branch $^{93}\mathrm{Sr} \xrightarrow{\beta^-} {}^{93}\mathrm{Y} \xrightarrow{\beta^-} {}^{93}\mathrm{Zr} \xrightarrow{\beta^-} {}^{93}\mathrm{Nb}$ with a branching ratio of $10.24 \pm 0.21\,\%$ [11]. Both have just one element more than the corresponding branches of ^{88}Br, but the latter is more complex due to isomeric states of ^{93}Y and ^{93}Nb that decay via internal transition to the ground state, and the $2\beta^-$ decay $^{94}\mathrm{Zr} \xrightarrow{2\beta^-} {}^{94}\mathrm{Mo}$. Such complexity was avoided by truncating the $\beta\gamma$ branch at ^{94}Y and the βn branch at ^{93}Sr. The half-lives of these isotopes (18.7 ± 0.1 min and 7.43 ± 0.03 min respectively [7,8]) are two orders of magnitude longer than the precursor's and therefore, they and their descendants make a negligible contribution to the beta counting rate within a measurement cycle.

The equivalent model becomes again necessary to deal with the 48 implantations that fit within a 9.024 s implantation-decay interval. The model for the beta counting rate (for the neutron counting rate see section 6.4.1) takes a more complex analytic form than for ^{88}Br due to the presence of the extra element in the $\beta\gamma$ branch:

$$r_\beta(t) = r^{\beta}_{\mathrm{bg}} + \varepsilon^{\beta}_1 \lambda_1 N_1(t) + P_n \varepsilon^{\beta}_1 \xi^{\beta}_2 \lambda_2 N_2(t) \tag{6.27}$$

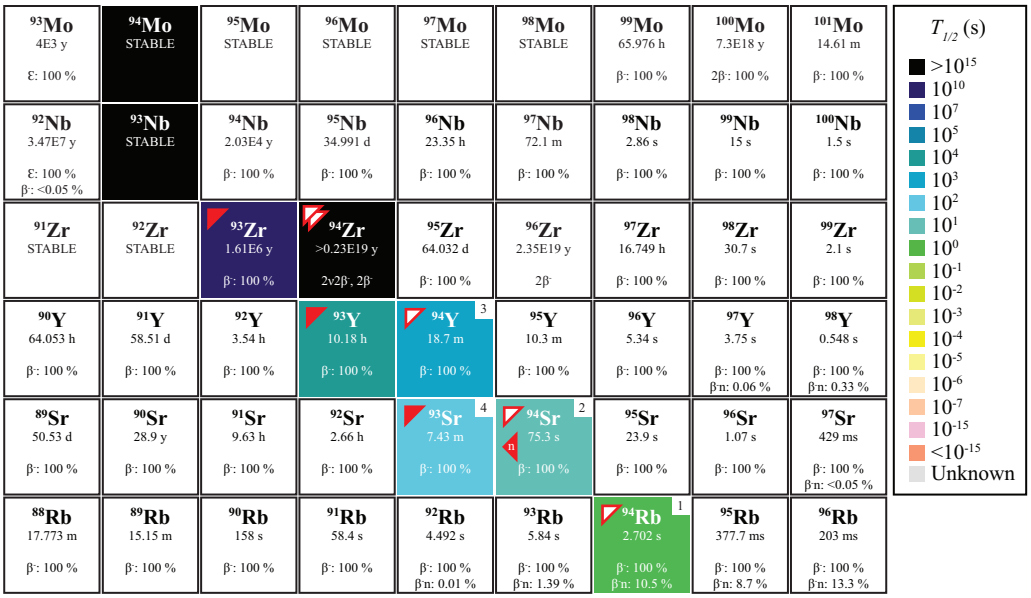

Figure 6.6: Radioactive decay chain of ^{94}Rb represented over the chart of nuclides. The $\beta\gamma$ and βn branches are indicated with white and red arrows respectively. The elements considered in the models for the evolution of the counting rates are indexed (upper right corners) according to the indexing rules of a GOD chain (section 6.1.1).

where $N_1(t)$ is given by equation 6.26 and:

$$N_2(t) = \frac{R_1}{(\lambda_2 - \lambda_1)} \begin{cases} 0 & \forall t \in [0, t_1'] \\ \left[1 - e^{-\lambda_1 (t - t_1')}\right] - \dfrac{\lambda_1}{\lambda_2}\left[1 - e^{-\lambda_2 (t - t_1')}\right] & \forall t \in [t_1', t_K] \\ \left[1 - e^{-\lambda_1 (t_K - t_1')}\right] e^{-\lambda_1 (t - t_K)} & \\ - \left[1 - e^{-\lambda_2 (t_K - t_1')}\right] e^{-\lambda_2 (t - t_K)} & \forall t \in [t_K, T] \end{cases} \tag{6.28}$$

The previous equation shows that considering radioactive elements beyond the precursor in the $\beta\gamma$ branch makes P_n a shape parameter that may affect the estimation of the other parameters. It also introduces a decay parameter λ_i and a detection parameter ξ_i^β per additional element, which are shape parameters as well. For this, P_n, λ_2 and ξ_2^β were considered uncertain parameters, the first two along with λ_1 constrained by a Gaussian prior PDF as described at the end of section 6.3.2 to propagate their uncertainties to the rest of the parameters.

Figure 6.7 shows the excellent quality of the fit over the entire measurement cycle. Any contribution from ^{94}Y, ^{93}Sr, and their descendants is included in the contribution of ^{94}Sr more than in the background, because it contributes to the counting rates more at the end than at the beginning of the cycle.

The parameter estimates and derived quantities are shown in table 6.5. The resulting value

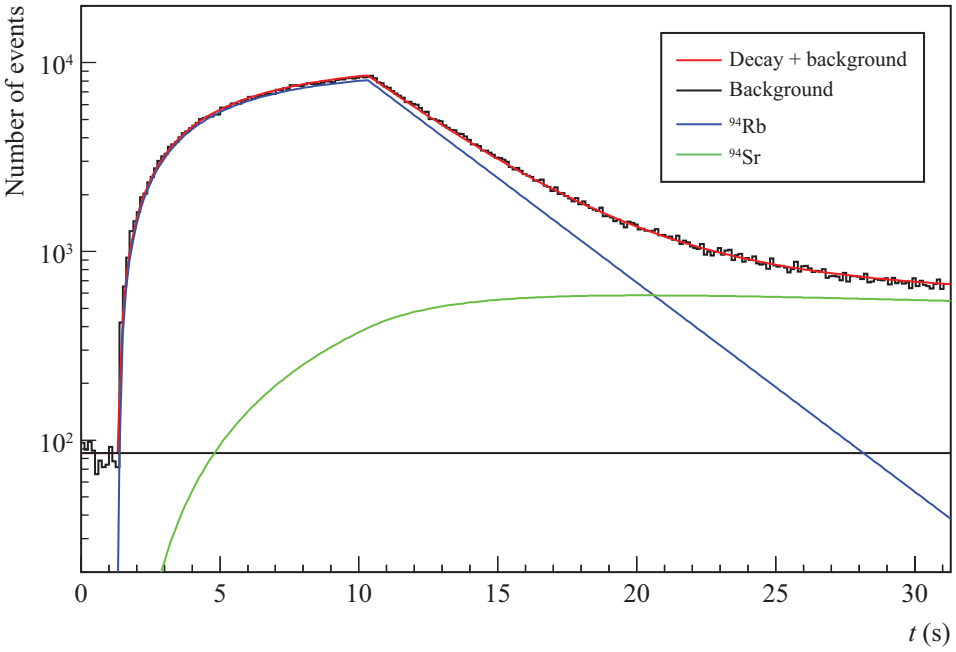

(a) Silicon detector

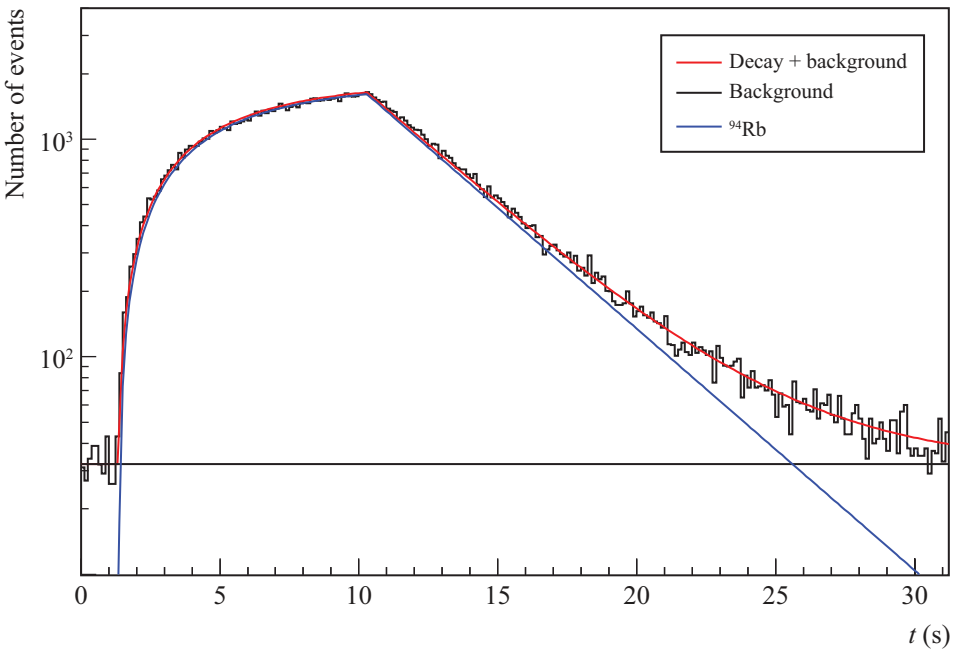

(b) BELEN20b

Figure 6.7: Simultaneous fit to the time distributions of beta and neutron detected events from the radioactive decay of ^{94}Rb.

of δ is 0.514 ± 0.011. $\xi_2^\beta = 1.000 \pm 0.009$ suggests that assuming the same beta detection efficiency for all elements of the chain — a common assumption in β-delayed neutron emission probability measurements— would be a valid approximation in this case.

Decay parameters:

$T^1_{1/2} \overset{c}{=} 2.702 \pm 0.005\,\mathrm{s}$ $T^2_{1/2} \overset{c}{=} 75.3 \pm 0.2\,\mathrm{s}$ $P_n \overset{c}{=} 10.24 \pm 0.21\,\%$

Implantation parameters:

$t_1 = 1.339^{+0.004}_{-0.003}$ s

Detection parameters:

$\xi_2^\beta = 1.000 \pm 0.009$

Yield parameters:

$N^\beta_{\mathrm{dec}} = 747800^{+1000}_{-1300}$ $N^\beta_{\mathrm{bg}} = 21300^{+900}_{-600}$ $N^n_{\mathrm{dec}} = 128200^{+400}_{-500}$ $N^n_{\mathrm{bg}} = 8020^{+220}_{-180}$

Derived quantities:

$N^\beta_{\mathrm{dec}}(^{94}\mathrm{Rb}) = 644000 \pm 1000$ $N^n_{\mathrm{dec}}(^{94}\mathrm{Rb}) = N^n_{\mathrm{dec}}$ $\delta = \varepsilon_1^\beta / \varepsilon_1^n = 0.514 \pm 0.011$

Table 6.5: Parameter estimates and derived quantities resulting from the analysis of the ^{94}Rb measurement. $\overset{c}{=}$ denotes constrained parameter (see section 6.3.2). The half-lives $T^i_{1/2}$ enter the model transformed into λ_i. The number of detected beta particles emitted by the precursor $N^\beta_{\mathrm{dec}}(^{94}\mathrm{Rb})$ used in the estimation of δ was obtained with equation 6.23.

6.4.3 ^{95}Rb

^{95}Rb undergoes beta decay to ^{95}Sr or ^{94}Sr with a half-life of just 377.7 ± 0.8 ms [7,8], followed by one-neutron emission in the latter case. Such a short half-life makes the general model applicable. Indeed, only 5 implantations were performed within a 768 ms implantation-decay interval, and that makes only 4 the implantation parameters η_k.

The decay to ^{95}Sr proceeds along the linear branch of subsequent β^- decays (the $\beta\gamma$ branch) $^{95}\mathrm{Sr} \xrightarrow{\beta^-} {}^{95}\mathrm{Y} \xrightarrow{\beta^-} {}^{95}\mathrm{Zr} \xrightarrow{\beta^-} {}^{95}\mathrm{Nb} \xrightarrow{\beta^-} {}^{95}\mathrm{Mo}$. ^{95}Y has a half-life of 10.3 ± 0.1 min [7,8], which is three orders of magnitude longer than the half-life of ^{95}Rb. The $\beta\gamma$ branch was truncated accordingly at ^{95}Y, avoiding the difficulty that would arise from including the $1/2^-$ isomeric state of ^{95}Nb around 235.69 keV. The other branch (the βn branch) coincides with the $\beta\gamma$ branch of ^{94}Rb, but with a branching ratio of $8.87 \pm 0.29\,\%$ [11]. The same arguments as before apply here to truncate this branch at ^{94}Sr.

Figure 6.8 shows the radioactive decay chain of ^{95}Rb represented over the chart of nuclides. See figure E.3 for a more detailed representation and relevant nuclear and decay data of its elements. Note that the structure of the truncated chains of ^{94}Rb and ^{95}Rb is the same. The models describing the evolution of the beta and neutron counting rates have

therefore the same analytic form as a function of the state variables for both. The state variables, however, now reflect jump discontinuities produced by the discrete implantation process:

$$\begin{aligned} N_1(t) &= \Delta N_1(t_1) \sum_{k=1}^{K} s(t-t_k) e^{-\lambda_1 (t-t_k)} \eta_k && \forall t \in [0,T] \\ N_2(t) &= \Delta N_1(t_1) \sum_{k=1}^{K} s(t-t_k) \left[\frac{e^{-\lambda_1 (t-t_k)} - \frac{\lambda_1}{\lambda_2} e^{-\lambda_2 (t-t_k)}}{\lambda_2 - \lambda_1} \right] \eta_k && \forall t \in [0,T] \end{aligned} \tag{6.29}$$

Figure 6.8: Radioactive decay chain of ^{95}Rb represented over the chart of nuclides. The $\beta\gamma$ and βn branches are indicated with white and red arrows respectively. The elements considered in the models for the evolution of the counting rates are indexed (upper right corners) according to the indexing rules of a GOD chain (section 6.1.1).

Like R_1 in the equivalent model, $\Delta N_1(t_1)$ is in the general model a scale parameter. As such, it does not affect the estimation of other parameters. The general model, however, depends on $K-1$ other implantation parameters η_k, which are shape parameters. These exhibit a weak correlation with other model parameters, but a strong positive correlation between them as shown in figure 6.9.

The simultaneous fit of the general model to the time distributions of beta and neutron detected events is shown in figure 6.10, and the parameter estimates and derived quantities are presented in table 6.6. The resulting value of δ is $0.494^{+0.017}_{-0.018}$.

Here again, the correlation matrix reveals interesting structural features of the model. First, note that ξ_2^{β} is correlated with the decay constants and the beta yields. This is not

Decay parameters:

$T^1_{1/2} \stackrel{c}{=} 377.7 \pm 0.8\,\mathrm{ms}$ $T^2_{1/2} \stackrel{c}{=} 23.90 \pm 0.14\,\mathrm{s}$ $P_n \stackrel{c}{=} 8.87 \pm 0.29\,\%$

Implantation parameters:

$\eta_2 = 2.13^{+0.05}_{-0.04}$ $\eta_3 = 2.52 \pm 0.05$ $\eta_4 = 2.58 \pm 0.06$ $\eta_5 = 2.61 \pm 0.05$

$t_1 = 1.3778 \pm 0.0001\,\mathrm{s}$

Detection parameters:

$\xi^\beta_2 = 1.00^{+0.03}_{-0.02}$

Yield parameters:

$N^\beta_{\mathrm{dec}} = 182200 \pm 500$ $N^\beta_{\mathrm{bg}} = 13100 \pm 200$ $N^n_{\mathrm{dec}} = 30600 \pm 200$ $N^n_{\mathrm{bg}} = 5380 \pm 110$

Derived quantities:

$N^\beta_{\mathrm{dec}}(^{95}\mathrm{Rb}) = 170300 \pm 500$ $N^n_{\mathrm{dec}}(^{95}\mathrm{Rb}) = N^n_{\mathrm{dec}}$ $\delta = \varepsilon^\beta_1/\varepsilon^n_1 = 0.494^{+0.017}_{-0.018}$

Table 6.6: Parameter estimates and derived quantities resulting from the analysis of the ^{95}Rb measurement. $\stackrel{c}{=}$ denotes constrained parameter (see section 6.3.2). The half-lives $T^i_{1/2}$ enter the model transformed into λ_i. The number of detected beta particles emitted by the precursor $N^\beta_{\mathrm{dec}}(^{95}\mathrm{Rb})$ used in the estimation of δ was obtained with equation 6.23.

difficult to understand. Variations in the decay constants are compensated by variations in ξ^β_2 to preserve the total yield. However, that takes the shape of the model away from the beta distribution. In consequence, the decay and background yields, which are the integrals of the r^β_{dec} and r^β_{bg} components of the model respectively, must change. The decay yields are key quantities in the estimation of δ (equation 6.23). The common approximation in β-delayed neutron emission probability measurements that the beta detection efficiency is the same for all elements of the decay chain may therefore lead to a significant systematic uncertainty. With the models parameterized in terms of ξ_i, such approximation is unnecessary, as those parameters are structurally identifiable. Nevertheless, the resulting estimate $\xi^\beta_2 = 1.00^{+0.03}_{-0.02}$ validates the approximation for ^{95}Rb. The correlation matrix also shows that t_1 is not correlated with the rest of the parameters. The jump discontinuities in the general model makes the posterior PDF very sensitive to t_1 as the low uncertainty in the resulting value $t_1 = 1.3778 \pm 0.0001\,\mathrm{s}$ (0.007 %) shows. This value falls very close to the lower limit of the interval [1.378, 1.379] where the true value of $t_1 =$ was concluded to lie by visual inspection of the beta distribution (table 6.2).

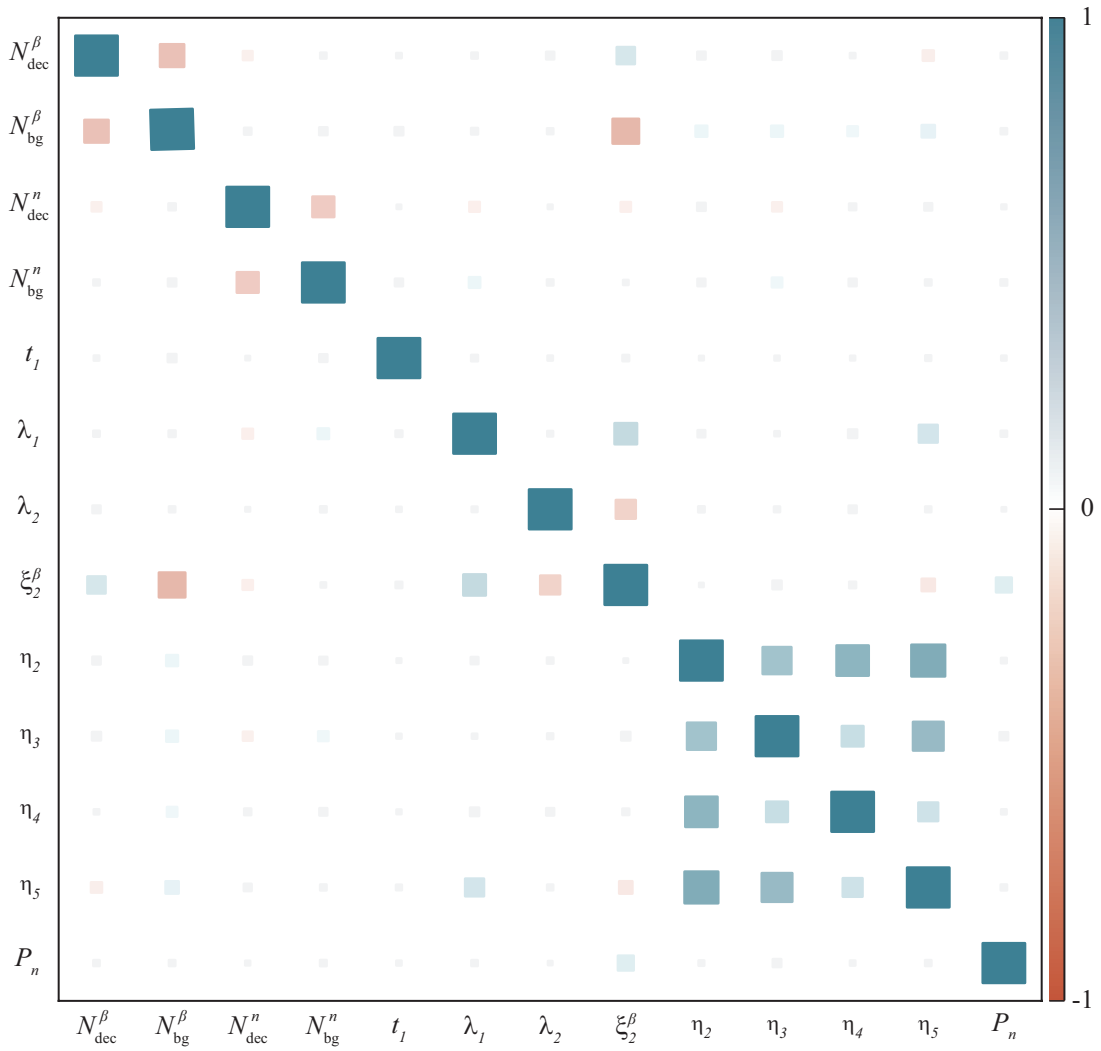

Figure 6.9: Correlation matrix of the parameters of the general model of the evolution of the beta and neutron counting rates in the measurement of ^{95}Rb.

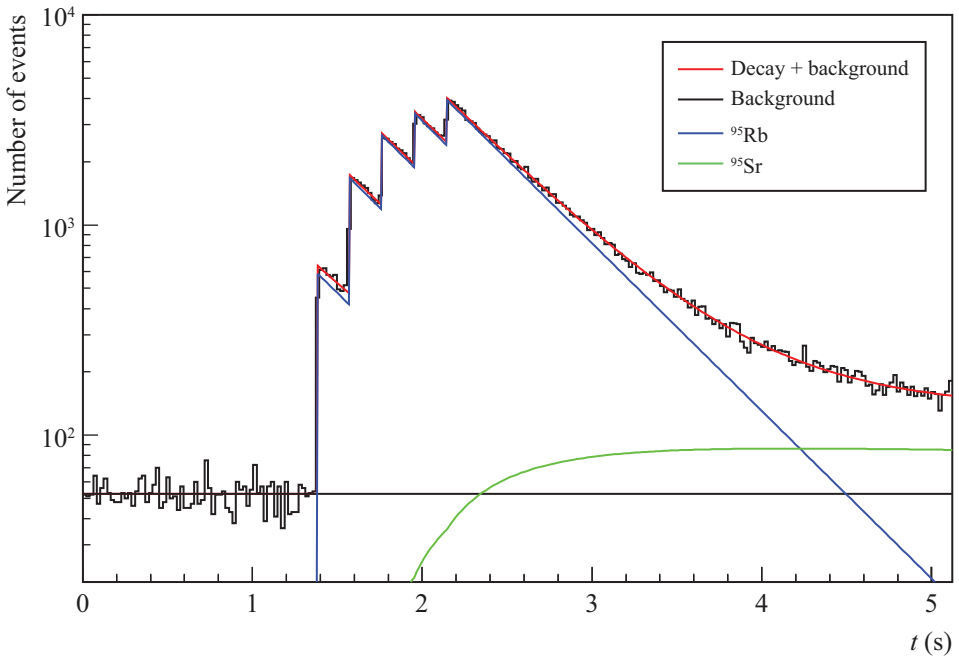

(a) Silicon detector

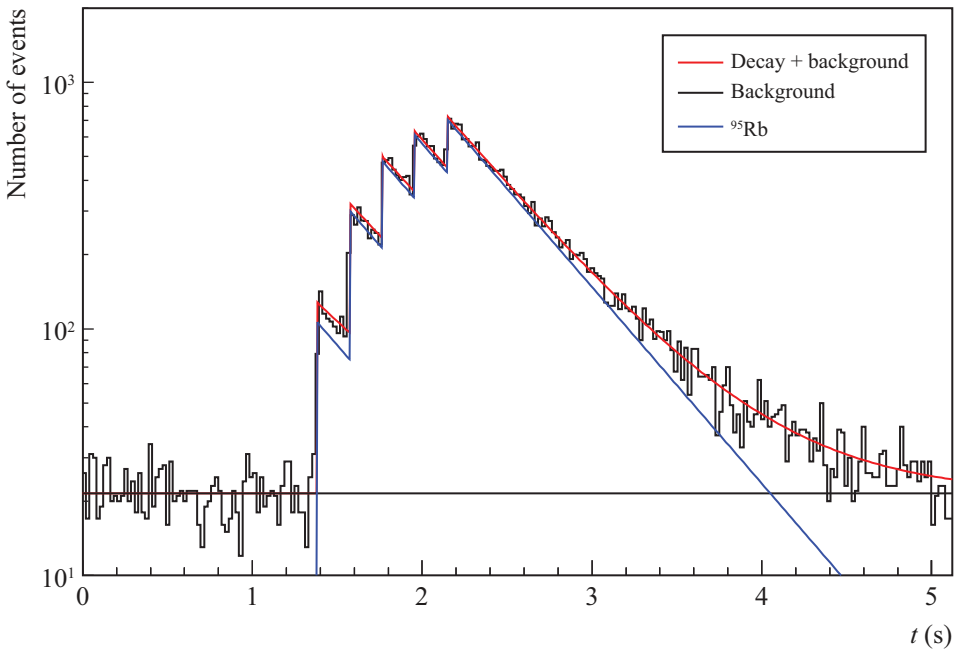

(b) BELEN20b

Figure 6.10: Simultaneous fit to the time distributions of beta and neutron detected events from the radioactive decay of ^{95}Rb.

6.4.4 ^{137}I

Figure 6.11 shows the radioactive decay chain of ^{137}I represented over the chart of nuclides. The chain is represented more in detail in figure E.4 along with relevant nuclear and decay data of all its elements.

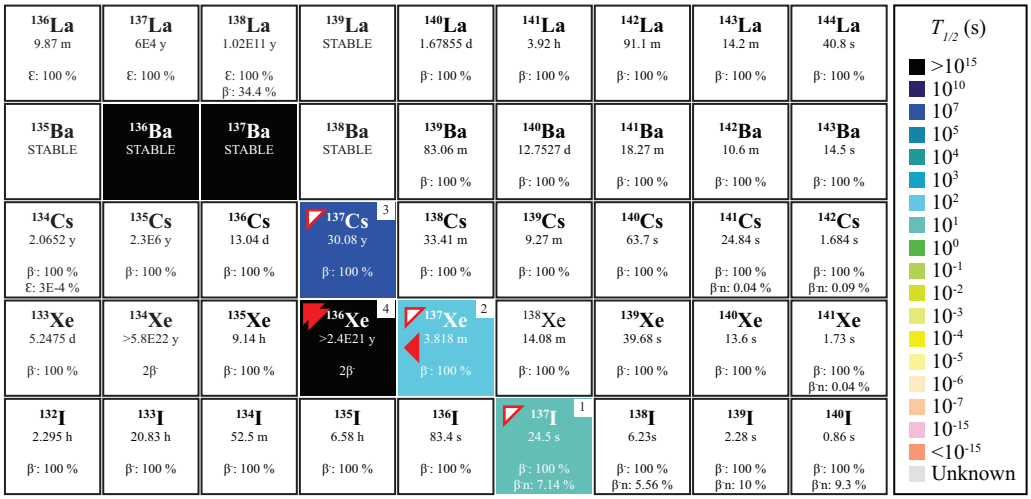

Figure 6.11: Radioactive decay chain of ^{137}I represented over the chart of nuclides. The $\beta\gamma$ and βn branches are indicated with white and red arrows respectively. The elements considered in the models for the evolution of the counting rates are indexed (upper right corners) according to the indexing rules of a GOD chain (section 6.1.1).

^{137}I has a half-life of 24.5 ± 0.2 s [160]. The beta decay to ^{137}Xe gives rise to the $\beta\gamma$ branch $^{137}\text{Xe} \xrightarrow{\beta^-} {}^{137}\text{Cs} \xrightarrow{\beta^-} {}^{137}\text{Ba}$. ^{137}I can also undergo beta decay followed by one-neutron emission to ^{136}Xe with a branching ratio of 7.33 ± 0.38 % [11], and the decay proceeds along the βn branch $^{136}\text{Xe} \xrightarrow{2\beta^-} {}^{136}\text{Ba}$. Both branches are short and linear. Only the $2\beta^-$ decay in the βn branch could complicate the construction of the model for the evolution of the beta counting rate. This, however, was not the case, because the $\beta\gamma$ and βn branches were truncated at ^{137}Cs and ^{136}Xe respectively. These isotopes have half-lives in the order of years, which makes them very unlikely to decay within a measurement cycle of 242.1 s.

An implantation every 0.191 s makes 378 implantations within a 72.384 s implantation-decay interval. The equivalent model must be applied in this case. With one radioactive element in the $\beta\gamma$ branch and none in the βn branch, the model has the same analytical form as the model for ^{94}Rb (section 6.4.2).

The simultaneous fit of the equivalent model to time distributions of beta and neutron detected events is shown in figure 6.12, and the parameter estimates and derived quantities are presented in table 6.7. The resulting value of δ is 0.51 ± 0.03. The quality of the fit is once again excellent, but at the expense of the rather low value $\xi_2^\beta = 0.510^{+0.016}_{-0.018}$, which

is about half the value 1.04 ± 0.04 calculated from the Monte Carlo simulations of the silicon detector (table 4.4). Such discrepancy cannot be explained by the effect of the beta intensity distribution of ^{137}I and ^{137}Xe in the beta detection efficiency, suggesting that a significant amount of the activity of ^{137}Xe may have been lost during the measurement. Previous studies have reported a similar effect, which was associated with the fast diffusion of noble elements from the implantation material [163]. Indeed, xenon diffuses in matter easier than other elements of similar size because it is a noble element. The lost ^{137}Xe activity by diffusion from the implantation tape is consistent with the low value of ξ_2^β obtained, as ^{137}Xe nuclei decaying far from the tape are less likely to be detected.

Decay parameters:

$T^1_{1/2} \stackrel{c}{=} 24.5 \pm 0.2\,\mathrm{s}$ $\quad T^2_{1/2} \stackrel{c}{=} 3.818 \pm 0.013\,\mathrm{min}$ $P_n \stackrel{c}{=} 7.33 \pm 0.38\,\%$

Implantation parameters:

$t_1 = 1.54^{+0.14}_{-0.06}$ s

Detection parameters:

$\xi_2^\beta = 0.510^{+0.016}_{-0.018}$

Yield parameters:

$N^\beta_{\mathrm{dec}} = 260100^{+1600}_{-1800}$ $\quad N^\beta_{\mathrm{bg}} = 15300^{+1800}_{-1400}$ $\quad N^n_{\mathrm{dec}} = 31600 \pm 300$ $\quad N^n_{\mathrm{bg}} = 29300 \pm 300$

Derived quantities:

$N^\beta_{\mathrm{dec}}(^{137}\mathrm{I}) = 219100^{+500}_{-900}$ $N^n_{\mathrm{dec}}(^{137}\mathrm{I}) = N^n_{\mathrm{dec}}$ $\quad \delta = \varepsilon_1^\beta/\varepsilon_1^n \stackrel{c}{=} 0.51 \pm 0.03$

Table 6.7: Parameter estimates and derived quantities resulting from the analysis of the ^{137}I measurement. $\stackrel{c}{=}$ denotes constrained parameter (see section 6.3.2). The half-lives $T^i_{1/2}$ enter the model transformed into λ_i. The number of detected beta particles emitted by the precursor $N^\beta_{\mathrm{dec}}(^{137}\mathrm{I})$ used in the estimation of δ was obtained with equation 6.23.

Compensating the activity loss of a noble element by diffusion with a constant reduction of the detection efficiency over the entire measurement cycle is equivalent to consider that all atoms of the noble element can diffuse out of the implantation tape[8], and that they do it at a rate proportional to the number of those atoms that remain inside. The latter approximation has been used before by several authors [20,163]. To illustrate this statement, assume that the diffusion process reduces the efficiency for a noble element X_i in the lth branch in a factor f. The evolution of the counting rate for that element would be $b_l(f\varepsilon_i^p)\lambda_i N_i(t)$, where ε_i^p is the efficiency for nuclei of that element decaying from the

[8] Bergmann et al. [163] observed the decay of samples of helium, krypton and xenon isotopes over time, and used an effective half-life to describe the evolution of the counting rates. They considered that only a fraction of the atoms of the noble element could diffuse out of the implantation substrate, but provided no arguments to support such assumption.

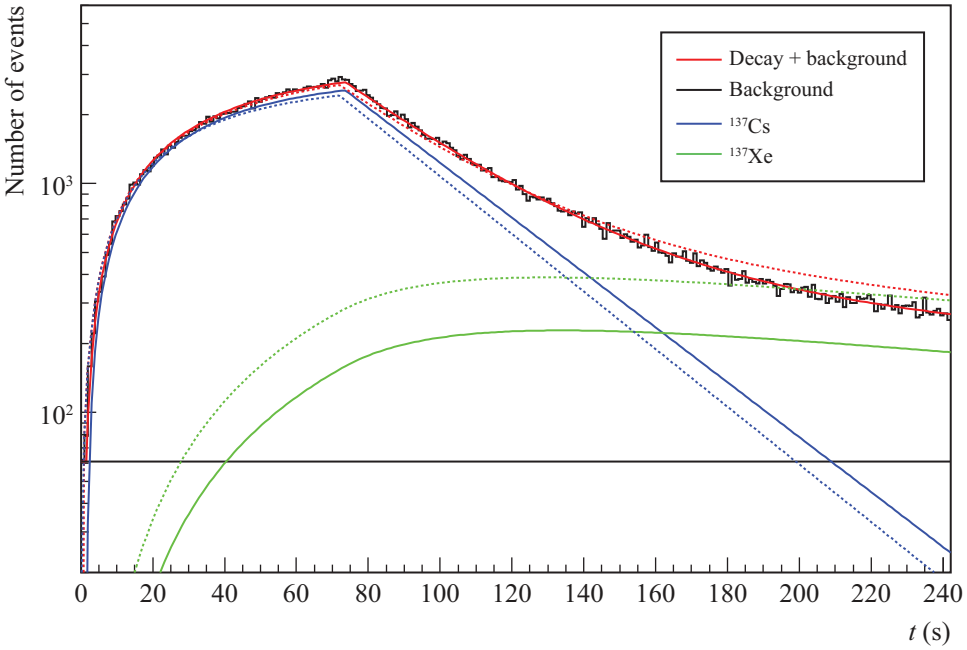

(a) Silicon detector

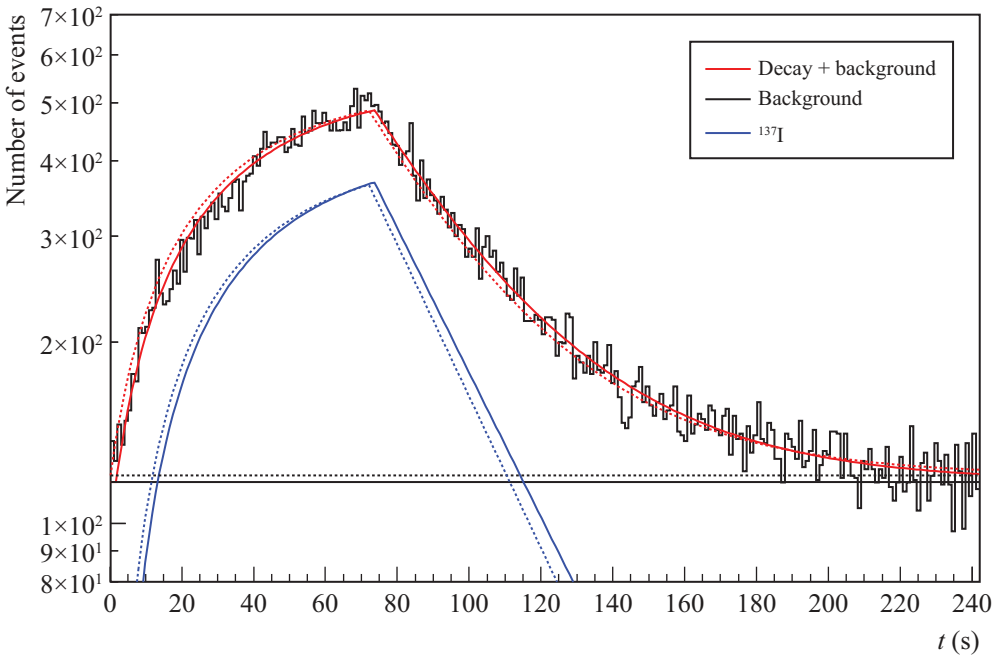

(b) BELEN20b

Figure 6.12: Simultaneous fit to the time distributions of beta and neutron detected events from the radioactive decay of ^{137}I. The result of neglecting the diffusion of xenon and the isotope-dependent effects on the efficiency of the silicon detector (i.e., fixing ξ_2^β at 1) is represented in discontinuous lines.

tape[9]. The previous equation can be rearranged as $b_l \varepsilon_i^p (f\lambda_i) N_i(t)$, and the process seen as the decay of the element with an effective decay constant $f\lambda_i$. Now, $f\lambda_i$ can be expressed as $\lambda_i - \lambda_i'$, where $\lambda_i' = (1-f)\lambda_i$. The Bateman equation for the noble element in terms of λ_i and λ_i' would be:

$$\frac{d}{dt}N_i(t) = -\lambda_i N_i(t) + \lambda_i' N_i(t) + \sum_{\substack{j=1 \\ j\neq i}}^{n} b_{ji}\lambda_j N_j(t) \tag{6.30}$$

Note that this is equation 6.2 with a new source term $\lambda_i' N_i(t)$ describing the loss by diffusion (hereafter the diffusion term), which is of the same form as the decay term $-\lambda_i N_i(t)$ but with opposite sign. The diffusion process is then in this approximation an exponential increasing process.

Adopting an exponential diffusion term is a crude approximation with no solid base. The right treatment of the diffusion process requires the solution of the diffusion equation and the evaluation of the diffusion flux at the surfaces of the tape, but it is unfeasible to include this in the models for the evolution of the counting rates. The diffusion equation is a parabolic partial differential equation with a complex solution that depends on the structure and chemical composition of the tape and the implantation profile, non of which are known with enough certainty. How the diffusion process is accounted for in the Bateman equations is therefore an important source of systematic uncertainty.

However the diffusion of xenon out of the tape is modeled, it is clear that the process cannot be neglected. Figure 6.12 shows in discontinuous lines a fit neglecting the diffusion of xenon and the isotope-dependent effects on the efficiency of the silicon detector by fixing ξ_2^β at 1. Note that the model fails to reproduce the experimental distributions. As a consequence, the value 0.91 ± 0.02 obtained for δ is strongly biased.

^{137}I is not the only one among the implanted isotopes with noble elements in its decay chain. ^{88}Br has two isotopes of krypton, but they barely contribute to the counting rates within the measurement cycles. The two isotopes of interest ^{86}As and ^{91}Br also have krypton isotopes in their decay chains.

6.5 Estimation of β-delayed neutron emission probabilities

The ratio $\delta = \varepsilon_1^\beta / \varepsilon_1^n$ is an experimental quantity that characterizes the detection system in efficiency. It is affected by isotope-dependent effects on the detection efficiency that result from differences in the neutron emission spectra and beta intensity distributions. Ignoring those effects may lead to significant systematic uncertainties.

The approach followed in this work to take those effects into account was not the cor-

[9]The implantation area on the tape is approximately 12.7 mm × 21 mm and the tape is just 40 µm thick. A particle moving in a lateral direction (i.e., perpendicular to the tape) will not travel long before leaving the tape from any of its sides. Thus, the effect of lateral diffusion on the detection efficiency can then be neglected against the effect of transverse diffusion.

rection of δ by Monte Carlo simulations as Agramunt et al. did in their paper on the characterization of BELEN20b [20]. Instead, the ratio $\kappa = {}^{\delta_{sim}}/_{\delta_{exp}}$, where *sim* and *exp* denote values obtained by Monte Carlo simulations and the analysis of the experimental data respectively, was used to constrain the estimation of the β-delayed neutron emission probability of ^{86}As and ^{91}Br. Both approaches are equivalent, but κ has a practical significance: it represents how biased the calculation of the detection efficiencies by Monte Carlo simulations are.

Table 6.8 compares the values of δ_{sim} obtained in this work (sections 4.1.4 and 4.2.3) with the values obtained by Agramunt et al. [20]. They are in excellent agreement with each other, but 25 % higher in average than the experimental values obtained in the previous sections. Most of this difference comes from the beta detection efficiency.

Isotope	$\boldsymbol{\varepsilon^{\beta}_{sim}}$ (%) (see table 4.4)	$\boldsymbol{\varepsilon^{n}_{sim}}$ (%) (see table 4.2)	$\boldsymbol{\delta_{sim}}$ (this work)	$\boldsymbol{\delta_{sim}}$ (Agramunt et al. [20])
^{88}Br	30.3 ± 0.2	46.75 ± 0.07	0.63 ± 0.02	0.623
^{94}Rb	30.3 ± 0.3	46.47 ± 0.07	0.62 ± 0.03	0.635
^{95}Rb	30.4 ± 0.3	45.98 ± 0.07	0.64 ± 0.03	0.645
^{137}I	30.18 ± 0.05	46.18 ± 0.07	0.6535 ± 0.0014	0.634

Table 6.8: Ratio $\delta = \varepsilon^{\beta}_{1}/\varepsilon^{n}_{1}$ for the reference isotopes calculated by Monte Carlo simulations of the detection system (sections 4.1.4 and 4.2.3). The low uncertainty in the ^{137}I value is due to the 100 % neutron intensity distribution concentrated at the ground state of ^{136}Xe, which allows to derive the beta intensity distribution of the precursor into the βn channel from the neutron emission spectrum instead of considering it a higher estimate.

The beta detection efficiencies calculated by Monte Carlo simulations are not reliable, as they are affected by large systematic uncertainties discussed in section 4.2. The calculation of the neutron detection efficiencies by Monte Carlo simulations, on the other hand, was successfully validated by Agramunt et al. [20] against a measurement with a ^{252}Cf source thanks to the significant improvement of the high-precision neutron model in GEANT4 performed in this work (appendix B). Using the experimental values of δ obtained for the reference isotopes in the previous sections and the calculated neutron detection efficiencies ε^{n}_{sim} shown in table 6.8, the experimental total beta detection efficiencies $\varepsilon^{\beta}_{exp}$ shown in table 6.9 were estimated.

Table 6.9 also shows estimates of the partial beta detection efficiencies in the $\beta\gamma$ and βn channels. The latter resulted from a Multiple Time Interval Analysis (MTIA) between beta and neutron detected events, and were used to calculate $\varepsilon^{\beta\gamma}_{exp}$ from equation 4.9.

The MTIA of coincidence measurements is a common technique in the determination of radioactive decay properties. It has been applied in the past to measure β-delayed neutron emission probabilities [17, see references to measurements with the n/β method therein], including in the analysis of the first experiment with BELEN at JYFL in 2009 [164]. The analysis takes advantage of the flat distribution of uncorrelated events from a homogeneous

Isotope	$\varepsilon^{\beta\gamma}_{\text{exp}}$ (%)	$\varepsilon^{\beta n}_{\text{exp}}$ (%)	$\varepsilon^{\beta}_{\text{exp}}$ (%)
^{88}Br	24.1 $\pm$ 0.8	22.1 $\pm$ 0.3	23.9 $\pm$ 0.7
^{94}Rb	23.8 $\pm$ 0.6	24.9 $\pm$ 0.3	23.9 $\pm$ 0.5
^{95}Rb	22.6 $\pm$ 0.9	24.3 $\pm$ 0.6	22.7 $\pm$ 0.8
^{137}I	23.77 $\pm$ 0.15	19.3 $\pm$ 0.4	23.45 $\pm$ 0.14

Table 6.9: Experimental detection efficiency of the silicon detector for the reference isotopes. $\varepsilon^{\beta\gamma}_{\text{exp}}$ and $\varepsilon^{\beta n}_{\text{exp}}$ are related to $\varepsilon^{\beta}_{\text{exp}}$ by equation 4.11.

Poisson process to estimate the number of correlated events $N_{\beta-n}$. Find the theoretical formalism of MTIA and its experimental validation in [165].

Figure 6.13 shows the multiple time interval distributions for the reference isotopes over a time window of ± 1 ms. The window is wide enough to observe all $\beta - n$ correlated events, as it covers the moderation time of the emitted neutrons in polyethylene ($\approx$100 µs in average). It is also short enough for the detection of uncorrelated neutrons to be considered a homogeneous Poisson process, and for the observation of correlated events with beta particles emitted by the descendants in the decay chain to be unlikely.

For $\Delta t < 0$, the distribution contains only uncorrelated events, as the emission of neutrons always follows the beta decay of the precursor. An Extended Maximum Likelihood Fit (EMLF) of a uniform PDF was performed accordingly in this region[10] to obtain the rate of uncorrelated events, which was then extrapolated to the rest of the window to estimate $N_1^{\beta-n}$ as the integral of the distribution above the background of uncorrelated events. With $N_1^{\beta-n}$, equations 1.3 and 1.4 combined allow to estimate the beta detection efficiency in the neutron emission channel as:

$$\varepsilon_{\beta n} = \frac{N_1^{\beta-n}}{Nn} \tag{6.31}$$

The experimental beta detection efficiency in the βn channel was used to reduce the uncertainty on δ_{sim} for the reference isotopes and ultimately the uncertainty on κ. Recall from chapter 4 that ε_β was calculated by Monte Carlo simulations with a large uncertainty on $\varepsilon_{\beta n}$ due to the lack of knowledge on the beta intensity distribution in the βn channel. $\varepsilon_{\beta n}$ was limited to the interval $[0, \varepsilon^{\beta n}_{\text{max}}]$, where $\varepsilon^{\beta n}_{\text{max}}$ is a higher estimate that results from the simulation with the beta intensity distribution that reproduces the neutron spectrum, considering that neutron emission populates the ground state of the daughter (section 4.2.3). The only exception is ^{137}I, whose neutron emission actually populates the ground state of ^{136}Xe always (see figure 4.15). $\varepsilon^{\beta n}_{\text{sim}}$ coincides with $\varepsilon^{\beta n}_{\text{max}}$ in this case. Thus, $\varepsilon^{\beta}_{\text{sim}}$ for ^{137}I is free of approximations on the beta intensity distribution. Comparing $\varepsilon^{\beta}_{\text{sim}}$ with $\varepsilon^{\beta}_{\text{exp}}$ for ^{137}I

[10] Some correlated events may fall in the $\Delta t < 0$ region close to zero due to the uncertainty in the determination of the signal timestamp by the DACQ. To account for this effect, the EMLF was performed from -1000 µs to -10 µs, and $N_1^{\beta-n}$ was estimated over the -10 µs to 1000 µs region.

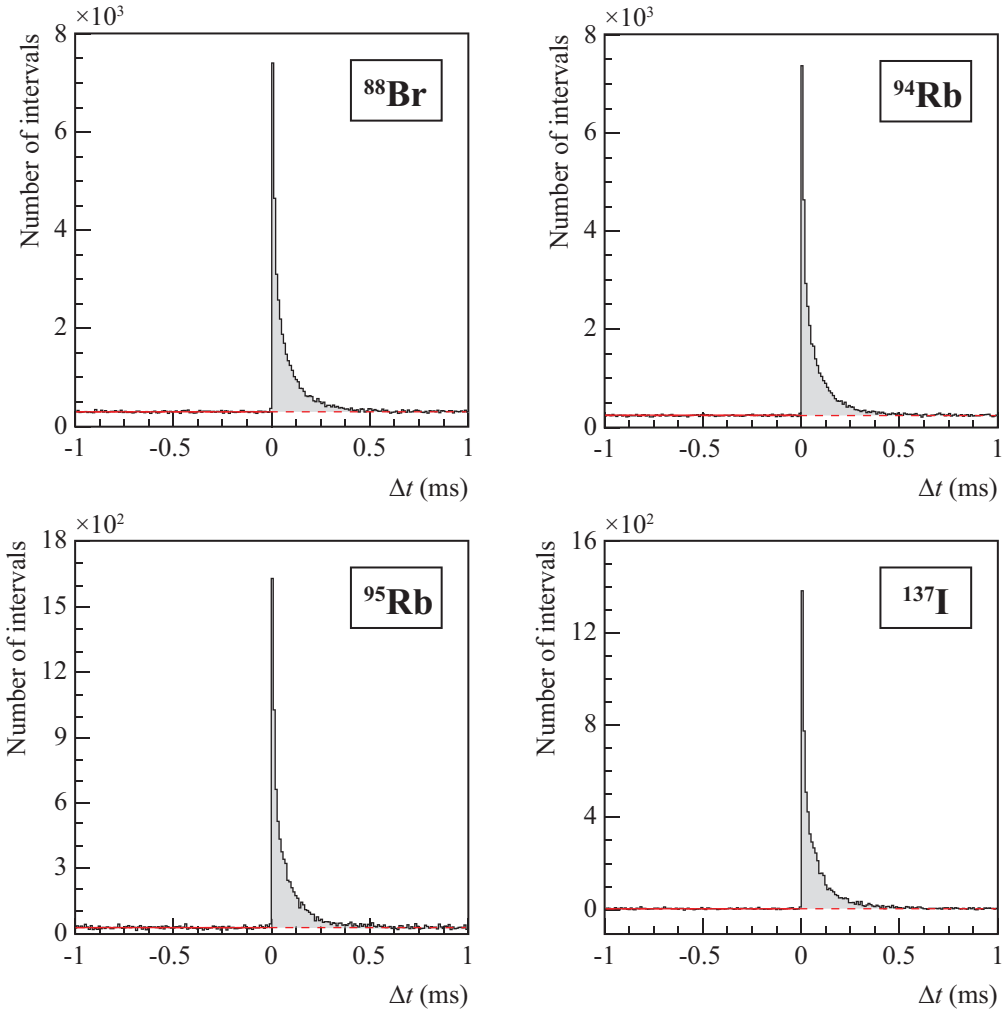

Figure 6.13: Multiple time interval distribution of beta and neutron detected events from the measurements with reference isotopes. The solid red line represents an Extended Maximum Likelihood Fit of a uniform PDF between 10 µs to 1000 µs, extended in a discontinuous line up to 1 ms.

(tables 6.8 and 6.9 respectively) allows to conclude then that the beta detection efficiency in the βn channel that would be obtained from Monte Carlo simulations with the real beta intensity distribution —if it was known— is in every case within the interval $[\varepsilon_{\mathrm{exp}}^{\beta n}, \varepsilon_{\mathrm{max}}^{\beta n}]$. This is a much narrower uncertainty interval for $\varepsilon_{\beta n}$ than $[0, \varepsilon_{\mathrm{max}}^{\beta n}]$. The new values of δ_{sim} calculated with this interval are shown in table 6.10. Note the significant reduction of the uncertainty.

Isotope	$\boldsymbol{\delta}_{\mathrm{sim}}$	$\boldsymbol{\delta}_{\mathrm{exp}}$	$\boldsymbol{\kappa} = \dfrac{\boldsymbol{\delta}_{\mathrm{sim}}}{\boldsymbol{\delta}_{\mathrm{exp}}}$
^{88}Br	0.648 ± 0.005	0.512 ± 0.014	1.27 ± 0.04
^{94}Rb	0.652 ± 0.007	0.514 ± 0.011	1.27 ± 0.03
^{95}Rb	0.661 ± 0.007	0.494 ± 0.017	1.34 ± 0.05
^{137}I	0.6535 ± 0.0014	0.51 ± 0.03	1.28 ± 0.07
Weighted average:			1.28 ± 0.02

Table 6.10: Ratio $\kappa = {}^{\delta_{\mathrm{sim}}}/_{\delta_{\mathrm{exp}}}$ representing how biased the calculation of the beta detection efficiencies by Monte Carlo simulations are. The values of δ_{sim} differ from those in table 6.8, because they were calculated with the reduced uncertainty interval for the beta detection efficiency in the neutron emission channel.

Table 6.10 also shows the estimates of κ. They are statistically compatible with each other. κ, as a quantity that combines experiment and simulation, is affected by statistical and systematic uncertainties from both. Whereas a great effort was devoted to preparing and modeling the experimental data to avoid or account for the most important sources of experimental systematic uncertainty, the Monte Carlo simulation of the detection system is affected by systematic uncertainties that are hard to quantify, e.g., the uncertainty from the geometrical modeling, material compositions and densities, room temperature, beam profile and position, nuclear models (thermal neutron scattering law, multiple electron scattering, ...) and data (beta intensity distribution, neutron emission spectrum, ...), etc. By adopting the confidence interval $[\varepsilon_{\mathrm{exp}}^{\beta n}, \varepsilon_{\mathrm{max}}^{\beta n}]$ for $\varepsilon_{\mathrm{sim}}^{\beta n}$, the systematic uncertainty from the lack of knowledge on the beta intensity distribution in the neutron emission channel is propagated to κ. In this sense, no correction of κ by isotope-dependent effects on the beta detection efficiency was performed, just the proper propagation of the associated uncertainty. The systematic uncertainty from the evaluation of the neutron emission spectra in ENDF/B-VIII.0, on the other hand, was neglected, as it concentrates most of the spectra in the design energy range of BELEN20b where the efficiency is almost independent on the initial neutron energy (see figures 4.9 and 4.8). More accurate measurements of the neutron emission spectra or measurements with a configuration of BELEN that extends the design energy range toward higher energies could further support this approximation. The other sources of systematic uncertainty affect all simulations equally.

κ was used as an external constraint in the estimation the delayed neutron emission probability of ^{86}As and ^{91}Br. κ itself is not a parameter of the models for the evolution of the

counting rates, but it relates to the model parameters through:

$$\kappa = \frac{\delta_{\text{sim}}}{\delta_{\text{exp}}} = \frac{1}{P_n}\left(\frac{N_1^n}{N_1^\beta}\right)\left[\frac{(1-P_n)\varepsilon_{\text{sim}}^{\beta\gamma} + P_n\varepsilon_{\text{sim}}^{\beta n}}{\varepsilon_{\text{sim}}^{n}}\right] \tag{6.32}$$

The constrain was imposed as a Gaussian prior PDF constructed from the weighted average of $\kappa = 1.28 \pm 0.02$. This is an approximation to the Cauchy distribution that describes κ, assuming that δ_{sim} and δ_{exp} are normally distributed.

6.5.1 ^{86}As

Theory predicts that ^{86}As may be a β-delayed two-neutron emitter [33], but with such a low probability (6.2991×10^{-4} %), the one- and two-neutron emission decay events would be hard to distinguish from each other with the low production yields of ^{86}As available nowadays. An experimental confirmation and ultimately the estimation of the delayed two-neutron emission probability requires higher production yields, more efficient detection systems, and further effort in modeling and reducing systematic uncertainties.

The radioactive decay of ^{86}As proceeds along two linear branches: the $\beta\gamma$ branch ^{86}Se$\longrightarrow$ ^{86}Br $\longrightarrow$^{86}Kr and the $\beta 1n$ branch ^{85}Se$\longrightarrow$^{85}Br$\longrightarrow$^{85}Kr$\longrightarrow$^{85}Rb. If ^{86}As was a delayed two-neutron emitter, it would decay into ^{84}Se and proceed along the $\beta 2n$ linear branch ^{84}Se$\longrightarrow$^{84}Br$\longrightarrow$^{84}Kr. Figure 6.14 represents the radioactive decay chain of ^{86}As as a delayed one-neutron emitter over the chart of nuclides. The chain is represented more in detail in figure E.5 along with relevant nuclear and decay data of all its elements.

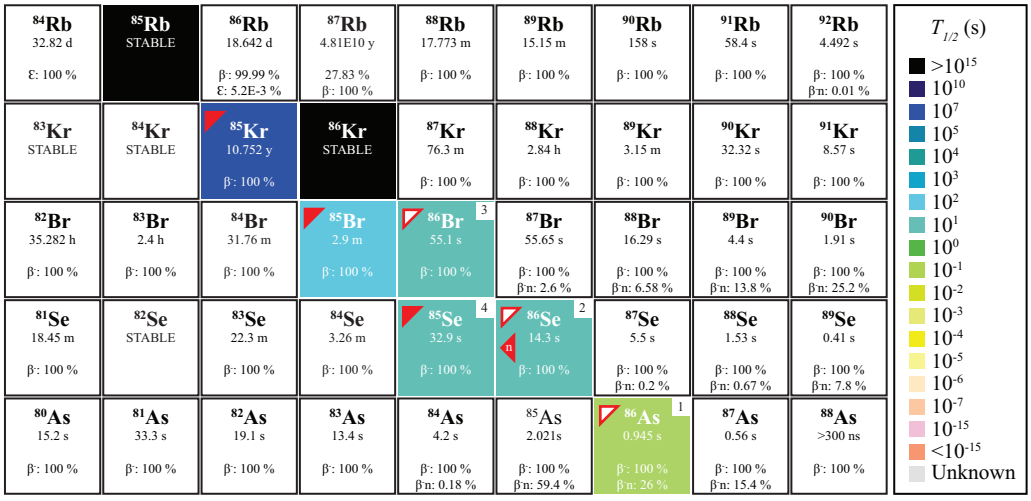

Figure 6.14: Radioactive decay chain of ^{86}As represented over the chart of nuclides. The $\beta\gamma$ and βn branches are indicated with white and red arrows respectively. The elements considered in the models for the evolution of the counting rates are indexed (upper right corners) according to the indexing rules of a GOD chain (section 6.1.1).

For the purpose of model reduction, the $\beta\gamma$ branch was truncated at ^{86}Br. The half-life of ^{86}Br is over 50 times the precursor's. Thus, its contribution and its descendants' to the counting rates is negligible within a measurement cycle. Following similar arguments, the $\beta 1n$ was truncated at ^{85}Se. The $\beta 2n$ branch, on the other hand, was omitted in the analysis, i.e., ^{86}As was considered a delayed one-neutron emitter.

Figure 6.15 shows the fit of the equivalent model to the time distribution of beta and neutron detected events. The obtained value of P_n —now the magnitude of interest— is $34.6 \pm 0.9\,\%$ ($2.7\,\%$). Unlike δ in the analysis of the measurements with the reference isotopes, P_n in this case is a model parameter and not a derived quantity. Other parameter estimates and derived quantities are shown in table 6.11.

Decay parameters:

$T^1_{1/2} \stackrel{c}{=} 945 \pm 8\,\mathrm{ms}$	$T^2_{1/2} \stackrel{c}{=} 14.3 \pm 0.3\,\mathrm{s}$	$P_n = 34.6 \pm 0.9\,\%$ ($2.7\,\%$)

Implantation parameters:

$t_1 = 1.402^{+0.005}_{-0.008}$ s

Detection parameters:

$\xi^\beta_2 = 1.29^{+0.06}_{-0.03}$	$\varepsilon^{\beta\gamma}_{\mathrm{sim}}(^{86}\mathrm{As}) \stackrel{c}{=} 30.20 \pm 0.05\,\%$	$\varepsilon^{n}_{\mathrm{sim}}(^{86}\mathrm{As}) \stackrel{c}{=} 46.06 \pm 0.07\,\%$
$\kappa = \delta_{\mathrm{sim}}/\delta_{\mathrm{exp}} \stackrel{c}{=} 1.28 \pm 0.02$		

Yield parameters:

$N^\beta_{\mathrm{dec}} = 50300 \pm 300$	$N^\beta_{\mathrm{bg}} = 6150^{+270}_{-190}$	$N^n_{\mathrm{dec}} = 28100^{+200}_{-300}$
$N^n_{\mathrm{bg}} = 2590^{+300}_{-200}$		

Derived quantities:

$N^\beta_{\mathrm{dec}}(^{86}\mathrm{As}) = 40800 \pm 300$	$N^n_{\mathrm{dec}}(^{86}\mathrm{As}) = N^n_{\mathrm{dec}}$	$\delta = \varepsilon^\beta_1/\varepsilon^n_1 = 0.503^{+0.012}_{-0.013}$

Auxiliary quantities from MTIA:

$N^{\beta-n}_1 = 6810 \pm 90$	$\varepsilon^{\beta n}_{\mathrm{exp}}(^{86}\mathrm{As}) = 24.3 \pm 0.2\,\%$

Table 6.11: Parameter estimates and derived quantities resulting from the analysis of the ^{86}As measurement. $\stackrel{c}{=}$ denotes constrained parameter (see section 6.3.2). The half-lives $T^i_{1/2}$ enter the model transformed into λ_i. The number of detected beta particles emitted by the precursor $N^\beta_{\mathrm{dec}}(^{86}\mathrm{As})$ used in the estimation of δ was obtained with equation 6.23.

The application of the equivalent model in the case of ^{86}As can be questioned. With 14 implantations per cycle within a 2.496 s implantation-decay interval the general model becomes too high-dimensional. However, 14 is not a large enough number of implantations to justify the application of the equivalent model. Actually, the jump discontinuities in the counting rates can be distinguished in figure 6.15. The condition of a large number of implantations upon which the equivalent model is based is subjective. More than "equivalent", the equivalent model is the limit of the general model as the number of implantations

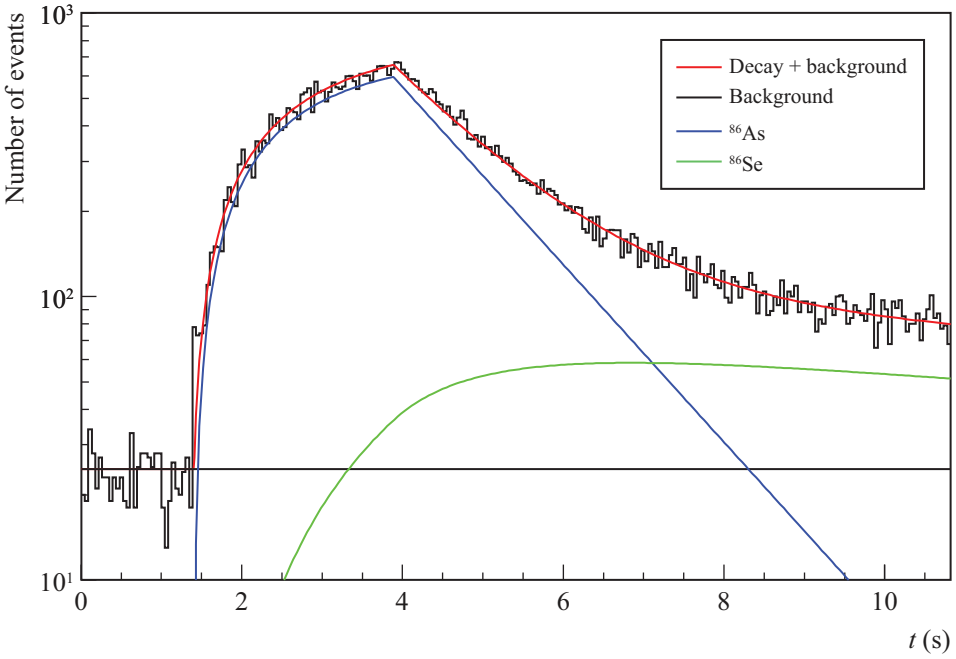

(a) Silicon detector

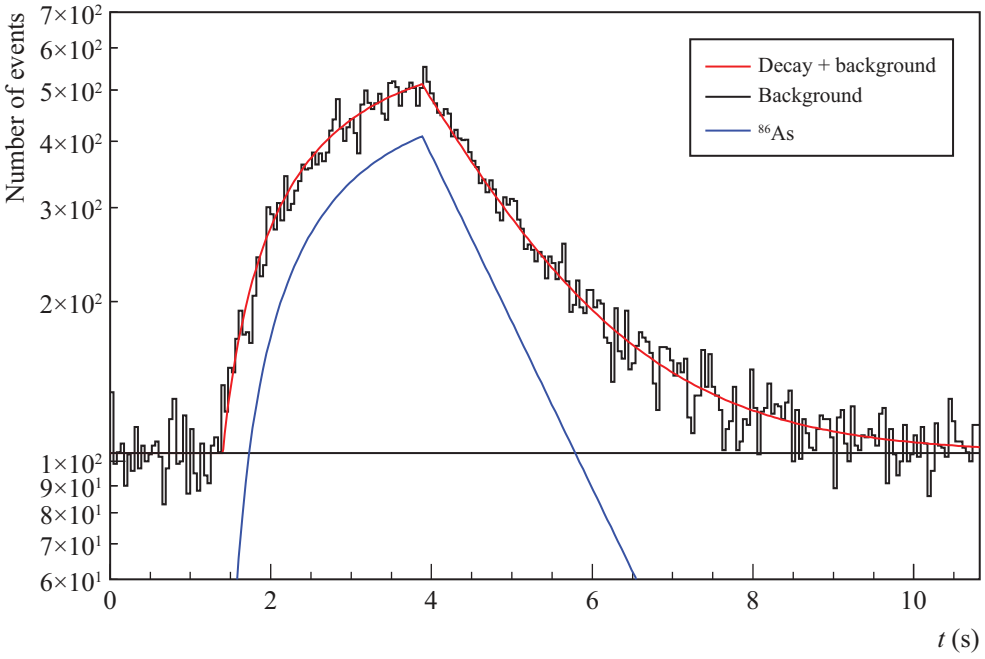

(b) BELEN20b

Figure 6.15: Simultaneous fit to the time distributions of beta and neutron detected events from the radioactive decay of ^{86}As.

grows. A real equivalent model would be a different parameterization that fits the data well and yields the same estimates of the parameters of interest. Hence, strictly speaking, the equivalent model is just a better or worse approximation in each case, better the larger number of implantations. Choosing a model is not just a matter of how exact it describes the experimental data. What makes a model better than others is a trade-off between plausibility, simplicity, capacity for prediction and generalization, and computational efficiency. Thus, the application of the equivalent model to estimate the delayed one-neutron emission probability of ^{86}As is justified in this sense. A warning is pertinent here on the unknown bias the choice of model may have introduced in the estimated value of P_n.

Table 6.11 shows other parameters of the posterior PDF that are not model parameters, namely the detection parameters $\varepsilon^{\beta}_{\mathrm{sim}}(^{86}\mathrm{As})$, $\varepsilon^{n}_{\mathrm{sim}}(^{86}\mathrm{As})$ and $\kappa = {}^{\delta_{\mathrm{sim}}}/_{\delta_{\mathrm{exp}}}$. These are prior information on the detection system that entered the parameter estimation process as a constraint on P_n via equation 6.32. The role of κ in the estimation of P_n goes beyond that of a simple constraint to render P_n identifiable. By imposing the constraint as a prior PDF constructed from weighted average of κ, the uncertainty in the efficiency characterization of the detection system, both experimental and obtained by Monte Carlo simulations, statistical and systematic, is propagated to P_n.

Note that the value of $\xi_2^{\beta} = 1.29^{+0.06}_{-0.03}$ is higher than 1. This cannot be explained by the effect of the beta intensity distribution on the beta detection efficiency. It reflects the compensation of neglecting the contribution of ^{85}Se to the beta counting rate. Including ^{85}Se in the model brought ξ_2 close to 1 without affecting the estimation of P_n, but made ξ_2^{β} practically non-identifiable.

The time interval distribution between beta and neutron events is shown in figure 6.16. Note that, due to the lower production yield of ^{86}As compared with reference isotopes and the significantly longer half-lives of the emitter and the daughter, the background of uncorrelated events is almost null. As for the reference isotopes, the number of uncorrelated events resulting from the Multiple Time Interval Analysis (MTIA) allowed to obtained the partial beta detection efficiency in the neutron emission channel $\varepsilon^{\beta n}_{\mathrm{exp}}$ by means of equation 6.31, and this was used to constrain the posterior PDF to the region $[\varepsilon^{\beta n}_{\mathrm{exp}}, \varepsilon^{\beta n}_{\mathrm{max}}]$, where $\varepsilon^{\beta n}_{\mathrm{max}}$ —just as a reminder— is the beta detection efficiency obtained from the neutron emission spectrum by Monte Carlo simulation of the silicon detector considering that neutron emission populates the ground state of the daughter nucleus.

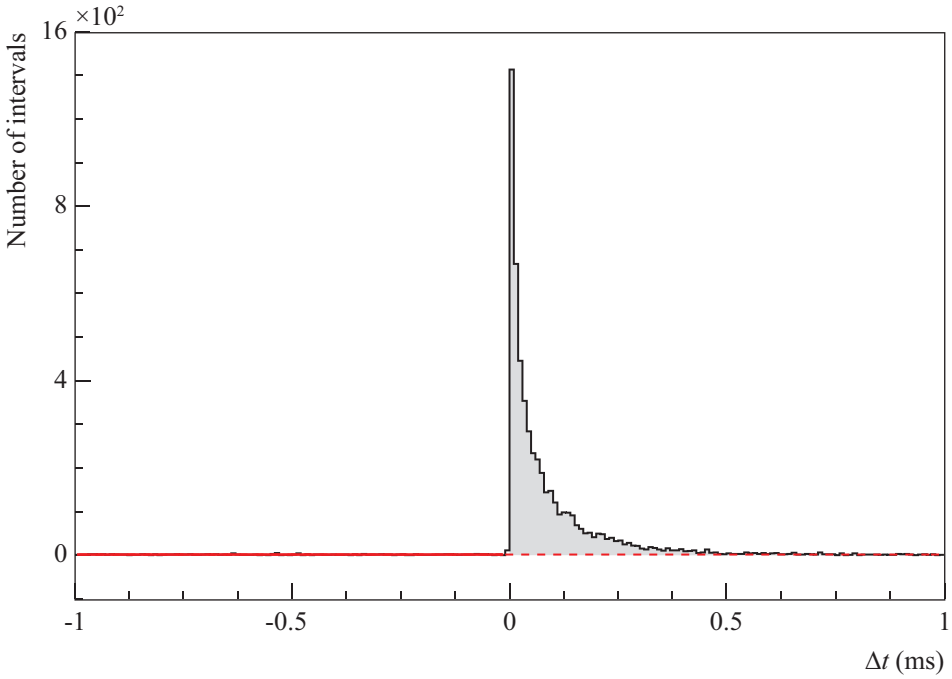

Figure 6.16: Multiple time interval distribution of beta and neutron detected events from the measurement of ^{86}As. The solid red line represents an Extended Maximum Likelihood Fit of a uniform PDF between 10 µs to 1000 µs. It is extended as a discontinuous line up to 1 ms.

6.5.2 ^{91}Br

The radioactive decay chain of ^{91}Br is significantly larger and more complex than the chains of the reference isotopes. It is represented in figure 6.17 over the chart of nuclides and more in detail in figure E.6 along with relevant nuclear and decay data of all its elements. The decay of ^{91}Br proceeds along two linear branches: the $\beta\gamma$ branch $^{91}\text{Kr}\longrightarrow{}^{91}\text{Rb}\longrightarrow{}^{91}\text{Sr}\longrightarrow{}^{91}\text{Y}\longrightarrow{}^{91}\text{Zr}$ and the βn branch $^{90}\text{Kr}\longrightarrow{}^{90}\text{Rb}\longrightarrow{}^{90}\text{Sr}\longrightarrow{}^{90}\text{Y}\longrightarrow{}^{90}\text{Zr}$. They were truncated at ^{91}Rb and ^{90}Kr respectively. The half-lives of these isotopes are two orders of magnitude longer than the precursor's and, therefore, they and and their descendants make a negligible contribution to the counting rates within a measurement cycle.

The short half-life of ^{91}Br (543 ± 4 ms) allowed to apply the general model as in the case of ^{95}Rb, since ions were implanted only seven times within a 1.152 s implantation-decay interval. However, six free implantation parameters η_k introduced a high computational cost in the parameter estimation process. Except for the model, the latter was no different than for ^{86}As.

The simultaneous fit of the general model to the time distributions of beta and neutron detected events is shown in figure 6.18, and the time interval distribution between beta and neutron events used to estimate $\varepsilon^{\beta n}_{\text{exp}}(^{91}\text{Br})$ to lower limit $\varepsilon^{\beta\gamma}_{\text{sim}}(^{91}\text{Br})$ is shown in figure 6.19. Table 6.12 presents the parameter estimates and derived quantities. The estimated value of P_n is $29.3^{+1.1}_{-0.8}$ % (3.2 %).

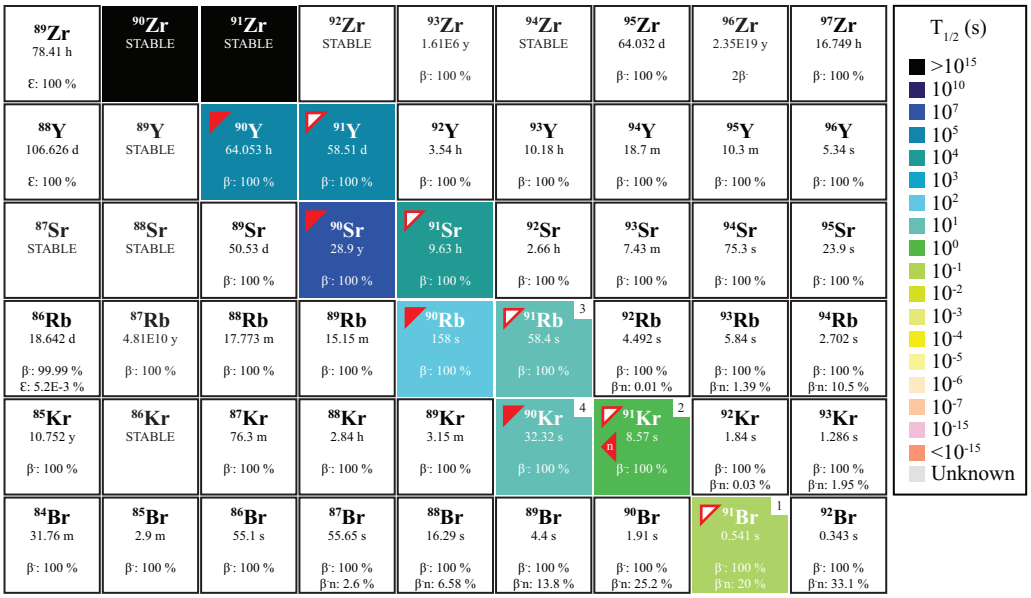

Figure 6.17: Radioactive decay chain of ^{91}Br represented over the chart of nuclides. The $\beta\gamma$ and βn branches are indicated with white and red arrows respectively. The elements considered in the models for the evolution of the counting rates are indexed (upper right corners) according to the indexing rules of a GOD chain (section 6.1.1).

Unlike for the reference isotopes and ^{86}As, the beta intensity distribution in the $\beta\gamma$ channel is not available for ^{91}Br in ENSDF. The value used to estimate P_n given in table 6.12 was obtained from the Monte Carlo simulation of the silicon detector with a uniform distribution of the beta intensity over 13 discrete end-point values measured by Graefenstedt et al. [138] (section 4.2.3). Whereas this is an approximation, it is not a bad one. All the end-points fall well above 3 MeV, where the efficiency curve is almost constant (figure 4.14). Thus, knowing the true intensity distribution will not yield a different efficiency.

Finally, it is important to notice the presence of krypton in the decay chain. It was pointed out at the end of section 6.4.4 that the loss of activity of noble elements by diffusion from the tape may be an important source of systematic uncertainty if ignored. Indeed, the resulting low estimate of $\xi_2^\beta = 0.587^{+0.008}_{-0.030}$ indicates a much lower detection efficiency for ^{91}Kr that cannot be explained by the beta intensity distribution. This confirms the hypothesis.

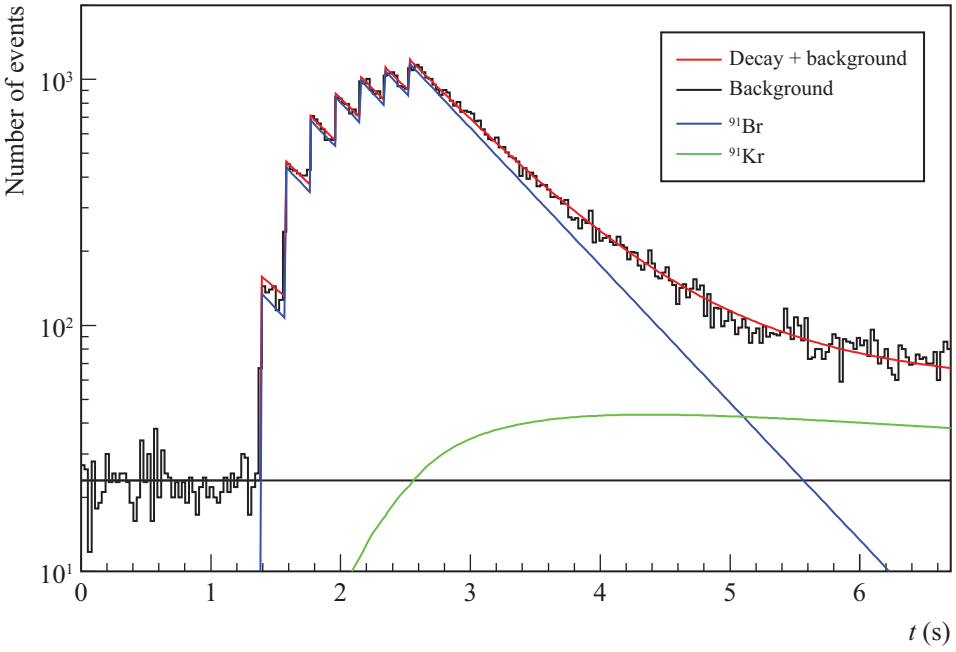

(a) Silicon detector

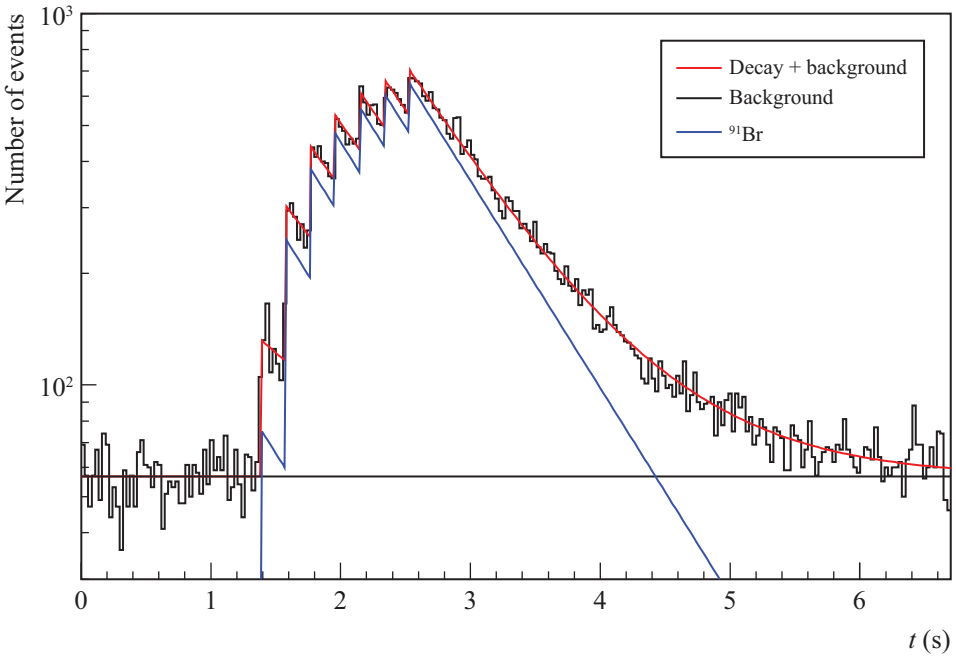

(b) BELEN20b

Figure 6.18: Simultaneous fit to the time distributions of beta and neutron detected events from the radioactive decay of ^{91}Br. The result of considering and neglecting the isotope-dependent effects on the efficiency of the silicon detector are represented with continuous and discontinuous lines, respectively.

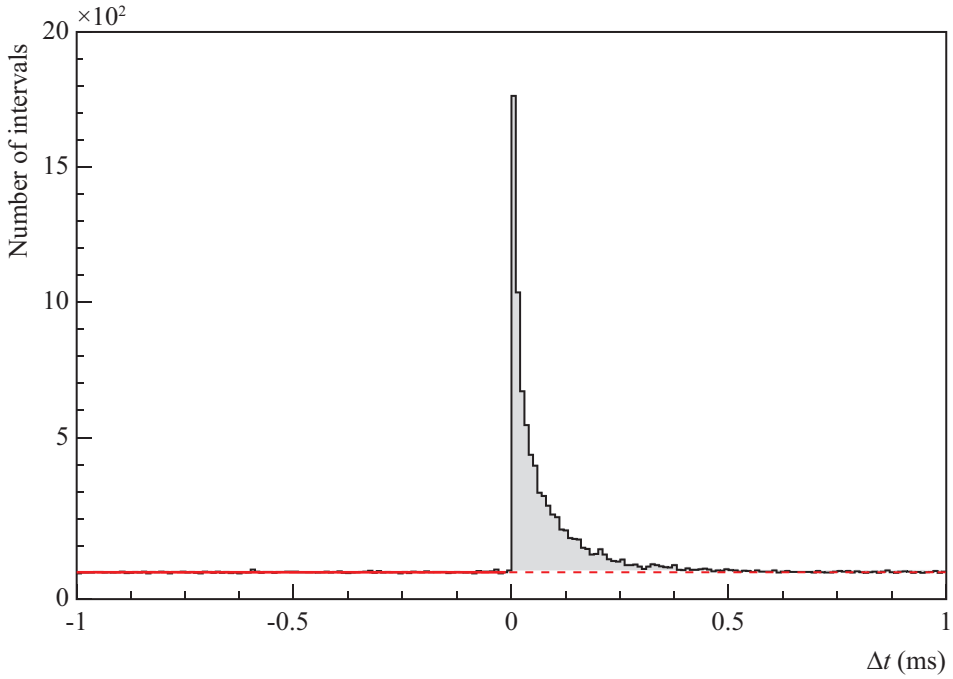

Figure 6.19: Multiple time interval distribution of beta and neutron detected events from the measurement of ^{91}Br. The solid red line represents an Extended Maximum Likelihood Fit of a uniform PDF between 10 µs to 1000 µs. It is extended as a discontinuous line up to 1 ms.

Decay parameters:

$T^1_{1/2} \stackrel{c}{=} 543 \pm 4\,\mathrm{ms}$	$T^2_{1/2} \stackrel{c}{=} 8.57 \pm 0.04\,\mathrm{s}$	$P_n = 29.3^{+1.1}_{-0.8}\,\%$ (3.2 %)

Implantation parameters:

$\eta_2 = 2.62^{+0.15}_{-0.08}$	$\eta_3 = 2.63^{+0.18}_{-0.05}$	$\eta_4 = 2.44^{+0.14}_{-0.09}$
$\eta_5 = 2.64^{+0.19}_{-0.08}$	$\eta_6 = 2.32^{+0.18}_{-0.07}$	$\eta_7 = 2.50^{+0.15}_{-0.07}$
$t_1 = 1.38040 \pm 0.00005$ s		

Detection parameters:

$\xi^\beta_2 = 0.587^{+0.008}_{-0.030}$	$\varepsilon^{\beta\gamma}_{\mathrm{sim}}(^{91}\mathrm{Br}) \stackrel{c}{=} 30.56 \pm 0.06\,\%$	$\varepsilon^{n}_{\mathrm{sim}}(^{91}\mathrm{Br}) \stackrel{c}{=} 45.49 \pm 0.07\,\%$
$\kappa = \delta_{\mathrm{sim}}/\delta_{\mathrm{exp}} \stackrel{c}{=} 1.28 \pm 0.02$		

Yield parameters:

$N^\beta_{\mathrm{dec}} = 66600 \pm 300$	$N^\beta_{\mathrm{bg}} = 5600^{+200}_{-100}$	$N^n_{\mathrm{dec}} = 33600^{+300}_{-200}$
$N^n_{\mathrm{bg}} = 14170^{+170}_{-190}$		

Derived quantities:

$\delta = \varepsilon^\beta_1/\varepsilon^n_1 = 0.521^{+0.017}_{-0.015}$	$N^\beta_{\mathrm{dec}}(^{91}\mathrm{Br}) = 59900 \pm 300$	$N^n_{\mathrm{dec}}(^{91}\mathrm{Br}) = N^n_{\mathrm{dec}}$

Auxiliary quantities from MTIA:

$N^{\beta-n}_1 = 7860 \pm 110$	$\varepsilon^{\beta n}_{\mathrm{exp}}(^{91}\mathrm{Br}) = 23.41^{+0.18}_{-0.15}\,\%$

Table 6.12: Parameter estimates and derived quantities resulting from the analysis of the ^{91}Br measurement. $\stackrel{c}{=}$ denotes constrained parameter (see section 6.3.2). The half-lives $T^i_{1/2}$ enter the model transformed into λ_i. The number of detected beta particles emitted by the precursor $N^\beta_{\mathrm{dec}}(^{91}\mathrm{Br})$ used in the estimation of δ was obtained with equation 6.23.

6.6 Discussion of results

Few measurements of the delayed neutron emission probability of ^{86}As and ^{91}Br have been performed to date, fewer in the case of ^{86}As. They are summarized in tables 6.13 and 6.14 respectively along with the latest evaluations. The scatter is huge, but there is a clear increasing pattern over the years that seems to converge to the true value with higher accuracy as the experimental techniques are improved. However, the lowest uncertainty among the previous measurements is still large (10.9 % for ^{86}As by Rudstam et al. [17] and 6.8 % for ^{91}Br by Aleklett et al. [26]). The results obtained in this work settle this situation. They are over 50 % more accurate than the most accurate of the previous measurements thanks to the use of advanced experimental techniques and a strong effort in preparing and modeling the experimental data and reducing systematic uncertainties.

The first measurements were performed with the fiss method (section 1.3.1), which relies on fission yields data. Fission yields are difficult to measure and probably constitute the major source of systematic uncertainty in those measurements. Rudstam et al. [17] reported revised values obtained with higher-quality fission yields. The mean value is higher in all cases as well as the uncertainty. This indicates that the fiss method is not very reliable. Indeed, the following measurements performed with the $n-\beta$ method, which is based on beta and neutron counting, are in general more accurate.

The previous ^{86}As measurement with the $n-\beta$ method by Rudstam et al. [17] yields a value 6 to 8 times higher than the first measurement with the fiss method by Kratz et al. [21]. The former, which is in agreement with the result obtained in this work, was adopted in the preparation of JEFF-3.3 and JENDL-4.0. While ENDF/B-VII.1 contains theoretical calculations by Kawano et al. [33], ENDF/B-VIII.0 incorporates an experimental one-neutron emission probability that is a preliminary result of this work [167]. This is the same value in ENSDF nowadays (as of July, 2020).

In the case of ^{91}Br, there are a few more measurements with the $n-\beta$ method that in general also yield higher values and are more accurate than the older measurements with the fiss method. Several of them (the four most recent) are statistically compatible with the result obtained in this work, not very accurate though. They may have been affected by the diffusion of krypton isotopes from the decay of ^{91}Br. The diffusion of noble elements in the radioactive decay chain was observed in this work in the ^{137}I and ^{91}Br measurements, and confirmed to be an important source of systematic uncertainty if ignored. Except for the Kratz & Herrmann [25] measurement, which consisted on measuring the activity of volatile elements, the rest were implantation measurements similar to the one performed in this work. None of the references to those measurements reported activity loss by diffusion or any other process. Thus, their results are likely to be biased. The measurement performed by Ewan et al. [28] may be the only exception. Since they normalized to the ratio of neutron to beta counting rates obtained with the P_n value of another bromine isotope, the effect of diffusion canceled out in the normalization. It is no wonder surprising that their estimated value 30.1 ± 2.1 % is so consistent with the value obtained in this work.

The P_n values of ^{91}Br in ENDF/B-VII.1 JEFF-3.3 and JENDL-4.0 are very similar to the value in ENSDF nowadays (as of July, 2020). They were derived from previous measurements with the $n-\beta$ method. In all cases, they are at variance with the result obtained in

Source	Experimental method (see section 1.3.1)	P_n (%)	Relative uncertainty (%)
Previous measurements			
Kratz et al. [21]	fiss	$3.8\,^{+\,1.7}_{-\,1.0}$	71.1
Kratz et al. [21][a)]	fiss	15 ± 11	73.3
Crançon et al. [22]	fiss	10.5 ± 2.2	30
Crançon et al. [22][a)]	fiss	12 ± 8	66.7
Rudstam et al. [17]	$n-\beta$	33.0 ± 3.6	10.9
Evaluations			
ENDF/B-VII.1 [45,166][c)]		12.48537	
ENDF/B-VIII.0 [38,39][b,c)]		35.5 ± 0.6	1.7
JEFF-3.3 [41]		33	
JENDL-4.0 [42,43]		33 ± 4	12.1
ENSDF [7,8,167][b)]		35.5 ± 0.6	1.7
Pfeiffer et al. [55]		26 ± 7	26.9
Liang et al. [168][d)]		35.4 ± 0.6	1.7
This work	$P_n\,{}^{A}_{Z}X$	34.6 ± 0.9	2.6

Table 6.13: Measurements and evaluations of the delayed neutron emission probability of ^{86}As.

[a] Rudstam et al. [17] reported the revised values of the Kratz et al. [21] and Crançon et al. [22] measurements respectively obtained with higher-quality fission yields.

[b] Preliminary result of this work presented in the 2013 *International Conference on Nuclear Data for Science and Technology* (ND2013), New York, USA.

[c] ^{86}As was considered a β-delayed one- and two-neutron emitter in the preparation of ENDF/B-VII.1 and ENDF/B-VIII.0. The neutron emission probabilities in ENDF/B-VII.1 resulted from theoretical calculations by Kawano et al. [33]. P_{1n} in ENDF/B-VIII.0 is a preliminary result of this work [167] (see note b)), which does not consider ^{86}As a two-neutron emitter. P_{2n}=6.2991 $\times\,10^{-4}$ % was adopted in both ENDF/B-VII.1 and ENDF/B-VIII.0.

[d] Weighted average of the Rudstam et al. [17] measurement and the preliminary result of this work reported in [167].

Source	Experimental method (see section 1.3.1)	P_n (%)	Relative uncertainty (%)
Previous measurements			
Kratz & Herrmann [25]	fiss	8.3 ± 2.5	30.1
Kratz & Herrmann [25][a)]	fiss	16 ± 5	31.3
Asghar et al. [23]	$n-\beta$	9.86 ± 1.97	20
Kratz [169]	$n-\beta$	14.1 ± 3.6	25.5
Aleklett et al. [26]	$n-\beta$	19.2 ± 1.3	6.8
Ewan et al. [28]	$n-\beta$	30.1 ± 2.1	7
Kratz et al. [29]	$n-\beta$	25.5 ± 3.5	13.7
Rudstam et al. [17]	$n-\beta$	22 ± 10	45.5
Evaluations			
ENDF/B-VII.1 [45,166][c)]		20 ± 3	15
JEFF-3.3 [41][b)]		20 ± 2	10
JENDL-4.0 [42,43][c)]		20 ± 3	15
ENSDF [7,8][c)]		19.5 ± 2.6	13.3
Pfeiffer et al. [55]		31.3 ± 6.0	19.2
Liang et al. [168][d)]		29.8 ± 0.8	2.7
This work	$P_n\,{}^{A}_{Z}X$	$29.3\ {}^{+\,1.1}_{-\,0.8}$	3.2

Table 6.14: Measurements and evaluations of the delayed neutron emission probability of ^{91}Br. ENDF/B-VIII.0 contains no delayed neutron emission data on ^{91}Br whatsoever.

[a] Rudstam et al. [17] reported the revised value of the Kratz & Herrmann [25] measurement obtained with higher-quality fission yields.

[b] Derived from measurements of Aleklett et al. [26], Ewan et al. [28], Mann et al, and Kratz et al. [29], along with datasets identified with M.C. Brady according to the description block.

[c] Unweighted average of the Asghar et al. [23], Kratz [169], Aleklett et al. [26], Ewan et al. [28], Kratz et al. [29] and Rudstam et al. [17] measurements, and the revised value $16 \pm 5\,\%$ of the Kratz & Herrmann [25] measurement by Rudstam et al. [17].

[d] Weighted average of the Ewan et al. [28], Kratz et al. [29], Rudstam et al. [17] measurement and the preliminary result $29.8 \pm 0.8\,\%$ of this work reported in [167].

this work. The latest evaluation of delayed neutron emission probabilities by Liang et al. [168] considers more recent measurements that bring the average closer to the value here obtained. It should be interpreted with caution though, since it includes the preliminary results of this work reported in [167]. The ^{86}As value in particular, because only one other measurement was used to derive it. The new values obtained in this work will be included in the Liang et al. [168] evaluation.

Model uncertainty is another important source of systematic uncertainty to discuss. Most articles on previous measurements of the delayed neutron emission probability of ^{86}As and ^{91}Br focus on the experimental method and provide few details on modeling and statistical inference. They are therefore difficult to judge in that regard. The values obtained in this work are not exempt of model uncertainty. The physical approximations adopted for model reduction, the choice of prior PDFs in BE, the truncation of the decay chains, the description of the diffusion process of noble elements, etc, they are all sources of model uncertainty that are difficult to quantify. However, a significant effort has been devoted in this work to avoid and reduce systematic uncertainties in general by, e.g., performing detailed simulations, deriving robust models, removing parameter redundancies, avoiding unnecessary physical approximations, and applying advance statistical inference methods. The preliminary results of this work reported by Agramunt et al. [167] did not address uncertainty propagation to such a large extent. In consequence, the new results are very similar to the previous ones with a larger but more accurate uncertainty. ENSDF should adopt the values from this work instead.

Chapter 7

Summary and conclusions

Nuclear technology developments and nuclear astrophysics studies impose high data requirements on neutron-rich nuclei in terms of amount and quality. Radioactive decay data on β-delayed neutron emitters are of particular relevance given the important role delayed neutrons play in both fields. In 2013, the International Atomic Energy Agency (IAEA) started Coordinated Research Project (CRP) on a *reference database for beta-delayed neutron emission evaluation* [170]. The database, which is in the process of publication [168], includes β-delayed neutron emission probabilities for 309 nuclei, about a hundred more than Evaluated Nuclear Structure Data File (ENSDF) to date (as of July, 2020) [7,8]. But there is a long road ahead to meet the delayed neutron data requirements of nowadays nuclear science and technology. The recent large-scale theoretical evaluation by Marketin et al. [6] on 5409 neutron-rich nuclei predicts that 90 % of them are β-delayed neutron emitters.

This manuscript reports on the measurement of the β-delayed neutron emission probability of ^{86}As and ^{91}Br performed at the Accelerator Laboratory of the Department of Physics of the University of Jyväskylä (JYFL), Finland, in 2010. The experiment was conducted as a collaboration between the Research Center for Energy, Environment and Technology (CIEMAT), the Spanish Institute of Corpuscular Physics (IFIC), the Polytechnic University of Catalonia (UPC) and the University of Jyväskylä. All four institutions have diverse but also common interests in the subject. At CIEMAT, the Nuclear Innovation Unit —where this work was performed— conducts nuclear data measurements for the development of advanced energy systems with a focus on closed fuel cycles and transmutation of MAs partitioned from nuclear waste. The driving interest behind this manuscript is therefore nuclear technology.

Contemporary and future nuclear energy programs aim to reach a high level of sustainability, safety, competitiveness and robustness [34]. The viability of those programs to meet such ambitious goals depends on the accurate description of the underlying physics in computational simulations [35] given the lack of practical experience with advanced nuclear energy systems in contrast with the conventional ones. Computational simulations are inherently dependent on models and experimental data. Whereas a rich experience has been gathered to date with simulation codes in support of nuclear energy systems, the

precision, accuracy, and completeness of the nuclear data are insufficient for the reliable and cost effective design and safety assessment of advanced systems.

It is within this context where the motivation for accurate measurements of the delayed neutron emission probability of ^{86}As and ^{91}Br arose. The relevance of these nuclei in nowadays nuclear technology developments was illustrated in chapter 2 with delayed neutron calculations on two European advanced reactor concepts: the European Sodium-cooled Fast Reactor (ESFR) and the European Facility for Industrial Transmutation (EFIT). These systems differ significantly from conventional nuclear reactors in the fuel and MAs inventories, and ^{86}As and ^{91}Br happen to be important contributors to the delayed neutron emission of major and minor actinides. The accurate measurement of their delayed neutron emission probabilities reported in this work is part of a large effort for improving the accuracy of decay data on the most relevant isotopes for nuclear technologies. In particular, accurate beta delayed neutron emission probabilities contribute to the improvement of summation calculations and serve to set constraints on fission yields, reducing any excess of conservatism in the reactor design and operation. This is precisely one of the conclusions of the CRP on a *reference database for beta-delayed neutron emission evaluation* [170], which will be taken into account in the CRP for *updating fission yield data for applications* started recently in June, 2020 [171].

^{86}As and ^{91}Br are short-lived, with half-lives of 945 ± 8 ms and 543 ± 4 ms half-lives respectively. A facility capable of producing intense and pure beams of exotic nuclei was therefore required to investigate their radioactive decay. The IGISOL facility at the Accelerator Laboratory fulfils these requirements combining the IGISOL technique with the JYFLTRAP at the end of a mass separator. With the IGISOL technique, ions are produced in a thin target from where they recoil out into a rare gas flow that thermalizes and sweeps them out for acceleration before isotopic separation. The thin target and rare gas flow provide the technique with chemical independence and a short delay time. Downstream of the mass separator, ions are then bunched for an effective injection into the JYFLTRAP where purification occurs.

Despite the fast extraction and purification techniques, exotic nuclei beams at IGISOL are produced with low intensities compare to those of stable nuclei due to the lower production cross section. Efficient and selective detection systems are therefore essential for accurate measurements of the decay properties of exotic nuclei. In view of this, complementary detection techniques optimized for different types of radiation were used in the experiment:

- the BEta deLayEd Neutron detector (BELEN) in its 20b configuration for neutron counting;
- a 0.5 mm thick silicon detector for beta detection; and
- a High-Purity Germanium (HPGe) detector to monitor the purity of the beam.

BELEN20b consists of 20 cylindrical ^{3}He neutron counters embedded in a $90 \times 90 \times 80$ cm block of High-Molecular-Weight PolyEthylene (HMWPE). The counters are symmetrically distributed around the shortest C_4 axis (the one joining the centroids of the opposite 90×90 cm faces) in two concentric rings (8 in the inner and 12 in the outer) to achieve

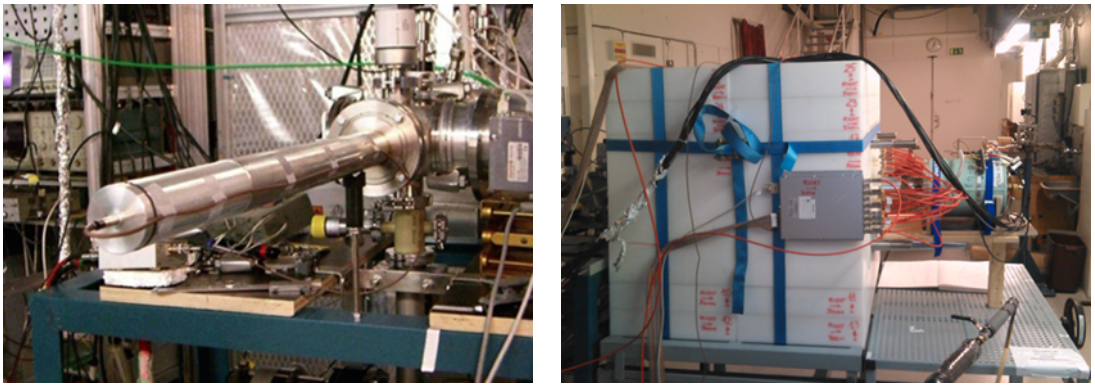

(a) Implantation system **(b)** Detection system

Figure 7.1: Implantation and detection systems.

a high neutron detection efficiency (about 47 %) as constant as possible between a few keV and a few MeV, which is the energy range of interest for β-delayed neutron emission studies. The beam was implanted onto a movable tape at the center of BELEN. Close behind the tape was placed the silicon detector. The tape and the detector were enclosed in the beampipe under vacuum by an end-cap with a LEMO connector for the detector high-voltage input and signal output. Figure 7.1 shows the implantation and detection systems. The HPGe detector is shown in figure 7.1(b) inserted from the opposite side of BELEN than the beamline into the same cavity.

The detection system operated in triggerless mode (i.e., all signals exceeding a given amplitude threshold were registered) with a Data ACQuisition system (DACQ) designed specifically for experiments with BELEN [20]. The DACQ, mostly based on commercial electronics, featured flash ADCs with a 100 MHz sampling frequency and a 16 bits resolution. These provided timestamp and energy information introducing just a 17 µs non-paralizable dead time.

The measurements were performed in cycles with a time structure optimized for each isotope according to its half-life. The background was measured during approximately 1.35 s at the beginning of each cycle. Then, the beam was implanted several times during a period about three times the half-life of the precursor, after which the implantation was stopped and the measurement continued for another seven half-lives approximately. At the end of each cycle, the activity was removed by moving the tape, and the timestamp scaler of the DACQ was reset to zero for the next cycle starting 2 s later. The cycle was repeated until enough statistics was gathered with the constraint of limited beam time.

This experiment was the second of its kind performed with BELEN at JYFL. With the DACQ still under test, it was not exempt of problems related to the data acquisition. A huge effort was devoted accordingly to the exploration, cleansing and preparation of the data for the analysis. In the process, errors in the data acquisition software were identified and corrected, which can be regarded as the first relevant contribution of this work to later and future measurement with BELEN.

Among the experimental methods to measure β-delayed one-neutron emission probabilities (section 1.3.1), the simplest in concept stems straight from the definition of the magnitude itself, i.e., the ratio of the number of beta decays followed by neutron emission to the total number of decays. For one-neutron emitters, the number of emitted neutrons determines the former. Thus, by separate counting of neutrons and beta particles emitted by the precursor, the delayed one-neutron emission probability can be obtained as:

$$P_n = \frac{\varepsilon_\beta}{\varepsilon_n} \frac{N_n}{N_\beta} \tag{7.1}$$

where, for beta particles and neutrons emitted by the precursor, ε denotes the detection efficiency and N the number of detected events. The $P_n\,{}^{A}_{Z}X$ method applied in this work makes use of the previous equation to characterize the detection system in efficiency with measurements on isotopes with well known values of P_n, namely ^{88}Br, ^{94,95}Rb, and ^{137}I, which are considered as reference for the purpose of data evaluation and measurements [11]. The same equation was used then to estimate P_n for ^{86}As and ^{91}Br.

β-delayed neutron emission probability measurements based on beta and neutron counting face one major challenge: they require disentangling the activity of the precursor from the activity of the rest of the radioactive decay chain, the electronic noise and the room background. This was achieved in this work by fitting a model to the time distribution of beta and neutron detected events. The model is based on a novel algebraic approach of solving the Bateman equations. It is analytical and can be applied to any decay chain regardless of its complexity. Many parameters of different nature enter the model (average detection efficiency for each isotope in the decay chain, half-lives, number of implanted ions in each implantation, etc.), and many of them are not identifiable from the structural point of view. The model was therefore reduced with convenient reparameterizations and prior information available on the experiment, underlying physical processes, and parameters. This lead to two variants of the model: the *general* and the *equivalent*. The latter, with fewer parameters, applies to measurements where the percursor's half-life is much larger than the time between successive implantations, and the number of implantations within the implantation-decay interval of the measurement cycle becomes too large for an efficient application of the general model. Figure 7.2 shows the time distribution of beta detected events from the measurement on ^{91}Br and ^{86}As illustrating the application of the general and equivalent variants of the model for the evolution of the counting rates. The structural identifiability of the general and equivalent models was analyzed in detail in appendix D. As a result, they could be further reduced to improve their identifiability and avoid the common approximation of the same beta detection efficiency for all elements in the decay chain adopted in previous works.

The main strength of this work lies in the application of Bayesian Estimation (BE), an advanced statistical inference framework that allowed for the complete propagation of uncertainties. Bayesian Estimation (BE) is based on the Bayes rule to construct the posterior PDF of the model parameters from the likelihood and a proposed prior PDF that represents the prior belief of the posterior PDF of the parameters before the observation of the data. Other advantages of applying Bayesian Estimation (BE) were the natural and principled way it offered for imposing external constraints to improve the model identifia-

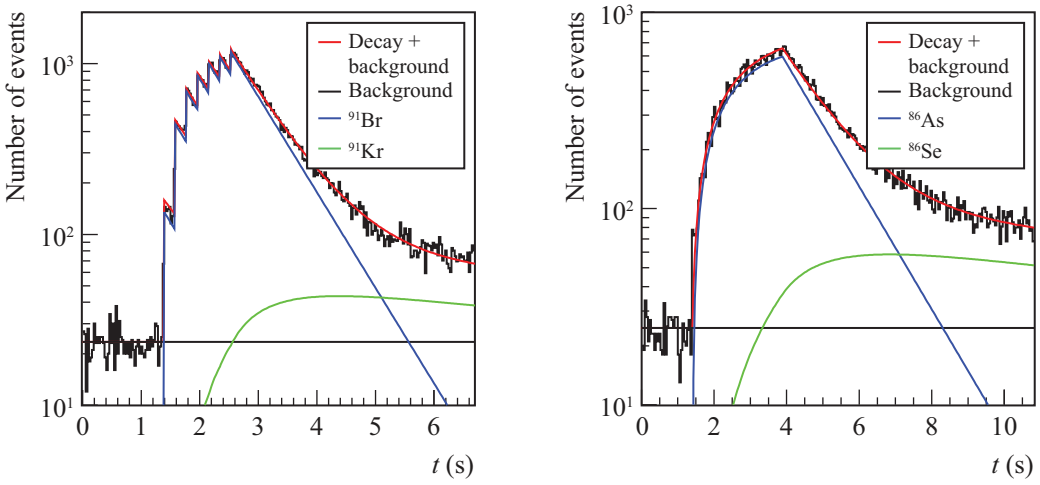

(a) General model **(b)** Equivalent model

Figure 7.2: Time distribution of beta detected events from the measurement on ^{91}Br and ^{86}As illustrating the application of the general and equivalent variants of the model for the evolution of the counting rates.

bility, and the possibility to work with unbinned rather than binned data, which removed the systematic uncertainty introduced by the loss of information that results always from binning. Point estimates reported in this work are Maximum A Posteriori (MAP) estimates obtained from searching the restricted parameter space for the global maximum of the posterior distribution. Error estimates are Highest Posterior Density Interval (HPDI), which are the smallest possible credible intervals. All were obtained from the joint PDF of the parameters of the models for the evolution of the beta and neutron counting rates. They are in consequence the common set of parameter estimates that describes the two distributions best, given the prior information available on the experiment, underlying physical processes, and parameters.

Monte Carlo simulations of the detection system presented in chapter 4 showed why the application of the $P_n\,{}^{A}_{Z}X$ method can be severely affected by systematic uncertainties if the dependence of the detection efficiencies on the spectrum of the emitted radiation is ignored, an approximation upon which the method relies when adopting for the isotopes of interest the same value of the ratio $\delta = \varepsilon_\beta/\varepsilon_n$ obtained from measurements with reference isotopes. This work makes use of Monte Carlo simulations of the silicon detector to propagate the uncertainty arising from the lack of knowledge on the beta intensity distribution in the neutron emission channel. It is the latter that is responsible for the lowest transition energies, for which the detection efficiency of the silicon detector is lower due to the effect of the electronic threshold. Monte Carlo simulations of BELEN20b are also used in this work to correct the results by the effect of the neutron emission spectrum on the detection efficiency.

Another relevant contribution of this work regards the improvement of the high-precision

neutron model in the GEANT4 Monte Carlo radiation transport code (appendix B), which had a great impact in the simulation of the performance of BELEN20b and newer configurations of the detector and reduced the model uncertainty in the calculation of the neutron detection efficiency. Previous versions of the code overestimated the thermal scattering cross section and sampled the final state of the neutron wrong. As a result, GEANT4 overestimated the neutron detection efficiency of BELEN20b by 7 % with respect to the MCNPX, which is a standard and well validated tool for the simulation of neutron interactions. The improvement of GEANT4 and a comprehensive verification against MCNPX were presented and discussed in the GEANT4 Hadronic Working Group Meeting on April 17, 2013 [172]. The corrections were accepted and incorporated in release GEANT4.10.0. Thanks to this contribution, the capacity of GEANT4 to simulate low-energy neutron interactions could be successfully validated against a measurement with a standard ^{252}Cf source [20].

Monte Carlo simulations entered the application of the $P_n\,{}^{A}_{Z}X$ method through the ratio $\kappa = {}^{\delta_{\rm sim}}/_{\delta_{\rm exp}}$, which represents how biased the Monte Carlo estimates of the detection efficiencies are due to various factors: geometrical modeling, material compositions and densities, room temperature, beam profile and position, nuclear models (thermal neutron scattering law, multiple electron scattering, etc.) and data, etc. The weighted average of κ obtained from the measurements with reference isotopes was used as a constraint to estimate the delayed neutron emission probability of the isotopes of interest, i.e., whatever the P_n value of an isotope is, it must produce the same value of κ. In contrast with δ, κ is isotope-independent provided that the neutron emission spectrum and the beta intensity distribution are well known, because the effect of these on the neutron and beta detection efficiencies respectively is present in both $\delta_{\rm sim}$ and $\delta_{\rm exp}$. This was confirmed by the low scatter of the values of κ obtained for the reference isotopes.

A key point in the determination of κ was the Monte Carlo estimation of the beta detection efficiencies. Whereas the beta intensity distribution in the $\beta\gamma$ channel is given in ENSDF for all of the implanted isotopes except ^{91}Br, the distribution in the βn channel is only given for ^{137}I. To circumvent this obstacle, the efficiency in the βn channel $\varepsilon^{\beta n}_{\rm sim}$ was considered uncertain within the interval $[\varepsilon^{\beta n}_{\rm exp}, \varepsilon^{\beta n}_{\rm max}]$. $\varepsilon^{\beta n}_{\rm max}$ is the higher estimate of $\varepsilon^{\beta n}_{\rm sim}$ that results from simulations with the beta intensity distribution that reproduces the neutron spectrum, considering that neutron emission only populates the ground state of the daughter nucleus. $\varepsilon^{\beta n}_{\rm exp}$, on the other hand, is the beta detection efficiency in the βn channel obtained from the Multiple Time Interval Analysis (MTIA) between beta and neutron detected events. Comparing $\varepsilon^{\beta}_{\rm sim}$ with $\varepsilon^{\beta}_{\rm exp}$ for ^{137}I allowed to adopt $\varepsilon^{\beta n}_{\rm exp}$ as a lower estimate of $\varepsilon^{\beta}_{\rm sim}$ in all cases, because the neutron emission by ^{137}I actually populates the ground state of ^{136}Xe every time. In consequence, $\varepsilon^{\beta n}_{\rm sim}$ coincides with $\varepsilon^{\beta n}_{\rm max}$ for ^{137}I, i.e., the total beta detection efficiency of ^{137}I is free of approximations on the beta intensity distribution.

The new values of the delayed neutron emission probability of ^{86}As and ^{91}Br reported in this work settle the large discrepancies between previous measurements and evaluations. They are over 50 % more accurate than the most accurate of the previous measurements, thanks to the use of advanced experimental techniques and the strong effort in preparing and modeling the experimental data and reducing systematic uncertainties.

For ^{86}As, P_n =34.6 $\pm$ 0.9 % (2.7 %) was obtained. A similar value slightly more accurate

$35.5 \pm 0.6\,\%$ ($1.7\,\%$) was adopted in the preparation of ENDF/B-VIII.0 and incorporated into ENSDF (as of July, 2020). That is a preliminary result of this work reported in [167] that did not address uncertainty propagation to such a large extent. In consequence, the result obtained in this work is very similar to the previous one with a larger but more accurate uncertainty. ENDF/B and ENSDF should adopt the new value instead.

In the case of ^{91}Br, the value of P_n obtained was $29.3^{+1.1}_{-0.8}\,\%$. Several previous measurements of the delayed neutron emission probability of ^{91}Br are statistically compatible with this result, not very accurate though. They may have been affected by the diffusion of krypton isotopes, a process identified as the cause of activity loss when noble elements are present in the radioactive decay chain. This effect, also observed in the ^{137}I measurement, can be an important source of systematic uncertainty if ignored. The models for the evolution of the beta and neutron counting rates derived in this work accounted for the effect of diffusion by a constant reduction of the beta detection efficiency over the measurement cycle.

The P_n values of ^{91}Br in ENDF/B-VII.1, JEFF-3.3, and JENDL-4.0 are very similar to the value $19.5 \pm 2.6\,\%$ in ENSDF nowadays (as of July, 2020). They are derived from previous measurements that are at variance with the result obtained in this work. The latest evaluation of delayed neutron emission probabilities by Liang et al. [168] considers more recent measurements that bring the average closer to the value here obtained. It should be interpreted with caution though, since it includes the preliminary results of this work reported in [167]. The ^{86}As value in particular, because only one other measurement was used to derive it. The new values obtained in this work are in the process to be included in the Liang et al. [168] evaluation.

To summarize, the key contributions of this work are, in order of appearance:

1. Realization of summation calculations to illustrate the specific roles of ^{86}As and ^{91}Br in delayed neutron calculations on two European advanced reactor concepts: the ESFR and EFIT.

2. Realization of a radioactive decay experiment with the BEta deLayEd Neutron detector (BELEN)20b and complementary detection techniques at the Accelerator Laboratory of the University of Jyväskylä, Finland, to measure the β-delayed neutron emission probability of ^{86}As and ^{91}Br.

3. Improvement and verification of the thermal neutron transport model in GEANT4.

4. In-depth exploration of the data acquired during the experiment that revealed errors in the data acquisition software.

5. Development of a general algebraic model for the evolution of the counting rates based on the Bateman equations, capable of handling branching in the radioactive decay chain without additional complexity.

6. Estimation of the β-delayed neutron emission probability of ^{86}As and ^{91}Br applying Bayesian inference and advanced modeling techniques that allowed for the complete propagation of uncertainties and lead to high accuracy. These results will be included in the Liang et al. [168] evaluation that has resulted from the CRP on a *reference*

database for beta-delayed neutron emission evaluation started by the International Atomic Energy Agency (IAEA) in 2013.

Chapter 8

Resumen y conclusiones

El desarrollo de tecnología nuclear y los estudios de astrofísica nuclear imponen altos requerimientos en términos de cantidad y calidad a los datos nucleares de núcleos ricos en neutrones. Los datos sobre el decaimiento radioactivo de núcleos emisores de neutrones retardados son de particular relevancia dado el importante papel que estos neutrones juegan en ambos campos. En 2003, la Organización Internacional de la Energía Atómica (OIEA) comenzó un Proyecto de Investigación Coordinado (CRP) para la *creación de una base de datos de referencia para evaluaciones de la emisión de neutrones retardados tras el decaimiento beta*. La base de datos, que está en proceso de publicación [168], incluye probabilidades de emisión de neutrones retardados para 309 núcleos, aproximadamente cien más que el Evaluated Nuclear Structure Data File (ENSDF) a día de hoy (a Julio, 2020) [7,8]. Sin embargo, queda un camino muy largo por recorrer para satisfacer los requerimientos de la ciencia y la tecnología nuclear actuales. La reciente evaluación teórica a gran escala de Marketin y col. [6] sobre 5409 núcleos ricos en neutrones predice que el 90 % de ellos emiten neutrones retardados tras el decaimiento beta.

El presente manuscrito aborda la medida de la probabilidad de emisión de neutrones retardados tras el decaimiento beta de ^{86}As y ^{91}Br realizada en el Laboratorio de Aceleradores del Departamento de Física de la Universidad de Jyväskylä (JYFL), Finlandia, en 2010. El experimento se llevó a cabo en el marco de una colaboración entre el Centro de Investigaciones Energéticas, Medioambientales y Tecnológicas (CIEMAT), el Instituto de Física Corpuscular (IFIC), la Universidad Politécnica de Cataluña (UPC) y la Universidad de Jyväskyä. Las cuatro instituciones tienen diversos pero también comunes intereses en el campo. En el CIEMAT, la Unidad de Innovación Nuclear —donde ha sido realizado este trabajo— mide datos nucleares para el desarrollo de sistemas avanzados de energía con énfasis en los ciclos cerrados de combustible y la transmutación de actínidos minoritarios extraídos de desechos nucleares. El interés principal tras este manuscrito es por tanto la tecnología nuclear.

Los programas actuales y futuros de energía nuclear aspiran a alcanzar un alto nivel de sostenibilidad, seguridad, competitividad y robustez [34]. La viabilidad de esos programas para alcanzar objetivos tan ambiciosos depende de la descripción precisa de la física subyacente en las simulaciones computacionales [35] dada la falta de experiencia prácti-

ca con sistemas avanzados de energía nuclear en comparación con los convencionales. Las simulaciones computacionales son inherentemente dependientes de modelos y datos experimentales. Mientras que la experiencia acumulada hasta hoy con códigos de simulación utilizados en el desarrollo de sistemas de energía nuclear es vasta, la precisión, incertidumbre y exhaustividad de los datos nucleares son insuficientes para el diseño fiable y económicamente efectivo de sistemas avanzados y la evaluación de su seguridad.

Es dentro de este contexto donde surgió la motivación para una medida precisa de la probabilidad de emisión de neutrones retardados tras el decaimiento beta de ^{86}As y ^{91}Br. La relevancia de estos núcleos en los desarrollos tecnológicos nucleares actuales fue ilustrada en el capítulo 2 con cálculos de neutrones retardados para dos conceptos europeos de reactores avanzados: el European Sodium-cooled Fast Reactor (ESFR) y la European Facility for Industrial Transmutation (EFIT). Estos sistemas difieren significativamente de los reactores nucleares convencionales en los inventarios de combustible y actínidos minoritarios, y ^{86}As y ^{91}Br están entre los contribuyentes más importantes a la emisión de neutrones de neutrones retardados de los actínidos. Las medidas precisas de la probabilidad de emisión de neutrones retardados de estos isótopos reportadas en este trabajo es parte de un gran esfuerzo por mejorar la precisión de los datos de decaimiento radioactivo de los isótopos más relevantes para la tecnología nuclear. En particular, estas medidas contribuyen a mejorar la calidad de los cálculos de suma de la emisión de neutrones retardados en sistemas avanzados de energía nuclear y sirven para restringir las distribuciones de productos de fisión, reduciendo así cualquier exceso de conservacionismo en el diseño y la operación de dichos sistemas. Esta es precisamente una de las conclusiones del CRP para la *creación de una base de datos de referencia para evaluaciones de la emisión de neutrones retardados tras el decaimiento beta* que se tendrá en cuenta en el CRP para la *actualización de las distribuciones de productos de fisión para aplicaciones* que recién comenzó en Junio de 2020 [171].

^{86}As y ^{91}Br decaen rápidamente con vidas medias de 945 ± 8 ms y 543 ± 4 ms respectivamente. Se requirió por tanto una instalación experimental capaz de producir haces de núcleos exóticos intensos y de alta pureza para investigar su decaimiento radioactivo. La instalación IGISOL en el Laboratorio de Aceleradores de JYFL cumple con estos requisitos combinando la técnica IGISOL con el sistema de trampas Penning JYFLTRAP situado tras un separador de masa. Con la técnica IGISOL se producen iones en un blanco delgado desde el cual escapan hacia un flujo de gas enrarecido que los termaliza y conduce para ser acelerados antes de someterlos a separación isotópica. El blanco delgado y el gas enrarecido aportan independencia química a la técnica y un tiempo de retraso corto. Pasado el separador de masa, los iones son empaquetados para su inyección efectiva en la JYFLTRAP donde ocurre la purificación.

A pesar de las técnicas de extracción rápida y purificación, los haces de núcleos exóticos en IGISOL son producidos con baja intensidad comparados con los haces de núcleos estables debido a la baja sección eficaz de producción. Sistemas de detección eficientes y selectivos se hacen por tanto necesarios para la medida precisa de las propiedades del decaimiento de núcleos exóticos. En consecuencia, se utilizaron en el experimento técnicas de detección complementarias para distintos tipos de radiación:

- el BEta deLayEd Neutron detector (BELEN) en su configuración 20b para el contaje

de neutrones;

- un detector de silicio de 0.5 mm de espesor para la detección de partículas beta; y
- un detector de High-Purity Germanium (HPGe) para monitorizar la pureza del haz.

BELEN20b consiste en 20 contadores de neutrones de ^{3}He cilíndricos incrustados en un bloque de polietileno de alta densidad molecular (HMWPE) de 90 cm × 90 cm × 80 cm. Los contadores están simétricamente distribuidos alrededor del eje C_4 más corto (el que une los centroides de las caras de 90 cm × 90 cm opuestas) en dos anillos concéntricos (8 en el interior y 12 en el exterior) para obtener una alta eficiencia de detección (47 % aproximadamente) lo más constante posible entre unos pocos keV y unos pocos MeV, que es el rango de energía de interés para estudios de la emisión de neutrones retardados tras el decaimiento beta. El haz se implantó sobre una cinta móvil en el centro de BELEN. Muy cerca por detrás de la cinta se situó el detector de silicio. La cinta y el detector quedaron en vacío dentro del tubo del haz cerrado por un tapón con un conector LEMO para la entrada del alto voltaje y la señal de salida. La figura 8.1 muestra los sistemas de implantación y detección. El detector HPGe se muestra en la figura 8.1(b) insertado desde la cara opuesta de BELEN por la que se insertó el tubo del haz en la misma cavidad.

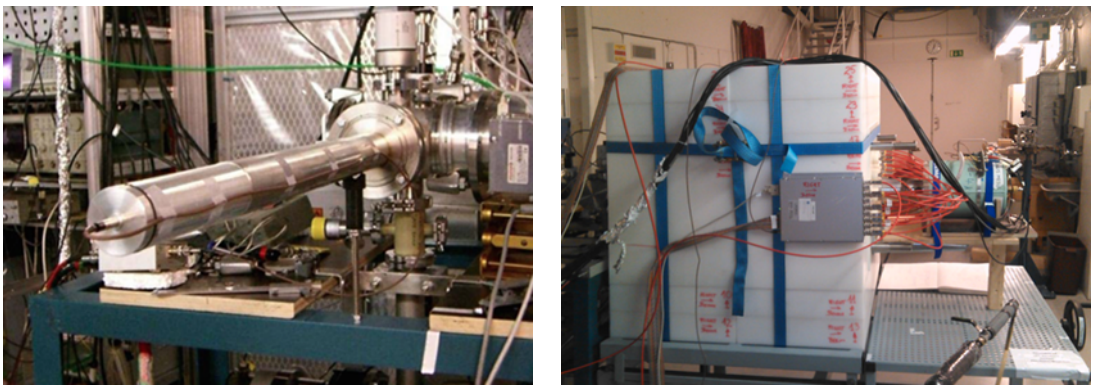

(a) Sistema de implantación **(b)** Sistema de detección

Figura 8.1: Sistemas de implantación y detección.

El sistema de detección se utilizó en modo triggerless (i.e., se registraron todas las señales que excedieran un umbral de amplitud dado) con un sistema de adquisición de datos (DACQ) diseñado específicamente para experimentos con BELEN [20]. El DACQ, basado mayormente en electrónica comercial, contó con flash ADCs de 100 MHz de frecuencia de muestreo y una resolución de 16 bits. Éstos generaron la información sobre el timestamp y la energía de la señal, introduciendo un tiempo muerto no-paralizable de apenas 17 µs.

Las medidas se realizaron en ciclos con una estructura optimizada para cada isótopo de acuerdo con su vida media. El fondo se midió durante aproximadamente 1.35 s al comienzo de cada ciclo. Luego se implantó el haz varias veces durante un período de aproximadamente tres vidas medias del precursor, tras el cual se detuvo la implantación y el ciclo de medición continuó durante aproximadamente siete vidas medias más. Al final de cada ciclo se retiró

la actividad remanente moviendo la cinta y se restableció a cero el timestamp scaler del DACQ para el próximo ciclo de medición que comenzó 2 s más tarde. El ciclo se repitió hasta obtener estadística suficiente con la limitación de un tiempo de haz limitado.

Este experimento fue el segundo de su tipo con BELEN en JYFL. Con el DACQ aún en prueba, no estuvo exento de problemas relacionados con la adquisición de datos. Se realizó por tanto un gran esfuerzo en la exploración, limpieza y preparación de los datos para el análisis. En este proceso se identificaron y corrigieron errores en el código de adquisición de datos, lo cual puede considerarse como la primera contribución relevante de este trabajo a medidas posteriores y futuras con BELEN.

Entre los métodos experimentales para medir la probabilidad de emisión de neutrones retardados tras el decaimiento beta, el más simple en concepto surge directamente de la definición de la magnitud en sí misa, i.e., la relación entre el número de decaimientos beta seguidos por la emisión de neutrones y el número total de decaimientos. Para emisores de un sólo neutrón, el número de neutrones emitidos determina el primero. De este modo, contando por separado neutrones y partículas betas emitidas por el precursor, la probabilidad de emisión de un neutrón puede obtenerse como:

$$P_n = \frac{\varepsilon_\beta}{\varepsilon_n} \frac{N_n}{N_\beta} \tag{8.1}$$

donde, para partículas beta y neutrones emitidos por el precursor, ε representa la eficiencia de detección y N el número de eventos detectados. El método $P_n\,{}^{A}_{Z}X$ aplicado en este trabajo hace uso de la ecuación anterior para caracterizar el sistema de detección en eficiencia con medidas con isótopos de P_n bien conocido. En concreto se utilizaron ^{88}Br, ^{94,95}Rb y ^{137}I, los cuales son considerados como referencia para la medida y evaluación de datos nucleares [11]. La misma expresión se utilizó posteriormente para determinar el valor de P_n de ^{86}As y ^{91}Br.

Las medidas de la probabilidad de emisión de neutrones retardados tras el decaimiento beta basadas en el contaje de partículas betas y neutrones se enfrentan con un reto importante: requieren la separación de la actividad del precursor de la actividad del resto de la cadena de desintegración, el ruido electrónico y el fondo ambiental. Esto se consiguió en este trabajo ajustando un modelo a las distribuciones temporales de eventos de partículas betas y neutrones detectados. El modelo está basado en un método algebraico novedoso de resolución de las ecuaciones de Bateman. Es analítico y puede aplicarse a cualquier cadena de desintegración independientemente de su complejidad. Muchos parámetros de distinta naturaleza entran en el modelo (eficiencias promedio de detección para cada isótopo de la cadena, vidas medias, número de iones implantados en cada implantación, etc.), y muchos de ellos no son identificables desde el punto de vista estructural. El modelo fue por tanto reducido con reparametrizaciones convenientes e información previa disponible sobre el experimento, procesos físicos subyacentes y parámetros. Esto condujo a dos variantes del modelo: la *general* y la *equivalente*. La segunda, con menos parámetros, se aplica a medidas donde la vida media del precursor es mucho mayor que el tiempo entre implantaciones sucesivas, y el número de implantaciones dentro del intervalo de implantación-decaimiento del ciclo de medición se hace demasiado grande para la aplicación eficiente de la variante

general. La figura 8.2 muestra la distribución temporal de eventos de partículas beta detectadas en las medidas con haces de ^{91}Br y ^{86}As ilustrando la aplicación de los modelos general y equivalente de la evolución de las tasas de contaje. La identificabilidad estructural de estos modelos se analizó en detalle en el apéndice D. Como resultado, ambos modelos se pudieron reducir aún más para mejorar su identificabilidad y evitar la aproximación frecuente de que la eficiencia beta se considera la misma para todos los elementos de la cadena de desintegración.

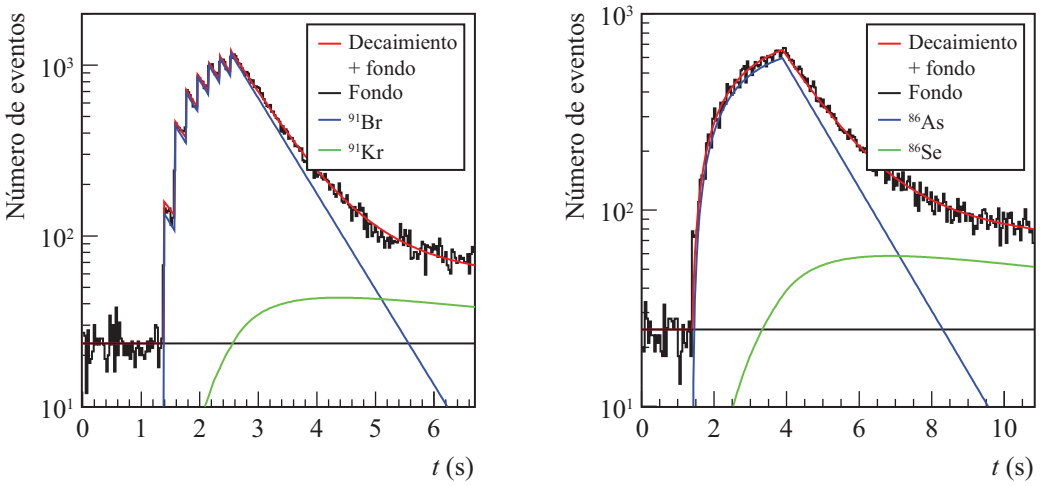

(a) General model **(b)** Equivalent model

Figura 8.2: Distribución temporal de eventos de partículas beta detectadas en las medidas con haces de ^{91}Br y ^{86}As ilustrando la aplicación de las variantes general y equivalente del modelo de la evolución de las tasas de contaje.

La principal fortaleza de este trabajo consiste en la aplicación de la Estimación Bayesiana (EB), un marco avanzado de inferencia estadística que permitió la propagación completa de las incertidumbres. La EB se basa en el teorema de Bayes para construir la PDF posterior de los parámetros del modelo a partir del likelihood y una PDF previa propuesta que representa el nivel de credibilidad de la PDF posterior sobre los parámetros antes de la observación de los datos. Otras ventajas de la aplicación de la EB fueron la manera natural y fundamentada que ofreció para imponer ligaduras externas para mejorar la identificabilidad del modelo, y la posibilidad de trabajar con datos independientes en lugar de datos agregados (histogramas), lo cual eliminó la incertidumbre sistemática por la pérdida de información que resulta siempre de la agregación. Los estimados centrales de los parámetros reportados en este trabajo son estimados Maximum A Posteriori (MAP) obtenidos de la búsqueda del máximo de la PDF posterior por todo el espacio de parámetros restringido. Todos fueron obtenidos a partir de la PDF posterior de los parámetros de los modelos de la evolución de las tasas de contaje de partículas beta y neutrones. Son por tanto el conjunto de parámetros que describe mejor las dos distribuciones simultáneamente dada la

información previa disponible sobre el experimento, los procesos físicos subyacentes y los parámetros.

Las simulaciones Monte Carlo del sistema de detección presentadas en el capítulo 4 mostraron la razón por la cual la aplicación del método $P_n\,{}^{A}_{Z}X$ puede verse seriamente afectada por incertidumbres sistemáticas si se ignora la dependencia de las eficiencias de detección con el espectro de la radiación emitida, una aproximación sobre la que el método se basa al adoptar para los isótopos de interés el mismo valor de $\delta = \varepsilon_\beta/\varepsilon_n$ obtenido de medidas con isótopos de referencia. Este trabajo hace uso de simulaciones Monte Carlo del detector de silicio para propagar la incertidumbre debida a la falta de conocimiento de la distribución de intensidad beta en el canal de emisión de neutrones. Es esta última la responsable de las transiciones energéticas más bajas, para las cuales la eficiencia del detector de silicio es más baja debido al efecto del umbral de detección. En este trabajo también se utilizaron simulaciones Monte Carlo de BELEN20b para corregir los resultados por el efecto del espectro de emisión de neutrones sobre la eficiencia de detección.

Otra contribución relevante de este trabajo consiste en la mejora del modelo de alta precisión para neutrones del código Monte Carlo de transporte de radiación GEANT4 (apéndice B), el cual tuvo un gran impacto en la simulación de BELEN20b y configuraciones más recientes del detector y redujo la incertidumbre de modelo en el cálculo de la eficiencia de detección de neutrones. Versiones previas del código sobrestimaban la sección eficaz de dispersión térmica y muestreaban mal el estado final del neutrón. En consecuencia, GEANT4 sobrestimaba la eficiencia de detección de neutrones de BELEN20b en un 7 % con respecto a MCNPX, una herramienta estándar y bien validada para la simulación de las interacciones de neutrones. La mejora de GEANT4 y su verificación exhaustiva contra MCNPX se presentaron y discutieron en la reunión del GEANT4 Hadronic Working Group Meeting del 17 de abril de 2013 [172]. Las correcciones fueron aceptadas e incorporadas en la versión GEANT4.10.0. Gracias a esta contribución, la fiabilidad de GEANT4 para simular interacciones de neutrones de bajas energías pudo ser validada contra una medida con una fuente estándar de ^{252}Cf [20].

Las simulaciones Monte Carlo se introdujeron en la aplicación del método $P_n\,{}^{A}_{Z}X$ a través de la relación $\kappa = \delta_{\mathrm{sim}}/\delta_{\mathrm{exp}}$, la cual representa cuán sesgados están los valores Monte Carlo de las eficiencias de detección debido a varios factores: modelado geométrico, composición y densidad de materiales, temperatura ambiente, perfil y posición del haz, modelos (ley de dispersión térmica de neutrones, dispersión múltiple de neutrones, etc.) y datos nucleares, etc. La media pesada de κ obtenida de las medidas con isótopos de referencia se utilizó como ligadura para estimar la probabilidad de emisión de neutrones retardados de los isótopos de interés, i.e., cualquiera sea el valor de P_n de un isótopo, debe producir el mismo valor de κ. A diferencia de δ, κ es independiente del isótopo siempre y cuando el espectro de emisión de neutrones y la distribución de la intensidad beta sean bien conocidos, porque el efecto de estos en las eficiencias de detección de neutrones y partículas beta respectivamente está presente tanto en δ_{sim} como en δ_{exp}. Esto quedó confirmado por la baja dispersión de los valores de κ obtenidos para los isótopos de referencia.

Un punto clave en la determinación de κ fue la estimación Monte Carlo de la eficiencia de detección de partículas beta. Si bien la distribución de intensidad beta en el canal $\beta\gamma$ está dada en ENSDF para todos los isótopos implantados excepto para el ^{91}Br, la distribución

en el canal βn sólo está dada para el ^{137}I. Para sortear este obstáculo, se consideró incierta la eficiencia de detección $\varepsilon^{\beta n}_{\mathrm{sim}}$ en el canal βn dentro del intervalo $[\varepsilon^{\beta n}_{\mathrm{exp}}, \varepsilon^{\beta n}_{\mathrm{max}}]$. $\varepsilon^{\beta n}_{\mathrm{max}}$ es un estimado superior de $\varepsilon^{\beta n}_{\mathrm{sim}}$ que resulta de simulaciones con la distribución de intensidad beta que reproduce el espectro de neutrones considerando que la emisión de neutrones puebla el estado fundamental del núcleo hijo. $\varepsilon^{\beta n}_{\mathrm{exp}}$, por otro lado, es la eficiencia beta en el canal βn obtenida del Multiple Time Interval Analysis (MTIA) entre eventos de partículas beta y neutrones detectados. Comparando $\varepsilon^{\beta}_{\mathrm{sim}}$ con $\varepsilon^{\beta}_{\mathrm{exp}}$ para ^{137}I permitió adoptar $\varepsilon^{\beta n}_{\mathrm{exp}}$ como un estimado inferior de $\varepsilon^{\beta}_{\mathrm{sim}}$ en todos los casos, porque la emisión de neutrones de ^{137}I puebla siempre el estado fundamental de ^{136}Xe. En consecuencia, $\varepsilon^{\beta n}_{\mathrm{sim}}$ coincide con $\varepsilon^{\beta n}_{\mathrm{max}}$ para ^{137}I, i.e., la eficiencia beta total para ^{137}I está libre de aproximaciones de la distribución de intensidad beta.

Los nuevos valores de la probabilidad de emisión de neutrones retardados de ^{86}As y ^{91}Br obtenidos en este trabajo resuelven las grandes discrepancias entre las medidas y evaluaciones previas. Son más del 50 % más precisas que la más precisa de las medidas previas, gracias al uso de técnicas experimentales avanzadas y al gran esfuerzo en la preparación y el modelado de los datos experimentales y en la reducción de incertidumbres sistemáticas.

Para ^{86}As se obtuvo P_n $=34.6 \pm 0.9\,\%$ (2.7 %). Un valor similar con una incertidumbre ligeramente menor $35.5 \pm 0.6\,\%$ (1.7 %) se adoptó en la preparación de ENDF/B-VIII.0 y se incorporó en ENSDF (a Julio de 2020). Ese es un resultado preliminar de este trabajo reportado en [167] que no fue objeto de una propagación de incertidumbres tan exhaustiva. En consecuencia, el resultado obtenido en este trabajo es muy similar al anterior con una incertidumbre ligeramente mayor. ENDF/B y ENSDF deberían adoptar el nuevo valor.

En el caso de ^{91}Br, el valor de P_n obtenido fue $29{,}3^{+1,1}_{-0,8}$ %. Varias medidas anteriores de la probabilidad de emisión de neutrones retardados de ^{91}Br son estadísticamente compatibles con este resultado, aunque no tan precisas. Es posible que hayan estado afectadas por la difusión de los isótopos de Kriptón, un proceso identificado como la causa de la pérdida de actividad cuando elementos nobles están presentes en la cadena de desintegración. Este efecto, también observado en la medida de ^{137}I, puede constituir una fuente importante de incertidumbre sistemática si se ignora. Los modelos para la evolución de las tasas de contaje de partículas beta y neutrones construidos en este trabajo tuvieron en cuenta el efecto de la difusión mediante una reducción constante de la eficiencia beta a lo largo del ciclo de medición.

Los valores de P_n de ^{91}Br en ENDF/B-VII.1, JEFF-3.3 y JENDL-4.0 son muy similares al valor $19.5 \pm 2.6\,\%$ en ENSDF actualmente (a Julio de 2020). Esos valores fueron obtenidos a partir de medidas previas que son estadísticamente incompatibles con el resultado de este trabajo. La evaluación más reciente de probabilidades de emisión de neutrones retardados realizada por Liang y col. [168] considera medidas más recientes que aproximan su promedio al valor aquí obtenido. Sin embargo, el valor reportado en Liang y col. [168] debe interpretarse con cautela, pues incluye el resultado preliminar de este trabajo reportado en [167]. El valor para ^{86}As en particular, ya que sólo una medida se utilizó para obtenerlo. Los nuevos valores obtenidos en este trabajo serán incluidos próximamente en la evaluación

de Liang y col. [168].

En resumen, las principales contribuciones de este trabajo son, en orden de aparición:

1. Realización de cálculos de suma para ilustrar el papel que juegan ^{86}As y ^{91}Br en los cálculos de neutrones retardados de dos conceptos europeos de reactores avanzados: el European Sodium-cooled Fast Reactor (ESFR) y la European Facility for Industrial Transmutation (EFIT).

2. Realización de un experimento de decaimiento radioactivo con el BEta deLayEd Neutron detector (BELEN)20b y técnicas complementarias de detección en el Laboratorio de Aceleradores de la Universidad de Jyväskylä, Finlandia, para medir la probabilidad de emisión de neutrones retardados de ^{86}As y ^{91}Br.

3. Mejora y verificación del modelo de transporte de neutrones térmicos en GEANT4.

4. Exploración exhaustiva de los datos adquiridos en el experimento que reveló errores en el software del sistema de adquisición.

5. Desarrollo de un modelo algebraico general para la evolución de las tasas de contajes basado en las ecuaciones de Bateman, aplicable a cadenas radioactivas con ramificación sin complejidad adicional.

6. Estimación de la probabilidad de emisión de neutrones retardados del ^{86}As y ^{91}Br aplicando inferencia bayesiana y técnicas avanzadas de modelación que permitieron una completa propagación de incertidumbres y condujeron a resultados de alta precisión. Estos resultados serán incluidos en la evaluación de Liang y col. [168] resultante del Proyecto de Investigación Coordinado (CRP) para la *creación de una base de datos de referencia para evaluaciones de la emisión de neutrones retardados tras el decaimiento beta* que comenzó la Organización Internacional de la Energía Atómica (OIEA) en el 2013.

Bibliography

[1] ROBERTS, R B; MEYER, R C & WANG, P. Further observations on the splitting of uranium and thorium. *Physical Review*. 1939, vol. 55, no. 5, pp. 510–511. ISSN 0031-899X. Available from DOI: 10.1103/PhysRev.55.510.2.

[2] MEITNER, L; HAHN, O & STRASSMANN, F. Über die Umwandlungsreihen des Urans, die durch Neutronenbestrahlung erzeugt werden. *Zeitschrift für Physik*. 1937, vol. 106, no. 3–4, pp. 249–270. ISSN 0044-3328. Available from DOI: 10.1007/BF01340321.

[3] ROBERTS, R B; HAFSTAD, L R; MEYER, R C, et al. The delayed neutron emission which accompanies fission of uranium and thorium. *Physical Review*. 1939, vol. 55, no. 7, pp. 664. ISSN 0031-899X. Available from DOI: 10.1103/PhysRev.55.664.

[4] PAPPAS, A C & SVERDRUP, T. Gross properties of delayed neutron emission and β-strength functions. *Nuclear Physics A*. 1972, vol. 188, no. 1, pp. 48–64. ISSN 0375-9474. Available from DOI: 10.1016/0375-9474(72)90179-0.

[5] VALENCIA, E; TAIN, J L; ALGORA, A, et al. Total absorption γ-ray spectroscopy of the β-delayed neutron emitters ^{87}Br, ^{88}Br and ^{94}Rb. *Physical Review C*. 2017, vol. 95, no. 2, pp. 024320. ISSN 2469-9993. Available from DOI: 10.1103/PhysRevC.95.024320.

[6] MARKETIN, T; HUTHER, L & MARTÍNEZ-PINEDO, G. Large-scale evaluation of β-decay rates of r-process nuclei with the inclusion of first-forbidden transitions. *Physical Review C*. 2016, vol. 93, no. 2, pp. 025805. ISSN 2469-9993. Available from DOI: 10.1103/PhysRevC.93.025805.

[7] *Evaluated Nuclear Structure Data File (ENSDF)* [online]. USA [visited on 2020-07-01]. Available from: http://www.nndc.bnl.gov/ensdf.

[8] TULI, J K. Evaluated Nuclear Structure Data File. *Nuclear Instruments and Methods in Physics Research A*. 1996, vol. 369, no. 2–3, pp. 506–510. ISSN 0168-9002. Available from DOI: 10.1016/S0168-9002(96)80040-4.

[9] DAS, S. The importance of delayed neutrons in nuclear research – A review. *Progress in Nuclear Energy*. 1994, vol. 28, no. 3, pp. 209–264. ISSN 0149-1970. Available from DOI: 10.1016/0149-1970(94)90001-9.

[10] RUDSTAM, G; FINCK, Ph; FILIP, A, et al. *Delayed neutron data for the major actinides*. 2002. Available also from: https://www.oecd-nea.org/science/wpec. Report NEA/WPEC-6. NEA. OECD.

[11] ABRIOLA, D; SINGH, B & DILLMANN, I. *Summary report of consultants'meeting on beta-delayed neutron emission evaluation*. Viena, Austria, 2011. Available also from: http://www-nds.iaea.org/publications/indc/indc-nds-0599.pdf. Report INDC(NDS)-0599. International Atomic Energy Agency (IAEA).

[12] BARAN, W & KENNETH, M. Effect of delayed neutrons on the stability of a nuclear power reactor. *Nuclear Science and Engineering*. 1966, vol. 24, no. 4, pp. 356–361. ISSN 0029-5639. Available from DOI: 10.13182/NSE66-A16405.

[13] REUSS, P. *Neutron physics*. Vancouver, Canada: EDP Sciences, 2008. ISBN 978275-9800414.

[14] ALGORA, A & TAIN, J L. Decay heat and nuclear data. In: MESQUITA, A Z (ed.). *Nuclear reactors*. Rijeka, Croatia: IntechOpen, 2012, chap. 5. Available from DOI: 10.5772/34622.

[15] ARNOULD, M; GORIELY, S & TAKAHASHI, K. The r-process of stellar nucleosynthesis: Astrophysics and nuclear physics achievements and mysteries. *Physics Reports*. 2007, vol. 450, no. 4–6, pp. 97–213. ISSN 0370-1573. Available from DOI: 10.1016/j.physrep.2007.06.002.

[16] LODDERS, K. Solar system abundances and condensation temperatures of the elements. *The Astrophysical Journal*. 2003, vol. 591, pp. 1210–1247. Available from DOI: 10.1086/375492.

[17] RUDSTAM, G; ALEKLETT, K & SIHVER, L. Delayed-neutron branching ratios of precursors in the fission product region. *Atomic Data and Nuclear Data Tables*. 1993, vol. 53, no. 1, pp. 1–22. ISSN 0092-640X. Available from DOI: 10.1006/adnd.1993.1001.

[18] REEDER, P L; WARNER, R A; EDMISTON, M D, et al. New delayed-neutron precursors from TRISTAN. In: MEYER, R A & BRENNER, S (eds.). *Nuclei off the line of stability*. Massachusetts, USA: American Chemical Society, 1986, vol. 324, chap. 25, pp. 171–176. ACS Symposium Series. ISBN 9780841210059. Available from DOI: 10.1021/bk-1986-0324.ch025.

[19] REEDER, P L; WARNER, R A; GILL, R L, et al. P_n measurements at TRISTAN by a beta-n coincidence technique. In: *Specialist' Meeting on Delayed Neutron Properties*. University of Birmingham, Birmingham, England, 1986.

[20] AGRAMUNT, J; TAIN, J L; GÓMEZ-HORNILLOS, M B, et al. Characterization of a neutron–beta counting system with beta-delayed neutron emitters. *Nuclear Instruments and Methods in Physics Research A*. 2016, vol. 807, pp. 69–78. ISSN 0168-9002. Available from DOI: 10.1016/j.nima.2015.10.082.

[21] KRATZ, J V; FRANZ, H & HERRMANN, G. Delayed-neutrons from arsenic isotopes ^{84}As, ^{85}As and ^{86}As. *Journal of Inorganic and Nuclear Chemistry*. 1973, vol. 35, no. 5, pp. 1407–1417. ISSN 0022-1902. Available from DOI: 10.1016/0022-1902(73)80226-X.

[22] CRANÇON, J; RISTORI, C; OHM, H, et al. Half-lives and P_n values of delayed-neutron precursors in the mass chains 85-87, 92, 135, 136 and 145. *Zeitschrift für Physik A*. 1978, vol. 287, no. 1, pp. 45–50. ISSN 0939-7922. Available from DOI: 10.1007/BF01408359.

[23] ASGHAR, M; GAUTHERON, J P; BAILLEUL, G, et al. The P_n values of the ^{235}U(n_{th},f) produced precursors in the mass chains 90, 91, 93-95, 99, 134 and 137-139. *Nuclear Physics A*. 1975, vol. 247, no. 2, pp. 359–376. ISSN 0375-9474. Available from DOI: 10.1016/0375-9474(75)90642-9.

[24] WAHL, A C. Nuclear-charge distribution and delayed-neutron yields for thermal-neutron-induced fission of ^{235}U, ^{233}U, and ^{239}Pu and for spontaneous fission of ^{252}Cf. *Atomic Data and Nuclear Data Tables*. 1988, vol. 39, no. 1, pp. 1–156. ISSN 0092-640X. Available from DOI: 10.1016/0092-640X(88)90016-2.

[25] KRATZ, K L & HERRMANN, G. Delayed-neutron emission from short-lived Br and I isotopes. *Nuclear Physics A*. 1974, vol. 229, no. 1, pp. 179–188. ISSN 0375-9474. Available from DOI: 10.1016/0375-9474(74)90684-8.

[26] ALEKLETT, K; HOFF, P; LUND, E, et al. Delayed neutron emission probabilities of the precursors ^{89,90,91}Br and ^{139,140,141}I. *Zeitschrift für Physik A*. 1980, vol. 295, no. 4, pp. 331–332. ISSN 0939-7922. Available from DOI: 10.1007/BF01412944.

[27] LUND, E; HOFF, P; ALEKLETT, K, et al. Delayed neutron emission probabilities of gallium, bromine, rubidium, indium, antimony, iodine, and cesium precursors. *Zeitschrift für Physik A*. 1980, vol. 294, no. 3, pp. 233–240. ISSN 0939-7922. Available from DOI: 10.1007/BF01438160.

[28] EWAN, G T; HOFF, P; JONSON, B, et al. Intense mass-separated beams of halogens and beta-delayed neutron emission from heavy bromine isotopes. *Zeitschrift für Physik A*. 1984, vol. 318, no. 3, pp. 309–314. ISSN 0939-7922. Available from DOI: 10.1007/BF01418088.

[29] KRATZ, K L; GABELMANN, H; PFEIFFER, B, et al. Onset of deformation in neutron-rich krypton isotopes. *Zeitschrift für Physik A*. 1988, vol. 330, no. 2, pp. 229–230. ISSN 0939-7922. Available from DOI: 10.1007/BF01293403.

[30] *Research Center for Energy, Environment and Technology. Nuclear Innovation Unit* [online] [visited on 2020-07-01]. Available from: http://win.ciemat.es/inweb.

[31] AZUMA, R E; CARRAZ, L C; HANSEN, P G, et al. First observation of beta-delayed two-neutron radioactivity: ^{11}Li. *Physical Review Letters*. 1979, vol. 43, no. 22, pp. 1652–1654. ISSN 1079-7114. Available from DOI: 10.1103/PhysRevLett.43.1652.

[32] HANSEN, P G & JONSON, B. *Beta-delayed particle emission from neutron-rich nuclei*. 1987. Available also from: https://cds.cern.ch/record/175600. Report CERN-EP-87-44. CERN.

[33] KAWANO, T; MÖLLER, P & WILSON, W B. Calculation of delayed-neutron energy spectra in a quasiparticle random-phase approximation–Hauser-Feshbach model. *Physical Review C*. 2008, vol. 78, no. 5, pp. 54601. ISSN 2469-9993. Available from DOI: 10.1103/PhysRevC.78.054601.

[34] *A technology roadmap for Generation IV nuclear energy systems*. 2002. Available also from: http://www.gen-4.org/PDFs/GenIVRoadmap.pdf. Report GIF-002-00. U.S. DOE Nuclear Energy Research Advisory Committee and the Generation IV International Forum.

[35] KONING, A J; BLOMGREN, J; JACQMIN, R, et al. *Nuclear data for sustainable nuclear energy*. 2009. ISSN 1018-5593. Available from DOI: 10.2787/14636. Report EUR 23977 EN - 2009. EC. JRC. IRMM.

[36] KEEPIN, G R & WEINBERG, A M. Physics of Nuclear Kinetics. *Physics Today*. 1967, vol. 20, no. 3, pp. 106–107. ISSN 0031-9228. Available from DOI: 10.1063/1.3034187.

[37] *Cross Section Evaluation Working Group (CSEWG)* [online] [visited on 2020-07-01]. Available from: http://www.nndc.bnl.gov/csewg.

[38] BROWN, D A; CHADWICK, M B; CAPOTE, R, et al. ENDF/B-VIII.0: The 8th Major Release of the Nuclear Reaction Data Library with CIELO-project Cross Sections, New Standards and Thermal Scattering Data. *Nuclear Data Sheets*. 2018, vol. 148, pp. 1–142. ISSN 0090-3752. Available from DOI: 10.1016/j.nds.2018.02.001.

[39] *Evaluated Nuclear Data File (ENDF)/B-VIII.0* [online]. USA [visited on 2020-07-01]. Available from: https://www.nndc.bnl.gov/endf/b8.0.

[40] *Nuclear Energy Agency Data Bank* [online] [visited on 2020-07-01]. Available from: https://www.oecd-nea.org/databank.

[41] *Joint Evaluated Fission and Fusion file (JEFF)-3.3* [online]. France [visited on 2020-07-01]. Available from: https://www.oecd-nea.org/dbdata/JEFF33.

[42] SHIBATA, K; IWAMOTO, O; NAKAGAWA, T, et al. JENDL-4.0: A new library for nuclear science and engineering. *Journal of Nuclear Science and Technology*. 2011, vol. 48, no. 1, pp. 1–30. Available from DOI: 10.1080/18811248.2011.9711675.

[43] *Japanese Evaluated Nuclear Data Library (JENDL)-4.0* [online]. Japan [visited on 2020-07-01]. Available from: https://wwwndc.jaea.go.jp/jendl/j40/j40.html.

[44] CACUCI, D G (ed.). *Handbook of nuclear engineering Vol. 1: Nuclear engineering fundamentals*. Springer, 2010. ISBN 9780387981307.

[45] CHADWICK, M B; HERMAN, M; OBLOŽINSKÝ, P, et al. ENDF/B-VII.1 Nuclear data for science and technology: Cross sections, covariances, fission product yields and decay data. *Nuclear Data Sheets*. 2011, vol. 112, no. 12, pp. 2887–2996. ISSN 0090-3752. Available from DOI: 10.1016/j.nds.2011.11.002.

[46] *Japanese Evaluated Nuclear Data Library (JENDL) FP Fission Yields Data File 2011 (JENDL/FPY-2011)* [online]. Japan [visited on 2020-07-01]. Available from: https://wwwndc.jaea.go.jp/ftpnd/jendl/jendl-fpy-2011.html.

[47] *Japanese Evaluated Nuclear Data Library (JENDL) Decay Data File 2015 (Japanese Evaluated Nuclear Data Library (JENDL)/DDF-2015)* [online]. Japan [visited on 2020-07-01]. Available from: https://wwwndc.jaea.go.jp/ftpnd/jendl/jendl-ddf-2015.html.

[48] KATAKURA, J & MINATO, F. *JENDL FP Decay Data File 2015*. 2016. Available from DOI: 10.11484/jaea-data-code-2015-030. Report JAEA-Data/Code 2015-030. JAEA.

[49] ENGLAND, T R & RIDER, B F. *Evaluation and compilation of fission product yields*. USA, 1993. Available also from: https://t2.lanl.gov/nis/publications/endf349.pdf. Report LA-UR-94-3106. LANL.

[50] KONING, A J; ROCHMAN, D; SUBLET, J C, et al. TENDL: Complete nuclear data library for innovative nuclear science and technology. *Nuclear Data Sheets*. 2019, vol. 155, pp. 1–55. ISSN 0090-3752. Available from DOI: https://doi.org/10.1016/j.nds.2019.01.002.

[51] KATAKURA, J. Development of JENDL decay and fission yield data libraries. *Nuclear Data Sheets*. 2014, vol. 118, pp. 104–107. ISSN 0090-3752. Available from DOI: 10.1016/j.nds.2014.04.011.

[52] KATAKURA, J. *JENDL FP Decay Data File 2011 and Fission Yields Data File 2011*. 2012. Available from DOI: doi.org/10.11484/jaea-data-code-2011-025. Report JAEA-Data/Code 2011-025. JAEA.

[53] AUDI, G; BERSILLON, O; BLACHOT, J, et al. The NUBASE evaluation of nuclear and decay properties. *Nuclear Physics A*. 2003, vol. 729, no. 1, pp. 3–128. ISSN 0375-9474. Available from DOI: 10.1016/j.nuclphysa.2003.11.001.

[54] AUDI, G; KONDEV, F G; WANG, M, et al. The Nubase2012 evaluation of nuclear properties. *Chinese Physics C*. 2012, vol. 36, no. 12, pp. 1157. ISSN 1674-1137.

[55] PFEIFFER, B; KRATZ, K L & MÖLLER, P. Status of delayed-neutron precursor data: half-lives and neutron emission probabilities. *Progress in Nuclear Energy*. 2002, vol. 41, no. 1–4, pp. 39–69. ISSN 0149-1970. Available from DOI: 10.1016/S0149-1970(02)00005-7.

[56] KELLETT, M A; BERSILLON, O & MILLS, R W. *The JEFF-3.1/-3.1.1 radioactive decay data and fission yields sub-libraries*. ISBN 978-92-64-99087-6. Available also from: https://www.oecd-nea.org/dbdata/nds_jefreports/jefreport-20/nea6287-jeff-20.pdf. JEFF report 20. Nuclear Energy Agency.

[57] KRATZ, K L & HERRMANN, G. Systematics of neutron emission probabilities from delayed neutron precursors. *Zeitschrift für Physik*. 1973, vol. 263, no. 5, pp. 435–442. ISSN 0044-3328. Available from DOI: 10.1007/BF01391992.

[58] GUDKOV, A N; KRIVASHEYEV, S V; KOLDOBSKI, A B, et al. Yields of Delayed Neutron Precursors in the Fission of Actinides. *Radiochimica Acta*. 1992, vol. 57, no. 2–3, pp. 69. ISSN 0033-8230. Available from DOI: 10.1524/ract.1992.57.23.69.

[59] SPRIGGS, G D; CAMPBELL, J M & PIKSAIKIN, V M. An 8-group delayed neutron model based on a consistent set of half-lives. *Progress in Nuclear Energy*. 2002, vol. 41, no. 1–4, pp. 223–251. ISSN 0149-1970. Available from DOI: 10.1016/S0149-1970(02)00013-6.

[60] CHADWICK, M B; OBLOŽINSKÝ, P; HERMAN, M, et al. ENDF/B-VII.0: Next generation evaluated nuclear data library for nuclear science and technology. *Nuclear Data Sheets*. 2006, vol. 107, no. 12, pp. 2931–3060. ISSN 0090-3752. Available from DOI: 10.1016/j.nds.2006.11.001.

[61] PIKSAIKIN, V M; EGOROV, A S; GREMYACHKIN, D E, et al. *New aggregate data in the IAEA reference database for beta-delayed neutron emission*. Viena, Austria, 2019. Available also from: https://www-nds.iaea.org/publications/indc/indc-nds-0784.pdf. Report INDC(NDS)-0784. International Atomic Energy Agency (IAEA).

[62] *Reference database for beta-delayed neutron emission* [online]. Viena, Austria [visited on 2020-07-01]. Available from: https://www-nds.iaea.org/beta-delayed-neutron/database.html.

[63] Actinide and fission product Partitioning and Transmutation. In: 13*th Information Exchange Meeting*. Seoul, Republic of Korea, 2014.

[64] *The Sustainable Nuclear Energy Technology Platform* [online] [visited on 2020-07-01]. Available from: https://snetp.eu.

[65] *Collaborative Project on European Sodium Fast Reactor (CP-ESFR)* [online] [visited on 2020-07-01]. Available from: https://cordis.europa.eu/project/id/232658.

[66] *Accelerator-Driven System and Fast Reactors (FR) in advanced nuclear fuel cycles: A comparative study*. OECD Publishing, 2002. Nuclear Development. ISBN 9264184821.

[67] *Implications of Partitioning and Transmutation in radioactive waste management*. Vienna, Austria: IAEA, 2004. Technical Reports Series, no. 435. ISBN 9201151047.

[68] *Advanced nuclear fuel cycles and radioactive waste management*. OECD Publishing, 2006. Nuclear Development. ISBN 9264024859. Available from DOI: https://doi.org/10.1787/9789264024861-en.

[69] RINEISKI, A; VEZZONI, B; ZHANG, D, et al. *ESFR core optimization and uncertainty studies*. IAEA, 2015. ISBN 9789201041142. ISSN 0074-1884.

[70] OCHOA, R; VÁZQUEZ, M; ÁLVAREZ-VELARDE, F, et al. A comparative study of Monte Carlo-coupled depletion codes applied to a sodium fast reactor design loaded with minor actinides. *Annals of Nuclear Energy*. 2013, vol. 57, no. 0, pp. 32–40. ISSN 0306-4549. Available from DOI: 10.1016/j.anucene.2013.01.039.

[71] DARNOWSKI, P & UZUNOW, N. Minor actinides impact on basic safety parameters of medium-sized sodium-cooled fast reactor. *Nukleonika*. 2015, vol. 60, no. 1, pp. 171–179. ISSN 1508-5791. Available from DOI: 10.1515/nuka-2015-0034.

[72] PETROVICH, C. *EFIT – Power deposition distribution and neutron source calculations by means of MCNPX*. 2007. Available from DOI: 10.13140/RG.2.2.34891.18723. Report FPN-P9EH-006. ENEA. Centro Ricerche Bologna.

[73] RADIATION SHIELDING INFORMATION CENTER. OAK RIDGE NATIONAL LABORATORY. *ORIGEN-2.2: Isotope generation and depletion code matrix exponential method*. 2002. Version 2.2. Available also from: http://www.oecd-nea.org/tools/abstract/detail/ccc-0371.

[74] ÁLVAREZ-VELARDE, F; LEÓN, P T & GONZÁLEZ-ROMERO, E. 9*th Information Exchange Meeting on Actinide and Fission Product P&T*. EVOLCODE2, a combined neutronics and burn-up evolution simulation code. OECD Publishing, 2006. Nuclear Development; Nuclear Science. ISBN 9789264990302.

[75] ANDREA, B; GIOVANNI, C; LUIGI, M, et al. EFIT: The European facility for industrial transmutation of minor actinides. In: 8*th International Topical Meeting on Nuclear Applications and Utilization of Accelerators (ACCAPP'07)*. Pocatello, Idaho, USA, 2007.

[76] ZWERMANN, W; KRZYKACZ-HAUSMANN, B; GALLNER, L, et al. Aleatoric and epistemic uncertainties in sampling based nuclear data uncertainty and sensitivity analyses. In: *International Conference on the Physics of Reactors 2012 (PHYSOR 2012)*. Knoxville, Tennessee, USA: American Nuclear Society (ANS), 2012, vol. 1, pp. 2816–2827. ISBN 9781622763894.

[77] JULIN, R & DENDOOVEN, P. The JYFL Accelerator Laboratory in Jyväskylä. *Nuclear Physics News*. 2000, vol. 10, no. 3, pp. 4–10. ISSN 1061-9127. Available from DOI: 10.1080/10506890009411534.

[78] PENTTILÄ, H. The layout of the IGISOL3 facility. *Hyperfine Interactions*. 2014, vol. 223, no. 1, pp. 5–16. ISSN 1572-9540. Available from DOI: 10.1007/s10751-012-0607-6.

[79] JOKINEN, A; ERONEN, T; HAGER, U, et al. Precision experiments on exotic nuclei at IGISOL. *International Journal of Mass Spectrometry*. 2006, vol. 251, no. 2–3, pp. 204–211. ISSN 1387-3806. Available from DOI: 10.1016/j.ijms.2006.01.043.

[80] KOLHINEN, V S; KOPECKY, S; ERONEN, T, et al. JYFLTRAP: a cylindrical Penning trap for isobaric beam purification at IGISOL. *Nuclear Instruments and Methods in Physics Research A*. 2004, vol. 528, no. 3, pp. 776–787. ISSN 0168-9002. Available from DOI: 10.1016/j.nima.2004.05.029.

[81] ÄRJE, J; ÄYSTÖ, J; HYVÖNEN, H, et al. The ion guide isotope separator on-line, IGISOL. *Nuclear Instruments and Methods in Physics Research A*. 1986, vol. 247, no. 3, pp. 431–437. ISSN 0168-9002. Available from DOI: 10.1016/0168-9002(86)90404-3.

[82] MOORE, I D; DENDOOVEN, P & ÄRJE, J. The IGISOL technique – Three decades of developments. *Hyperfine Interactions*. 2014, vol. 223, no. 1, pp. 17–62. ISSN 1572-9540. Available from DOI: 10.1007/s10751-013-0871-0.

[83] TASKINEN, P; PENTTILÄ, H; ÄYSTÖ, J, et al. Efficiency and delay of the fission ion guide for on-line mass separation. *Nuclear Instruments and Methods in Physics*

Research A. 1989, vol. 281, no. 3, pp. 539–546. ISSN 0168-9002. Available from DOI: 10.1016/0168-9002(89)91488-5.

[84] KRAMIDA, A; RALCHENKO, Yu; READER, J, et al. *Atomic spectra database (version 5.7)* [online]. Gaithersburg, Maryland, USA, 2019 [visited on 2020-07-01]. Available from DOI: 10.18434/T4W30F.

[85] ÄYSTÖ, J. Development and applications of the IGISOL technique. *Nuclear Physics A*. 2001, vol. 693, no. 1–2, pp. 477–494. ISSN 0375-9474. Available from DOI: 10.1016/S0375-9474(01)00923-X.

[86] NIEMINEN, A; CAMPBELL, P; BILLOWES, J, et al. On-line ion cooling and bunching for collinear laser spectroscopy. *Physical Review Letters*. 2002, vol. 88, no. 9, pp. 094801. ISSN 1079-7114. Available from DOI: 10.1103/PhysRevLett.88.094801.

[87] ERONEN, T; KOLHINEN, V S; ELOMAA, V V, et al. JYFLTRAP: A Penning trap for precision mass spectroscopy and isobaric purification. *The European Physical Journal A*. 2012, vol. 48, no. 4, pp. 1–21. ISSN 1434-601X. Available from DOI: 10.1140/epja/i2012-12046-1.

[88] BROWN, L S & GABRIELSE, G. Geonium theory: Physics of a single electron or ion in a Penning trap. *Reviews of Modern Physics*. 1986, vol. 58, no. 1, pp. 233–311. ISSN 1539-0756. Available from DOI: 10.1103/RevModPhys.58.233.

[89] CALVIÑO, F; CORTÉS, G; RIEGO, A, et al. *TDR BEta deLayEd Neutron detector (BELEN)*. 2014. Available also from: http://www.fair-center.eu/fileadmin/fair/publications%7B%5C_%7Dexp/TDR%7B%5C_%7DHISPEC%7B%5C_%7DDESPEC%7B%5C_%7DBELEN%7B%5C_%7Dpublic.pdf. Report.

[90] RUBIO, B. DEcay SPECtroscopy (DESPEC) at the new FAIR-NUSTAR facility. *International Journal of Modern Physics E*. 2006, vol. 15, no. 8, pp. 1979–1988. ISSN 0218-3013. Available from DOI: 10.1142/S0218301306005484.

[91] ROSNER, G. Future facility: FAIR at GSI. *Nuclear Physics B*. 2007, vol. 167, pp. 77–81. ISSN 0920-5632. Available from DOI: 10.1016/j.nuclphysbps.2006.12.089.

[92] *LND, Inc. – Designers and manufacturers of nuclear radiation detectors* [online]. Oceanside, New York, USA [visited on 2020-07-01]. Available from: http://www.lndinc.com.

[93] *252248: Cylindrical high temperature He3 neutron detector* [online]. LND, Inc. [visited on 2020-07-01]. Available from: https://www.lndinc.com/products/neutron-detectors/252248.

[94] MAZED, D; MAMERI, S & CIOLINI, R. Design parameters and technology optimization of ^{3}He-filled proportional counters for thermal neutron detection and spectrometry applications. *Radiation Measurements*. 2012, vol. 47, no. 8, pp. 577–587. ISSN 1350-4487. Available from DOI: 10.1016/j.radmeas.2012.06.002.

[95] GÓMEZ-HORNILLOS, M B; CABALLERO, R; CALVIÑO, F, et al. *Delayed neutron measurements for advanced reactor technologies and astrophysics*. 2010. JYFL proposal.

[96] RIEGO, A & CORTES, G. *Design of the BELEN detector for wide energy range with at and high detection efciency*. Barcelona, Spain, 2016. PhD thesis. Polytechnic University of Catalonia (UPC), Department of Physics.

[97] AGOSTINELLI, S; ALLISON, J; AMAKO, K, et al. GEANT4–A simulation toolkit. *Nuclear Instruments and Methods in Physics Research A*. 2003, vol. 506, no. 3, pp. 250–303. ISSN 0168-9002. Available from DOI: 10.1016/S0168-9002(03)01368-8.

[98] WATERS, L S; MCKINNEY, G W; DURKEE, J W, et al. The MCNPX Monte Carlo radiation transport code. *AIP Conference Proceedings*. 2007, vol. 896, no. 1, pp. 81–90. ISSN 0094-243X. Available from DOI: 10.1063/1.2720459.

[99] GÓMEZ-HORNILLOS, M B; GORLYCHEV, V; CABALLERO, R, et al. Monte Carlo simulations for the study of a moderated neutron detector. *Journal of the Korean Physical Society*. 2011, vol. 59, no. 2, pp. 1573–1576. ISSN 1976-8524. Available from DOI: 10.3938/jkps.59.1573.

[100] GÓMEZ-HORNILLOS, M B; GORLYCHEV, V; CABALLERO, R, et al. Design and commissioning of the BEta deLayEd Neutron detector. *Nuclear Instruments and Methods in Physics Research*. 2013. ISSN 0168-9002.

[101] ENGER, S A; MUNCK AF ROSENSCHÖLD, Per; REZAEI, A, et al. Monte Carlo calculations of thermal neutron capture in gadolinium: a comparison of GEANT4 and MCNP with measurements. *Medical Physics*. 2006, vol. 33, no. 2, pp. 337–341. ISSN 0094-2405. Available from DOI: 10.1118/1.2150787.

[102] MENDOZA, E; CANO-OTT, D; GUERRERO, C, et al. *New evaluated neutron cross section libraries for the GEANT4 code*. Vienna, Austria, 2012. Available also from: https://www-nds.iaea.org/publications/indc/indc-nds-0612. IAEA technical report INDC(NDS)-0612. IAEA.

[103] CSEWG. *Data formats and procedures for the evaluated nuclear data files ENDF/B-VI and ENDF/B-VII*. ENDF-6 formats manual. Ed. by HERMAN, M & TRKOV, A. USA, 2009. Available also from: https://www.bnl.gov/isd/documents/70393.pdf.

[104] *GEANT4 physics reference manual*. Geneva, Switzerland, 2019. Available also from: http://geant4-userdoc.web.cern.ch/geant4-userdoc/UsersGuides/PhysicsReferenceManual/html/index.html.

[105] *MCNPX user's manual (version 2.7.0)*. 2011.

[106] MENDOZA, E; CANO-OTT, D; KOI, T, et al. New standard evaluated neutron cross section libraries for the GEANT4 code and first verification. *IEEE Transactions on Nuclear Science*. 2014, vol. 61, no. 4, pp. 2357–2364. ISSN 1558-1578. Available from DOI: 10.1109/TNS.2014.2335538.

[107] MENDOZA, E & CANO-OTT, D. *Update of the evaluated neutron cross section libraries for the GEANT4 code*. Vienna, Austria, 2018. Available also from: https://www-nds.iaea.org/publications/indc/indc-nds-0758. IAEA technical report INDC(NDS)-0758. IAEA.

[108] MENDOZA, E & CANO-OTT, D. *Evaluated neutron cross section libraries for the GEANT4 code* [online] [visited on 2020-07-01]. Available from: https://www-nds.iaea.org/geant4.

[109] SQUIRES, G L. *Introduction to the theory of thermal neutron scattering*. 3rd ed. Cambridge University Press, 2012. ISBN 9781139107808. Available from DOI: 10.1017/CBO9781139107808.

[110] KNOLL, G F. *Radiation detection and measurement*. 4th ed. John Wiley & Sons, Inc., 2010. ISBN 9780470131480.

[111] COURSEY, J S; SCHWAB, D J; TSAI, J J, et al. Atomic weights and isotopic compositions [online]. 2010 [visited on 2020-07-01]. Available from: http://physics.nist.gov/comp.

[112] KOPPEL, J U & HOUSTON, D H. *Reference manual for ENDF thermal neutron scattering data*. San Diego, California, USA, 1968. Available from DOI: 10.2172/4075168. Report GA-8774. Gulf General Atomic, Inc.

[113] KOPPEL, J U; TRIPLETT, J R & NALIBOFF, Y D. *GASKET: A unified code for thermal neutron scattering*. San Diego, California, USA, 1966. Available from DOI: 10.2172/4457209. Report GA-7417. Gulf General Atomic, Inc.

[114] SEARS, V F. Neutron scattering lengths and cross sections. *Neutron News*. 1992, vol. 3, no. 3, pp. 26–37. ISSN 1044-8632. Available from DOI: 10.1080/10448639208218770.

[115] BERGLUND, M & WIESER, M E. Isotopic compositions of the elements 2009. *Pure and Applied Chemistry*. 2011, vol. 83, no. 2, pp. 397–410. ISSN 1365-3075. Available from DOI: 10.1351/PAC-REP-10-06-02.

[116] CARLSON, A D; PRONYAEV, V G; CAPOTE, R, et al. Evaluation of the neutron data standards. *Nuclear Data Sheets*. 2018, vol. 148, pp. 143–188. ISSN 0090-3752. Available from DOI: https://doi.org/10.1016/j.nds.2018.02.002.

[117] SHALEV, S; FISHELSON, Z & CUTTLER, J M. The wall effect in ^{3}He counters. *Nuclear Instruments and Methods*. 1969, vol. 71, no. 3, pp. 292–296. ISSN 0029-554X. Available from DOI: 10.1016/0029-554X(69)90317-6.

[118] KUDO, K; TAKEDA, N; URITANI, A, et al. Ideal response function of a ^{3}He proportional counter to thermal neutrons determined by different length counters. *Nuclear Instruments and Methods in Physics Research Section B*. 2004, vol. 213, pp. 305–309. ISSN 0168-583X. Available from DOI: 10.1016/S0168-583X(03)01633-1.

[119] BERGER, M J; COURSEY, J S; ZUCKER, M A, et al. *Stopping-power & range tables for electrons, protons, and helium ions* [online]. Gaithersburg, Maryland, USA, 2005 [visited on 2020-07-01]. Available from DOI: 10.18434/T4NC7P. NIST.

[120] *Plásticos Lutesor, S.A.* [online] [visited on 2020-07-01]. Available from: http://www.lutesor.com.

[121] *Prospector materials database* [online] [visited on 2020-07-01]. Available from: https://www.ulprospector.com.

[122] PETERSEN, H. *The properties of helium: Density, specific heats, viscosity, and thermal conductivity at pressures from 1 to 100 bar and from room temperature to about 1800 K*. Copenhagen, Denmark, 1970. ISBN 9788755000353. Risö report 224. Danish Atomic Energy Commission. Research Stablishment Risö.

[123] *Shielding physics list: for shielding, underground and high energy applications* [online] [visited on 2020-07-01]. Available from: https://www.slac.stanford.edu/comp/physics/geant4/slac_physics_lists/shielding/shielding.html.

[124] MCKINNEY, G W; DURKEE, J W; HENDRICKS, J S, et al. MCNPX2.5.0 – New features demonstrated. In: SOCIETY, American Nuclear (ed.). *The Monte Carlo method: Versatility unbounded in a dynamic computing world*. Chattanooga, Tennessee, USA, 2005. No. LA-UR-04-8695.

[125] HENDRICKS, J S; MCKINNEY, G W; WATERS, L S, et al. *MCNPX extensions version 2.5.0*. 2005. No. LA-UR-05-2675.

[126] WANG, M; AUDI, G; WAPSTRA, A H, et al. The Ame2012 atomic mass evaluation. *Chinese Physics C*. 2012, vol. 36, no. 12, pp. 1603–2014. ISSN 1674-1137. Available from DOI: 10.1088/1674-1137/36/12/003.

[127] *Reference neutron radiations - Part 1: Characteristics and methods of production*. Geneva, Switzerland, 2001. Available also from: https://www.iso.org/standard/

25666.html. Standard ISO 8529-1:2001. International Organization for Standardization.

[128] SOTI, G; WAUTERS, F; BREITENFELDT, M, et al. Performance of GEANT4 in simulating semiconductor particle detector response in the energy range below 1 MeV. *Nuclear Instruments and Methods in Physics Research A*. 2013, vol. 728, pp. 11–22. ISSN 0168-9002. Available from DOI: 10.1016/j.nima.2013.06.047.

[129] LECHNER, A; PIA, M G & SUDHAKAR, M. Validation of GEANT4 low energy electromagnetic processes against precision measurements of electron energy deposition. *IEEE Transactions on Nuclear Science*. 2009, vol. 56, no. 2, pp. 398–416. ISSN 1558-1578. Available from DOI: 10.1109/TNS.2009.2013858.

[130] BATIČ, M; HOFF, G; PIA, M G, et al. Validation of GEANT4 simulation of electron energy deposition. *IEEE Transactions on Nuclear Science*. 2013, vol. 60, no. 4, pp. 2934–2957. ISSN 1558-1578. Available from DOI: 10.1109/TNS.2013.2272404.

[131] KIM, S H; PIA, M G; BASAGLIA, T, et al. Validation test of GEANT4 simulation of electron backscattering. *IEEE Transactions on Nuclear Science*. 2015, vol. 62, no. 2, pp. 451–479. ISSN 1558-1578. Available from DOI: 10.1109/TNS.2015.2401055.

[132] BASAGLIA, T; HAN, M C; HOFF, G, et al. Quantitative test of the evolution of GEANT4 electron backscattering simulation. *IEEE Transactions on Nuclear Science*. 2016, vol. 63, no. 6, pp. 2849–2865. ISSN 1558-1578. Available from DOI: 10.1109/TNS.2016.2617834.

[133] WAUTERS, F; KRAEV, I; ZÁKOUCKÝ, D, et al. A GEANT4 Monte-Carlo simulation code for precision β spectroscopy. *Nuclear Instruments and Methods in Physics Research A*. 2009, vol. 609, no. 2–3, pp. 156–164. ISSN 0168-9002. Available from DOI: 10.1016/j.nima.2009.08.026.

[134] URBÁN, L. *A model for multiple scattering in GEANT4*. Geneva, Switzerland, 2006. Available also from: http://cds.cern.ch/record/1004190. Report CERN-OPEN-2006-077. CERN.

[135] LEWIS, H W. Multiple scattering in an infinite medium. *Physical Review*. 1950, vol. 78, no. 5, pp. 526–529. Available from DOI: 10.1103/PhysRev.78.526.

[136] HAUF, S; KUSTER, M; BATIČ, M, et al. Radioactive decays in GEANT4. *IEEE Transactions on Nuclear Science*. 2013, vol. 60, no. 4, pp. 2966–2983. ISSN 1558-1578. Available from DOI: 10.1109/TNS.2013.2270894.

[137] KRANE, K S. *Introductory nuclear physics*. 3rd ed. Chichester, New York: John Wiley & Sons, Inc., 1987. ISBN 9780471805533.

[138] GRAEFENSTEDT, M; KEYSER, U; MÜNNICH, F., et al. Experimental beta-decay energies of ^{91,92}Br. *Nuclear Physics A*. 1989, vol. 491, no. 3, pp. 373–382. ISSN 0375-9474. Available from DOI: 10.1016/0375-9474(89)90573-3.

[139] *ROOT Data Analysis Framework* [online] [visited on 2020-07-01]. Available from: https://root.cern.ch.

[140] ANTCHEVA, I; BALLINTIJN, M; BELLENOT, B, et al. ROOT – A C++ framework for petabyte data storage, statistical analysis and visualization. *Computer Physics Communications*. 2009, vol. 180, no. 12, pp. 2499–2512. ISSN 0010-4655. Available from DOI: 10.1016/j.cpc.2009.08.005.

[141] *Quantities and units – Part 2: Mathematics*. Geneva, Switzerland, 2019. Available also from: https://www.iso.org/standard/64973.html. Standard ISO 80000-2:2019. International Organization for Standardization.

[142] RUTHERFORD, E. *Radio-activity*. Dover Publications, 1904. ISBN 9780486495859.

[143] BATEMAN, H. Solution of a system of differential equations occurring in the theory of radioactive transformations. In: *Proceedings of the Cambridge Philosophical Society, Mathematical and Physical sciences*. 1910, vol. 15, pp. 423–427.

[144] ZHOU, Z; YAN, D; ZHAO, Y, et al. Kinetics analysis and quantitative calculations for the successive radioactive decay process. *Nuclear Physics A*. 2015, vol. 933, pp. 143–153. ISSN 0375-9474. Available from DOI: 10.1016/j.nuclphysa.2014.11.001.

[145] BOYCE, W E & DIPRIMA, R C. *Elementary differential equations and boundary value problems*. 9th ed. John Wiley & Sons, Inc., 2008. ISBN 9780470383346.

[146] YUAN, D & KERNAN, W. Explicit solutions for exit-only radioactive decay chains. *Journal of Applied Physics*. 2007, vol. 101, no. 9, pp. 094907-1–12. Available from DOI: 10.1063/1.2715785.

[147] MOLER, C & VAN LOAN, C. Nineteen dubious ways to compute the exponential of a matrix, twenty-five years later. *SIAM Review*. 2003, vol. 45, no. 1, pp. 3–49. ISSN 0036-1445. Available from DOI: 10.1137/S00361445024180.

[148] AMAKU, M; PASCHOLATI, P R & VANIN, V R. Decay chain differential equations: Solution through matrix algebra. *Computer Physics Communications*. 2010, vol. 181, no. 1, pp. 21–23. ISSN 0010-4655. Available from DOI: 10.1016/j.cpc.2009.08.011.

[149] KABANIKHIN, S I. Definitions and examples of inverse and ill-posed problems. *Journal of Inverse and Ill-posed Problems*. 2008, vol. 16, no. 4. ISSN 1569-3945. Available from DOI: 10.1515/JIIP.2008.019.

[150] DISTEFANO, J & COBELLI, C. On parameter and structural identifiability: Nonunique observability/reconstructibility for identifiable systems, other ambiguities, and new definitions. *IEEE Transactions on Automatic Control*. 1980, vol. 25, no. 4, pp. 830–833. ISSN 1558-2523. Available from DOI: 10.1109/TAC.1980.1102439.

[151] VERKERKE, W & KIRKBY, D. *The RooFit toolkit for data modeling*. Stanford, USA, 2003. Available also from: https://cds.cern.ch/record/622147. Report physics/0306116. SLAC National Accelerator Laboratory.

[152] MONETA, L; BELASCO, K; CRANMER, K S, et al. The RooStats project. In: 13*th International Workshop on Advanced Computing and Analysis Techniques in Physics Research (ACAT2010), Jaipur, India*. Italy: Proceedings of Science, 2010, vol. 93, p. 57. ISSN 1824-8039. Available from DOI: 10.22323/1.093.0057.

[153] RICHEY, M. The evolution of Markov Chain Monte Carlo methods. *The American Mathematical Monthly*. 2010, vol. 117, no. 5, pp. 383–413. ISSN 1930-0972. Available from DOI: 10.4169/000298910x485923.

[154] METROPOLIS, N; ROSENBLUTH, A W; ROSENBLUTH, M N, et al. Equation of state calculations by fast computing machines. *The Journal of Chemical Physics*. 1953, vol. 21, no. 6, pp. 1087–1092. ISSN 0021-9606. Available from DOI: doi:10.1063/1.1699114.

[155] HASTINGS, W K. Monte Carlo sampling methods using Markov chains and their applications. *Biometrika*. 1970, vol. 57, no. 1, pp. 97–109. ISSN 0006-3444. Available from DOI: 10.1093/biomet/57.1.97.

[156] BJØRNSTAD, J F. On the generalization of the likelihood function and the likelihood principle. *Journal of the American Statistical Association*. 1996, vol. 91, no. 434, pp. 791–806. ISSN 0162-1459. Available from DOI: 10.1080/01621459.1996.10476947.

[157] LIBERZON, D. *Switching in systems and control*. Boston, USA: Birkhäuser Boston, 2003. Systems & Control: Foundations & Applications. ISBN 9781461200178. Available from DOI: 10.1007/978-1-4612-0017-8.

[158] SCHITTKOWSKI, K. *Numerical data fitting in dynamical systems*. 1st ed. Springer, USA, 2002. Applied Optimization. ISBN 9781475760507. Available from DOI: 10.1007/978-1-4419-5762-7.

[159] KAWASE, Y; FUNAKOSHI, Y & OKANO, K. Search for an isomer in ^{94}Rb. *Zeitschrift für Physik A*. 1984, vol. 318, no. 2, pp. 191–193. ISSN 0939-7922. Available from DOI: 10.1007/BF01413467.

[160] RUDSTAM, G; SHALEV, S & JONSSON, O C. Delayed neutron emission from separated fission products. *Nuclear Instruments and Methods*. 1974, vol. 120, no. 2,

pp. 333–344. ISSN 0029-554X. Available from DOI: 10.1016/0029-554X(74)90055-X.

[161] JAMES, F & WINKLER, M. *MINUIT user's guide*. Geneva, Switzerland, 2004. Available also from: https://www.cern.ch/minuit.

[162] BAKER, S & COUSINS, R D. Clarification of the use of CHI-square and likelihood functions in fits to histograms. *Nuclear Instruments and Methods in Physics Research*. 1984, vol. 221, no. 2, pp. 437–442. ISSN 0167-5087. Available from DOI: 10.1016/0167-5087(84)90016-4.

[163] BERGMANN, U C; DIGET, C Aa; RIISAGER, K, et al. Beta-decay properties of the neutron-rich $^{94-99}$Kr and $^{142-147}$Xe isotopes. *Nuclear Physics A*. 2003, vol. 714, no. 1–2, pp. 21–43. ISSN 0375-9474. Available from DOI: 10.1016/S0375-9474(02)01352-0.

[164] GÓMEZ-HORNILLOS, M B; RISSANEN, J; TAÍN, J L, et al. β-delayed neutron emission studies. *Hyperfine Interactions*. 2014, vol. 223, no. 1, pp. 185–194. ISSN 1572-9540. Available from DOI: 10.1007/s10751-012-0617-4.

[165] HASHIMOTO, T; NOGUCHI, M; WASHIO, H, et al. Principle of single and multiple time interval analysis applicable to radioactive nuclides with half-lives of millisecond order. *Journal of Radioanalytical and Nuclear Chemistry*. 1992, vol. 159, no. 2, pp. 375–387. ISSN 1588-2780. Available from DOI: 10.1007/BF02040731.

[166] *Evaluated Nuclear Data File (ENDF)/B-VII.1* [online]. USA [visited on 2020-07-01]. Available from: https://www.nndc.bnl.gov/endf/b7.1.

[167] AGRAMUNT, J; GARCÍA, A R; ALGORA, A, et al. New beta-delayed neutron measurements in the light-mass fission group. *Nuclear Data Sheets*. 2014, vol. 120, pp. 74–77. ISSN 0090-3752. Available from DOI: 10.1016/j.nds.2014.07.010.

[168] LIANG, J; SINGH, B; MCCUTCHAN, E A, et al. (accepted for publication). *Nuclear Data Sheets*. 2020.

[169] KRATZ, K L. Independent fission yields and neutron emission probabilities of short-lived halogen isotopes. *Radiochimica Acta*. 1978, vol. 25, no. 1, pp. 1–8. ISSN 2193-3405. Available from DOI: 10.1524/ract.1978.25.1.1.

[170] *CRP on a reference database for beta-delayed neutron emission evaluation* [online] [visited on 2020-07-08]. Available from: https://www.iaea.org/es/projects/crp/f41030.

[171] *CRP on updating fission yield data for applications* [online] [visited on 2020-07-08]. Available from: https://www.iaea.org/es/projects/crp/f42007.

[172] GARCIA, A R; MENDOZA, E & CANO-OTT, D. Validation of the thermal neutron physics in GEANT4. In: *GEANT4 Hadronic Group Meeting*. 2013. Available also from: https://indico.cern.ch/event/245281.

[173] HOFER, E. *Probabilistische Unsicherheitsanalyse von Ergebnissen umfangreicher Rechenmodelle*. Cologne, Germany, 1993. Report GRS-A-2002. Global Research for Safety (GRS).

[174] PESCHKE, J & KRZYKACZ-HAUSMANN, B. *Methodenentwicklung zur Durchführung von Unsicherheits- und Sensitivitätsanalysen im Rahmen einer probabilistischen Dynamikanalyse*. Cologne, Germany, 2010. Report GRS-A-3556. Global Research for Safety (GRS).

[175] ROCHMAN, D; MARCK, S C van der; KONING, A J, et al. Uncertainty propagation with fast Monte Carlo techniques. *Nuclear Data Sheets*. 2014, vol. 118, pp. 367–369. ISSN 0090-3752. Available from DOI: 10.1016/j.nds.2014.04.082.

[176] BRIESMEISTER, J F (ed.). *MCNP – A general Monte Carlo N-particle transport code*. 2000. No. LA-13709-M.

[177] LASL GROUP X-6. *MCNP – A general Monte Carlo code for neutron and photon transport*. 1979. No. LA-7396-M.

[178] HARTLING, K; CIUNGU, B; LI, G, et al. The effects of nuclear data library processing on GEANT4 and MCNP simulations of the thermal neutron scattering law. *Nuclear Instruments and Methods in Physics Research A*. 2018, vol. 891, pp. 25–31. ISSN 0168-9002. Available from DOI: 10.1016/J.NIMA.2018.02.053.

[179] *NJOY – Nuclear data processing code* [online] [visited on 2020-07-01]. Available from: https://njoy.lanl.gov.

[180] MACFARLANE, R E & KAHLER, A C. Methods for processing ENDF/B-VII with NJOY. *Nuclear Data Sheets*. 2010, vol. 111, no. 12, pp. 2739–2890. ISSN 0090-3752. Available from DOI: 10.1016/j.nds.2010.11.001.

[181] MACFARLANE, R E; MUIR, D W; BOICOURT, R M, et al. *The NJOY nuclear data processing system, version 2016*. 2017. No. LA-UR-17-20093. Available from DOI: 10.2172/1338791.

[182] TABATA, T; ITO, R & OKABE, S. An empirical equation for the backscattering coefficient of electrons. *Nuclear Instruments and Methods*. 1971, vol. 94, no. 3, pp. 509–513. ISSN 0029-554X. Available from DOI: 10.1016/0029-554X(71)90013-9.

[183] DAPOR, M. *Transport of energetic electrons in solids*. Springer International Publishing, 2014. Springer Tracts in Modern Physics. ISBN 9783319038834. Available from DOI: 10.1007/978-3-319-03883-4.

[184] WALTER, E. *Identifiability of state space models*. Berlin, Heidelberg: Springer, 1982. Lecture Notes in Biomathematics. ISBN 9783642618239. Available from DOI: 10.1007/978-3-642-61823-9.

[185] CHIS, O T; BANGA, J R & BALSA-CANTO, E. Structural identifiability of systems biology models: a critical comparison of methods. *PloS one*. 2011, vol. 6, no. 11. ISSN 1932-6203. Available from DOI: 10.1371/journal.pone.0027755.

Appendix A

Fast uncertainty propagation in Monte Carlo simulations

The straight forward way of propagating uncertainties in Monte Carlo simulations is repeating the simulation with a different random input vector each time and calculating the uncertainty of the quantity of interest as the standard deviation of the resulting distribution. This method, known as the GRS method [173], becomes unfeasible when a single calculation has a high computational cost. Reliable uncertainties need to be estimated within a reasonable time frame.

A fast variant of the GRS method was recently proposed by Zwermann et al. [76]. It exploits a result in probability theory that reads: the covariance of two identically distributed and conditionally independent output variables Y_1 and Y_2 given the input vector $\boldsymbol{X}$ equals the variance of the conditional expectation $E[Y|\boldsymbol{X}]$, i.e.: $\mathrm{var}(E[Y|\boldsymbol{X}]) = \mathrm{cov}(Y_1, Y_2)$ [174]. Let $\{\boldsymbol{x}_i^1\}$ and $\{\boldsymbol{x}_i^2\}$ be two sets of random input vectors where $i \in \mathbb{N}^*_{\leq n}$. The fast GRS method applies then by simulating m events on each set, such that:

1. m/n events are simulated with a seed s_1 on each vector of set $\{\boldsymbol{x}_i^1\}$; and
2. m/n events are simulated with a different seed s_2 on each vector of set $\{\boldsymbol{x}_i^2\}$.

The result is two sets $\boldsymbol{y}_1$ and $\boldsymbol{y}_2$ of output variables of n elements each, whose covariance is the epistemic uncertainty of Y, i.e., the uncertainty from the incomplete knowledge of $\boldsymbol{X}$.

The GRS method and its fast variant are compared in table A.1, where the advantages of the latter become clear. Note that the fast GRS method takes only twice the time of a single simulation with the GRS method. Moreover, the time the GRS method takes, unlike its fast variant, scales up with n.

Run	GRS [173]					Fast GRS [76]				
	Input vector	**Seed**	**Number of events**	**Execution time**	**Estimated quantity**	**Input vector**	**Seed**	**Number of events**	**Execution time**	**Estimated quantity**
1	$\boldsymbol{x}_1$	s_1	m	T	$y_1 \pm \sigma_1^{\text{stat}}$	$\boldsymbol{x}_1^1$	s_1	m/n	T/n	y_1^1
2	$\boldsymbol{x}_2$	s_2	m	T	$y_2 \pm \sigma_2^{\text{stat}}$	$\boldsymbol{x}_2^1$	s_1	m/n	T/n	y_2^1
$\vdots$	$\vdots$	$\vdots$	$\vdots$	$\vdots$	$\vdots$	$\vdots$	$\vdots$	$\vdots$	$\vdots$	$\vdots$
n	$\boldsymbol{x}_n$	s_n	m	T	$y_n \pm \sigma_n^{\text{stat}}$	$\boldsymbol{x}_n^1$	s_1	m/n	T/n	y_n^1
n+1						$\boldsymbol{x}_1^2$	s_2	m/n	T/n	y_1^2
n+2						$\boldsymbol{x}_2^2$	s_2	m/n	T/n	y_2^2
$\vdots$						$\vdots$	$\vdots$	$\vdots$	$\vdots$	$\vdots$
$2n$						$\boldsymbol{x}_n^2$	s_2	m/n	T/n	y_n^2
Result:			$n \times m$	$n \times T$	$\langle y \rangle$, σ_y, $\langle \sigma_{\text{stat}} \rangle$ $\sigma_{\boldsymbol{x}}^2 = \langle \sigma_{\text{stat}} \rangle^2 - \sigma_y^2$			$2m$	$2T$	$\langle y \rangle$ $\sigma_{\boldsymbol{x}}^2 = \text{cov}(\boldsymbol{y}_1, \boldsymbol{y}_2)$

Table A.1: Comparison between the GRS method and its fast variant to propagate uncertainties in Monte Carlo simulations [taken from 175].

Appendix B

Performance of MCNPX and GEANT4 in the simulation of thermal neutron interactions in polyethylene

The performance of MCNPX and GEANT4 in describing thermal neutron interactions in polyethylene was compared by generating 1 MeV neutrons isotropically from the center of a 10 cm in radius polyethylene sphere and calculating the fluence transmitted through the sphere surface. The transmitted fluence is an integral probe of the accuracy of the simulation. It was estimated with MCNPX using tally F2, which is a surface crossing fluence estimator [105]. With GEANT4, on the other hand, the energy (E) and cosine of the angle between the lineal momentum and the surface normal (μ) were registered for each neutron crossing the surface, and the fluence was calculated in the same way as tally F2 in MCNPX:

$$\phi(E) = \frac{1}{A} \sum_i \frac{w_i}{|\mu_i|} \tag{B.1}$$

where A is the area of the surface and w_i the weight of the ith neutron [176]. The previous sum runs over all neutrons with energy E. To avoid singularities, μ was set to 0.05 when it was lower than 0.1 as tally F2 does in MCNPX [177].

Figure B.1 shows the energy distribution of the transmitted fluence resulting from the simulation of 10^7 neutron histories with MCNPX and GEANT4.9.03.p02 using different thermal scattering models. Details on material definitions and data libraries were given in section 4.1.4. Note in the first place that the transmitted fluence at thermal energies is lower when the thermal scattering law is used instead of the Free Gas model. This illustrates the importance of using thermal scattering data for an accurate description of thermal neutron interactions. On the other hand, discrepancies are also observed between codes —less significant though— using the same model. They exist in both the magnitude and position

of the thermal peak, with GEANT4.9.03.p02 producing a higher peak shifted toward higher energies. Similar discrepancies have been observed in the past [106,178].

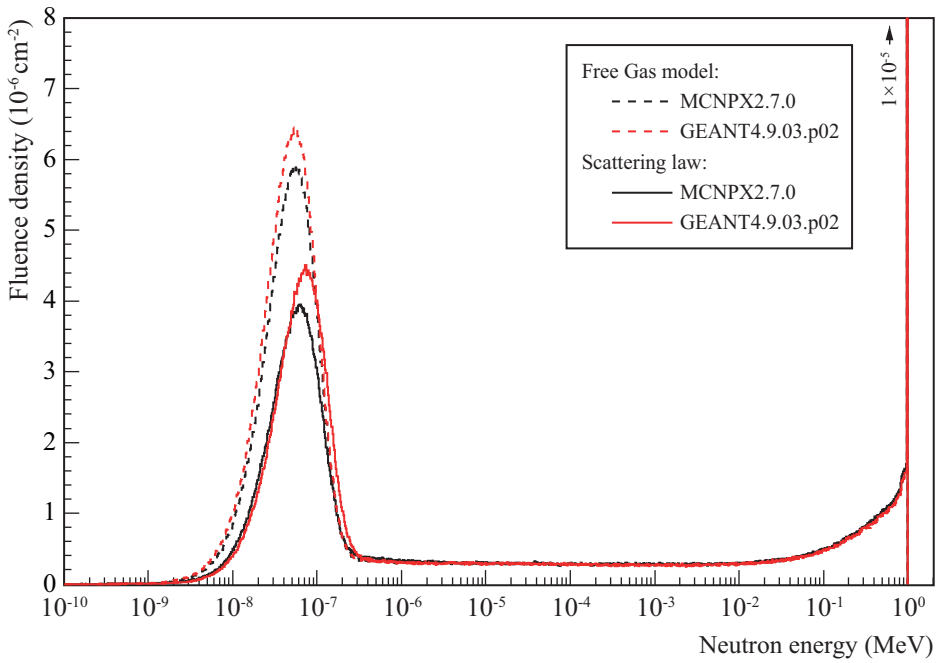

Figure B.1: Neutron fluence (per generated neutron) transmitted through the surface of a 10 cm in radius polyethylene sphere, calculated with MCNPX and GEANT4.9.03.p02 using different thermal scattering models. 1 MeV neutrons were generated isotropically at the center of the sphere.

Figure B.2 compares the results obtained with MCNPX and releases 9.03.p02 and 10.02.p02 of GEANT4 using the thermal scattering law. The results are similar above 4 eV, which is the higher energy limit of the thermal cross section data in ENDF/B. This was verified to be also the case when using the Free Gas model. Below 4 eV, GEANT4.9.03.p02 produces larger discrepancies with MCNPX than GEANT4.10.02.p02 in the magnitude and position of the thermal peak that suggest a buggy implementation of the data processing and sampling algorithms. Indeed, the enhanced agreement of GEANT10.02.p02 with MCNPX is the result of a comprehensive debug of classes *G4NeutronHPThermalScatteringData* and *G4NeutronHPThermalScattering* in GEANT4.9.03.p02 in this work. Those classes are devoted to loading, preparing and using the thermal scattering data. A close look into their implementation revealed wrong calls to the interpolation/extrapolation routines and bugs in the implementation of the routines themselves. Corrections and a comprehensive validation against MCNPX were presented and discussed in the GEANT4 Hadronic Working Group Meeting on April 17, 2013 [172]. The corrections were accepted and incorporated in release GEANT4.10.0. They constitute a significant contribution to the high-precision model G4ParticleHP in GEANT4 that had a great impact in the simulation of the performance of BELEN20b and newer configurations of the detector.

Hartling et al. [178] compared recently the MCNPX and GEANT4 sampling methods, and went a step further to investigate the effects of data processing and representation

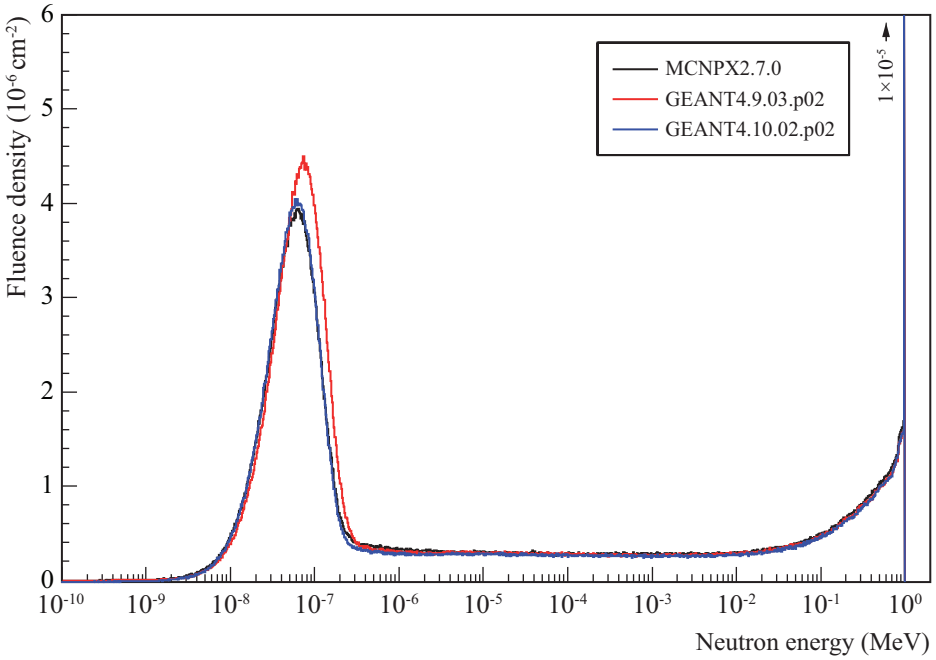

Figure B.2: Neutron fluence (per generated neutron) transmitted through the surface of a 10 cm in radius polyethylene sphere, calculated with MCNPX and different releases of GEANT4 using the thermal scattering law. 1 MeV neutrons were generated isotropically at the center of the sphere.

on the simulation of thermal neutron interactions. They showed that the thermal neutron transmissions calculated from MCNPX and GEANT4 simulations become statistically consistent when the code-specific data libraries are generated with the same reconstruction tolerance for the cross sections and number of equally probable cosine bins between -1 and 1 for the angular and energy-angle distributions. NJOY [179–181] was used to generate the code-specific data libraries used in this work. Whereas, a tolerance of 0.001 and 16 equally probable bins were used to generate table poly.60t in library sab2002, a much higher tolerance of 0.02 and only 8 bins were used for G4NDL-4.5. The remaining discrepancies between MCNPX and GEANT4.10.02.p02 observed in figure B.2 can therefore be attributed to differences in the generation of the libraries.

Appendix C

Validation of the multiple scattering model in GEANT4 against electron backscattering experiments

Soti et al. [128] measured and simulated with GEANT4 the response of a 1.5 mm PIPS detector to a ^{60}Co source. The good agreement obtained validates the electromagnetic models registered in the Standard physics list of GEANT4. However, that agreement was achieved after a systematic study of the effects of different simulation parameters in the detector response. The parameters investigated were those relevant to the simulation of electron interactions and the production of secondary electrons.

The Standard list includes both single and multiple electron scattering models. For low-energy electrons (below 100 MeV) only the latter is activated [104]. The model in question is the Urban model [134], which is based on the theory of H.W. Lewis [135]. A detail presentation of the model is out of the scope of this work, but in essence, it uses analytic functions to describe the distribution of moments of the angular and spatial displacements in the theory of H.W. Lewis to sample the final state. The Urban model is implemented in class *G4UrbanMscModel*. None of the values of the step limitation parameters set therein by default are changed in the distributed Standard list.

Multiple scattering models in GEANT4 are controlled by three main step limitation parameters: geometry factor (F_G), range factor (F_R) and skin [104]. For the simulation of the silicon detector used in the experiment at JYFL described in chapter 3, only the first two are relevant. The skin parameter defines a region near the volume boundaries where single scattering is applied, but this is never the case for the simulation of low-energy electrons with the Standard list.

The geometry factor ensures a minimal number of steps (2.5 by default) within each volume. It is used to prevent particles from crossing a volume in a single step when scattering in the volume occurs, by limiting the step length to a maximum of D/F_G, where D is the distance to the next boundary in the direction of the particle. The range factor (0.04 by default), on the other hand, limits the step length at the beginning of a track and after a

boundary cross to $F_R \max(R, \lambda)$, where R denotes range and λ mean free path. This way, low-energy particles are prevented from penetrating volumes too deep in the first step that they cannot reach again the crossed boundary. Clearly, the range factor has a significant impact on backscattering.

The simulation of electron backscattering is a sensitive probe for scattering models. Since the most basic observable in backscattering experiments is the backscattering coefficient (the ratio of the number of backscattered to impinging electrons), its assessment can be preparatory to the validation of more complex observables on which the accuracy of scattering models have a significant impact.

Tabata et al. [182] obtained the following empirical equation for the backscattering coefficient of monoenergetic electrons impinging at normal incidence onto a thick target:

$$\eta(T) = \frac{a_1}{1 + a_2 T^{a_3}} \tag{C.1}$$

where T is the kinetic energy of the incident electron in units of rest energy and the coefficients a_{1-3} are specific for the target. This equation and the determination of its coefficients resulted from a systematic analysis of multiple experiments. It is valid for $Z \geq 6$ between 50 keV and 22 MeV, and deviates from the data in Root Mean Square (RMS) up to about 7 %.

Simulations were performed to validate the use of the Urban model against equation C.1 in the simulation of the response of the silicon detector to beta decay. The requirement of a thick target limited the validation to energies for which the range is less than twice the detector thickness, because the backscattering coefficient increases with the target thickness and saturates at a thickness about half the range [182].

Figure C.1 shows the energy dependence of the electron range in silicon retrieved from the Electron STopping powers And Ranges (ESTAR) database [119]. Observe that a 1 mm range (twice the thickness of the detector) corresponds to 500 keV. The simulations were performed for this energy accordingly.

The simulations consisted of monoenergetic electrons impinging normally at the center of a 0.5 mm thick slab of pure silicon, large enough to avoid losses by lateral displacement. A hemispherical sensitive surface behind the source tallied the backscattered electrons. All these elements were placed in vacuum to remove the contribution of spurious interactions in air. A sketch of the geometry is shown in figure C.2.

Table C.1 shows the backscattering coefficient calculated for different combinations of production cut and range factor values. The geometry factor was kept at its default value, as it was not observed to have a significant effect on the backscattering coefficients. This was also noted by Soti et al. [128]. To exclude secondary electrons, an energy threshold was set at 50 eV according to the conventional experimental practice[1] [131,183].

[1] The energy distribution of secondary electrons is concentrated at a peak below 50 eV [183, section 1.5].

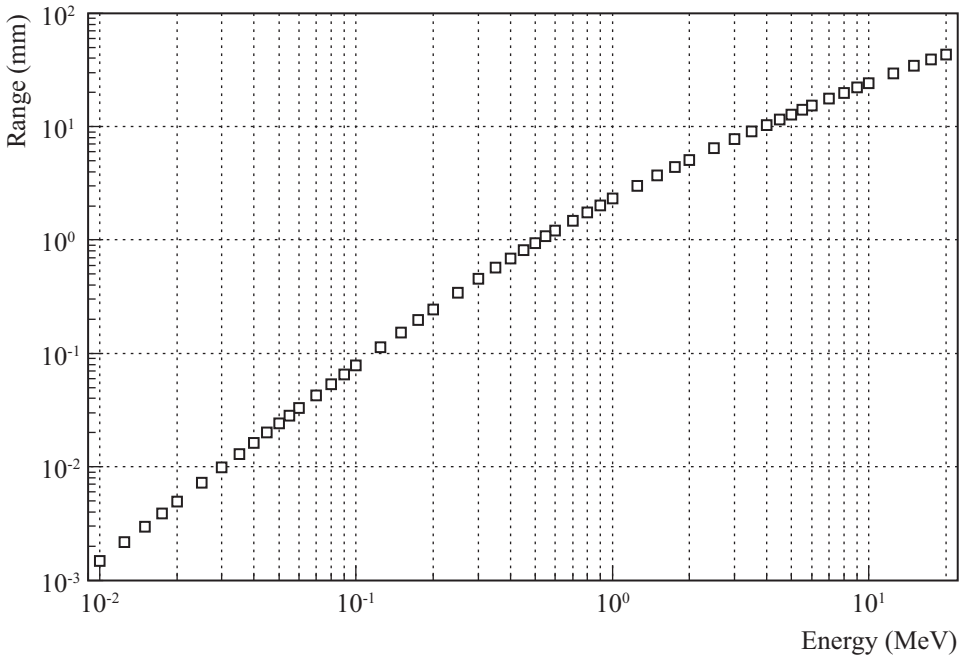

Figure C.1: Electron range in silicon [119].

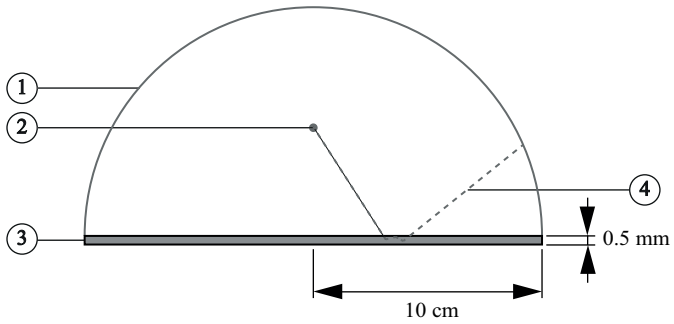

Figure C.2: Geometrical setup in electron backscattering simulations. — 1) Sensitive surface; 2) electron source; 3) silicon slab; 4) sample electron trajectory.

CFS_e (µm)	F_R			
	0.0002	**0.002**	**0.02**	**0.04**
0.1	12.12	12.03	12.70	12.71
1	12.34	12.10	12.52	12.63
10	11.17	11.22	11.28	11.43
100	11.03	11.00	11.24	11.63
1000	11.16	10.87	11.30	11.35

Table C.1: Backscattering coefficients (in %) for different values of the production cut for secondary electrons CFS_e and range factor. The geometry factor was set to its default value of 2.5. The relative statistical uncertainty is <1 %.

For 500 keV, equation C.1 gives a backscattering coefficient of 11.4 ± 0.8 %. Comparing this value with those in table C.1 allows to conclude that the best results are obtained for a production cut of 10 µm and a range factor of 0.04, which is the default value.

Figure C.3 compares the energy dependence of the backscattering coefficients calculated from equation C.1 and resulting from the simulations with the adopted values of the multiple scattering model parameters. Note that the simulations underestimate Tabata's equation below 400 keV and become at variance below 150 keV. A similar result was obtained by Soti et al. [128], not only with the Urban model. This may have affected the shape of the response function of the silicon detector used in the experiment at JYFL and biased the calculation of the beta detection efficiency.

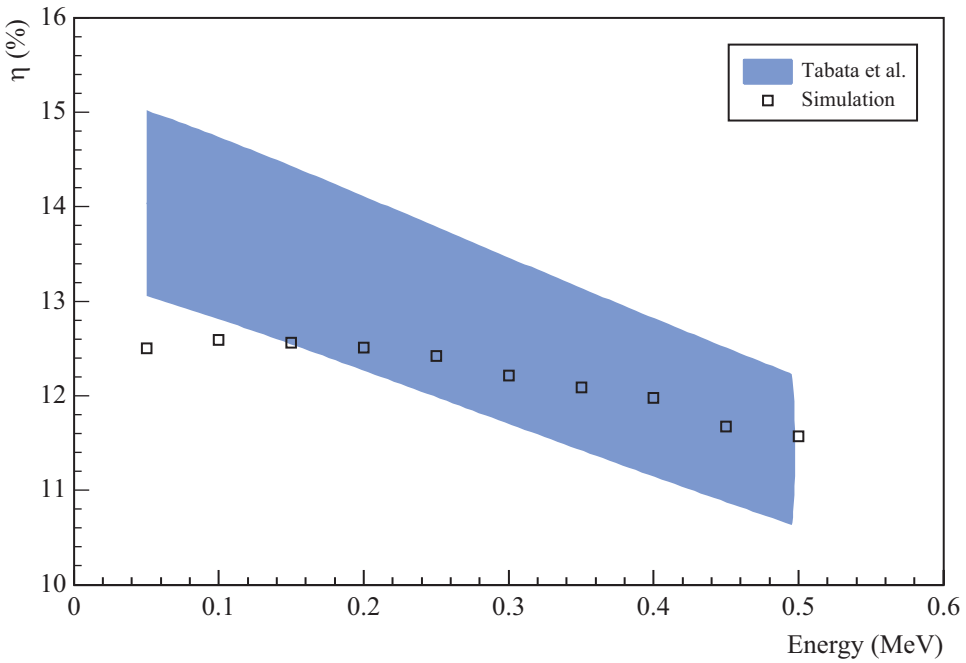

Figure C.3: Energy dependence of the backscattering coefficients calculated by Monte Carlo simulations and equation C.1 [182].

Appendix D

Structural identifiability analysis

Several methods exist to analyze the structural identifiability of parameters in dynamical models [184,185]. The simplest in concept —the one applied in this work— consist of testing the uniqueness of the parameters against the *indistinguishability* of the model output over the parameter space, i.e., whether for any two vectors $\boldsymbol{\omega}$ and $\boldsymbol{\omega}^*$ of the parameter space the model output is or not the same.

For analyzing the structural identifiability of the reduced models for the evolution of the beta and neutron counting rates derived in section 6.1 (the term "reduced" will be omitted hereafter), it is convenient to express the models as the sum of the contributions from each branch and the precursor's. Calling b_l the branching ratio of the decay $X_1 \rightarrow X_1^l$ (see figure 6.2 for the indexing convention), the Bateman equations in matrix form for the lth branch are:

$$\frac{d}{dt}\mathbf{N}_l(t) = \mathbf{A}_l\mathbf{N}_l(t) + b_l\lambda_1 N_1(t)\boldsymbol{u}_1^l \tag{D.1}$$

where the coefficients matrix $\mathbf{A}_l$ is a bidiagonal matrix with all elements in the diagonal below the main one equal to 1. The general and equivalent models in terms of the state variable of the precursor of the chain $N_1(t)$ and the state vectors of the branches $\mathbf{N}_l(t)$ now read:

$$r_p(t) = \varepsilon_1^p\lambda_1 N_1(t) + \sum_{l=1}^{L}\mathbf{E}_l^p\boldsymbol{\Lambda}_l\mathbf{N}_l(t) \tag{D.2}$$

where $\mathbf{E}_l^p$ and $\boldsymbol{\Lambda}_l^p$ are the equivalents to vector $\mathbf{E}_p$ and matrix $\boldsymbol{\Lambda}_p$ respectively defined for the lth branch.

Note that the fraction of the decay rate of the precursor into the lth branch constitutes a source term in equation D.1. The solution 6.14 for the non-homogeneous Bateman equations obtained for the equivalent model applies here as well with $\mathbf{R}(t) = b_l\lambda_1 N_1(t)\boldsymbol{u}_1^l$, where $N_1(t)$ is just the solution of $\frac{d}{dt}N_1(t) = -\lambda_1 N_1(t)$. The same reasoning used in

section 6.1.1 to derive equation 6.6 for the state vector in the general model leads to:

$$N_1(t) = \sum_{k=1}^{K} s(t - t_k)\Delta N_1(t_k) e^{-\lambda_1 (t - t_k)} \tag{D.3}$$

With this equation, the following analytic solution of equation D.1 for the entire measurement cycle is obtained by mathematical induction:

$$\mathbf{N}_l(t) = b_l \sum_{k=1}^{K} s(t - t_k)\Delta N_1(t_k) \int_{t_k}^{t} \lambda_1 e^{-\lambda_1 (t' - t_k)} e^{\mathbf{A}_l (t - t')} dt' \boldsymbol{u}_1^l \tag{D.4}$$

Note that the integral in the previous equation grows continuously from zero as t exceeds t_k. Therefore, jump discontinuities in the source term do not propagate to $\mathbf{N}_l(t)$.

Inserting equations D.3 and D.4 into equation D.2 the model reads:

$$r_p(t) = \sum_{k=1}^{K} s(t - t_k)\Delta N_1(t_k) \left[\lambda_1 \varepsilon_1^p e^{-\lambda_1 (t - t_k)} + \sum_{l=1}^{L} b_l \mathbf{E}_l^p \mathbf{\Lambda}_l \mathbf{I}_l^k(t) \boldsymbol{u}_1^l \right] \tag{D.5}$$

where $\mathbf{I}_l^k(t)$ represents the integral in equation D.4. $\mathbf{I}_l^k(t)$ does not depend on b_l. Thus, all dependence of the model on b_l in the previous equation is explicit. Moreover, the branching ratios and the implantation and decay parameters, which are the parameters whose structural identifiability is to be analyzed, are explicit as well. Hence the convenience of the general model expressed in this form.

The following theorem facilitates the structural identifiability analysis of the general model:

Theorem 1. *A parameter ω_i of the general model is structurally non-identifiable if $\forall k \in \mathbb{N}^*_{\leq K}$, the indistinguishability of the kth term of the outer sum in equation D.5 $\forall t \in [t_k, T]$ does not lead to $\omega_i = \omega_i^*$.*

Proof. Rewrite equation D.5 as:

$$r_p(t) = \sum_{k=1}^{K} s(t - t_k) r_k^p(\boldsymbol{\omega}, t) \tag{D.6}$$

where:

$$r_k^p(\boldsymbol{\omega}, t) = \Delta N_1(t_k) \left[\lambda_1 \varepsilon_1^p e^{-\lambda_1 (t - t_k)} + \sum_{l=1}^{L} b_l \mathbf{E}_l^p \mathbf{\Lambda}_l \mathbf{I}_l^k(t) \boldsymbol{u}_1^l \right] \tag{D.7}$$

is the contribution of the kth implantation to the decay rate and $\boldsymbol{\omega}$ represents a vector in the parameters space. Note that the step function centered at t_k cancels all terms where $t < t_k$. Thus, $r_p(t) = r_1^p(\boldsymbol{\omega}, t)$ in $[t_1, t_2)$, $r_p(t) = r_1^p(\boldsymbol{\omega}, t) + r_2^p(\boldsymbol{\omega}, t)$ in $[t_2, t_3)$, and so on.

Suppose now that multiple values of ω_i produce the same value of $r_1^p(\boldsymbol{\omega}, t)$ for any $t \in [t_1, T)$. In that case, ω_i would be structurally non-identifiable in $[t_1, t_2)$, where $r_p(t) = r_1^p(\boldsymbol{\omega}, t)$. It may be that ω_i is not a parameter of $r_2^p(\boldsymbol{\omega}, t)$, in which case it wouldn't change $r_2^p(\boldsymbol{\omega}, t)$ either in $[t_2, T)$. ω_i is then structurally non-identifiable in $[t_2, t_3)$, where $r_p(t) = r_1^p(\boldsymbol{\omega}, t) + r_2^p(\boldsymbol{\omega}, t)$. If on the contrary ω_i is also a parameter of $r_2^p(\boldsymbol{\omega}, t)$, the same multiple values of ω_i that produce the same value of $r_1^p(\boldsymbol{\omega}, t)$ for any $t \in [t_1, T)$ might or not produce the same value of $r_2^p(\boldsymbol{\omega}, t)$ for any $t \in [t_2, t_3)$. If they do, those values of ω_i wouldn't change $r_p(t)$ for any $t \in [t_1, t_3)$ and ω_i would be structurally non-identifiable in that interval. This reasoning implies that, to prove the structural non-identifiability of a parameter ω_i in $[t_1, t_3)$, it is enough to prove it for $r_1^p(\boldsymbol{\omega}, t)$ in $[t_1, T)$ and $r_2^p(\boldsymbol{\omega}, t)$ in $[t_2, T)$. Extending this conclusion to the subsequent subintervals of the measurement cycle the theorem is proved.

■

In the waiting interval $[0, t_1)$ (see figure 6.1), all parameters are structurally non-identifiable because the model output is null. The application of theorem 1 reduces then to proof the structural non-identifiability of parameters for the kth term of D.5 (equation D.7) in $[t_k, T]$.

The indistinguishability of $r_k^p(\boldsymbol{\omega}, t)$ in terms of any two vectors $\boldsymbol{\omega}$ and $\boldsymbol{\omega}^*$ of the parameter space reads: $r_k^p(\boldsymbol{\omega}, t) = r_k^p(\boldsymbol{\omega}^*, t)$. For $t = t_k$, $\mathbf{I}_l^k(t) = \mathbf{0}$ and the sum over l in equation D.7 becomes null. That leaves $\Delta N_1(t_k)\varepsilon_1^p = \Delta N_1^*(t_k)\varepsilon_1^{p*}$. Using this relationship, the indistinguishability of $r_k^p(\boldsymbol{\omega}, t)$ reduces to:

$$\Delta N_1(t_k) \sum_{l=1}^{L} b_l \mathbf{E}_l^p \boldsymbol{\Lambda}_l \mathbf{I}_l^k(t) \boldsymbol{u}_1^l = \Delta N_1^*(t_k) \sum_{l=1}^{L} b_l^* \mathbf{E}_l^{p*} \boldsymbol{\Lambda}_l \mathbf{I}_l^k(t) \boldsymbol{u}_1^l \tag{D.8}$$

where the asterisk indicates dependence with the elements of $\boldsymbol{\omega}^*$.

Now, the integral term in equation D.4 can be solved analytically. The solution is a square matrix whose elements are linear combinations of $e^{-\lambda_1 t}$ and $e^{-\lambda_i^l t}$, which are linearly independent functions. $\mathbf{E}_l^p \boldsymbol{\Lambda}_l \mathbf{I}_l^k(t) \boldsymbol{u}_1^l$ is therefore a span of that set of exponential functions. Since all the branches are different by definition, even if they share some elements, the sets of exponential functions for any two branches are linearly independent. Consequently, the terms $\mathbf{E}_l^p \boldsymbol{\Lambda}_l \mathbf{I}_l^k(t) \boldsymbol{u}_1^l$ are linearly independent as well and their coefficients on both sides of equation D.8 can be equated. That leads to $\Delta N_1(t_k) b_l \mathbf{E}_l^p = \Delta N_1^*(t_k) b_l^* \mathbf{E}_l^{p*}$. The indistinguishability of the general model is reduced at the end to the system of equations:

$$\begin{aligned} \Delta N_1(t_k)\varepsilon_1^p &= \Delta N_1^*(t_k)\varepsilon_1^{p*} \\ \Delta N_1(t_k) b_l \mathbf{E}_l^p &= \Delta N_1^*(t_k) b_l^* \mathbf{E}_l^{p*} \end{aligned} \tag{D.9}$$

Consider the proportionality relation $\varepsilon_i^* = \rho_i \varepsilon_i$ with $\rho_i \in \mathbb{R}_{\geq 0}$. The previous system of equations reduces to $\Delta N_1(t_k) = \rho_1 \Delta N_1^*(t_k)$ and $\rho_1 b_l = \rho_i b_l^* \quad \forall i > 1$. The parameters

$\Delta N_1(t_k)$, b_l and ε_i are therefore structurally non-identifiable, as for any set of values of ρ_i it is always possible to find two different values of $\Delta N_1(t_k)$, b_l, and ε_i that fulfil the system of equations D.9 and therefore the indistinguishability of $r_k^p(\boldsymbol{\omega}, t)$.

Consider now the equivalent model, where $N_1(t)$ reads:

$$N_1(t) = \frac{R_1}{\lambda_1} \begin{cases} 0 & \forall t \in [0, t_1] \\ 1 - e^{-\lambda_1(t-t_1)} & \forall t \in [t_1, t_K] \\ e^{-\lambda_1(t-t_K)} \left[1 - e^{-\lambda_1(t_K-t_1)}\right] & \forall t \in [t_K, T] \end{cases} \tag{D.10}$$

Solving equation D.1 with the previous equation in the source term leads to a more complex analytic form than equation D.4 for $\mathbf{N}_l(t)$ in the general model. The explicit form does not add much to the analysis so it will not be presented here. It is enough to mention that the equivalent model can be represented as:

$$r_p(t) = R_1 \left[\varepsilon_1^p \lambda_1 N_1(t) + \sum_{l=1}^{L} b_l \mathbf{E}_l^p \mathbf{\Lambda}_l \mathbf{I}_l(t) \boldsymbol{u}_1^l \right] \tag{D.11}$$

where $\mathbf{I}_l(t)$ is a sum of integrals whose analytic solutions are linear combinations of $e^{-\lambda_1 t}$ and $e^{-\lambda_i^l t}$, just like $\mathbf{I}_l^k(t)$ for the general model. The model indistinguishability posed for the equivalent model in the previous form reads:

$$R_1 \left[\varepsilon_1^p \lambda_1 N_1(t) + \sum_{l=1}^{L} b_l \mathbf{E}_l^p \mathbf{\Lambda}_l \mathbf{I}_l(t) \boldsymbol{u}_1^l \right] = R_1^* \left[\varepsilon_1^{p*} \lambda_1 N_1(t) + \sum_{l=1}^{L} b_l^* \mathbf{E}_l^{p*} \mathbf{\Lambda}_l \mathbf{I}_l(t) \boldsymbol{u}_1^l \right] \tag{D.12}$$

The same conclusion drawn before on the linear independence of the terms $\mathbf{E}_l^p \mathbf{\Lambda}_l \mathbf{I}_l^k(t) \boldsymbol{u}_1^l$ in equation D.5 can be drawn on the terms $\mathbf{E}_l^p \mathbf{\Lambda}_l \mathbf{I}_l(t) \boldsymbol{u}_1^l$ in equation D.11. Moreover, the term $\lambda_1 \varepsilon_1^p N_1(t)$ and the terms $\mathbf{E}_l^p \mathbf{\Lambda}_l \mathbf{I}_l(t) \boldsymbol{u}_1^l$ are linearly independent as well, because the latter have non-null components on a wider set of exponentials that include $e^{-\lambda_1 t}$. Coefficients can therefore be equated on both sides of equation D.12, reducing the model indistinguishability to the following system of equations:

$$\begin{aligned} R_1 \varepsilon_1^p &= R_1^* \varepsilon_1^{p*} \\ R_1 b_l \mathbf{E}_l^p &= R_1^* b_l^* \mathbf{E}_l^{p*} \end{aligned} \tag{D.13}$$

The structural identifiability analysis proceeds from here in a similar way as from the system of equations D.9 for the general model, but the dynamics is different in the implantation-decay and decay intervals and theorem 1 cannot be applied. The following theorem and its corollary, which apply also to the general model, must be applied instead:

Theorem 2. *A parameter ω_i of either the general or the equivalent model is structurally identifiable if it structurally identifiable in some subinterval of the measurement cycle.*

Proof. Being structurally identifiable in a given subinterval of the measurement cycle means that any deviation from its true value affects the model output and thus the quality of the fit, not only in the subinterval, but over the entire cycle. The parameter is therefore structurally identifiable. ■

Corollary 2.1. *A parameter ω_i of either the general or the equivalent model is structurally non-identifiable if it structurally non-identifiable in every subinterval of the measurement cycle.*

Theorem 2 and its corollary 2.1 imply that the structural identifiability analysis must be conducted separately on each interval. However, this is unnecessary. In the implantation-decay and decay intervals, the analysis is based on the system of equations D.13, which does not depend on time. Consequently, the analysis yields the same results in both intervals. If the system of equations D.13 leads to $\omega_i = \omega_i^*$, parameter ω_i would be structurally identifiable in virtue of theorem 2. The contrary $\omega_i \neq \omega_i^*$ would imply that parameter ω_i is structurally non-identifiable in virtue of the corollary 2.1, because they would be structurally non-identifiable in the implantation-decay and decay intervals and also in the waiting interval for the same reason as before in the analysis on the general model.

The similarity between equations D.9 and D.13 allows to conclude that parameters b_l and E_i are not structurally identifiable either in the equivalent model. In the case of R_1, it plays the same role in equations D.13 as $\Delta N_1(t)$ in equations D.9. Therefore, like $\Delta N_1(t)$, R_1 is not structurally identifiable.

Consider again the second set of equations in the systems of equations D.9 and D.13 expressed as $\rho_1 b_l = \rho_i b_l^* \quad \forall i > 1$, where $\rho_i \in \mathbb{R}_{\geq 0}$ satisfies $\varepsilon_i^* = \rho_i \varepsilon_i$. Combining any two of these equations leads to $b_l(\rho_i - \rho_j) = 0$. Solutions exist then iff, for any two elements i and j of the lth branch, $\rho_i = \rho_j$, i.e., if $\mathbf{E}_l^p$ is proportional to $\mathbf{E}_l^{p*}$. The contrary leaves only the trivial solution $b_l = b_l^* = 0$, which can be ignored as it contradicts any prior evidence of existence of the lth branch. Out of convenience in the analysis that follows, express the proportionality relation $\varepsilon_i^* = \rho_i \varepsilon_i$ as $\varepsilon_1^* = \rho \varepsilon_1$ for the precursor of the chain and $\mathbf{E}_l^p = \rho_l \mathbf{E}_l^{p*}$ for all the elements of the lth branch. This is just a redefinition of the underscript of ρ, which now indicates the index of the branch. Equation $\rho_1 b_l = \rho_i b_l^* \quad \forall i > 1$ becomes under this notation $\rho b_l = \rho_l b_l^*$.

A common approach to circumvent the structural non-identifiability of b_l is to consider that the detection efficiencies for the same particle type are equal for all elements of the decay chain [20]. This makes $\rho_l = \rho$, which leads to $b_l = b_l^*$ and therefore renders b_l structurally identifiable. The approximation is good when the isotope-dependent effects on the detection efficiencies are negligible. When they are not, it can be a significant source of systematic uncertainty. This approach is however unnecessary if the models are conveniently reparameterized.

Define η_k as the ratio ${}^{\Delta N_1(t_k)}/_{\Delta N_1(t_1)}$. The system of equations D.9 in terms of η_k be-

comes:

$$\begin{aligned} \Delta N_1(t_1)\eta_k\varepsilon_1^p &= \Delta N_1^*(t_1)\eta_k^*\varepsilon_1^{p*} \\ \Delta N_1(t_1)\eta_k b_l \mathbf{E}_l^p &= \Delta N_1^*(t_1)\eta_k^* b_l^* \mathbf{E}_l^{p*} \end{aligned} \tag{D.14}$$

Since $\eta_1 = \eta_1^* = 1$ by definition, the first equation for $k = 1$ gives $\Delta N_1(t_1)\varepsilon_1^p = \Delta N_1^*(t_1)\varepsilon_1^{p*}$. This result applied on the same equation leads to $\eta_k = \eta_k^*$ for any value of k. This is a rather interesting result: the ratio between any two implantation parameters is structurally identifiable despite the implantation parameters independently are not. Thus, the new parameterization of the general model in terms of $\Delta N_1(t_1)$ and η_k reduces the number of structurally non-identifiable implantation parameters to a single one: $\Delta N_1(t_1)$.

Now, the fact that a non-trivial solution for the second equation of system D.9 exists only iff $\mathbf{E}_l^p$ is proportional to $\mathbf{E}_l^{p*}$ implies that the ratio of ε_p of any two elements of the branch is structurally identifiable, because $\varepsilon_i^p/\varepsilon_j^p = \cancel{\rho}\varepsilon_i^{p*}/\cancel{\rho}\varepsilon_j^{p*} \quad \forall i, j$. This suggests that there may be a reparameterization of the model in terms of ratios between elements of $\mathbf{E}_p$ that reduces the number of structurally non-identifiable parameters. The alternative parameterization indeed exists. Define the ratios $\xi_i^p = \varepsilon_i^p/\varepsilon_1^p$. In terms of these and η_k, the general model reads:

General Model

$$\boxed{r_p(t) = \Delta N_1(t_1)\varepsilon_1^p \mathbf{\Xi}_p \mathbf{\Lambda} \sum_{k=1}^{K} s(t - t_k) e^{\mathbf{A}(t-t_k)} \eta_k \boldsymbol{u}_1 \qquad \forall t \in [0, T]} \tag{D.15}$$

where $\mathbf{\Xi}_p$ is the row vector of elements ξ_i^p. Equations D.14 become:

$$\begin{aligned} \Delta N_1(t_1)\varepsilon_1^p\eta_k\xi_1^p &= \Delta N_1^*(t_1)\varepsilon_1^{p*}\eta_k^*\xi_1^{p*} \\ \Delta N_1(t_1)\varepsilon_1^p\eta_k b_l \mathbf{\Xi}_l^p &= \Delta N_1^*(t_1)\varepsilon_1^{p*}\eta_k^* b_l^* \mathbf{\Xi}_l^{p*} \end{aligned} \tag{D.16}$$

Knowing that $\xi_1^p = \xi_1^{p*} = 1$ by definition and following the same reasoning as before on equations D.14, the previous system leads to $b_l \mathbf{\Xi}_l^p = b_l^* \mathbf{\Xi}_l^{p*}$. Note that the knowledge of the detection parameters ξ_i^p in this parameterization leads to $b_l = b_l^*$, i.e., renders the parameters b_l identifiable. The opposite applies as well.

In the case of the equivalent model, a similar analysis leads to the same results for the structural identifiability of b_l and ξ_i^p. The only difference lies in the analysis of the implantation parameters. R_1, which is the single implantation parameter in the equivalent model, plays a similar structural role than $\Delta N_1(t_1)$ in the general model and therefore is also structurally non-identifiable.

The general model in the form of equation D.15 and the equivalent model in terms of ξ_i^p as presented next are the parameterizations of both models used in the estimation of the β-delayed neutron emission probability of ^{86}As and ^{91}Br in this work.

Equivalent Model

$$\boxed{r_p(t) = R_1 \varepsilon_1^p \boldsymbol{\Xi}_p \boldsymbol{\Lambda} \begin{cases} 0 & \forall t \in [0, t_1] \\ \mathbf{A}^{-1} \left[\mathbf{I} - e^{\mathbf{A}(t-t_1)} \right] \boldsymbol{u}_1 & \forall t \in [t_1, t_K] \\ e^{\mathbf{A}(t-t_K)} \mathbf{A}^{-1} \left[\mathbf{I} - e^{\mathbf{A}(t_K-t_1)} \right] \boldsymbol{u}_1 & \forall t \in [t_K, T] \end{cases}} \tag{D.17}$$

Appendix E

Nuclear and radioactive decay data

Isotope	Q_β (MeV) [126]	$Q_{\beta n}$ (MeV) [126]	$T_{1/2}$ (s)			P_n (%) [11]
^{88}Br	8.975 ± 0.004	1.922 ± 0.003	16.34	± 0.08	[17]	6.75 ± 0.18
^{94}Rb	10.283 ± 0.003	3.453 ± 0.008	2.702	± 0.005	[159]	10.24 ± 0.21
^{95}Rb	9.228 ± 0.021	4.880 ± 0.022	0.3777	± 0.0008	[7,8]	8.87 ± 0.29
^{137}I	6.027 ± 0.009	2.001 ± 0.009	24.5	± 0.2	[160]	7.33 ± 0.38
^{86}As	11.541 ± 0.004	5.380 ± 0.004	0.945	± 0.008	[17]	
^{91}Br	9.867 ± 0.004	5.781 ± 0.004	0.543	± 0.004	[7,8]	

Table E.1: Nuclear and radioactive decay data on the reference isotopes (^{88}Br, ^{94,95}Rb and ^{137}I) and the isotopes of interest (^{86}As and ^{91}Br).

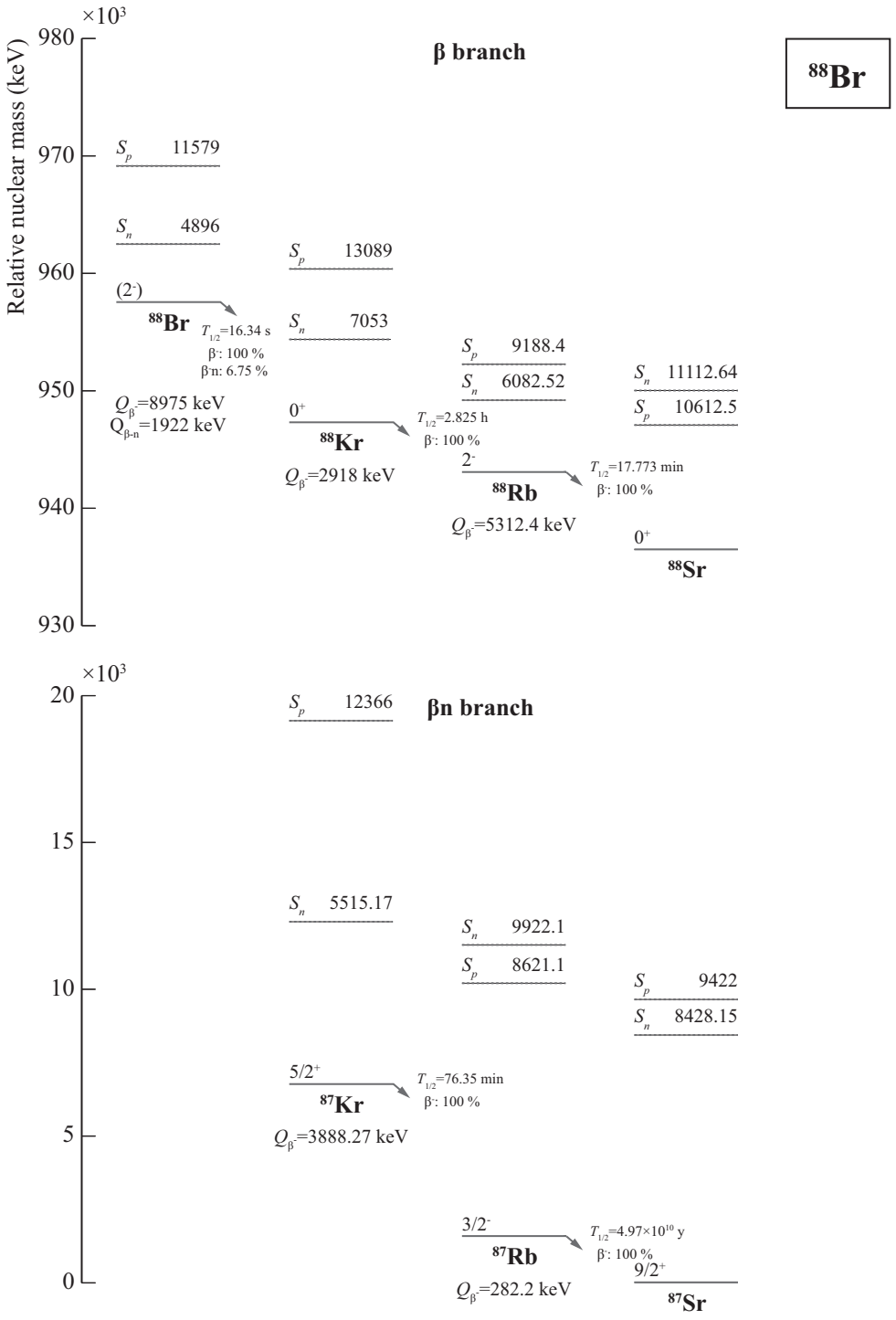

Figure E.1: Mass-chain radioactive decay scheme of ^{88}B. The ground and relevant isomeric (with half-lives greater than 1 ms) states are represented by heavy lines whose vertical position represents the mass of the nuclide relative to the most beta-stable isobar. The neutron and proton separation energies are represented by dashed lines. Lines were separated when necessary to accommodate the labels above. All nuclear and radioactive decay data were taken from ENSDF [7,8], except P_n for ^{88}B, which was taken from [11].

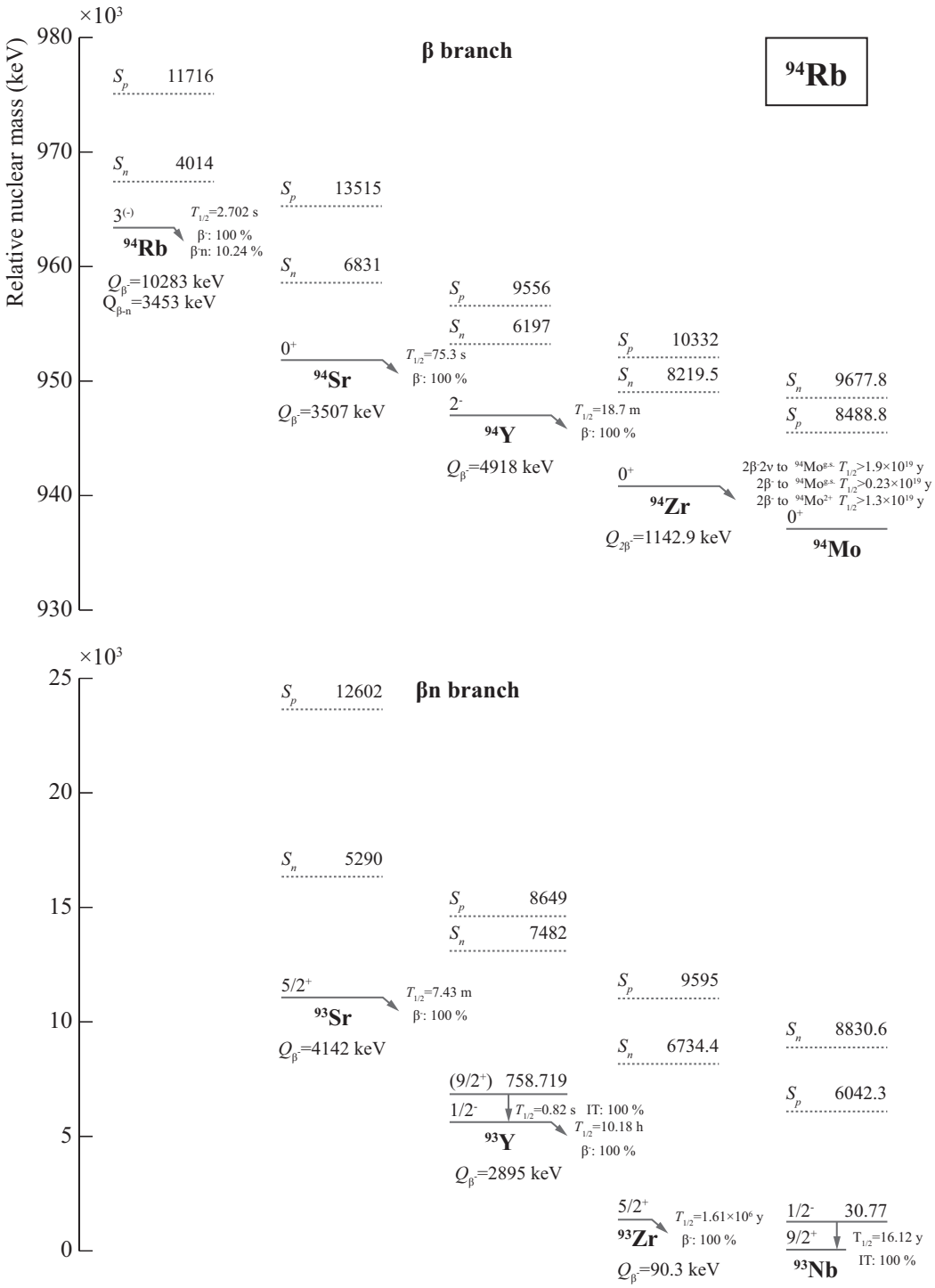

Figure E.2: Mass-chain radioactive decay scheme of ^{94}Rb. The ground and relevant isomeric (with half-lives greater than 1 ms) states are represented by heavy lines whose vertical position represents the mass of the nuclide relative to the most beta-stable isobar. The neutron and proton separation energies are represented by dashed lines. Lines were separated when necessary to accommodate the labels above. All nuclear and radioactive decay data were taken from ENSDF [7,8], except P_n for ^{94}Rb, which was taken from [11].

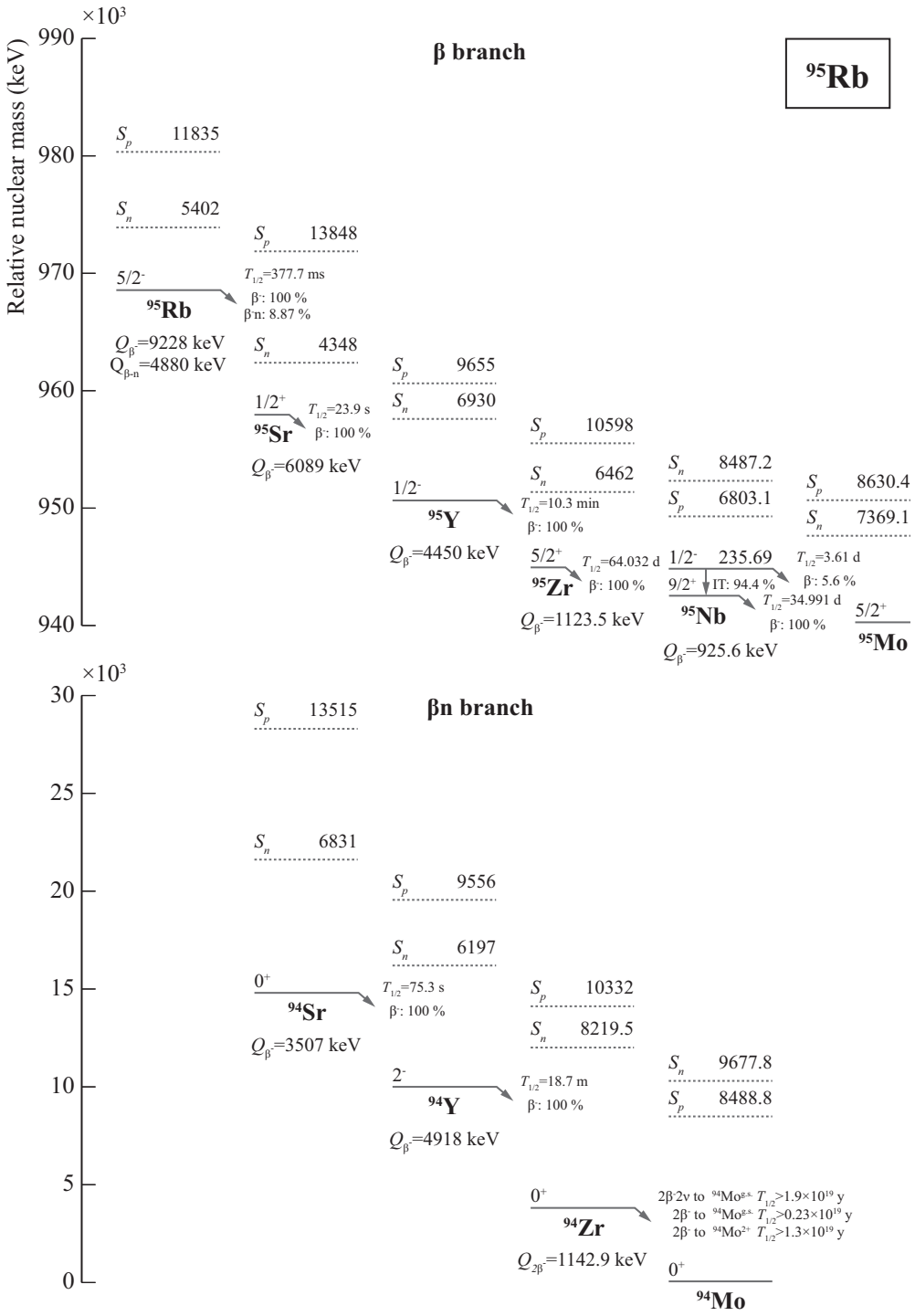

Figure E.3: Mass-chain radioactive decay scheme of ^{95}Rb. The ground and relevant isomeric (with half-lives greater than 1 ms) states are represented by heavy lines whose vertical position represents the mass of the nuclide relative to the most beta-stable isobar. The neutron and proton separation energies are represented by dashed lines. Lines were separated when necessary to accommodate the labels above. All nuclear and radioactive decay data were taken from ENSDF [7,8], except P_n for ^{95}Rb, which was taken from [11].

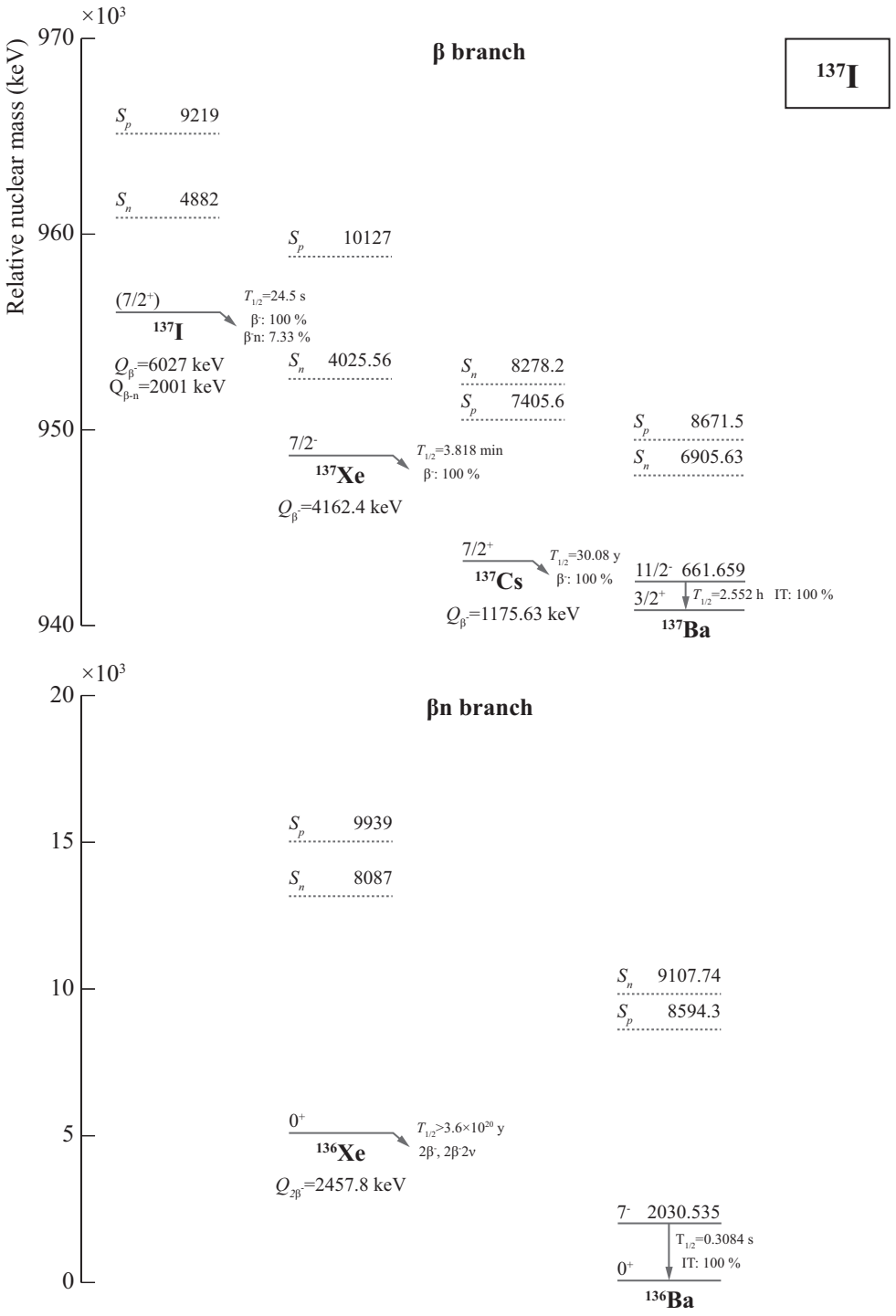

Figure E.4: Mass-chain radioactive decay scheme of ^{137}I. The ground and relevant isomeric (with half-lives greater than 1 ms) states are represented by heavy lines whose vertical position represents the mass of the nuclide relative to the most beta-stable isobar. The neutron and proton separation energies are represented by dashed lines. Lines were separated when necessary to accommodate the labels above. All nuclear and radioactive decay data were taken from ENSDF [7,8], except P_n for ^{137}I, which was taken from [11].

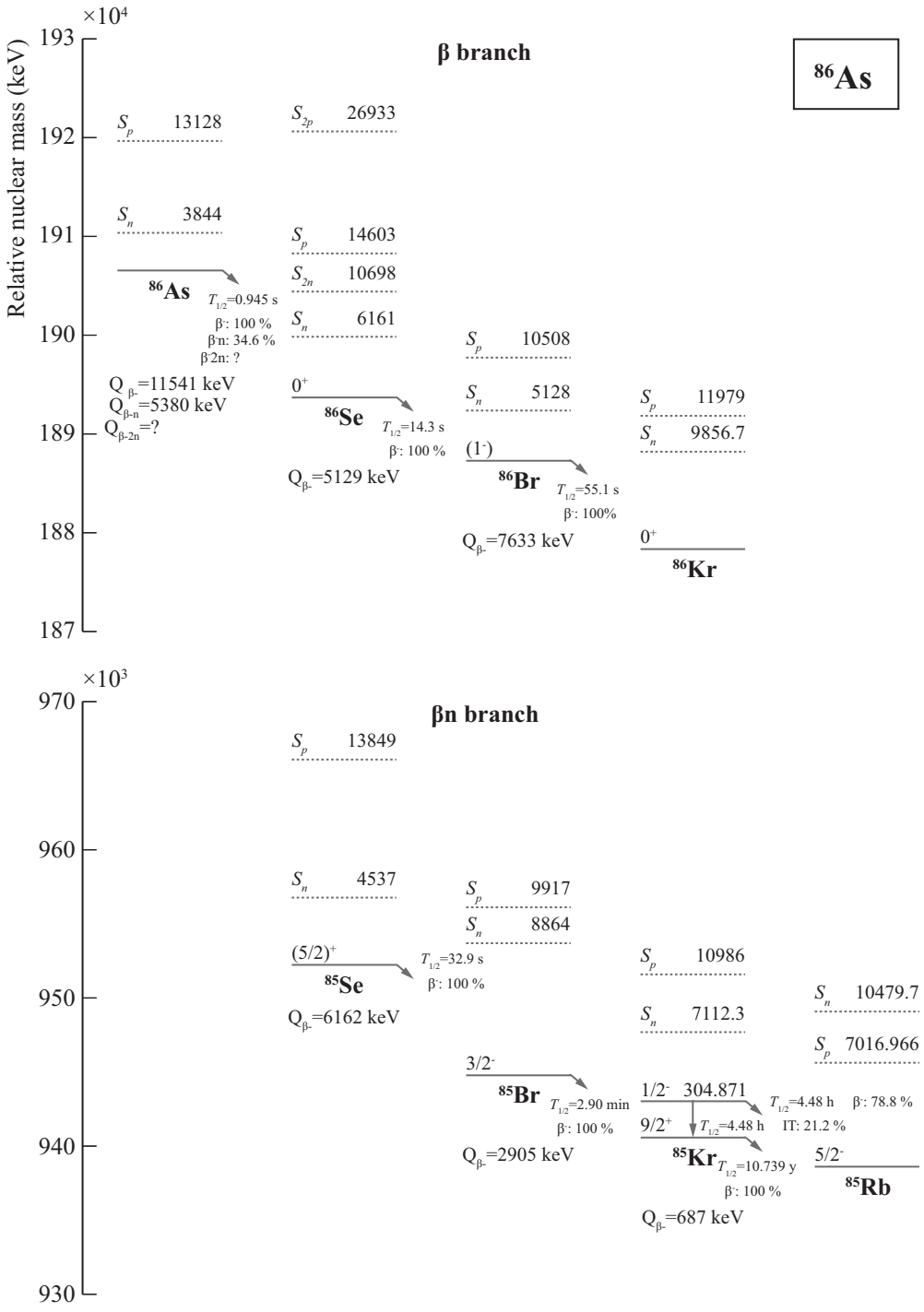

Figure E.5: Mass-chain radioactive decay scheme of ^{86}As. The ground and relevant isomeric (with half-lives greater than 1 ms) states are represented by heavy lines whose vertical position represents the mass of the nuclide relative to the most beta-stable isobar. The neutron and proton separation energies are represented by dashed lines. Lines were separated when necessary to accommodate the labels above. All nuclear and radioactive decay data were taken from ENSDF [7,8], except P_n for ^{86}As, which is the reported obtained in this work. Continued on next page.

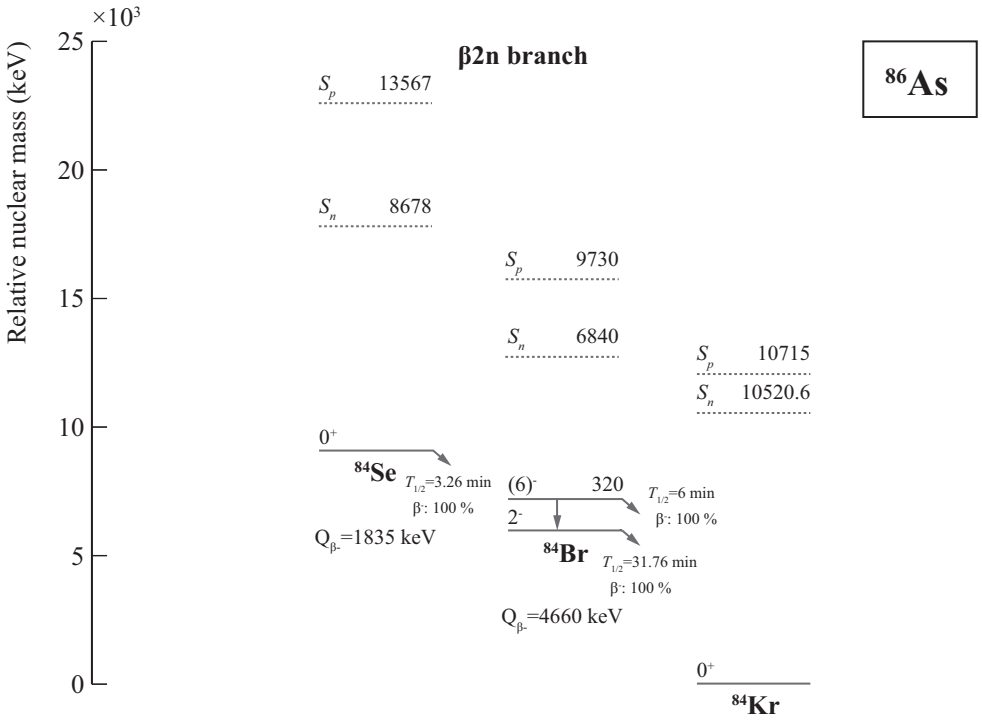

Figure E.5: (Continued from previous page) Mass-chain radioactive decay scheme of ^{86}As. The ground and relevant isomeric (with half-lives greater than 1 ms) states are represented by heavy lines whose vertical position represents the mass of the nuclide relative to the most beta-stable isobar. The neutron and proton separation energies are represented by dashed lines. Lines were separated when necessary to accommodate the labels above. All nuclear and radioactive decay data were taken from ENSDF [7,8], except P_n for ^{86}As, which is the result reported in this work. Continued on next page.

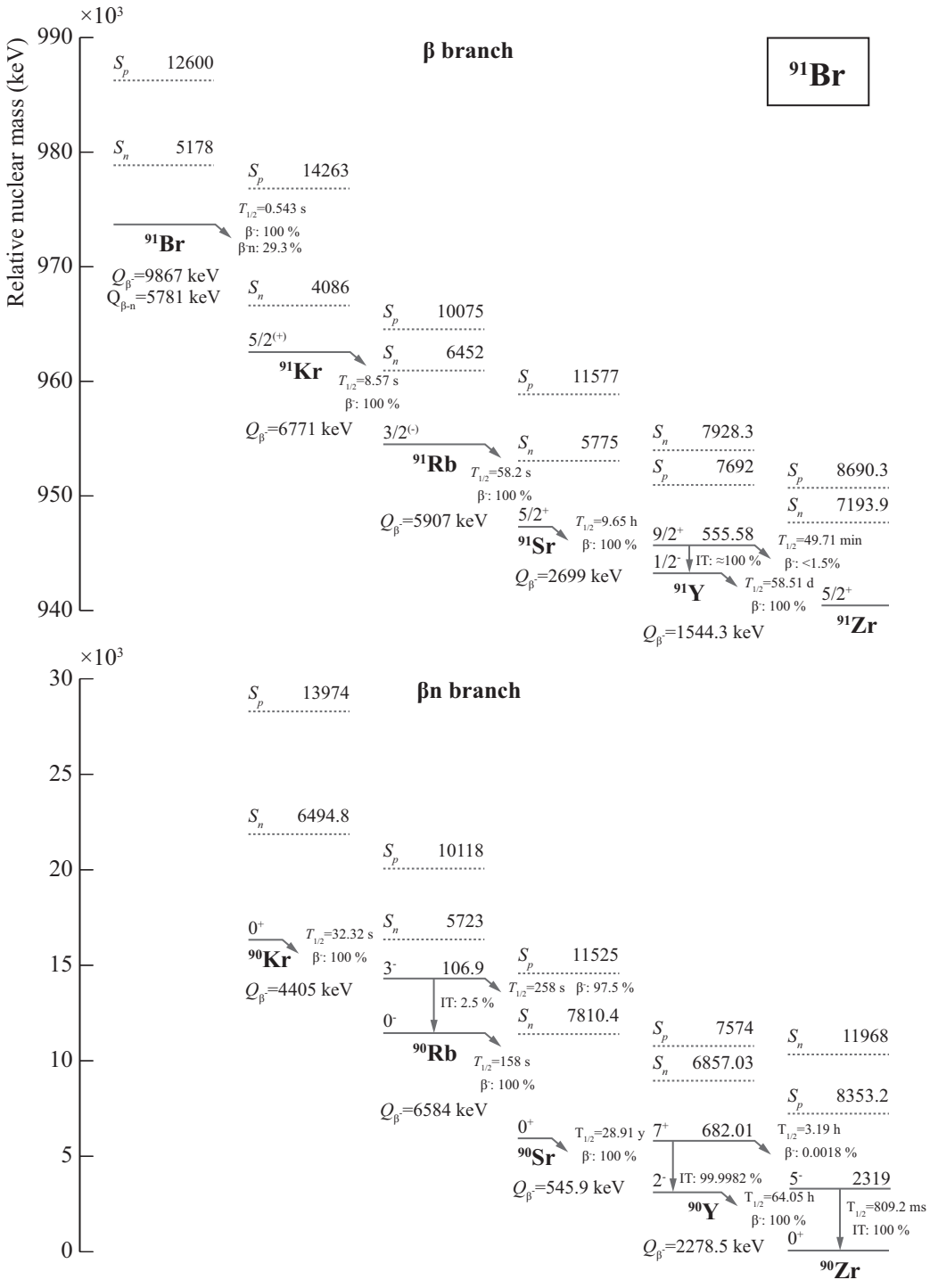

Figure E.6: Mass-chain radioactive decay scheme of ^{91}Br. The ground and relevant isomeric (with half-lives greater than 1 ms) states are represented by heavy lines whose vertical position represents the mass of the nuclide relative to the most beta-stable isobar. The neutron and proton separation energies are represented by dashed lines. Lines were separated when necessary to accommodate the labels above. All nuclear and radioactive decay data were taken from ENSDF [7,8], except P_n for ^{91}Br, which is the result reported in this work.